Insights into the shallow intrusion of rhyolite from field, textures, and drilling the IDDP-1 magma well, Krafla, Iceland

A thesis submitted in partial fulfilment of the requirements for the degree of

Doctor of Philosophy

Elodie Saubin

School of Earth and Environment

University of Canterbury

January 2020

On top of the fossil rhyolite magma chamber of Slaufrudalur, Iceland, a stormy day. View towards the South.

Eyes on the rock

Hold after hold

We reach a peak

Below unseen

Acknowledgements

These three years of Ph.D in a country I had never been before, surrounded by a language I was at first barely speaking, literally at the other side of the world from my home country, are rich of people to acknowledge for their support.

Firstly, I want to thank Hugh Tuffen, supervisor since my Master years, who was the key towards all of these exciting projects. My choice of working with him was this kind of decisive turnover that can happen in one's life. Hugh, thanks for being Hugh, thanks for having survived so far.

Huge greetings to my primary Ph.D. supervisor Ben Kennedy, who made of these three years a path punctuated by beers and BBQs. Thanks for this great balance in your supervision between freedom and feedbacks, your continuous presence, and the diversity of approaches I learned from you.

Thanks obviously to the rest of my dream supervision team - Marlene Villeneuve, for the great dynamic we had together on the field – Ian Schipper, for guiding me in the excitement of EPMA and 3D imaging – Alex Nichols, the favourite recipient of my SOS alerts when fighting with geochemistry. Thanks also to these special additions in supervision, with Anette Mortensen, primordial provider of drilling engineering knowledge, and Jim Cole, the last polisher of most Chapters. Thanks to the last-minute helpers Méline, Janina, Leru', Salahedine, and Georgie.

The University of Canterbury has an exceptionally great team of administrative and technician staff. My deepest acknowledgements to Janet and Rebekah; Jonathan, Rob, Matt, Chris, John and Anekant; Sacha, Sarah and Cathy, who all super kindly guided me in the use of laboratories, field gear, software and other technological challenges. You all made my life at UC incredibly easy. I also shared this doctoral path with our large and diversified postgrad team, source of very happy moments, escapes and mutual support. Special thanks to the French and Brazilian teams.

Thanks to the MBIE for funding this Ph.D. and the many travels which in this context took me for a world tour. Thrice. Thanks to the local Icelandic farmers who welcomed us on their lands with cakes and minerals. Thanks to the National Power Company of Iceland, for hosting us on this majestuous volcanic land.

Missing land, missing friends and missing family, these feelings were absolutely appeased by the continuous discovery of postcards and French cheese in my mail box. Thank you so much, cherished people from the other hemisphere! And many thanks obviously to the Edenya community, my anker to the French language. This procrastinating passion eased the difficult months and kept me ashore.

Thanks to my flatmates Evelyne, Ben and Tom, who accepted that during the last six months the dinner table became my office, and never complained to flat with a zombie.

Thanks Salahedine for your primordial love, care, help and support during these long three years, the foundation on which I could stand. Thanks Prashant for the dance breaks, thanks Merisha for having kidnapped me when I was drowning. Thanks Nick, for the dreams we share, the present we balance towards, and for indubitably having made New Zealand a place I want to come back to.

Thanks, eventually, to all things I enjoyed here. For New Zealand volcanoes to exist – Tēna koe Ruaumoko. For cliffs to be climbed, waves to be surfed, hot pools to be found - Tēna koe Papatūānuku. World, I am coming back to you.

Kia Ora

Abstract

This thesis focusses on shallow intrusions of rhyolite, in the context of heat resources for geothermal development. Rhyolite is the dominant sub-surface magma type at the roots of some of the most vigorous geothermal systems worldwide, including Krafla, in Iceland, and the Taupo Volcanic Zone, in New Zealand. Supercritical fluids located in deeper and hotter environments than those conventionally extracted provide more efficient energy production and greater power output. As potential reservoir, the margins of magma chambers constitute an enticing new target.

The Iceland Deep Drilling Project consortium accidentally drilled magma in 2009 at Krafla, at 2 km depth. This IDDP-1 well was the hottest geothermal well worldwide, with high productive capability (35 MWe). Based on this experience, a new consortium, the Krafla Magma Testbed (KMT), aims to drill back into this magma body for geothermal exploration, creation of research opportunities and monitoring. Improved scientific knowledge of the targeted reservoir is critical to the success of the project, and is the topic of this thesis.

The main objectives of this work are (1) to characterize rock properties at the margins of shallow rhyolite intrusions, specifically around the active Krafla rhyolite magma body, (2) to constrain the size and structure of this intrusion, and (3) to better understand magma response to drilling. Results are obtained via four complementary approaches:

Firstly, fossil rhyolite intrusions in Iceland are used as a macro-scale analogy of rock properties around active intrusions. Four field case studies are compared to investigate the host rock response to intrusion, with field measurement of rock strength, permeability and fracture density, as well as textural and lithological information on the intrusions.

Secondly, chilled margins thickness and the extent of impacted host rocks of a further 14 intrusions that emplaced at <1 km depth and are <1 km thick are compared to a numerical model of heat transfer by thermal diffusion. Deviation from the heat diffusion model is discussed to determine the dominant processes of heat exchange at the magma/host rocks interface.

Thirdly, insights specific to the active rhyolite body at Krafla are gained through micro-scale characterisation of magmatic glass and host felsite drilling particles. These were retrieved from the IDDP-1 well as a time-series, after the drilling bit encountered magma. Analyses of texture

and geochemistry are combined with previous results from the literature to examine possible scenarios of magma genesis, storage and reaction to drilling.

Fourthly, drilling logs recorded during the IDDP-1 drilling are examined to interpret lithology and rock mass conditions in the blind zone at the chamber margin, from which no cuttings were returned to the surface. Monitored drilling parameters are used to identify rock masses in terms of relative strength, fracture properties and permeability.

The field results reveal that the impact of shallow rhyolite intrusions on surrounding host rocks is dependent on the initial host rocks properties, which in turn influence the style of magma propagation. Initially weak, porous and highly-permeable conglomerate and hyaloclastite respond by pore occlusion, with permeability decreasing accordingly. Their ductile compaction accommodates magma propagation, allowing irregular intrusive geometries to form. In contrast, initially strong, low-permeability basaltic lava and welded ignimbrite respond by brittle deformation, with intense fracturing associated with weakening.

Rhyolitic intrusions in Iceland have variably sized and fractured chilled margins, with a maximum possible thickness of ~7 m. The aureole width in host rocks increases with increasing intrusion size, but aureole formation around < 10 m wide intrusions requires more rapid heat transfer than provided by conduction alone. For these small intrusions, intense fracture development in chilled margins could allow fluid advection and convection to significantly boost the heat transfer.

At Krafla, isotopic compositions and thermodynamic analysis suggest that the rhyolite melts formed by partial melting of felsite possibly triggered by the heat released from a shallow magma intrusion, and promoted by hydrothermal circulation. The presence of lenses of distinct magma composition and texture does not support intense magma convection. The main brown melt generated by high degree felsite partial melting is overlain by a clear melt formed by low-degree partial melting, and which is richer in silica, crystals, and vesicles. As the drill bit approached the magma, it encountered a ~14.5 m thick weak zone, where permeability have been enhanced by thermal cracking of hot rocks in contact with cold drilling fluids. Below this, a stronger ~8 m thick lithology, possibly damaged by the intrusion, separated the magma from the overlying hydrothermal system. Magma then responded to the encounters by limited bubble growth, deformation and nucleation, and caused systematic and consistent reaction of the drilling parameters, revealing it was approached nine times over three drilling attempts.

The trend revealed by the field data implies that knowledge of the aureole extent can inform the thickness of the intrusive shallow rhyolite body impacting the host rock. Based on our interpretation of lithologies around the active intrusion at Krafla, the most likely range of aureole size (8-22 m) implies a 700-1100 m thick magma body, considering limitations provided by the analogy examination. This large dimension suggests that the rhyolite may be older than the last eruptive activity (Krafla Fires, 1975-1984).

The results and implications of this thesis contribute towards an understanding of shallow rhyolite intrusions as roots for hydrothermal systems. The multidisciplinary approach also helps to bridge the fields of drilling engineering, rock mechanics and volcanology, which is essential for future developments of geothermal energy production.

Table of contents

List of Figures

List of Tables

UNIVERSITY OF CANTERBURY
Te Whare Wānanga o Waitaha
CHRISTCHURCH NEW ZEALAND

Deputy Vice-Chancellor's Office
Postgraduate Research Office

Co-Authorship Form

This form is to accompany the submission of any thesis that contains research reported in co-authored work that has been published, accepted for publication, or submitted for publication. A copy of this form should be included for each co-authored work that is included in the thesis. Completed forms should be included at the front (after the thesis abstract) of each copy of the thesis submitted for examination and library deposit.

Please indicate the chapter/section/pages of this thesis that are extracted from co-authored work and provide details of the publication or submission from the extract comes:
Chapter 2 - Comparative field study of shallow rhyolite intrusions in Iceland: emplacement mechanisms and impact on country rocks
Published in the Journal of Volcanology and Geothermal Research

Please detail the nature and extent (%) of contribution by the candidate:
95 % of the research is the candidates original work. The fieldwork, results extraction and interpretation, and writing of the manuscript was completed by the candidate. Co-authors provided extended assistance on the field for data collection, dialogue, suggestions for revision, and editorial comments

Certification by Co-authors:

If there is more than one co-author then a single co-author can sign on behalf of all

The undersigned certifies that:

- The above statement correctly reflects the nature and extent of the PhD candidate's contribution to this co-authored work
- In cases where the candidate was the lead author of the co-authored work he or she wrote the text

Name: *Ben Kennedy* Signature: Date: *18/01/2020*

UNIVERSITY OF CANTERBURY
Te Whare Wānanga o Waitaha
CHRISTCHURCH NEW ZEALAND

Deputy Vice-Chancellor's Office
Postgraduate Research Office

Co-Authorship Form

This form is to accompany the submission of any thesis that contains research reported in co-authored work that has been published, accepted for publication, or submitted for publication. A copy of this form should be included for each co-authored work that is included in the thesis. Completed forms should be included at the front (after the thesis abstract) of each copy of the thesis submitted for examination and library deposit.

Please indicate the chapter/section/pages of this thesis that are extracted from co-authored work and provide details of the publication or submission from the extract comes:

Chapter 3 - Rapid heat transfer at the margins of thin rhyolite intrusions

Will be submitted for publication at the time of the Ph.D defense.

Please detail the nature and extent (%) of contribution by the candidate:

80 % of the research is the candidates original work. The fieldwork, results extraction and interpretation, and writing of the manuscript was completed by the candidate. Co-authors provided the modelling script and insight, assistance on the field, dialogue, suggestions for revision, and editorial comments

Certification by Co-authors:

If there is more than one co-author then a single co-author can sign on behalf of all

The undersigned certifies that:

- The above statement correctly reflects the nature and extent of the PhD candidate's contribution to this co-authored work
- In cases where the candidate was the lead author of the co-authored work he or she wrote the text

Name: *Ben Kennedy* Signature: Date: *18/01/2020*

UNIVERSITY OF CANTERBURY
Te Whare Wānanga o Waitaha
CHRISTCHURCH NEW ZEALAND

Deputy Vice-Chancellor's Office
Postgraduate Research Office

Co-Authorship Form

This form is to accompany the submission of any thesis that contains research reported in co-authored work that has been published, accepted for publication, or submitted for publication. A copy of this form should be included for each co-authored work that is included in the thesis. Completed forms should be included at the front (after the thesis abstract) of each copy of the thesis submitted for examination and library deposit.

Please indicate the chapter/section/pages of this thesis that are extracted from co-authored work and provide details of the publication or submission from the extract comes:

Chapter 4 - Textural and geochemical window into the IDDP-1 rhyolitic melt, Krafla, Iceland, and its reaction to drilling

Has been submitted for publication in GSA Bulletin

Please detail the nature and extent (%) of contribution by the candidate:

95 % of the research is the candidates original work. The sample preparation, textural and chemical analyses, the construction of the story, and writing of the manuscript was completed by the candidate. Co-authors provided TGA, X-ray tomography and TCEA data, as well as dialogue, suggestions for revision, directions for interpretation and editorial comments

Certification by Co-authors:

If there is more than one co-author then a single co-author can sign on behalf of all

The undersigned certifies that:

- The above statement correctly reflects the nature and extent of the PhD candidate's contribution to this co-authored work
- In cases where the candidate was the lead author of the co-authored work he or she wrote the text

Name: *Ben Kennedy* Signature: Date: *18/01/2020*

UNIVERSITY OF CANTERBURY
Te Whare Wānanga o Waitaha
CHRISTCHURCH NEW ZEALAND

Deputy Vice-Chancellor's Office
Postgraduate Research Office

Co-Authorship Form

This form is to accompany the submission of any thesis that contains research reported in co-authored work that has been published, accepted for publication, or submitted for publication. A copy of this form should be included for each co-authored work that is included in the thesis. Completed forms should be included at the front (after the thesis abstract) of each copy of the thesis submitted for examination and library deposit.

Please indicate the chapter/section/pages of this thesis that are extracted from co-authored work and provide details of the publication or submission from the extract comes:

Chapter 5 - A method to inform rock properties in blind zones from drilling logs. Application to the IDDP-1 well

Will be submitted for publication as part of another manuscript

Please detail the nature and extent (%) of contribution by the candidate:

99 % of the research is the candidates original work. The review, the method development, the application to the IDDP-1 case study and interpretation, and writing of the manuscript was completed by the candidate. The chart for rock properties interpretation is a co-work, and co-authors also provided geothermal engineering insight, dialogue and editorial comments

Certification by Co-authors:

If there is more than one co-author then a single co-author can sign on behalf of all

The undersigned certifies that:

- The above statement correctly reflects the nature and extent of the PhD candidate's contribution to this co-authored work
- In cases where the candidate was the lead author of the co-authored work he or she wrote the text

Name: *Ben Kennedy* Signature: Date: *18/01/2020*

Chapter 1 – Introduction

In the current transition into renewable energies, geothermal resources are gaining increasing attention from governments. Their use is geographically limited to active hydrothermal fields or areas of high heat flow, mostly distributed around volcanic centres and therefore unequally distributed around the globe (e.g. Reinsch et al., 2017). The countries with the largest geothermal energy production capacity are the US, Indonesia, Philippines, Turkey, New Zealand, Mexico, Italy and Iceland (Chamorro et al., 2012). This thesis is focused on Iceland specifically, and on the potential for utilising magma directly to produce geothermal energy, and providing insights on the rhyolite-sourced analogue geothermal systems in New Zealand.

This thesis is motivated by improving our knowledge of the margins of rhyolite magma chambers and their potential to generate geothermal energy. This work and its conclusions are restricted to shallow rhyolite intrusions (<2-3 km depth), as proposed targets for geothermal drilling, investigated by the Krafla Magma Testbed (KMT) project for an extensive scientific and geothermal exploration at Krafla, Northern Iceland. The work described herein contributes directly to KMT research, as well adding to the knowledge of magma storage and margin properties, by addressing these main questions:

1. What are the rock properties at the margins of shallow rhyolite intrusions, specifically around the active Krafla rhyolite magma body?
2. What are the size and structure of the active Krafla rhyolite intrusion?
3. How does magma react to drilling, and drilling react to magma?

1.1 Thesis format

This thesis has been written to allow individual chapters to be published as is. Each core chapter, Chapters 2, 3, 4 and 5, represents a published or publishable piece of work, and contains the necessary literature review. They build on each other as a natural progression towards a conceptual model (Fig.1.6).

Chapter 1 sets out the thesis research questions and aims. In order to avoid repetition, I do not present an extensive introductory literature review, but a very brief introduction to the

geological and geothermal context of the thesis. Specific research questions and aims are summarised in Table 1.

In Chapter 2, I use fossil rhyolite intrusions in Iceland as analogues to the active rhyolite Krafla intrusion, to investigate rock properties and lithologies at the margins. I compare four intrusions from three field sites, within four country rock types, using in-field measurements of rock permeability and hardness, fracture mapping, and information on intrusive emplacement. I investigate how the rock responds to intrusion, including how its properties change towards the margins.

In Chapter 3, I extend the field-case study to 14 intrusions in order to investigate intrusion-scale variations at the margins, in the impacted country rocks (aureole) and in the chilled rhyolite. I complement my results with a thermal model and interpret the heat flux at the interface, concluding on the role and implications of fluids and heat convection / advection at the margins.

Chapter 4 focusses on the active Krafla rhyolite intrusion. I use the cuttings (glass and felsite) recovered from the well after the magma interception, combined with the main drilling events, to constrain the origin of the magma, its storage structure and its reaction to drilling. Methods include componentry, vesicle texture and geochemistry. I use these to interpret magmatic processes occurring at the margins of the active Krafla rhyolite magma body.

Over these three chapters, the focus therefore changes from country-rocks at the margins, to the interface including the chilled magma, to the magma at the intrusion roof. Chapter 5 considers the geothermal drilling context. I develop a method to interpret rock properties from the evolution of drilling parameters, in blind zones where no cuttings are retrieved and thus there are no direct insights on the geology. I apply this method to the active Krafla case study, and based on the findings of the previous three chapters I interpret rock properties and lithologies at the margins of the Krafla magma body, and constrain its size.

Chapter 6 summarizes the key findings of this thesis and their implications for magma drilling in general, the KMT especially, and wider research concerning rhyolite intrusions. The sustainable role of geothermal energy development is addressed in line with this thesis, and ideas are explored for future research.

TABLE 1.1. THESIS ORGANISATION

	Questions addressed	Specific aims
Chapter 2	*What are the properties of country rocks at the margins of shallow rhyolite intrusions?*	Measure rock strength, permeability and fracturing around 3 shallow fossil intrusions, within 4 different country rocks.
	How might country rock influence the emplacement of the intrusion?	Record lithological information and magma emplacement textures to relate to observations of surrounding rock properties.
Chapter 3	*Does the thickness of intrusion impact the extent of damage and alteration in country rocks and the extent of the chilled margins?*	Record the thicknesses of altered/damaged aureole and chilled margins for a range of shallow rhyolite intrusion sizes.
	What are the dominant mechanisms of heat transfer between the magma and the country rock?	Build a simple numerical model of heat transfer by conduction, to compare with field data, constrain and discuss the involved heat exchange processes
Chapter 4	*What is the magma structure in the intrusion margin?*	Analyse the time series of IDDP-1 obsidian and felsite cuttings, in terms of texture (vesicles, crystals) and chemistry (major element, water content, hydrogen isotopes).
	How did magma react to drilling?	Compare and place into context the new IDDP-1 data sets with those from recent studies.
	What is the origin of the IDDP-1 intrusion?	Construct a conceptual model for the active rhyolitic magma body at Krafla.
Chapter 5	*What are the rock properties in the blind zone as the IDDP-1 intrusion is approached?*	Review drilling parameters and their relationship to rock properties at depth.
		Develop a method to interpret rock properties from monitored drilling parameters only.
	What is the size of the intrusion?	Apply the method to interpret the IDDP-1 blind zone interval. Integrate the results from Chapters 2, 3, 4 to constrain the interpretations.
Chapter 6	*What are the overarching conclusions of the thesis?*	Present the key findings in the context of a conceptual model.
	What is the role of this thesis within future research directions towards sustainable energy?	Examine the implications for a sustainable geothermal context and highlight key directions for future work.

1.2 Background

1.2.1 Background geology

The focus of this thesis is a shallow rhyolite magma in Iceland. However, the University of Canterbury, hosting this work, is located in New Zealand, also a major innovator in geothermal energy. Thus naturally, New Zealand's geothermal setting is compared to Iceland's and how the results of this thesis apply to New Zealand are examined.

Iceland is located on the rift between the Eurasian and North-American plates. Magmatic activity is dominantly basaltic in composition (Walker, 1974; Sigurdsson, 1977; Thordarson and Larsen, 2007). However, rhyolitic and andesitic magma are generated at Krafla and other central volcanoes by partial melting of altered basaltic crust and/or fractional crystallisation (e.g. Jónasson, 1994; Gunnarsson et al., 1998). The resultant rhyolites have higher temperatures and lower viscosities compared to subduction zone rhyolites such as those in New Zealand (Reid, 1983; Zierenberg et al., 2012). Krafla, on the extensional rift in NE Iceland, is a caldera fed by a bimodal magma plumbing system between 2 and 8 km depth (Einarsson, 1978; Kennedy et al., 2018). These extended reservoirs cause eruptions from caldera faults and vents, and regional fissures. The host caldera-fill formations are mostly hyaloclastites and lavas, with minor glacial sediments (Þorsteinsdóttir, 2017; Fig.1.1).

The key locations that are referred to throughout this thesis, geothermal fields and fossil rhyolite intrusions in Iceland, are identified in Figure 1.1.

With the Pacific plate subducting under northern New Zealand, most of the New Zealand geothermal activity occurs in the extensional Taupo Volcanic Zone (TVZ) running parallel to the subduction zone (Wilson et al., 1995; Cole and Spinks, 2009). The TVZ is one of the most active rhyolitic centres on Earth, where the geothermal resources have a long history of exploitation and the geology has been extensively studied (e.g. Wilson et al., 1995; Harrison and White, 2004; Fig.1.2). The hosting rocks are greywacke or andesitic and rhyolitic volcanic rocks (including ignimbrites) associated with calderas and buried cone volcanoes (Rosenberg et al., 2009; Milicich et al., 2013a; Siratovich et al., 2014; McNamara et al., 2014). In contrast to Krafla, evidence for contemporary shallow rhyolitic bodies in the TVZ is scarce, with subduction zone rhyolite having lower temperatures and higher viscosity than Icelandic rhyolites (Zierenberg et al., 2012; Reid, 1983). Mafic intrusive reservoirs in the lower crust are suspected to be the heat source for the rhyolitic plumbing system extending upwards within the

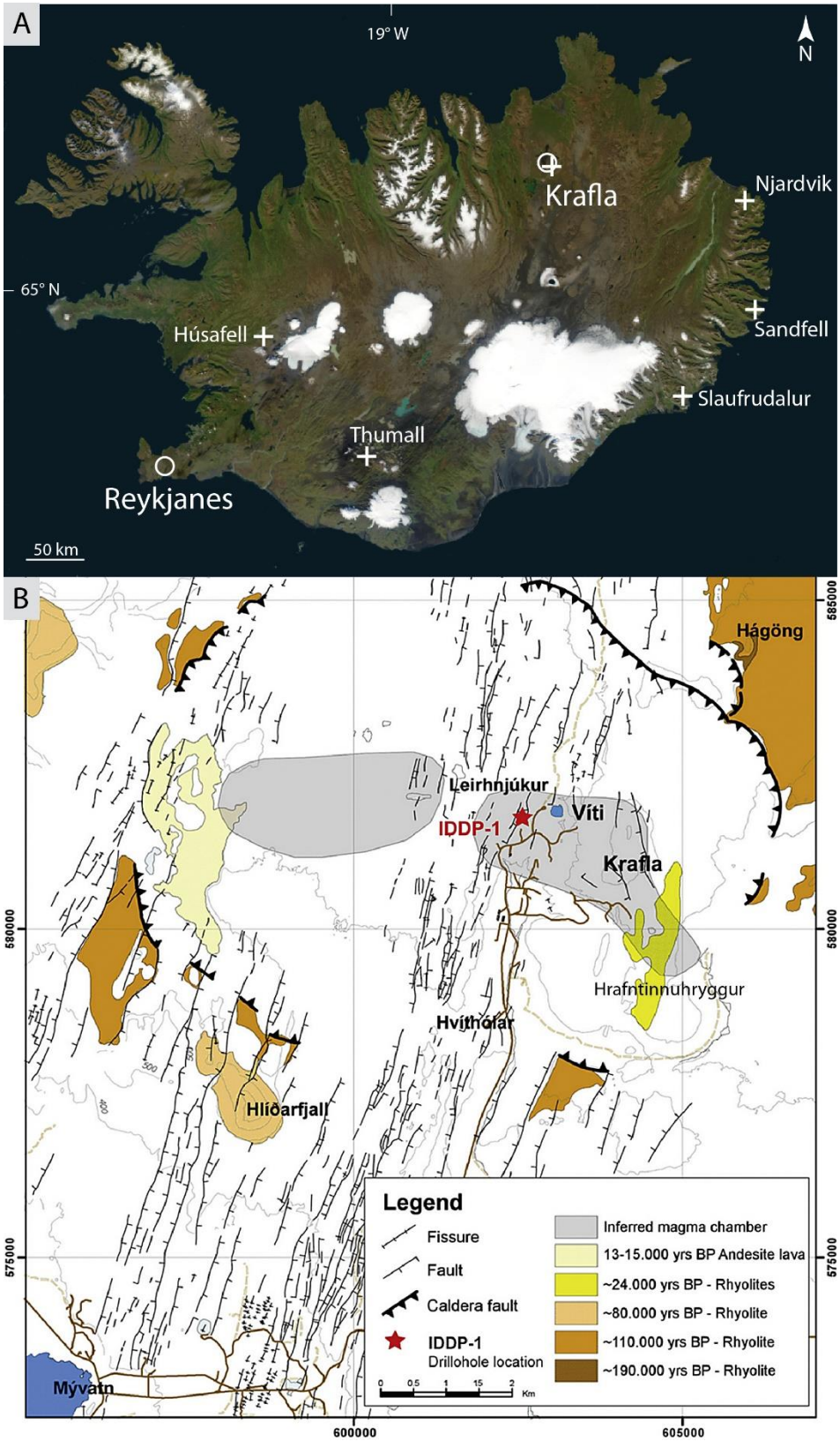

Figure 1.1. Maps of Iceland and the Krafla area, showing the key locations for this thesis. A) Geothermal fields (circles), and field areas for Chapters 2 and 3 (crosses). B) Krafla caldera bisected by a NNE–SSW fissure swarm. The red star marks the location of the IDDP-1 well (Chapters 4 and 5). Hrafntinnuhryggur is another field area included in Chapters 2 and 3. After Masotta et al., 2018.

upper crust (Harrison and White, 2004; Charlier et al., 2005; Shane et al., 2008). As such, it is still expected to find active rhyolite intrusions at shallow depth in the TVZ, within the caldera volcanoes (Fig.1.2). Most of the surface fossil rhyolitic bodies are interpreted to be lava domes, although it is sometimes unknown whether they are lava or intrusions (e.g. Wood et al., 2001; Milicich et al., 2013b). The shallow volcanic lithologies encountered by geothermal wells are mostly eruptive deposits, with rare occurrence of plutonic rocks (Browne et al., 1992; Brown et al., 1998).

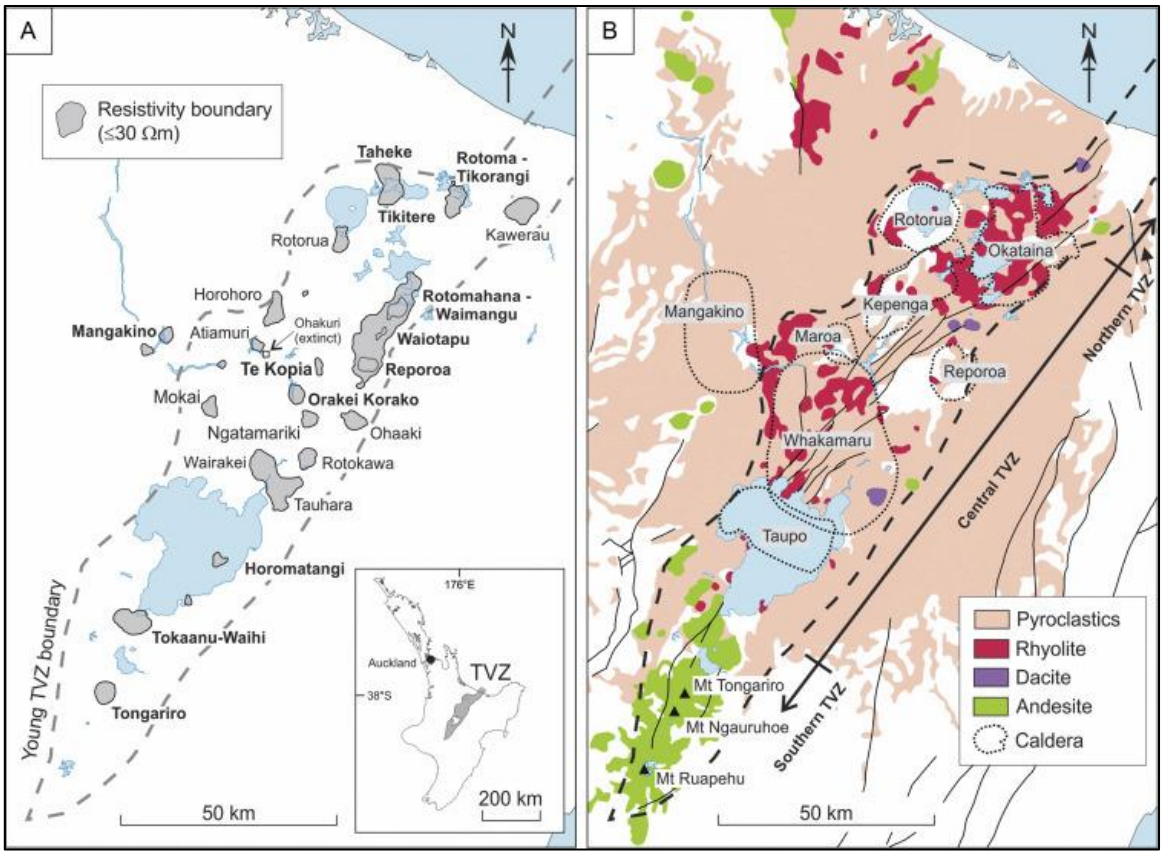

Figure 1.2. Simplified maps of the Taupo Volcanic Zone (TVZ). A) Outlines of geothermal fields. The inset map indicates the location of TVZ on the North Island of New Zealand. B) Geology, caldera outlines and fault structures. After Simpson and Bignall, 2016.

Rhyolitic activity including intrusion of shallow rhyolite magma bodies (e.g. Wilson et al., 1995) is common in the TVZ and Krafla. These bodies can be large and are capable of producing significant eruptible volumes. Rhyolite magma has accumulated in a reservoir beneath Lake Taupo in the TVZ (Illsley-Kemp et al., 2019), and above the main basaltic chamber at Krafla. Many similarities exist despite the different tectonic settings and magma generation mechanisms: both systems are dominated by caldera volcanism and rifting, with normal faults controlling large scale permeability (e.g. Einarsson, 1978; Wilson et al., 1995); and locally variably fractured and altered pyroclastic rocks and lavas form pathways barriers and reservoirs, punctuated by dykes and sills (e.g. Rosenberg et al., 2009; Þorsteinsdóttir, 2017). At both settings these intrusive complexes become the shallow roots (i.e. direct source) of some of the most vigorous hydrothermal systems used for geothermal energy production globally.

1.2.2 Geothermal energy development

Geothermal energy is currently largely under-used, representing <1% of energy consumption worldwide, while the potential is 10-100 times larger (World Energy Council, 2010; Lavallée et al., 2020). Both Iceland and New Zealand have a long history of geothermal energy exploration and use, and actively seek to develop geothermal technology. Geothermal energy provides nearly 90% of the space heating in Icelandic buildings, and more than 30% and 17% of Iceland and New Zealand's electricity, respectively (Nielsen et al, 2000; Arnórsson et al, 2008; Climo et al., 2016).

The research in this thesis is taking a step beyond traditional geothermal resources and is focusing on drilling into magma to explore the possibility of using geothermal energy from the magma/rock interface. Typically, capped hydrothermal fluids (mostly meteoric water) can be extracted at a temperature up to 300 °C from 1-3 km deep (Elders et al., 2019) and liquid magma is avoided in reason of engineering challenges within this extreme and poorly known environment. As fluids are brought back to the surface in the production well, the pressure drop causes them to cross the phase boundary and change into a hot vapor. This geothermal vapor goes through turbines, which ultimately redistributes heat and produces electricity. Once cooled down, the water is reinjected into the system through injection wells (Fig.1.3). In countries where geothermal resources are limited, such as France, Enhanced Geothermal Systems (EGS) are used involving rock fracking by fluid pressure introduced in initially dry rocks, to create an exploitable hydrothermal system (e.g. Lu, 2018). However, geothermal energy currently produced in this way is limited (Fig.1.4). Both EGS and conventional drilling require technological developments in order to make a more significant contribution to our energy

needs. In US, the Frontier Observatory for Research in Geothermal Energy (FORGE) initiative is dedicating a field site to EGS testing for development (Allis et al., 2016).

There is increased excitement around exploring supercritical conditions that can be reached at the high temperatures and pressures found at the margins of magma chambers (374 °C at 22.1 MPa for pure water; Bischoff and Rosenbauer, 1988). As supercritical fluids have high enthalpy and buoyancy, their decompression produces a superheated steam (e.g. Friðleifsson and Elders. 2007), which extraction corresponds to one order of magnitude greater thermal power output, associated with a conversion efficiency three times that of the actual conversion (Fig.1.4; Albertsson et al., 2003; Friðleifsson et al., 2003; Friðleifsson and Elders 2005; Tester, 2006).

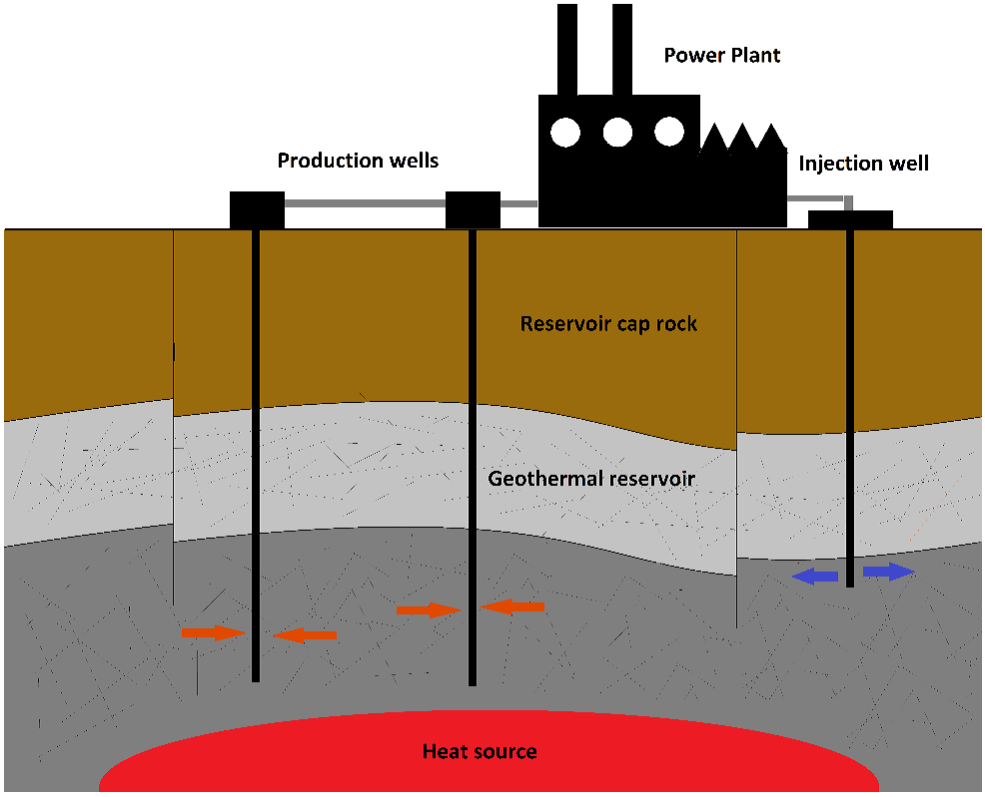

Figure 1.3. Schematic of the exploitation of a hydrothermal system. Hot fluids (steam and water; red arrows) are extracted from production wells, pass through turbines and the cold water (blue arrows) is injected back into the reservoir. After Eggertsson, 2019.

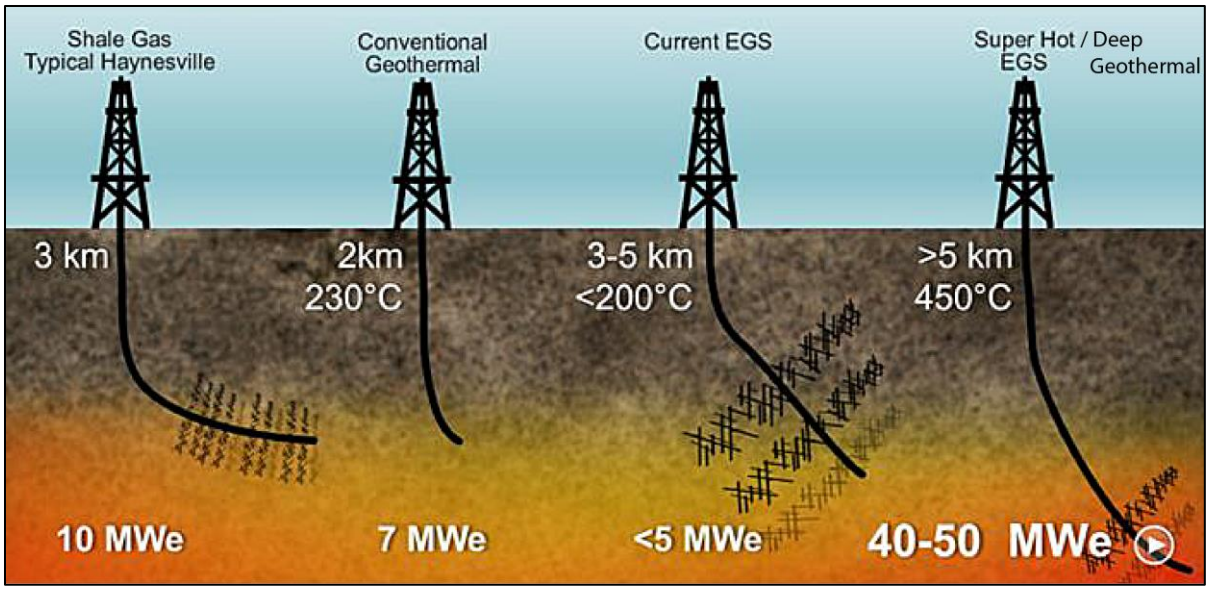

Figure 1.4. Schematic model showing comparative energy output for different well types. After Fridleiffsson et al., 2019.

Three recent geothermal exploration attempts have accidentally drilled into magma, opening the way to these new geothermal targets directly at the roots of hydrothermal systems: Kilauea, in Hawaii, where dacite magma was encountered in 2005 at 2488 m depth (Teplow et al., 2009), Krafla, in Iceland, with rhyolite magma encountered at 2104 m depth in 2009 (Hólmgeirsson et al., 2010), and Menengai, in Kenya, where multiple drillings into syenite magma, 2 km beneath the caldera floor, occurred since 2011 (Mbia et al., 2015). The Iceland Deep Drilling Project (IDDP) is a consortium created following the idea of geothermal exploration into supercritical conditions, proposed at the 2000 World Geothermal Congress (Friðleifsson and Albertsson, 2000; Elders et al., 2001). The IDDP-1 well was completed in 2009 at the Krafla geothermal field in Iceland (Fig.1.1B). The encountered magma was >2 km shallower than predicted, blocking the path to reach supercritical fluids (Elders et al., 2011). Still, production testing indicated a high productive capability (35 MW), and it became the world's hottest geothermal well (452° C at the well head, Friðleifsson et al., 2010). This unexpected experience highlighted the potential of drilling into magma, and presented new challenges for drilling engineering to drill and preserve the wells in these extreme conditions (Hólmgeirsson et al., 2018). Following this success, the IDDP-2 well was completed in 2017 in the Reykjanes field (Fig.1.1A), reaching supercritical pressure at a depth of 4 km and confirming the potential of drilling into this extreme environment (Friðleifsson and Elders, 2017). Other projects are arising worldwide with similar exploration objectives, such as Japan Beyond Brittle, DESCRAMBLE in Italy, GEMex in Mexico, Newberry Deep Drilling in USA and Krafla Magma Testbed in

Iceland (KMT; Reinsh et al., 2017). Efforts also continue in New Zealand after the completion of New Zealand Hotter and Deeper investigation (Ministry of Economic Development, 2010).

1.1.3 IDDP-1 and KMT

The IDDP-1 vertical well was drilled with the purpose of reaching high-enthalpy supercritical fluids, close to the margin of the "Krafla magma chamber" at a depth of >4 km. Cuttings returned via the drilling mud revealed five extrusive formations of basaltic lavas and hyaloclastites until a depth of 1362 m, succeeded by an intrusive complex of basaltic dykes and dolerites. The rock type becomes dominantly felsitic below 2020-2025 m (Fig.1.5; Mortensen et al, 2014). The total loss of drilling fluids circulation below 2070 m depth prevented any cuttings from being retrieved further downhole, and this interval will be referred to as the blind zone. Drilling had to be stopped when undetected rhyolitic magma was encountered at only 2104 m depth (Friðleifsson et al., 2010). The drill bit approached magma three times, with two side-tracks necessary due to repeated sticking (Fig.1.5). On the third approach, magma pushed up on the drill bit, and ultimately plugged the lowest ~20 m of the hole. The cause of drilling difficulties was revealed by the retrieval of fresh obsidian cuttings (ISOR, 2009; Friðleifsson et al., 2010). These quenched glass particles now provide an unprecedented opportunity to characterise the margin of an active shallow rhyolite intrusion.

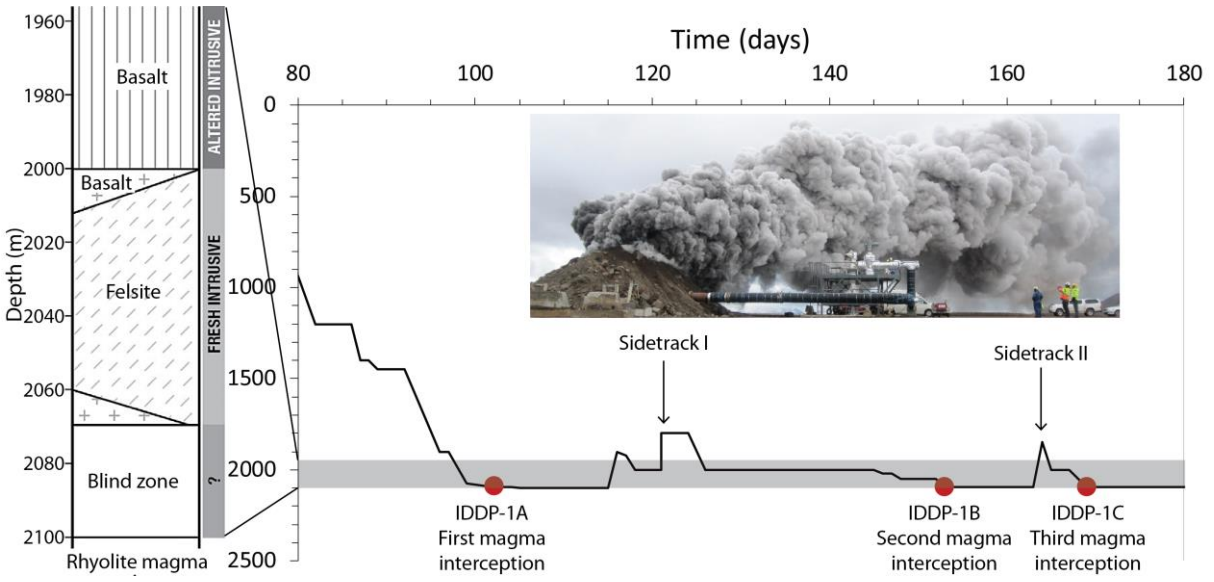

Figure 1.5. Depth of the IDDP-1 drill bit with time, Krafla, Iceland, with insights into the last geological units encountered in the blind zone interval (log on the left, corresponding to the grey band on the main graph). Adapted from Schiffman et al., 2014, and Pálsson et al., 2014. Picture of the dark smoke released at the beginning of the flow test after completion (Credit: Landsvirkjun).

The KMT project (http://kmt.is) was initiated by John Eichelberger, with teams from the Icelandic Geothermal Research Group (GEORG), the British Geological Survey and the National Institute of Geophysics and Volcanology of Italy (INGV), and involves an extensive number of international collaborators, including the University of Canterbury. It aims to drill directly into magma, in order to create a first magma observatory, 'an international, open access, scientific platform to advance understanding, monitoring, and use of magmatic and superhot hydrothermal systems' (Hólmgeirsson et al., 2018). If successful, it will become a global testbed for monitoring subsurface magma, assessing hazards and geothermal productivity, and developing geothermal technology (Eichelberger, 2019).

IDDP-1 drilling located the top of the magma body, and thus provides the ideal site to conduct this project. KMT aims to drill close to the IDDP-1 well, back through the same rock lithologies (Fig.1.6) to core through magma. The success of any new "magma wells" first requires several technical challenges to be overcome. The current drill and sensor technology are being developed to sustain the extreme conditions at depth on a long timescale (corrosion by acidic fluids, high temperature and pressure; Reinsch et al., 2017 and references therein; Hólmgeirsson et al., 2018). However, little is known about the blind zone and successful drilling requires a better knowledge of the physical properties of intrusion margins (e.g., conditions, rock properties, permeabilities), to improve not only the efficiency of drilling but also a technology that will be sustainable for long-term observations. It is also critical to develop a better understanding of magma behaviour in response to drilling, and the reaction of drilling to magma. This will help in anticipating drilling difficulties when encountering magma, and being able to correctly interpret the fluctuation of drilling parameters at depth. In order to understand the properties and distribution of the magma it is useful to consider the processes of melt emplacement and genesis, the intrusion size and the relationship between magma and their host rocks. Key parameters, such as magma viscosity, impact heat transfer to the overlying fluid reservoir and its geothermal potential (e.g. Bostick and Pawlewicz, 1984).

If successful in Iceland, the research by KMT could lead to energy being safely extracted directly from magma via power stations where conditions are suitable in other countries. Geothermal drilling and volcano monitoring in New Zealand would undoubtedly benefit hugely from the research advances proposed by KMT.

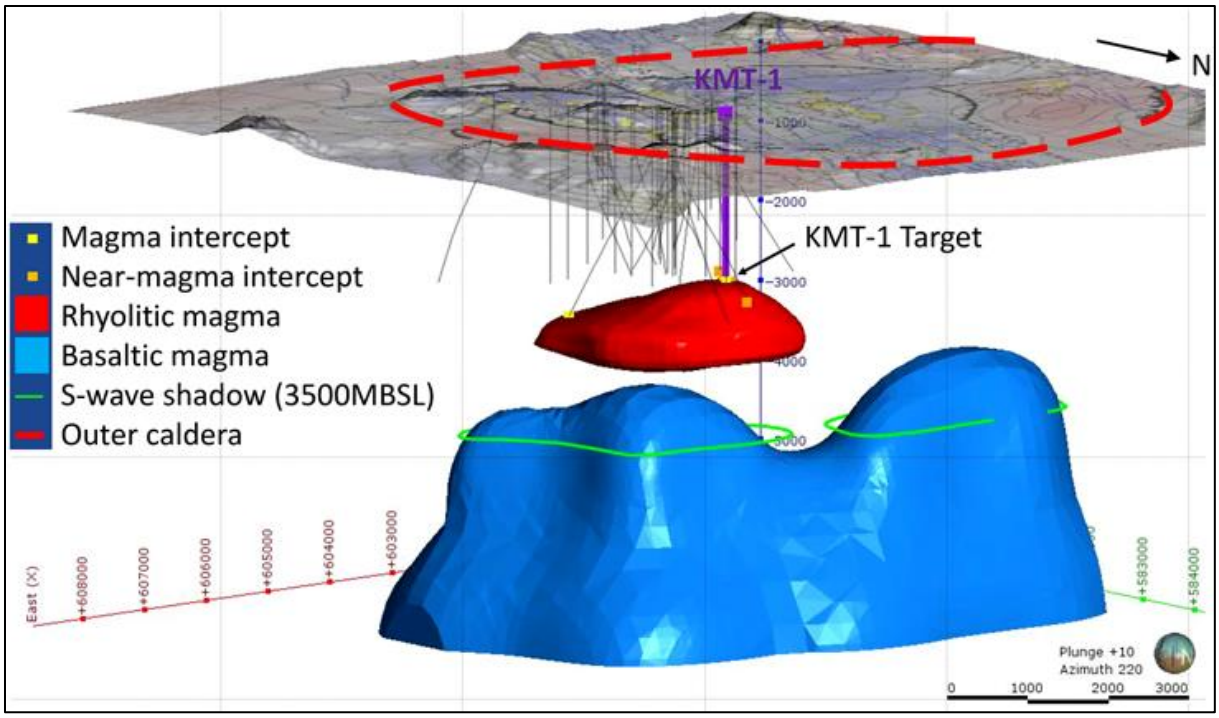

Figure 1.6. Simplified 3D schematic of the main magma reservoirs beneath Krafla caldera (dashed red line), with geothermal boreholes (gray) and planned KMT-1 borehole (purple) closely following the trajectory of the IDDP-1. The location of the IDDP-1 rhyolite magma body (red) is based on data from the boreholes (yellow and orange squares). The rhyolite body sits above a larger basaltic magma reservoir (blue). After Eichelberger, 2019. Credit: J. W. Catley.

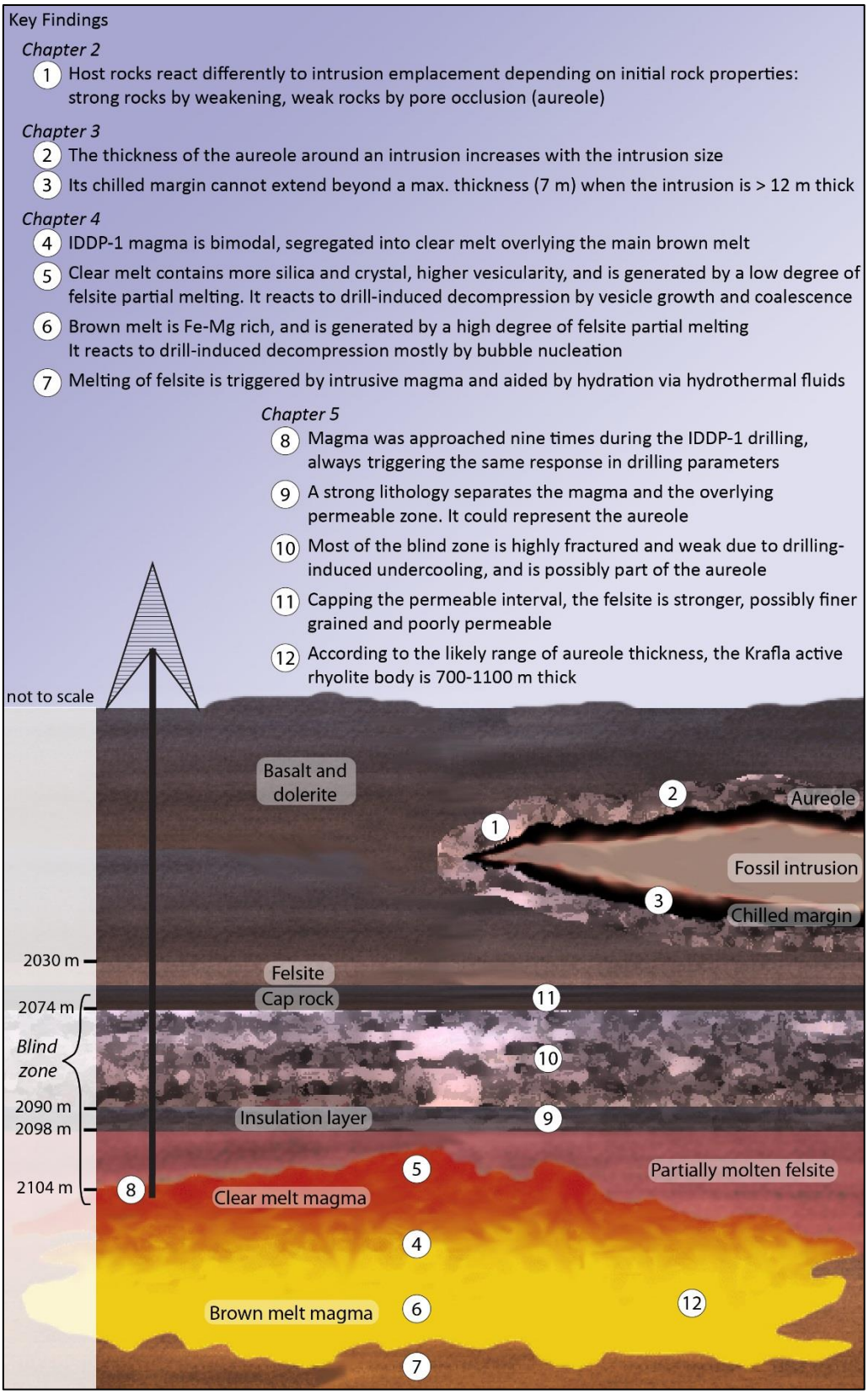

Figure 1.7. Key findings from the core chapters of this dissertation. Below surface schematic based on interpretations from the IDDP-1 drilling (main intrusion in the sketch) and contribution in general knowledge of shallow rhyolite intrusions (smaller fossil intrusion). For more details about specific findings, see the related chapter. Adapted from Caricchi and Blundy, 2015.

1.3 Scientific Contributions

At the time of thesis submission, Chapter 2 has been published in Journal of Volcanology and Geothermal Research, Chapter 3 is ready to be submitted awaiting final comments from the last co-author, and Chapter 4 has been submitted to the Geological Society of America Bulletin. Chapter 5 is the basis for two future papers, which are still being developed. Results from all the chapters have been presented at conferences, workshops and/or seminars.

1.3.1 Peer-reviewed Journal articles

Saubin, E., Kennedy, B. M., Tuffen, H., Nichols A. R. L., Villeneuve M., Bindeman I., Mortensen A., Schipper C. I., Wadsworth F. B., Watson T., Zierenberg R., 2019. Textural and geochemical window into the IDDP-1 rhyolitic melt, Krafla, Iceland, and its reaction to drilling. Accepted in GSA Bulletin pending revisions.

Saubin, E., Kennedy, B. M., Tuffen, H., Villeneuve, M., Davidson, J., Burchardt, S., 2019. Comparative field study of shallow rhyolite intrusions in Iceland: emplacement mechanisms and impact on country rocks. Journal of Volcanology and Geothermal Research, doi: 10.1016/j.jvolgeores.2019.106691

1.3.2 Conference and workshop abstracts

Eichelberger, J., Carrigan, C., Ingolfsson, H.P., Lavallée, Y., Ludden, J., Markusson, S., Mortensen, A., Papale, P., Sigmundsson, F., Saubin, E., Tester, J.W., Consortium, T.K., 2020 (postponed to 2021). Magma-sourced geothermal energy and plans for Krafla Magma Testbed. Proceedings World Geothermal Congress 8, 37027, Reykjavik

Saubin, E., Kennedy, B., Tuffen, H., Villeneuve, M., Davidson, J., Burchardt, S., 2019. Comparative field study of shallow rhyolite intrusions in Iceland: emplacement mechanisms and impact on country rocks. International Union of Geodesy and Geophysics IUGG19-1931, Montreal

Saubin, E., Watson, T., Kennedy, B., Villeneuve, M., Tuffen, H., Davidson, J., Burchardt, S., W. von aulock, F., Schipper, I., Mortensen, A., Eichelberger, J., Lavallée, Y., 2018. Drilling into magma: Application for New Zealand geothermal energy. Geological Society of New Zealand B1-14, Napier

Saubin, E., Kennedy, B., Villeneuve, M., Tuffen, H., Burchardt, S., Davidson, J., W. von Aulock, F.., 2018. Margins of rhyolite intrusions: a potential geothermal target. KMT workshop Wairakei, NZ and KMT-GEORG Meeting Nov. 2018, Reykjavik.

Saubin, E., Villeneuve, M., Mortensen, A., Kennedy, B., 2018. Drilling data in blind zones: how it can inform geological interpretation. KMT Workshop Wairakei, NZ and KMT-GEORG Meeting Nov. 2018, Reykjavik.

Saubin, E., Watson, T., Nichols, A., Tuffen, H., Schipper, I., Kennedy, B., 2018. Insight into margins of rhyolite intrusion from glass cuttings, IDDP-1 well, Krafla. KMT Workshop Wairakei, NZ and KMT-GEORG Meeting Nov. 2018, Reykjavik.

Saubin, E., Kennedy, B., Tuffen, H., Villeneuve, M., Nichols, A., Watson, T., Schipper, I., Bindeman, I., Mortensen, A., Zierenberg, R., 2017. Reaction of rhyolite magma to its intersection with the IDDP-1s well, Krafla, 2009. AGU fall meeting 2017 NH11A-0088

1.4 Originality

This thesis is part of an international effort towards the development of geothermal energy production directly from magma. Following IDDP-1 in 2009 in Iceland, a consortium was initiated by John Eichelberger around the Krafla Magma Testbed (www.kmt.is). The project has received international and government interest, with a wide range of contributing scientists and institutions worldwide. A Catalyst fund grant was awarded to Ben Kennedy in New Zealand by the Ministry of Business, Innovation and Employment, to facilitate this journey. The research questions to address in the context of the KMT were distributed among the collaborating universities and the leading researchers which formed the basis for this Ph.D topic. The supervisory team was therefore large (Ben Kennedy, University of Canterbury, NZ, Hugh Tuffen, Lancaster University, UK, Marlene Villeneuve, University of Canterbury, NZ, Ian Schipper, Victoria University of Wellington, NZ), as the multi-disciplinary approach favoured overlapping in-between teams, and many who were not official supervisors also extensively supported me in this work (Alex Nichols, University of Canterbury, NZ, Anette Mortensen, Landsvirkjun, Iceland, Yann Lavallée, University of Liverpool, UK).

Anette Mortensen was my contact from Landsvirkjun, the National Power Company of Iceland. She provided the IDDP-1 cuttings samples and the raw drilling data, as well as internal drilling

reports, and greatly contributed to the drilling engineering knowledge I gained through this Ph.D, which formed the basis for Chapters 4 and 5. My critical and full-picture understanding of the IDDP-1 and KMT events and context mostly comes from discussions with Ben Kennedy, John Eichelberger (University of Alaska Fairbanks, USA), Wilfred Elders (University of California Riverside, USA), Anette Mortensen, Robert Zierenberg (University of California-Davis, USA), Yan Lavallée and Hugh Tuffen.

The field work contributing to the Chapters 2 and 3 has been planned with Ben Kennedy, and the field areas have been introduced by Hugh Tuffen and Steffi Burchardt (Uppsala University, Sweden). I received additional help from Jonathan Davidson (University of Canterbury, New Zealand), Felix Von Aulock (University of Liverpool, UK), Marlene Villeneuve and Einar Bessi Gestsson (Uppsala University, Sweden). Combined with the field data, the script for the numerical model of heat transfer by conduction was written by Hanfei Wang (University of Canterbury, NZ). The smaller-scale componentry of the IDDP-1 cuttings has been analysed at the Lancaster University, UK, under the guidance of Hugh Tuffen, who later performed additional Thermo-Gravimetric Analyses. Our fruitful discussions have contributed greatly to the interpretations and implications presented in the Chapter 4, together with insights from Kim Berlo and Stephan Kolzenburg, from McGill University, Canada. The X-ray photogrammetry has been conducted by Fabian Wadsworth at the Ludwig-Maximilians University of Munich, Germany (now at Durham University, UK), and later processed at the Victoria University of Wellington, NZ, with Ian Schipper, who also guided me in the use of the electron microprobe (EPMA). The EPMA geochemical analyses were planned and discussed with Alex Nichols, as well as were the thermo-chemical elemental analyses (TCEA) performed by Ilya Bindeman at the University of Oregon, USA. The preparation of samples and their textural sorting were conducted at the University of Canterbury, NZ. The methodology of interpretation of rock properties through drilling parameters (Chapter 5) was guided by Marlene Villeneuve and aided by Carlos Kazianis (Trans-Orient Petroleum Ltd).

Kelly Russell and an anonymous reviewer provided constructive feedback on Chapter 2, contributing to its improvement for publication in the *Journal of Volcanology and Geothermal Research*. Although Jim Cole was not an official supervisor, he helped in the refinement of most of the chapters, and in the organisation of workshops conducted around this thesis. The whole thesis has benefited from intense and thorough discussions with Yan Lavallée and Jackie Kendrick (University of Liverpool, UK). The co-authors of each section are listed at the start of the chapters.

1.5 References

Albertsson, A., Bjarnason, J. Ö., Gunnarsson, T., Ballzus, C., Ingason, K., 2003. The Iceland Deep Drilling Project: Fluid handling, evaluation, and utilization. 8.

Allis, R., Moore, J., Davatzes, N., Gwynn, M., Hardwick, C., Kirby, S., McLennan, J., Pankow, K., Potter, S., Simmons, S. F., 2016. EGS concept testing and development at the Milford, Utah FORGE site. In Proceedings

Arnórsson, S., Axelsson, G., Saemundsson, K., 2008. Geothermal systems in Iceland. Jökull.

Bischoff, J. L., Rosenbauer, R. J., 1988. Liquid-vapor relations in the critical region of the system NaCl-H2O from 380 to 415°C: A refined determination of the critical point and two-phase boundary of seawater. Geochimica et Cosmochimica Acta, 52(8), 2121–2126, doi: 10.1016/0016-7037(88)90192-5

Bostick, N. H., Pawlewicz, M. J., 1984. Paleotemperatures based on vitrinite reflectance of shales and limestone in igneous dike aureoles in the Upper Cretaceous Pierre Shale, Walsenburg, Colorado.

Brown, S. J. A., Burt, R. M., Cole, J. W., Krippner, S. J. P., Price, R. C., Cartwright, I., 1998. Plutonic lithics in ignimbrites of Taupo Volcanic Zone, New Zealand; sources and conditions of crystallisation. Chemical Geology, 148(1), 21–41, doi: 10.1016/S0009-2541(98)00026-6

Browne, P. R. L., Graham, I. J., Parker, R. J., Wood, C. P., 1992. Subsurface andesite lavas and plutonic rocks in the Rotokawa and Ngatamariki geothermal systems, Taupo Volcanic Zone, New Zealand. Journal of Volcanology and Geothermal Research, 51(3), 199–215, doi: org/10.1016/0377-0273(92)90123-U

Caricchi, L., Blundy, J., 2015. The temporal evolution of chemical and physical properties of magmatic systems. Geological Society, London, Special Publications, 422(1), 1–15, doi: 10.1144/SP422.11

Chamorro, C. R., Mondéjar, M. E., Ramos, R., Segovia, J. J., Martín, M. C., Villamañán, M. A., 2012. World geothermal power production status: Energy, environmental and economic study of high enthalpy technologies. Energy, 42(1), 10–18, doi: 10.1016/j.energy.2011.06.005

Elders, B. L. A., Wilson, C. J. N., Lowenstern, J. B., Blake, S., Van Calsteren, P. W., Davidson, J. P., 2005. Magma Generation at a Large, Hyperactive Silicic Volcano (Taupo, New Zealand) Revealed by U–Th and U–Pb Systematics in Zircons. Journal of Petrology, 46(1), 3–32, doi: 10.1093/petrology/egh060

Climo, M., Milicich, S. D., White, B., 2016. A history of geothermal direct use development in the Taupo Volcanic Zone, New Zealand. Geothermics, 59, 215–224, doi: 10.1016/j.geothermics.2015.07.004

Cole, J. W., Spinks, K. D., 2009. Caldera volcanism and rift structure in the Taupo Volcanic Zone, New Zealand. Geological Society, London, Special Publications, 327(1), 9–29, doi: 10.1144/SP327.2

Eggertsson, G. H., 2019. Constraining mechanical and permeability properties of the Krafla geothermal reservoir, North-East Iceland [Doctoral thesis]. University of Liverpool.

Eichelberger, J., 2019. Planning an International Magma Observatory. Eos, 100.

Einarsson, P., 1978. S-wave shadows in the Krafla Caldera in NE-Iceland, evidence for a magma chamber in the crust. Bulletin Volcanologique, 41(3), 187–195, doi: 10.1007/BF02597222

Elders, W.A., Friðleifsson, G.Ó., Saito, S., 2001. The Iceland Deep Drilling Project: a search for supercritical fluids. Trans. Geothermal Resources Council 21, 297–300.

Elders, W. A., Friðleifsson, G. Ó., Zierenberg, R. A., Pope, E. C., Mortensen, A. K., Guðmundsson, Á., Lowenstern, J. B., Marks, N., Owens, L., Bird, D. K., Reed, M., Olsen, N., Schiffman, P., 2011. Origin of a rhyolite that intruded a geothermal well while drilling at the Krafla volcano, Iceland. Geology 39(3), 231–234, doi: 10.1130/G31393.1

Elders, W. A., Osborn, W. L., Raju, A. S. K., Martinez-Morales, A., 2019. The Future Role of Geothermal Resources in Reducing Greenhouse Gas Emissions in California and Beyond. Proceedings 44th Workshop Geothermal Reservoir Engineering, 9.

Friðleifsson, G. O., Albertsson, A., 2000. Deep geothermal drilling on the Reykjanes ridge opportunity for international collaboration. Proceeding World Geothermal Congress, 7

Friðleifsson, G. Ó., Albertsson, A., Stefánsson, B., 2003. The Iceland Deep Drilling Project, Deep Vision and Future Plans. Proceedings of the Geothermal Conference IGC-2003 Reykjavik, September 2003, Session 6, 31–37.

Friðleifsson, G. O., Elders, W. A., 2005. The Iceland Deep Drilling Project: a search for deep unconventional geothermal resources. Geothermics, 34(3), 269–285, doi: 10.1016/j.geothermics.2004.11.004

Friðleifsson, G. O., Elders, W. A., 2007. Progress report on the Iceland Deep Drilling Project (IDDP), doi: 10.2204/iodp.sd.4.04.2007

Friðleifsson, G. Ó., Pálsson, B., Stefánsson, B., Albertsson, A., Gunnlaugsson, E., Ketilsson, J., Lamarche, R., & E Andersen, P., 2010. Iceland Deep Drilling Project. The first IDDP drill hole drilled and completed in 2009. Proceedings World geothermal congress, p. 4

Friðleifsson, G. Ó., Elders, W. A., 2017. Successful drilling for supercritical geothermal resources at Reykjanes in SW Iceland. 13.

Gunnarsson, B., Marsh, B. D., Taylor, H. P., 1998. Generation of Icelandic rhyolites: silicic lavas from the Torfajökull central volcano. Journal of Volcanology and Geothermal Research, 83(1–2), 1–45.

Harrison, A. J., White, R. S., 2004. Crustal structure of the Taupo Volcanic Zone, New Zealand: Stretching and igneous intrusion. Geophysical Research Letters, 31(13), doi: 10.1029/2004GL019885

Hólmgeirsson, S., Gudmundsson, A., Pálsson, B., Bóasson, H. Á., Ingason, K., Þórhallsson, S., 2010. Drilling operations of the First Iceland Deep Drilling Well (IDDP). Proceeding World Geothermal Congress.

Hólmgeirsson, S., Ingólfsson, H. P., Eichelberger, J., Pye, S., Normann, R., Kaldal, G. S., Blankenship, D., Mortensen, A., Markusson, S., Paulsson, B., Karlsdottir, S. N., Olafsdottir S., Gardarsson, S. M., Tester, J., Lavallée, Y., 2018. Krafla Magma Testbed (KMT): Engineering challenges of drilling into magma and extracting its energy. 13.

Illsley-Kemp, F., Michailos, K., Chamberlain, C. J., Savage, M. K., Wilson, C. J. N., & Barker, S. J., 2019. Modern volcano-tectonic interactions at Taupō volcano, New Zealand, revealed by a decade of seismic activity. AGU Fall Meeting 2019.

ISOR, 2009. IDDP-1 - Krafla, Vitismor - Production casing (No. 119). ISOR Iceland geosurvey, internal drilling report

Jónasson, K., 1994. Rhyolite volcanism in the Krafla central volcano, north-east Iceland. Bulletin of Volcanology, 56(6–7), 516–528.

Kennedy, B. M., Holohan, E. P., Stix, J., Gravley, D. M., Davidson, J. R. J., Cole, J. W., 2018. Magma plumbing beneath collapse caldera volcanic systems. Earth-Science Reviews, 177, 404–424, doi: 10.1016/j.earscirev.2017.12.002

Lavallée, Y., Lamur, A., Kendrick, J. E., Eggertsson, G. H., Weaver, J., Eichelberger, J. C., Papale, P., Sigmundsson, F., Dingwell, D. B., Markússon, S. H., Mortensen, A. K., 2020 (postponed to 2021). Thermal manipulation of magma boundaries: Advancing controls on fluid flow via the Krafla Magma Testbed (KMT). Proceeding World Geothermal Congress, 11.

Lu, S. M., 2018. A global review of enhanced geothermal system (EGS). Renewable and Sustainable Energy Reviews, 81, 2902-2921

Masotta, M., Mollo, S., Nazzari, M., Tecchiato, V., Scarlato, P., Papale, P., Bachmann, O., 2018. Crystallization and partial melting of rhyolite and felsite rocks at Krafla volcano: A comparative approach based on mineral and glass chemistry of natural and experimental products. Chemical Geology, 483, 603–618, doi: 10.1016/j.chemgeo.2018.03.031

Mbia, P. K., Mortensen, A. K., Oskarsson, N., Hardarson, B., 2015. Sub-surface geology, petrology and hydrothermal alteration of the Menengai geothermal field, Kenya: case study of wells MW-02, MW-04, MW-06 and MW-07. In Proceedings World Geothermal Congress (p. 20).

McNamara, D. D., Faulkner, D., McCarney, E., 2014. Rock properties of greywacke basement hosting geothermal reservoirs, New Zealand: Preliminary results. In 39th Workshop on Geothermal Reservoir Engineering. Stanford University.

Milicich, S. D., Wilson, C. J. N., Bignall, G., Pezaro, B., Bardsley, C., 2013a. Reconstructing the geological and structural history of an active geothermal field: A case study from New Zealand. Journal of Volcanology and Geothermal Research, 262, 7–24, doi: 10.1016/j.jvolgeores.2013.06.004

Milicich, S. D., Wilson, C. J. N., Bignall, G., Pezaro, B., Charlier, B. L. A., Wooden, J. L., Ireland, T. R., 2013b. U–Pb dating of zircon in hydrothermally altered rocks of the Kawerau Geothermal Field, Taupo Volcanic Zone, New Zealand. Journal of Volcanology and Geothermal Research, 253, 97–113, doi: 10.1016/j.jvolgeores.2012.12.016

Ministry of Economic Development, 2010. Geothermal energy: summary of emerging technologies and barriers to development. New Zeland, MBIE report 1006360

Mortensen, A. K., Egilson, Gautason, B., Arnadottir, S., Gudmundsson, A., 2014. Stratigraphy, alteration mineralogy, permeability and temperature conditions of well IDDP-1, Krafla, NE-Iceland. 49, 31–41, doi: 10.1016/j.geothermics.2013.09.013

Nielsen, G., Maack, R., Gudmundsson, A., Gunnarsson, G. I., 2000. Completion of Krafla geothermal power plant. Proceeding World Geothermal Congress.

Pálsson, B., Hólmgeirsson, S., Guðmundsson, Á., Bóasson, H. Á., Ingason, K., Sverrisson, H., Thórhallsson, S., 2014. Drilling of the well IDDP-1. Geothermics, 49, 23–30, doi: 10.1016/j.geothermics.2013.08.010

Reid, F., 1983. Origin of the rhyolitic rocks of the taupo volcanic zone, New Zealand. Journal of Volcanology and Geothermal Research, 15(4), 315–338, doi: 10.1016/0377-0273(83)90105-1

Reinsch, T., Dobson, P., Asanuma, H., Huenges, E., Poletto, F., Sanjuan, B., 2017. Utilizing supercritical geothermal systems: a review of past ventures and ongoing research activities. Geothermal Energy, 5(1), doi: 10.1186/s40517-017-0075-y

Rosenberg, M. D., Bignall, G., Rae, A. J., 2009. The geological framework of the Wairakei–Tauhara Geothermal System, New Zealand. Geothermics, 38(1), 72–84, doi: 10.1016/j.geothermics.2009.01.001

Schiffman, P., Zierenberg, R. A., Mortensen, A. K., Frioleifsson, G. O., Elders, W. A., 2014. High temperature metamorphism in the conductive boundary layer adjacent to a rhyolite intrusion in the Krafla geothermal system, Iceland. Geothermics, 49, doi: 10.1016/j.geothermics.2012.11.002

Shane, P., Nairn, I. A., Smith, V., Darragh, M., Beggs, K., Cole, J. W., 2008. Silicic recharge of multiple rhyolite magmas by basaltic intrusion during the 22.6 ka Okareka Eruption Episode, New Zealand. Lithos, 103(3–4), 527–549, doi: 10.1016/j.lithos.2007.11.002

Sigurdsson, H., 1977. Generation of Icelandic rhyolites by melting of plagiogranites in the oceanic layer. Nature, 269(5623), 25–28.

Simpson, M. P., Bignall, G., 2016. Undeveloped high-enthalpy geothermal fields of the Taupo Volcanic Zone, New Zealand. Geothermics, 59, 325–346, doi: 10.1016/j.geothermics.2015.08.006

Siratovich, P. A., Heap, M. J., Villenueve, M. C., Cole, J. W., Reuschlé, T., 2014. Physical property relationships of the Rotokawa Andesite, a significant geothermal reservoir rock in the Taupo Volcanic Zone, New Zealand. Geothermal Energy, 2(1), 10, doi: 10.1186/s40517-014-0010-4

Teplow, W., Marsh, B., Hulen, J., Spielman, P., Kaleikini, M., Fitch, D., Rickard, W., 2009. Dacite melt at the Puna geothermal venture wellfield, Big Island of Hawaii. Geothermal resources council transactions, 33, 989-994.

Tester, J.W. (Ed.), 2006. The future of geothermal energy: impact of enhanced geothermal energy (EGS) on the United States in the 21st century. MIT Panel Report to the US Department of Energy, pp. 1–54

Thordarson, T., Larsen, G., 2007. Volcanism in Iceland in historical time: Volcano types, eruption styles and eruptive history. Journal of Geodynamics, 43, 118–152.

Walker, G. P. L., 1974. Eruptive mechanisms in Iceland. In L. Kristjansson (Ed.), Geodynamics of Iceland and the North Atlantic Area, 189–201.

Wilson, C. J. N., Houghton, B. F., McWilliams, M. O., Lanphere, M. A., Weaver, S. D., Briggs, R. M., 1995. Volcanic and structural evolution of Taupo Volcanic Zone, New Zealand: a review. Journal of Volcanology and Geothermal Research, 68(1), 1–28, doi: 10.1016/0377-0273(95)00006-G

Wood, C. P., Brathwaite, R. L., Rosenberg, M. D., 2001. Basement structure, lithology and permeability at Kawerau and Ohaaki geothermal fields, New Zealand. Geothermics, 30(4), 461–481, doi: 10.1016/S0375-6505(01)00003-7

World Energy Council, 2010. World Energy Resources: 2010 Survey

Zierenberg, R. A., Schiffman, P., Barfod, G. H., Lesher, C. E., Marks, N. E., Lowenstern, J. B., Mortensen, A. K., Pope, E. C., Bird, D. K., Reed, M. H., Friðleifsson, G. Ó., Elders, W. A., 2012. Composition and origin of rhyolite melt intersected by drilling in the Krafla geothermal field, Iceland. Contributions to Mineralogy and Petrology, 165(2), 327–347, doi: 10.1007/s00410-012-0811-z

Þorsteinsdóttir, U., 2017. A 3D geological static field model of the Krafla geothermal area; constructing a workflow for the Pico Alto geothermal area. Doctoral dissertation, University of Iceland.

Chapter 2 – Comparative field study of shallow rhyolite intrusions in Iceland: emplacement mechanisms and impact on country rocks

E. Saubin[1], B. Kennedy[1], H. Tuffen[2], M. Villeneuve[1], J. Davidson[1], S. Burchardt[3]

[1] *Department of Geological Sciences, University of Canterbury, Christchurch New Zealand*

[2] *Lancaster Environment Centre, Lancaster University, Lancaster, UK*

[3] *Department of Earth Science, Uppsala University, Uppsala, Sweden*

2.1 Abstract

Shallow silicic intrusions are known to exist in many active volcanoes and can fuel both eruptions and hydrothermal fields. However, our knowledge of magma intrusions remains far from complete, and processes occurring at intrusion margins are poorly understood. In this field-based study, we characterise four shallows, dissected rhyolitic intrusions at three sites in Iceland (Njarðvík-Dyrfjöll, Krafla and Húsafell central volcanoes). We focus on the relationship between intrusion emplacement mechanisms and country rock response, employing scanline mapping of fractures and in-situ rock property measurements (hardness and permeability) along transects from the intrusion margins to damaged and undamaged country rocks.

We identify various scenarios of shallow intrusion emplacement style, based upon their diverse geometry and lithofacies architecture. Additional information from rock properties and characteristics of fractures and vesicles, indicates that initial country rock properties strongly influence the emplacement style. We identify two discrete types of country rock response to magma injection. The matrix permeability of weak, porous and permeable lithologies (conglomerate and hyaloclastite) is reduced by >1 order of magnitude adjacent to intrusions due to pore occlusion. Stronger and denser, low-permeability lithologies (basalt and welded

ignimbrite) undergo a decrease in hardness by a factor >2 related to an up to fivefold increase in fracture density, with no significant change in matrix permeability.

Our observations highlight the importance of robust characterisation of the mechanical properties of caldera-filling or geothermal reservoir formations, for appropriate forecasting of magma mobility, geophysical data interpretation, and geothermal resources characterisation.

2.2 Introduction

Magmatic activity in Iceland is dominantly basaltic in composition (Walker, 1974; Sigurdsson, 1977; Thordarson and Larsen, 2007). However, rhyolitic magma is generated at central volcanoes by partial melting of altered basaltic crust and/or fractional crystallisation (e.g. Jónasson, 1994; Gunnarsson et al., 1998), producing rhyolites with higher temperatures and lower viscosity compared to subduction zone rhyolites (Zierenberg et al., 2012; Reid, 1983). These intrusive complexes become the shallow roots of some of the most vigorous hydrothermal systems, used for geothermal energy production in Iceland (e.g. Krafla). Supercritical fluids suitable for powerful energy extraction can be stored at the margins of the intrusions (40-50 MWe per well; Albertsson et al., 2003), where rock properties likely control both eruption and energy potential (e.g. Lamur et al., 2017; Eggertsson et al., 2018; Mordensky et al., 2018a and b).

Processes related to magma transport in volcanic plumbing systems are the subject of active research, illustrated in recent studies reviewing melt segregation, emplacement and storage systems (e.g. Holness, 2018; Healy et al., 2018). Magma emplacement style depends on physical properties and structure of surrounding rocks, regional tectonics and magma rheology (Pollard, 1973; Spence and Turcotte, 1985; Hutton, 1988; Clemens and Petford, 1999; Galland et al., 2006; Mattsson et al. 2018; Stephens et al., 2018; Burchardt et al. 2019). As examples, transition from a dyke to a sill is associated to a variation of strength in layered country rocks (Kavanagh et al., 2006; Maccaferri et al., 2011) and/or to the occurrence of a strong compressive tectonic stress (Gudmundsson., 1990; Maccaferri et al., 2011), and the intrusion width is affected by the country rock lithology and magma viscosity (e.g. Krumbholz et al., 2014). Propagating magma exploits pre-existing discontinuities in country rock (Lamur et al., 2017; Le Corvec et al., 2013), but also creates new fractures at the tips, with hydraulic tensile fracturing or shear faulting (Mathieu et al., 2008; Kavanagh, 2018). The opening direction of

intrusions is therefore a result of stresses and country-rocks properties (Kavanagh, 2018). These fracturing processes include the formation of tuffisite veins, which open pathways for silicic magma to propagate, degas, and erupt (e.g. Stasiuk et al., 1996; Tuffen and Dingwell, 2005; Saubin et al., 2016). They form by exsolved magmatic gas that inject into fractures within country rocks (Heiken et al., 1988). Continued propagation of pressurised magmatic fluids can widen the veins, facilitating magma emplacement (Stasiuk et al., 1996; Tuffen and Dingwell, 2005; McGowan, 2016).

Besides fracturing occurring at the intrusive tips, country rocks can be locally deformed and fractured along the contacts (Kavanagh and Sparks, 2011). Strong, low-porosity material undergoes limited elastic or inelastic deformation response to pressure increase associated with intrusion, leading to material failure (e.g. Paterson et al., 1996). In contrast, weak, porous units favour the circulation of hot fluids causing thermal alteration and thermal fracturing, and will undergo significant ductile deformation with shear failure (Delaney et al., 1986; Wong and Baud, 2012; Mordensky et al., 2019). Within the intrusion, small-scale (millimetre) perlitic fracture networks can develop in quenched glassy margins (von Aulock et al., 2013), facilitating significant ingress of external water. In the country rock at the immediate vicinity of the intrusion, the high fracture density is associated with permeability increase. This may create conditions suitable for a geothermal resource with circulation of high-enthalpy fluids (e.g. Carrigan; 1986; Paterson et al., 1996; Scott et al., 2017; Mordensky et al., 2018a, 2018b).

Magma propagation and country rock response elucidate textural, as well as structural adjustments. High internal shear stress and rapid quenching at the contact can form platy jointing (Conway et al., 2015; Magnall et al., 2018). Contact-parallel flow colour banding can occur in the glass, reflecting variable cooling rates, incremental pulses of magma emplacement, or shear-driven crystal variation (Tuffen and Castro, 2009; McGowan, 2016; Mattsson et al., 2018). These magma flows can be associated with decompression, which causes melt to degas through vesicle nucleation and growth (e.g. Hamada et al., 2010). Parameters impacting this magma response include the decompression rate, magma viscosity, volatile content and quench rate (e.g. Sparks, 1978; Papale et al., 1998; Shea et al., 2010; von Aulock et al., 2017). The melt flow deforms vesicles according to the strain rate, which changes depending on the velocity gradient across the intrusion (e.g. Rust et al., 2003; Okumura et al., 2009; Dingwell et al., 2016). Secondary changes may be caused by coalescence, outgassing or relaxation, and a pumiceous foam can form for highly-vesicular magma, then fragment or collapse (Westrich et al., 1988; Okumura et al., 2006; Kennedy et al., 2016). Vesicle size distribution can consequently be an

indicator of degassing processes, and vesicle shapes and orientations can record processes related to stress and flow direction (e.g. Sparks, 1978; Stasiuk et al., 1996; Manga et al., 1998; Shea et al., 2010; Toramaru, 2014; Dingwell et al., 2016; Wadsworth et al., 2017).

The heat transfer to the country rock and the related hydrothermal alteration are dominantly controlled by intrusion thickness (e.g. Annen, 2017). Heat transfer can be associated with heat convection or advection by hydrothermal fluids in presence of a developed fracture network (e.g. Parmentier and Schedl, 1981; Huppert et Sparks, 1989). Hot aqueous fluids drive mineralogical, chemical and textural changes in the rock, with released oxygen causing oxidation and thus colour change, together with iron leaching (e.g. Pirajino, 2008). Heating of the country rock can cause dehydration of mineral species, reactions between minerals, or dissolution (e.g. Galushkin, 1997; Siratovich et al., 2011; Farquharson et al., 2018; Mordensky et al., in press). Despite the importance of these processes in country rock alteration, chemical impacts of intrusions are beyond the scope of this study.

This paper presents field case studies of four fossil rhyolitic intrusions from three shallow plumbing systems in Iceland. Rock mass properties are investigated in and around similar dimension intrusions, within distinct country rocks. Vesicle populations in intrusions record cooling, degassing and emplacement processes, whereas field estimates of rock hardness, permeability and fracture density in country rocks indicate the mechanical and thermal impacts of intrusion at the interface. We conceptualise the influence of the country rock and intrusion style on the emplacement, degassing, and geothermal potential of rock masses surrounding shallow rhyolite intrusions.

2.3 Methodology

The field areas (Fig.2.1) all comprise one or more shallow rhyolite body, intruded within diverse country rock lithologies. These sites were chosen to represent similar intrusion compositions, dimensions and emplacement depths, at relatively unweathered and accessible outcrops. We conducted qualitative and quantitative assessment of intrusion dimensions, geometries, and vesicle populations including density, size and orientation. In the country rocks, information were primarily collected in the damaged zone, but also in the undamaged country rock away from the intrusion as a control. It concerns the lithofacies architecture, rock

properties including hardness and permeability, and details of fracture populations such as density, size and orientation. The term "damaged zone" in this study refers to both hydrothermal alteration and intrusion-triggered mechanical damage. Additional features at the interface such as tuffisite veins and brecciated zones are also included in the descriptions. Figure S2.1 (Supplementary Material) shows the measurement locations.

2.3.1 3D photogrammetric reconstruction

Models of the three field areas were constructed from photography using the structure from motion (SfM) photogrammetric technique in the Agisoft Photoscan (Metashape) software. Images were collected using either an unmanned aerial vehicle (UAV; DJI phantom 3), or a combination of both the UAV and a handheld camera. The UAV photographs were geo-tagged using a standard GPS and the final models have a ~3 m RMS error in location, with resolution of ~10 mm/pixel. They are used to approximate the three-dimensional intrusion geometries (Figs.2.2, 3, 4). Contacts and faults orientation were measured in-the field with a compass clinometer, constraining the 3D models. Compass measurements were corrected with 10° of declination at Njarðvík-Dyrfjöll (Landsendi outcrop), 11° at Krafla (Hrafntinnuhryggur outcrop) and 13° at Húsafell (West and East outcrops), appropriate for the date of fieldwork in 2017 and 2018.

2.3.2 Rock properties

Permeability and hardness are estimated in the field with the respective use of TinyPerm (Farquharson et al., 2015) and Schmidt hammer (Aydin and Basu, 2005). Although such field techniques lack the accuracy of equivalent laboratory measurements, they permit collection of large in-situ datasets and can be used to reflect relative spatial variation within the outcrop (Mordensky et al., 2018b).

The TinyPerm is a portable air permeameter used perpendicular to smooth surfaces. Air is drawn through the volume of rock adjacent to the nozzle, with a vacuum initially created at the nozzle-rock interface (Mordensky et al., 2018b). The permeability calculation is described in Brown and Smith (2013). The use of the TinyPerm is validated by laboratory measurements of permeability on a heterogeneous block of hyaloclastite from the field site of Krafla (Fig.2.1), which provided the same range of relative values to the field permeameter results, with natural variability of half an order of magnitude (Eggertsson et al., 2018). Absolute values should however be considered as approximate, with uncertainties ± 5 % (Brown and Smith, 2013). We

differentiate in this paper the matrix permeability measured with the TinyPerm and the rock mass permeability, which takes into account fractures and lithological structures.

Field rock hardness was determined using a type-L Schmidt hammer, requiring a minimum of 10 measurements at each location (ASTM, 2001). The final value is calculated from the average, as suggested in Amaral et al. (1999). The inbuilt spring-driven piston is released on a rock surface, and a correlation chart relates the registered rebound value to rock strength (e.g. Deere and Miller, 1966; del Potro and Hürlimann, 2008; Mordensky et al., 2018b). The absolute values of strength are however not well constrained for these rocks, and rock hardness measurements assess relative spatial variation only. Laboratory measurements of Uniaxial Compressive Strength (UCS) were performed by Eggertsson (2019) on two Icelandic rocks (dense basalt lava and hyaloclastite) among the four we encounter in this study.

Field conditions were highly variable (outcrop quality, dimensions and accessibility). Despite efforts made to conduct consistent measurements, inter-site fluctuations were unavoidable. Measurements were recorded over two field seasons and the large number of scientists involved also impacts the data consistency. We focus our results on systematic measurements of rock properties conducted at ~5-10 cm intervals along 1-4 m long transects: 2 transects out of the 5 from Landsendi, 3 out of the 9 from Hrafntinnuhryggur, 1 from the 4 at Húsafell West, and the 2 from Húsafell East. Measurements were made on smooth surfaces free from water and lichen, avoiding macro-fractures. At each point, 1-6 good TinyPerm measurements (with smooth temporal decay of pressure differential) were recorded depending on time allocated per outcrop. We aimed for ~10 Schmidt hammer measurements close to the measurement points for the TinyPerm. As Schmidt hammer rebound can damage the rock, permeability was measured first, and each rebound was conducted on a slightly different but adjacent surface. Results presented herein are calculated from the average of measurements for each point.

The lithologies are sorted according to the Geotechnical Classification of Volcanic Material procedure (GCVM, Del Potro and Hurliman, 2008), which includes the alteration and damage degree. Initially used for characterisation of material stability, it is also strongly related to drillability and relevant for geothermal.

2.3.3 Fractures

Our approach limits the permeability measurements to the rock matrix, as we intentionally avoided visible fractures. Rock mass permeability is considered through 1D mapping of spacing and dimensions of discontinuities, recorded using the simple scanline method in Manda and

Mabee (2010). Scanline transects were typically 1-2 m in length, with >25 counted fractures, located in each lithology and across the contact in representative areas. Measurements concerned all discontinuity types (joints, bedding, faults, veins), their orientation, length and aperture, together with additional geometry factors and external effects (results can be made available on request). Average fracture density (number of fractures per metre) and average fracture area (length multiplied by aperture) were calculated for each country rock lithology.

Only a subset of the scanlines meets our need for a clear distinction between damaged and non-damaged country rock: 1 scanline out of the 6 from Landsendi, 3 out of the 11 from Hrafntinnuhryggur, 2 out of the 4 from Húsafell West and the 2 from Húsafell East. At Landsendi, we used photos taken by a handheld camera at resolution of 1 mm/pixel to record fractures spacing, length and aperture along two additional transects, in locations inaccessible in the field. Higher resolution information on fracture density was collected at the best quality Húsafell West outcrop, where we counted the number of fractures over a 50 cm length parallel to the contact, repeating this measurement every 5-10 cm along the scanline transects. At Húsafell East, the two scanlines were completed with 6 photo-based transects to create a similar high-resolution fracture density profile (c.f. Supplementary Material, Fig.S2.1, Table S2.2).

2.3.4 Textures

Vesicularity was estimated at Landsendi using a vesicularity reference chart every ~2 m along the outcrop. At each site, the orientation, elongation and width of the biggest-sized vesicles were recorded every ~2-5 m along and across the intrusion, at the core, sill tips, top or bottom contact, and near features such as faults or internal rock deformation. The outcrop surfaces restrict the measurements to two-dimensions data. Vesicles size was measured with a mm-precision scale, resulting in resolution of 0.5 mm. Vesicles equivalent diameter (diameter of the rounded-shape vesicle of same area) and shape ratio (short axis divided by long axis) were calculated.

2.3.5 Statistical testing

We use the method of one-way analysis of variance (ANOVA; Fisher, 1925) to determine the significance of trends when those are unclear. It is the case for our permeability results, which variations within damaged country rocks are compared with variations in the undamaged rocks. The calculation compares the means of the two groups, taking into account their variance and resulting in an overall p-value (Miller and Rupert, 1997). The two groups are considered significantly different within the 95 % confidence interval when p-value <0.05. If p-value

>0.05, the difference is not statistically significant. The data analysis for this study was generated using the Real Statistics Resource Pack software (Zaiontz, 2018).

2.4 Geological setting and description of intrusions

The three selected central volcanoes in Iceland are Njarðvík-Dyrfjöll, Krafla and Húsafell (Fig.2.1).

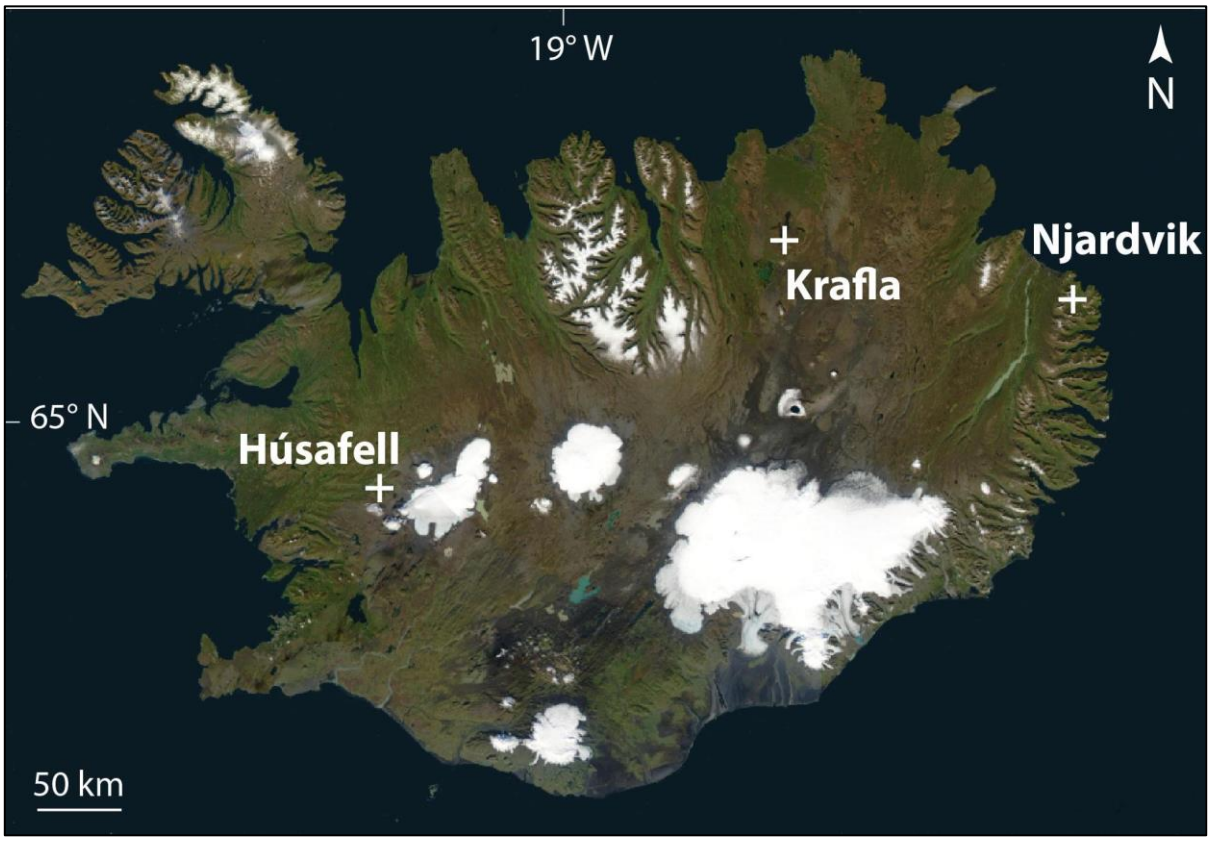

Figure 2.1. Map of central volcano field areas in Iceland (image from NASA). Refer to Table 2.1 for the outcrop coordinates.

2.4.1 Njarðvík-Dyrfjöll

The ~12 Ma Neogene Njarðvík-Dyrfjöll volcano in the East Fjords hosts an extensive system of rhyolitic dykes and sills. At the base of the exposed succession is a >300m thick sub-volcanic rhyolitic body cut by basaltic dykes. This is overlain by >500 m of basaltic lavas intruded by rhyolite (Gustafsson, 1992; Burchardt, 2008). The dykes extending from the rhyolitic intrusion at the base feed a ~100 m thick, irregular rhyolitic lava, which caps the basalt unit. Rhyolitic and basaltic intrusions crosscut each other, and indicate the existence of a source magma

chamber near the centre of the caldera (Burchardt et al., 2011). The lens-shaped 1-4 m thick Landsendi sill is located on a peninsula east of the fjord Njarðvík, surrounded by fractured basaltic lavas (Fig.2.2). Its emplacement depth is estimated at 500 m, indicated by the elevation of the coeval subaerial rhyolite lava higher in the sequence (Burchardt, 2008).

2.4.2 Krafla

The Krafla volcanic complex consists of a central caldera located in the northern rift zone of Iceland, associated with an elongate N-S trending fissure swarm (e.g. Thordarson and Larsen, 2007). Its activity is related to the rifting, with repeated inflation stages and subsidence events (Björnsson et al., 1979). The caldera is filled with basaltic hyaloclastites and lavas, whereas rhyolitic products are concentrated at and around the caldera rims. The last eruptions were basaltic and occurred between 1975-84 (e.g. Jónasson, 1994). Hrafntinnuhryggur is a dominantly obsidian ridge following the N-S fissure swarm trend, near the south-east rim of the Krafla caldera, formed in a small-volume rhyolitic fissure eruption at ~24 ka (Tuffen and Castro, 2009). At the south of the ridge, glacial erosion to ≤90 m beneath the syn-eruptive surface reveals a discordant rhyolitic feeder dyke intruding basalts and hyaloclastites that are overlain by small, obsidian-rich lava bodies (Fig.2.3).

2.4.3 Húsafell

Húsafell volcano in west Iceland was active 3-2.3 Ma ago (Saemundsson and Noll 1974), with three phases of silicic volcanism including the emplacement of significant volumes of ignimbrite. Numerous dykes, sheets, domes and vents were emplaced during the final silicic phase. They are extensively dissected in the valleys of Deildargil and Hringsgil, where these intrusions emplaced at ~500m depth and cut a series of conglomerates, ignimbrites and basaltic lavas (McGowan, 2016). The selected outcrops contain a rhyolitic intrusion of complex geometry exposed on both sides of the N-S trending Deildargil valley. On the east outcrop, the ~2m thick inclined sheet-like body propagates through conglomerate. On the west outcrop, it follows the lower boundary of a welded ignimbrite overlaying the conglomerate unit (Fig.2.4). It also cut as a dyke through a basaltic lava towards the northern end of the area.

2.5 Comparative results

An overview of the four intrusions is presented in Table 2.1.

TABLE 2.1. DESCRIPTION OF INTRUSIONS

Field site	UTM	Paleo-depth (m)	Type	Dip °	Thickness (m)	Country rock type	Intact rock strength (MPa)
Njarðvík-Dyrfjöll – Landsendi outcrop	65°33'55.75N 13°48'58.93W	500	Lens-shaped sill	10-20	1-4	Basalt lava	90
Krafla – Hranftinnuhryggur outcrop	65°41'13.62N 16°43'40.42W	90-40	Steep conduit	80	3-7	Hyaloclastite	15
Húsafell West outcrop	64°41'23.27N 20°57'20.85W	500	Irregular sheet	45 to 05	~ 2	Welded ignimbrite	115
Húsafell East outcrop	64°41'25.78N 20°57'16.44W	500	Sill	10	~ 2	Conglomerate	05

Note: Emplacement depth estimated from topography and literature (Burchardt, 2008; Tuffen and Castro, 2009; Mc Gowan, 2016).
Undamaged country rock uniaxial compressive strength is estimated using our Schmidt hammer data adjusted with reference to values by Eggertsson (2019).

2.5.1 The intrusions

2.5.1.1 Landsendi (Njarðvík-Dyrfjöll)

Orientation measurements of the contact and vesicles, and intrusive geometry of the sill tip at Landsendi, are consistent with a sill propagating towards the NE at a low discordant angle of <30° (Fig.2.2A). Zones of high vesicularity are associated with a higher dip in vesicle orientations and located at the sill tip or adjacent to major faults (Fig.2.2B). Sill thickness abruptly decreases towards the tip cavity, and the intrusion roof is displaced by several sub-vertical faults, into which rhyolite flow banding is deflected. Near the middle of the outcrop, an additional scree-hidden fault corresponds to an elevation difference of a few metres between the southern and the northern sections (Fig.2.2B). The rhyolite at the contact with country rock is colour-banded and contains spherulites (Fig.S2.2. Supplementary Material). A strongly fractured, friable, clay-rich layer is located at the inner marginal zone, between devitrified margins and intrusion core. These platy joints become progressively denser towards the coherent rhyolite at the sill core.

2.5.1.2 Hrafntinnuhryggur (Krafla)

We characterise two parts of the Hrafntinnuhryggur feeder dyke: (1) its southern-most extent and deepest dissection (90 m), where the dyke is ~2 m thick and cuts through basalt; (2) its shallower dissection (30-50 m) 150 m to the north, where the ~7-m-thick intrusion penetrates massive to crudely bedded basaltic hyaloclastite and flares upwards and northwards to form the columnar-jointed base of associated lava (Fig.2.3). In the near-complete obsidian sheet, micro-crystalline and/or devitrified rhyolite is locally but rarely present, although predominant in the overlying dyke-fed lava bodies (Fig.2.3C; Tuffen and Castro, 2009). Vesicle orientations within the intrusion show neighbouring opposite dipping directions, and flow complexity is also highlighted by a layer of hyaloclastite subdividing the intrusion in two parallel sections at the deepest dissection (Fig.2.3C). Dense glass progressively transitions to highly vesicular glass towards the intrusion margins, then to pumice breccia at the contact with country rocks. This breccia consists of fibrous, tube-like pumices (0.1-10 cm), rare lithic clasts (<3 cm) and dense glassy particles (<1 cm; Fig.2.7F).

2.5.1.3 Húsafell

A complex intrusive architecture is present at Húsafell (Fig.2.4D). Due to the strong similarity in intrusion dimensions and textures, and to the progressive continuity in orientations, we assume that intrusive segments along the valley are all parts of one single intrusion separated by a scree-buried fault zone (Fig.2.4A). At the western outcrops, an intrusive finger is present underneath the rigid layer of welded ignimbrite. Another finger cuts through it, resulting in a step-wise transgressive sill which follows the tuffisite veins. Two metres above the top contact, a >50 cm thick, near-horizontal tuffisite vein cuts friable, less densely-welded ignimbrite and extends over many tens of metres (Fig.2.4B). A few major faults cut through the valley, displacing many of the studied formations (Fig.2.4A). The horizontal tuffisite is therefore probably connected with the intrusion at depth, but erosion has removed any evidence for a connection. Quenched margins at the contact are irregular in thickness, especially at the east outcrop where their fingering into the conglomerate follows fine-grained zone and deviates around coarser zones (Fig.2.4C). We use the northern section to illustrate features that are of better quality than at other localities, although it is not part of outcrops characterised for this study.

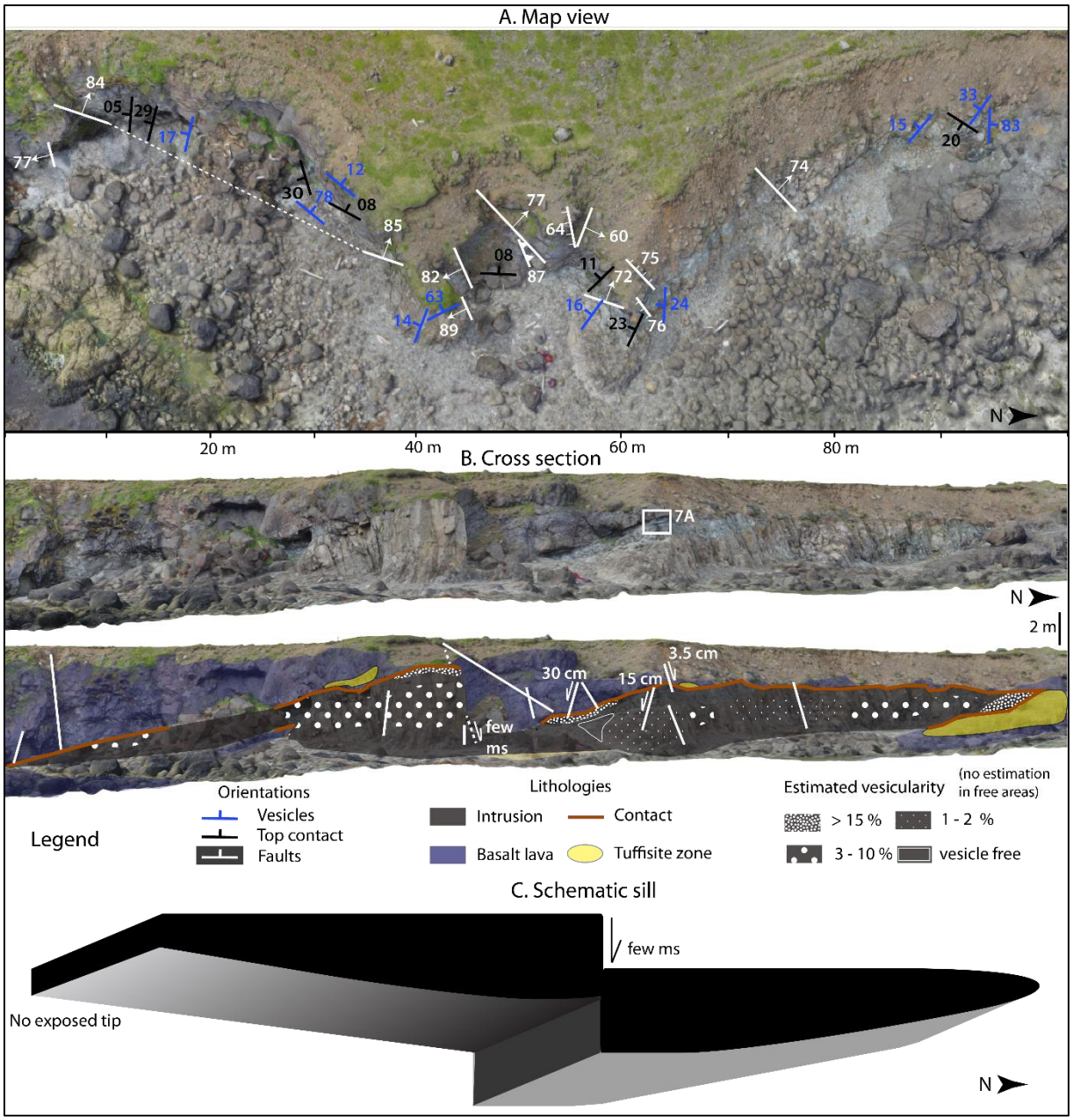

Figure 2.2. Landsendi 1-4 m thick sill in the Njarðvík-Dyrfjöll volcano. A) Map view of the intrusion with orientation of contacts, faults and vesicles. Vesicles in the intrusion core dip at 14-33□, and >63□ at intrusion margins. B) Photograph (top) and interpreted (bottom) cross-section of the intrusion with vesicularity estimations, faults and areas containing tuffisites. Location of Figure 2.7A is indicated by a white box. Some faults displace the sill by a few cms to >2 m. The cross section corresponds to the area in A, with horizontal-vertical scale difference caused by the perspective. C) Three-dimensional sketch of the intrusion, based on 3D photogrammetry and field insight into top and bottom contacts. The schematic is simplified to roughly highlight the intrusion shape.

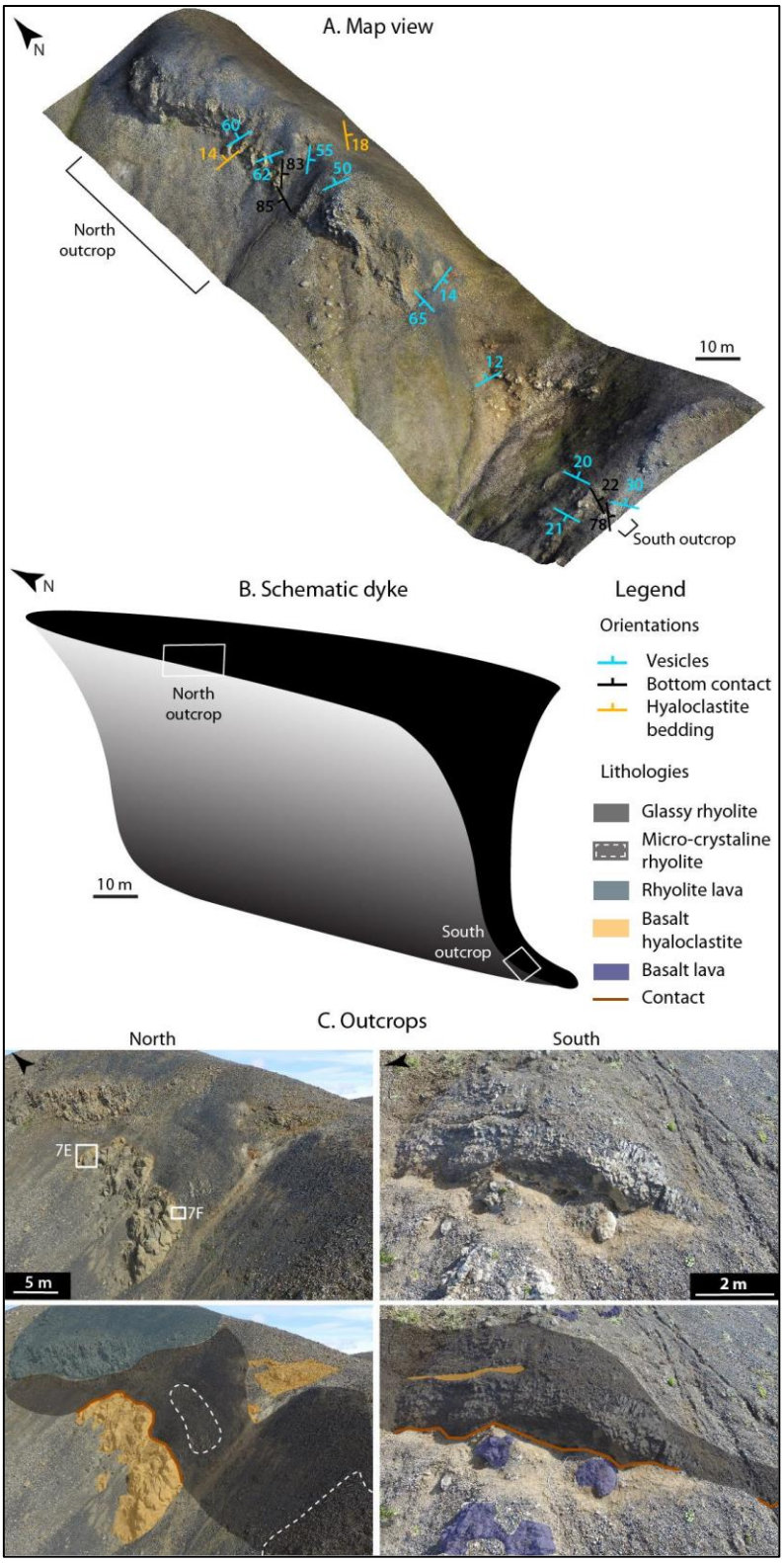

Figure 2.3. Feeder dyke at the south of Hrafntinnuhryggur, Krafla. A) Map view from photogrammetry reconstruction, with orientations of intrusion margins, hyaloclastite bedding and vesicles within the intrusion. B) Simplified 3D sketch of the dyke geometry, with location of the two outcrops. The scale is roughly similar to the map in A. C) Photograph (top) and interpreted (bottom) cross sections of north and south outcrops, with location of pictures for Figures. 2.7E, 7F. Change in scale from A is caused by perspective effect.

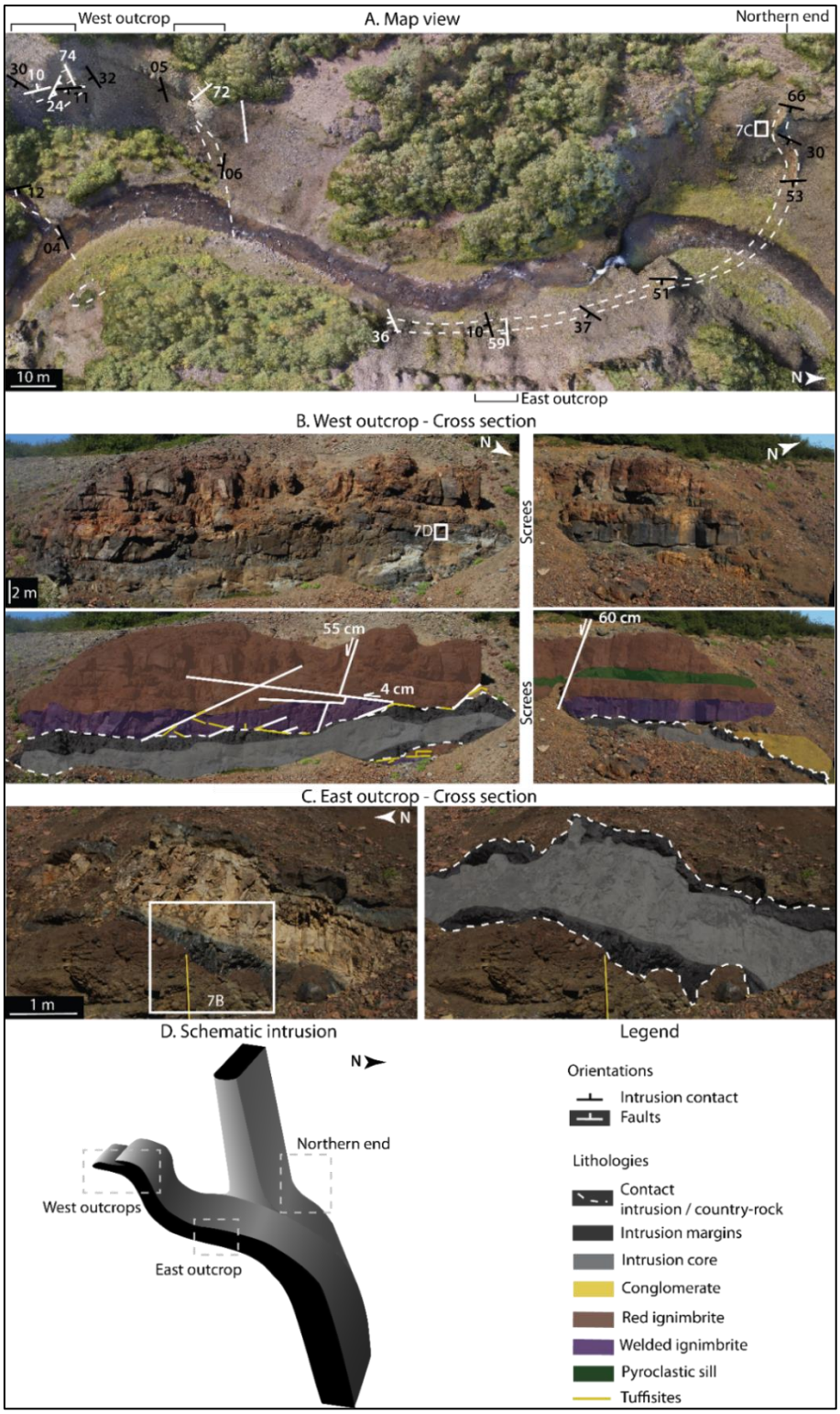

Figure 2.4. Intrusive system at Deildargil, Húsafell. A) Map view constructed from photogrammetry with orientation of intrusive contacts and faults, location of main outcrops and picture from 7C (white box). B) Photograph (top) and interpreted (bottom) cross section of Húsafell West, with highlighted faults and lithologies, and location of picture for Figure 2.7D. 15 m scree-covered metres separate the lateral pictures. C) Photograph (left) and interpreted (right) cross section of rhyolite intrusion through conglomerate at Húsafell East, with location of picture for Figures 2.7B. D. Simplified 3D geometry of the ~2 m thick intrusion. Not to scale.

2.5.1.4 Textures and vesicles in intrusions

We now present the textural features of all the intrusions collectively to illustrate commonalities and distinctions.

All micro-crystalline cores are fine-grained, consisting of quartz and feldspar with ~1 mm long phenocrysts (Fig.2.8C). They sharply transition towards glassy quenched margins, which exhibit a colour gradient from dark blue or green to black (Fig.2.7B). Margins consist of dense and nearly crystal-free obsidian (~3% quartz and feldspar phenocrysts), locally devitrified (containing spherulites and/or lithophysae, Fig.S2.2) and with green amygdales (secondary mineral precipitation within cavities. Figs.2.7A; 2.8B). They are also cut by columnar joints, sub-parallel curviplanar fractures and perlitic cracks (Fig.2.8A), and progressively alter to clay minerals in zones of high fracture density.

Estimated vesicularity in all the intrusions is ≤5-10 % at cores, increasing towards intrusive tips and margins. However, the three field sites show major differences in vesicle size and shape, plotted in Figure 2.5 with relative distance from the intrusion tip for localities of Landsendi and Húsafell West. The lines defined by data for small vesicles are artefacts caused by the measurement resolution (each line corresponds to an increment of 0.5 mm in the short axis).

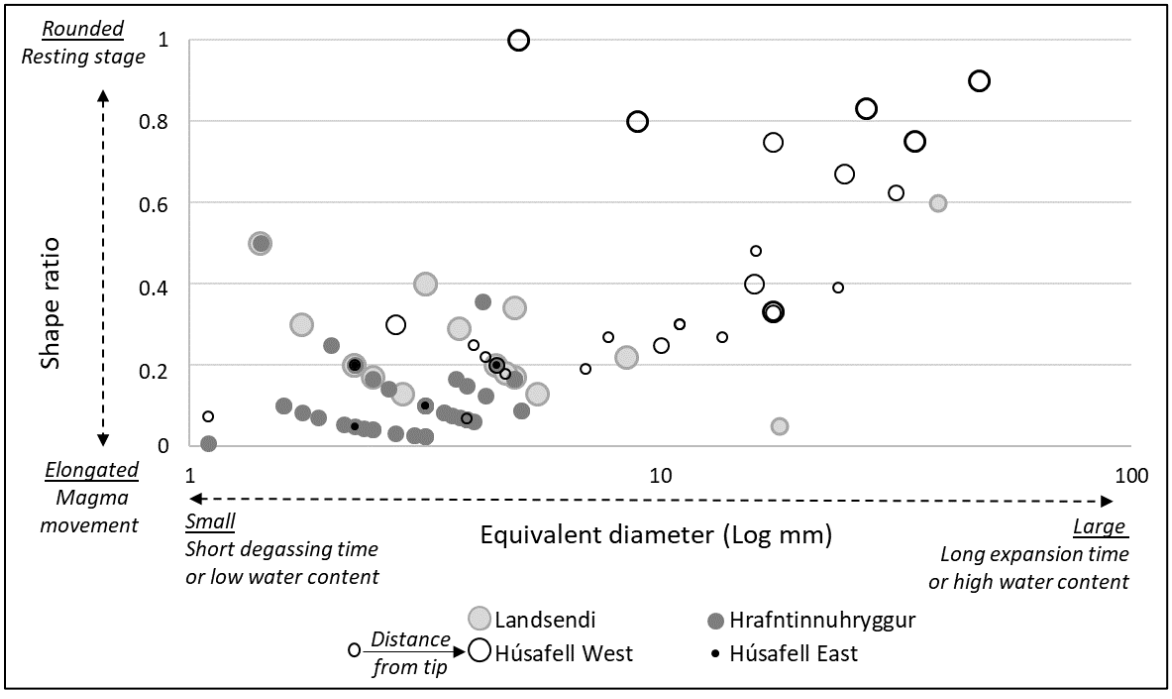

Figure 2.5. Vesicle size and shape ratio within the intrusions. Each data point represents the largest vesicle in a zone (sill tip, roof, core and bottom of intrusion. c.f. Supplementary Material Fig.S2.1 and Table S2.3). Data from the sill tip at Landsendi are represented with smaller dots and data at Húsafell West are divided into 4 zones: sill tip (smallest dots), 1.5 m away, 5.5 m away and 8.5 m away from the sill tip (largest dots).

At Landsendi, vesicles are small (mean 7 mm in equivalent diameter) and elongate (average shape ratio 0.3). The two largest vesicles were both measured at the sill tip. At Hrafntinnuhryggur, vesicles are smaller (mean 3 mm) and have the lowest shape ratio at 0.1 (highly elongate), with decreasing shape ratio for increasing vesicle size. At Húsafell West, vesicles are the largest (12 mm) and have the highest shape ratio of 0.4 (most spherical). However, vesicle shape ratio decreases towards the intrusive tip, from >0.8 to <0.4, as vesicles become progressively more elongate. The shape ratio also increases with vesicle size, as largest vesicles are the most spherical. At Húsafell East, vesicles are small (3 mm) and strongly elongate (shape ratio <0.2), similar to Hrafntinnuhryggur vesicles, although there is no discernible trend.

2.5.2 The intrusion-country rock interface

The intrusion-country rock interface (logged for each site on Fig.2.6) highlights that rhyolite is systematically chilled at the contact. Figure 2.7 shows associated features of particular interest, and lithologies are pictured in Figure 2.8. We observe stratigraphic differences for each site, which can nevertheless be paired: At Landsendi and Húsafell West, tuffisite breccia separates the intrusion from the country rock (Fig.2.7D) and tuffisite veins propagate into the country rock (Fig.2.7C). At Hrafntinnuhryggur and Húsafell East, the rhyolite is directly in contact with the country rock, which shows a colour variation (Fig.2.7B, E, F).

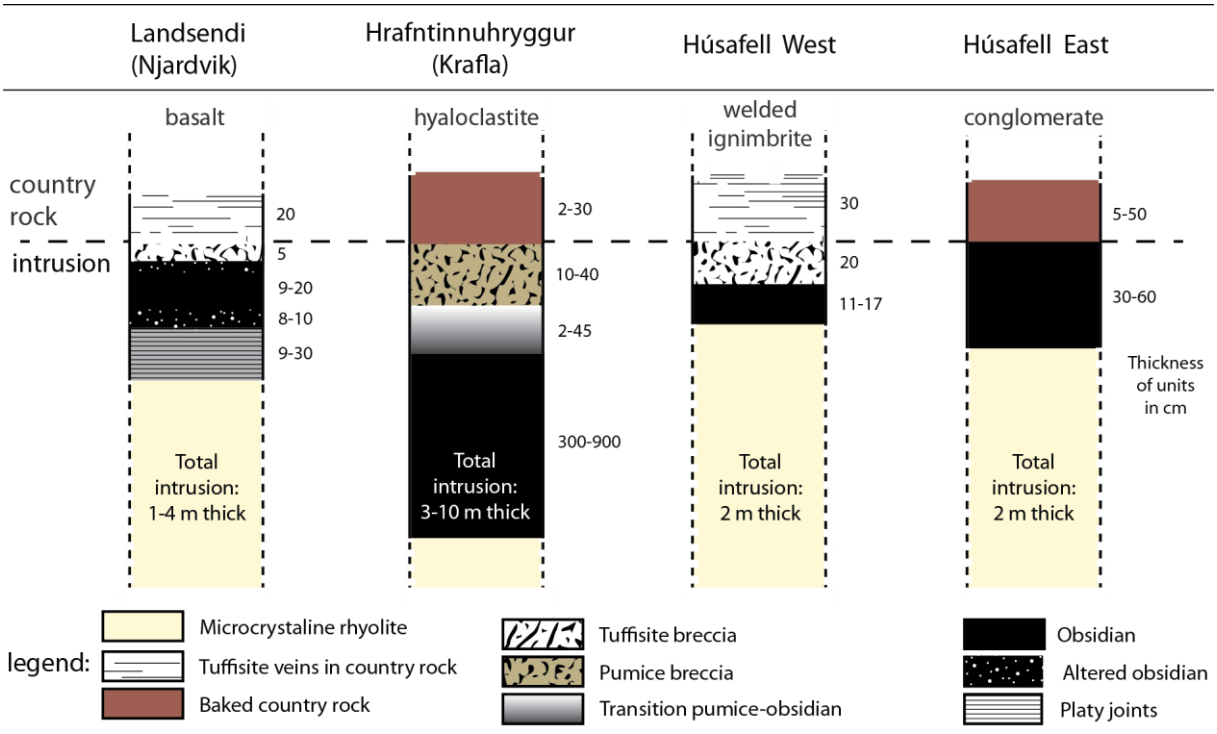

Figure 2.6. Geological logs of intrusion-country rock interfaces. Thickness given next to each unit is in cm. Country rocks are either baked (hyaloclastite at Hrafntinnuhryggur and conglomerate at Húsafell East) or brecciated and fractured (basalt at Landsendi and welded ignimbrite at Húsafell West). Damage zone thickness is estimated from macro-scale visible indicators, and so are minima as micro-scale alteration is likely more extensive.

Figure 2.7. Intrusive materials and country rocks. Contacts are outlined with a white dashed line. A) Platy zone at Landsendi, in between devitrified obsidian and rhyolite core in the intrusion. B) Húsafell East. Directly at the contact, rhyolite is quenched and conglomerate is baked. C) Tuffisite veins (contours in back line) cutting through basalt at the northern end of Húsafell site. D) Húsafell West. Tuffisite breccia between rhyolitic glass and ignimbrite. E) Hyaloclastite at Hrafntinnuhryggur, with colour gradient towards the contact. F) Pumice breccia at the contact with hyaloclastite at Hrafntinnuhryggur.

2.5.2.1 Landsendi – Basalt

Undamaged basalt lava units at Landsendi are exposed in irregular ~3 m-thick sheets with poorly vesicular coherent dense core and ~5 mm long feldspar phenocrysts (Fig.2.8D). Damaged basaltic lava (Fig.2.8H) has vesicles filled with green amygdales and contains fractures exploited by tuffisite veins a few millimetres to ~10 cm wide (similar to Fig.2.7C). In the immediate vicinity of the intrusion, fracture density increases. At the northern sill tip, erosion exposes a ~10 m² surface of underlying basalt covered by an irregular layer of 5 cm-thick tuffisite breccia (Fig.2.2B). At the intrusion roof, similar breccia appears as local ~20 cm long patches, at one occasion associated with a syn-emplacement fault (Fig.2.2B). The tuffisite veins are in general filled by predominantly well-sorted, partially rounded and fine-grained (<1mm) material in complex depositional structures, with occasional coarser (1-5mm), poorly-sorted lenses or layers (similar to Fig. 2.7C). Clasts include lithics derived from the country rocks, juvenile pumices, glass and micro-crystalline rhyolite associated with the intrusion. Tuffisite breccias (Fig.2.7D) are coarser-grained equivalents of the tuffisite veins, but are finer-grained, less pumice-rich and more compacted than pumice breccia (Fig.2.7F).

2.5.2.2 Hrafntinnuhryggur - Hyaloclastite

At Hrafntinnuhryggur, Pleistocene basaltic hyaloclastite was emplaced subglacially (Tuffen and Castro, 2009) and exhibits complex bedding, which may have been deformed or displaced by the intrusion. Bedding irregularity and the rarity of outcrops prevent any systematic record of orientations (Fig.2.3A). Undamaged hyaloclastite is mostly poorly sorted and pale yellowish-brown to grey. It consists of a fine-grained palagonitic matrix with heterogeneously dispersed, 1-20 cm long, angular clasts of crystalline basalt, and predominantly glassy <5 mm long clasts (Fig.2.8G). Within ~40 cm of the intrusion margin, the altered hyaloclastite displays an orange colour (Figs.2.7E; 2.8K).

2..5.2.3 Húsafell West – Welded ignimbrite

Undamaged welded ignimbrite from the Deildargil ignimbrite formation is a 1.6 m-thick near-horizontal sheet densely compacted into glass. It contains 4-5 cm long and >2 cm wide horizontal fiamme, rare 2 mm long, predominantly feldspathic phenocrysts, and many 1-3 cm lithophysae (Fig.2.8E). The damaged welded ignimbrite is highly fractured, and these fractures have white alteration haloes <5 mm wide (Fig.2.8I). Tuffisite breccias are emplaced along the intrusion margins, forming a <~5 cm thick irregular unit (Fig.2.7D). Tuffisite veins cut the ignimbrite, <1 m from the intrusion (Fig.2.7C). One notable sub-horizontal vein cuts friable ignimbrite ~2 m above the intrusion, reaching ~50 cm thick and exposed over ~60 m. It contains

complex sedimentary structures, with interfingering and injection into fragments of friable ignimbritic country rock at the upper and lower vein walls.

2.5.2.4 Húsafell East – Conglomerate

The contact intrusion-conglomerate at Húsafell East is very sharp and undisturbed by any vein or breccia, and the quenched margins follow the country rock irregularities. Undamaged conglomerate is typically massive and poorly-sorted, but locally bedded, with a fine-grained pale grey to yellow matrix. The largest clasts are a few cm in size (Fig.2.8F). The damaged conglomerate is more compact and of a browner colour with fractures extending ~10 cm from intrusion margins (Figs.2.8J; 2.7B).

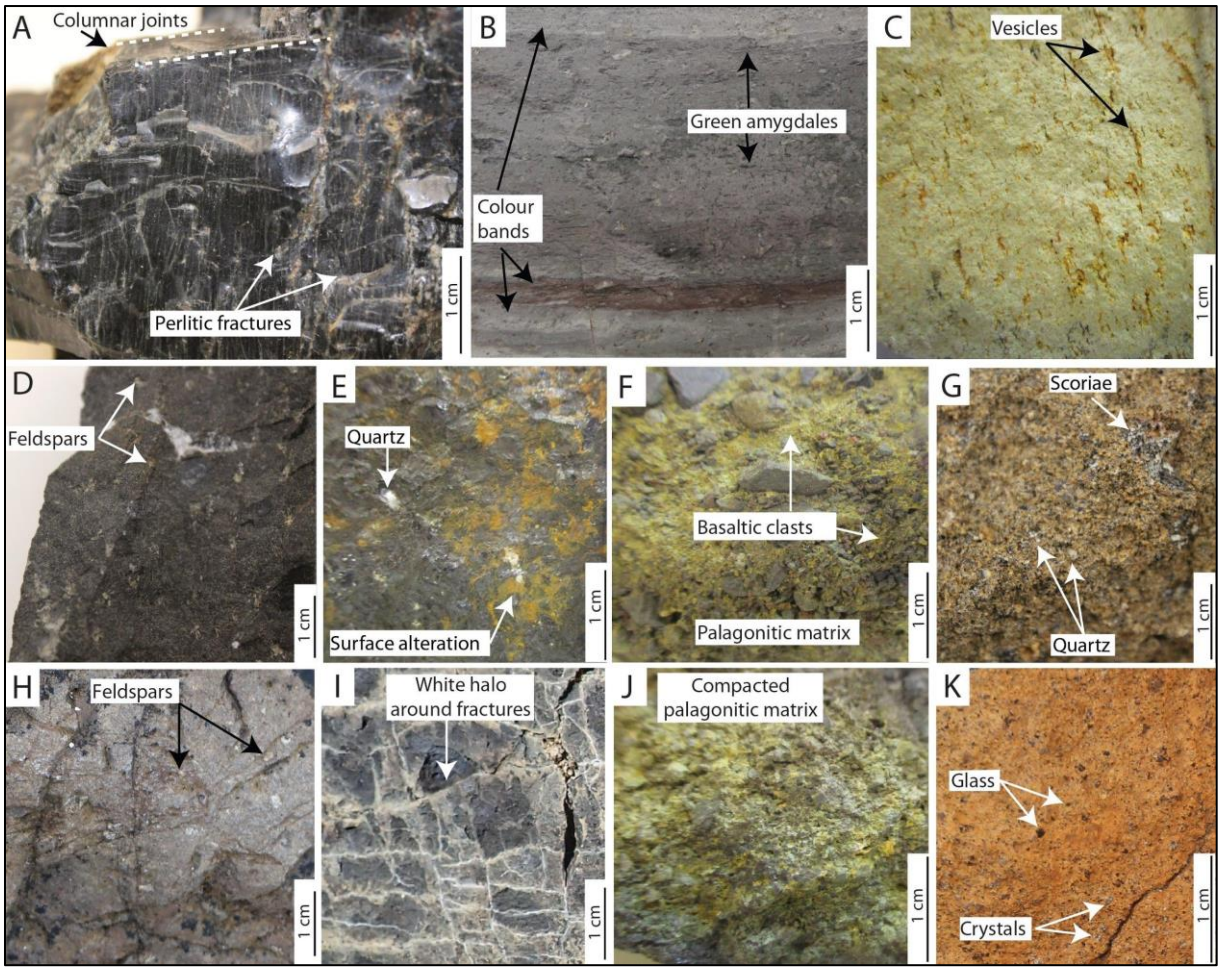

Figure 2.8. Geotechnical units. A) Obsidian from the glassy margin at Húsafell East. B) Devitrified chilled margins with colour bands at Landsendi. C) Rhyolite core from Landsendi. D) Undamaged basalt lava from Landsendi. E) Undamaged welded ignimbrite at Húsafell West. F) Undamaged conglomerate at Húsafell East. G) Undamaged hyaloclastite at Hrafntinnuhryggur with palagonitic matrix. H) Damaged basalt at Landsendi. I) Damaged welded ignimbrite at Húsafell West J) Damaged conglomerate at Húsafell East. K) Damaged hyaloclastite at Hrafntinnuhryggur.

2.5.3 The impact on country rocks

2.5.3.1. Geotechnical units

We sort the lithologies into 11 geotechnical units according to the classification by del Potro and Hurliman (2008), illustrated in Figure 2.8 and briefly described in Table 2.2: Rhyolite intrusions are subdivided into obsidian margins (Fig.2.8A), clay-rich altered zones (Fig.2.8B) and crystalline cores (Fig.2.8C). Country rocks include undamaged basalt lava (Fig.2.8D), welded ignimbrite (Fig.2.8E), conglomerate (Fig.2.8G), hyaloclastite (Fig.2.8I) and their damaged equivalents (Fig.2.8F, 8H, 8J, 8K, respectively).

TABLE 2.2. GEOTECHNICAL UNITS

Geotechnical unit	**Location**	**Quality (sub-unit)**	**Description**
Rhyolite - Crystalline core	All sites	Fresh	Very fine-grained with feldspar phenocrysts (masses of feldspar, SiO_2 polymorphs and oxides). Low vesicularity.
Rhyolite - Obsidian margins		Fresh	Near crystal-free perlitic obsidian with variable vesicle content. Colour bands.
		Altered	Strongly devitrified and commonly further altered to an assemblage of clay minerals.
Basalt lava	Landsendi	Undamaged	Coherent dense core poorly vesicular, finely crystalline groundmass with feldspar phenocrysts.
		Damaged	As above but cut by fractures and tuffisite veins. Vesicles filled with green alteration minerals.
Hyaloclastite	Hrafntinnuhryggur	Undamaged	Poorly sorted with angular, glassy and crystalline lava clasts cemented in a fine-grained palagonitic matrix. Brown-grey.
		Damaged	Orange colour. Fractures < 20 cm long.
Welded ignimbrite	Húsafell West	Undamaged	Densely welded, nearly porosity-free glassy ignimbrite with distinctive near-horizontal elongated fiamme. Contains 2 mm phenocrysts and 1-3 cm lithophysae.
		Damaged	Highly fractured, with white alteration halo. Cut by tuffisite veins.
Conglomerate	Húsafell East	Undamaged	Massive, poorly-cemented polymictic conglomerate with grey to yellow weakly palagonitised matrix and prominent rounded basaltic clasts. Local better-sorted, bedded lenses.
		Damaged	As above but fractured, with a yellow to brown or red matrix.

2.5.3.2 Field assessment of rock properties

Tinyperm and Schmidt hammer measurements of permeability and relative hardness are presented in Figures 2.9 and 2.10, respectively. Measurements extend 1.4-3.2 m from the contact into the country rock, with 4-15 measurement points per transect. The permeability increase towards the contact in the damaged basalt and welded ignimbrite is > 1 order of magnitude over ~30 cm, which does not exceed the variability in the undamaged country rock, and is not statistically significant. The variability in undamaged conglomerate and hyaloclastite is smaller (~half an order of magnitude, Fig.2.9; Eggertsson et al., 2018) and permeabilities decrease towards the intrusion by >1 order of magnitude over 20-40 cm, from $5 \cdot 10^{-13}$ to 10^{-14} and $5 \cdot 10^{-12}$ to 10^{-13} m², respectively. These variations thus exceed that of the variability in undamaged rocks and the significance is confirmed by the ANOVA statistical analysis of the results (p-values < 0.04).

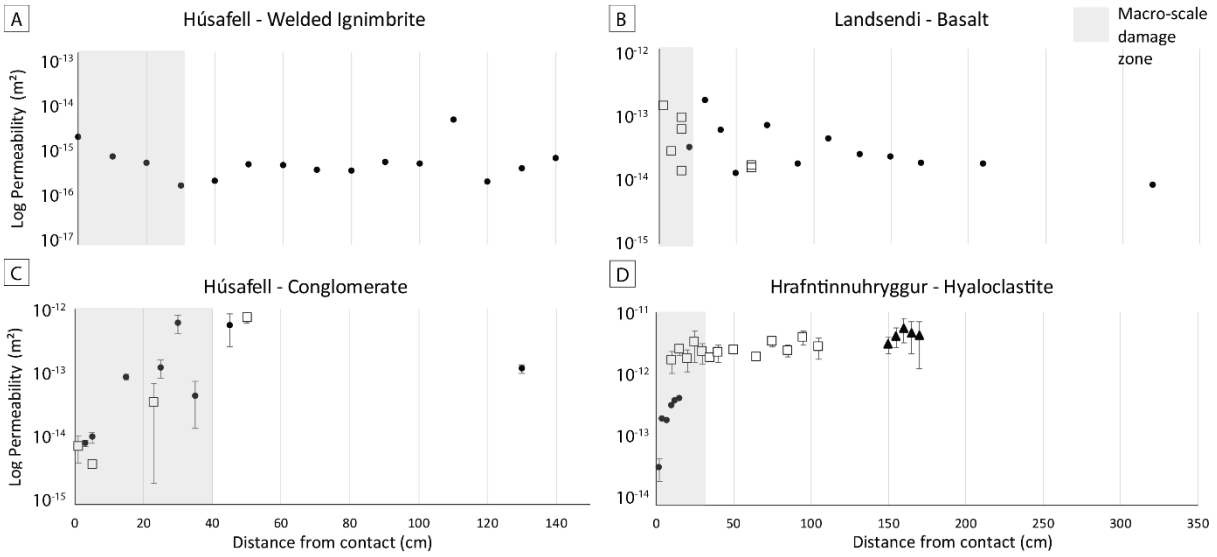

Figure 2.9. Permeability transects within country rocks. Grey areas show the extent of visible macro-scale damage at the measurement location. Each transect through the same country rock is represented by a different symbol. Error bars are one standard deviation where several measurements were made. Points without error bar were measured once (c.f. Supplementary Material, Table S2.1). Values have inherent uncertainties of a factor of 1.05 (Brown and Smith, 2013). A) Transects in welded ignimbrite start at the intrusion roof. B) Profiles in basalt both start at the intrusion roof. C) Profiles in conglomerate, one from the roof (squares), one from the base of the intrusion (circles). D) Profiles in the hyaloclastite at Hrafntinnuhryggur, starting at the intrusion base.

The hardness significantly decreases by a factor >2 towards the intrusion in welded ignimbrite and basalt, with the change initiated at ~60 cm and ~90 cm from the contact, respectively (Fig.2.10). These distances are greater than the distance at which macro-scale damage are recorded.

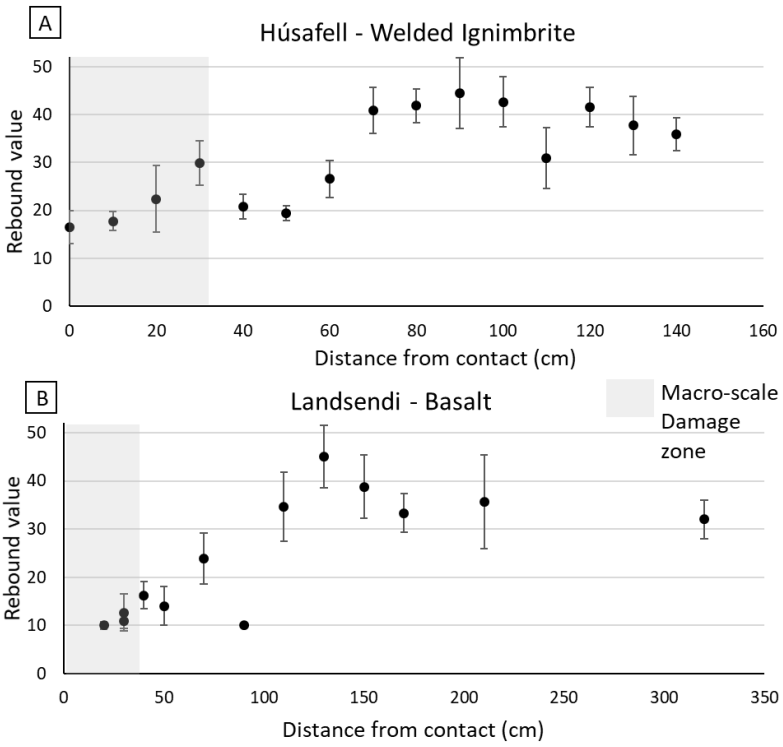

Figure 2.10. In-situ Schmidt hammer rebound along transects in the country rocks. The rebound value is proportional to rock hardness. Each point on the graph represents the average of ~10 measurements, with error bars representing one standard deviation. Grey areas show the extent of macro-scale damage at the transect location. A) Welded ignimbrite at Húsafell. B) Basalt at Landsendi. Conglomerate and hyaloclastite hardness were too low to be measured using a Schmidt hammer.

2.5.3.3 Fracture assessment

Fracture density and area at Húsafell are plotted against distance from the contact and averaged per transect and lithology for each outcrop in Figure 2.11. Data are available in Supplementary Material (Fig.S2.1, Table S2.2). Changes in fracturing from undamaged to damaged welded ignimbrite and conglomerate are illustrated in Figures 2.11C and 11D, respectively. In undamaged country rocks, fracture density is typically 7 fractures per metre within the welded ignimbrite (at ~80 cm from intrusion) and 2 fractures per metre in conglomerate (at ~50 cm from intrusion) (Fig.2.11A). These values progressively increase towards the contact by a factor of 5-7 (up to 51 and ~10 fractures, respectively). In the damaged zones of the four rock types, the average fracture density systematically exceeds that of the equivalent undamaged rock while the average fracture area is smaller (Fig.2.11B). Fracture density is higher in undamaged basalt and welded ignimbrite (18 and 22 fractures per metre, respectively) than in undamaged conglomerate and hyaloclastite (5 and 7 fractures per metre).

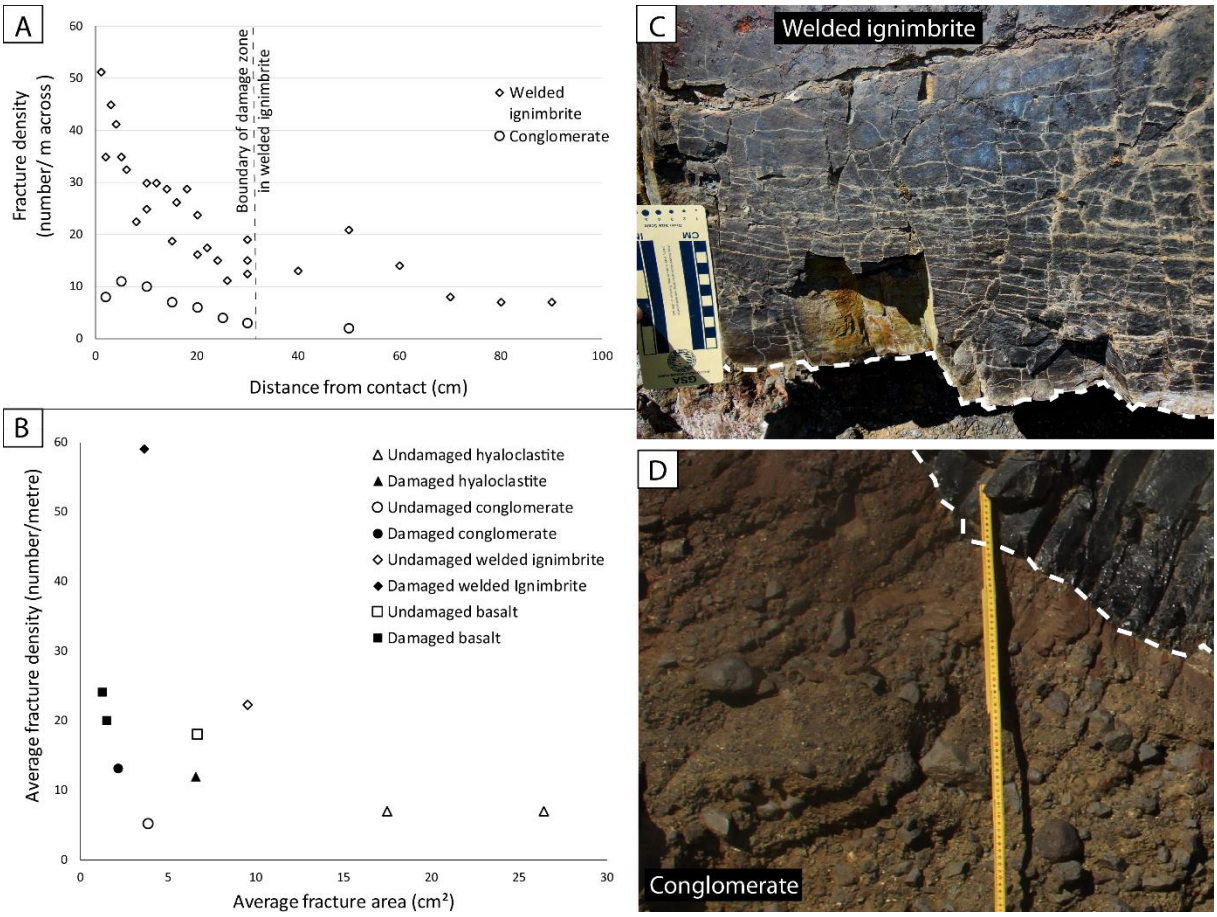

Figure 2.11. Fracture distribution in country rocks. A) Fracture density at Húsafell with distance from the intrusion. The dotted line at 30 cm corresponds to the boundary of the macro-scale damage zone in welded ignimbrite. In conglomerate, this zone is irregular, 5-50 cm thick. B) Average fracture density versus average fracture area in undamaged (empty symbols) and damaged (full symbols) country rocks. Each data point represents one set of measurements. C) Fractured welded ignimbrite at the contact (white dashed line) with the intrusion at Húsafell West. D) Fractured conglomerate at the contact (white dashed line) with the intrusion at Húsafell East.

2.5.4 Summary of the results

At Landsendi, a sill intrudes into competent basalt lava (Fig.2.8D) to form an intrusion containing stretched vesicles <15 mm long (Fig.2.5) with platy jointing and devitrification of the rhyolite near the margins (Figs.2.7A; 2.8B). The country rock is cut by tuffisite veins (similar to Fig.2.7C) and by additional macro-fractures at the intrusion interface (Fig.2.8H), evidenced by a slight increase in fracture density (Fig.2.11B) and decreased hardness by a factor >2 (Fig.2.10B).

At Hrafntinnuhryggur, a near-surface dyke intrudes through basaltic hyaloclastite and results in an obsidian intrusion with highly stretched vesicles (Fig.2.5). At the margins, a progressive vesicularity gradient marks the transition towards a pumice breccia (Fig.2.7F). The surrounding

hyaloclastite is compact and discoloured (Figs.2.7E; 2.8G, 8K), damaged by a few short fractures (Fig.2.11B) with matrix permeability reduction of > 1 order of magnitude (Fig.2.9D).

At Húsafell, a sill intrudes through conglomerate, deflecting at the base of a basalt lava and arresting at the base of a brittle welded ignimbrite, where the intrusion contains large and rounded vesicles (Fig.2.5). The conglomerate at the contact is discoloured (Figs.2.7B; 2.8J; 2.11D), with a slight increase in fracture density (Fig.2.11) and an order of magnitude matrix permeability decrease (Fig.2.9C). Where the intrusion encountered the welded ignimbrite and basalt, the interface is surrounded by tuffisite breccia (Fig.2.7D) and the country rock is cut by tuffisite veins (Fig.2.7C). The number of fractures in the welded ignimbrite increases by ≤7 times (Fig.2.11) and the hardness decreases by a factor >2 (Fig.2.10A).

2.6 Discussion

The four intrusions in this study are all rhyolitic in composition, <7 m in thickness and formed during single intrusive events in broadly similar settings and depths within Icelandic central volcanoes. They can be differentiated in terms of emplacement mechanism and influence on the surrounding rock. However, as the intrusion thicknesses—the primary factor controlling rock damage (Annen, 2017)—are broadly similar, and magma compositions lie within a restricted rhyolitic range, the mechanical response to intrusions should mostly reflect the diverse country rock type.

Direct comparison between sites have some limitations due to variation in viscosity, flow history, and fluid cooling. We estimate that water content differs by <1 wt % between the intrusions (0.3-0.4 wt. % at Hrafntinnuhryggur, Tuffen and Castro, 2009; ~1 wt. % at Húsafell, McGowan, 2016). The maximum difference in silica content is estimated ~5 wt % (~75 wt % at Hrafntinnuhryggur, Tuffen and Castro, 2009; ~72 wt % SiO_2 at Húsafell, McGowan, 2016). Temperature can also vary by >100 °C for rhyolitic magmas. These parameters impact the magma viscosity, and thus the intrusive emplacement and heat transfer. Our poor control on viscosity limits interpretation for vesicle response to stress, relaxation and degassing within magma. Considering that static magma versus flowing magma also impact the heat flux (Tsang et al., 2019), another limitation is the eruption-feeding dyke at Hrafntinnuhryggur, implying a flowing magma, while no conclusive evidence demonstrates whether the Landsendi or Húsafell

magma erupted. An additional difference between sites is a potentially meltwater-assisted cooling at Krafla (Tuffen and Castro, 2009).

2.6.1 Emplacement processes

The intrusions in this study comprise sills, dykes, and conduits: the main types of shallow intrusions at Icelandic central volcanoes (other types include laccoliths, lopoliths, inclined sheets).

2.6.1.1 Landsendi

At Landsendi, shallow dipping lava units control the intrusion shape and associated damage. The feeder system for the Landsendi sill is not visible, but the middle fault could be related to a feeder dyke or inclined sheet, which could have impacted the intrusion geometry with thickening in the central part (laccolith or lopolith; Mathieu et al., 2008; Schmiedel et al., 2017). The intrusion shape appears unaffected by regional tectonic stresses (NNE-SSW extension; Burchardt et al., 2011) and rhyolite flow banding deflection into faults at the intrusion roof indicates syn-emplacement faulting. The tuffisite breccia at the tip is emplaced against the basaltic country rock (Fig.2.2B), recording initial emplacement of a fragmental gas-pyroclast mixture during pathway opening. Within the intrusion, the presence of inner platy-fractured joints (Fig.2.7A) is consistent with a quenching, shearing accommodation zone of outer magma during lateral propagation at high strain rates in the intrusion core. The vesicle population is small yet elongate (average 7 mm in equivalent diameter, 0.3 in shape ratio, Fig.2.5), consistent with a brief phase of vesicle growth or a low water content, high shear stresses and minimal relaxation, and thus swift initial emplacement and cooling. At the sill tip, vesicles are larger and have the most extreme values in shape ratio (Fig.2.5, the two >10 mm diameter vesicles, with shape ratios of 0.05 and 0.6), indicating a higher variety of vesicle processes, such as coalescence and relaxation, locally occurring together.

2.6.1.2 Hrafntinnuhryggur

The shallow subglacial hyaloclastite environment at Hrafntinnuhryggur plays an important role in emplacement processes. High glass content and pervasive fracturing in the dyke, together with the absence of a platy-fractured zone (Fig.2.6), indicate rapid quenching consistent with shallow emplacement at proximity with ice. Pumice breccia is found only at this field site, the shallowest of the three, and indicates fragmentation of highly-vesicular magma prior to ascent of less-vesicular dyke-filling magma, or prior to foam collapse. The greater vesicle elongation (average shape ratio of 0.1; Fig.2.5) suggests higher shear stresses than at the other intrusions,

especially considering that this feeder dyke has lower water content and silica than Húsafell intrusion, and thus a higher viscosity and higher resistance to deformation for a similar temperature. The shape ratio decreases with increasing vesicle size (i.e. larger vesicles are more elongated; Fig.2.5) and could relate to coalescence caused by shearing during magma propagation. The magma could have had a vesicular texture similar to volcanic conduits: large, elongated vesicles on the margins and small rounded vesicles closer to the centre.

2.6.1.3 Húsafell

The intrusion style at Húsafell particularly reflects the intruded country rock type. In the soft, weak conglomerate on the east side, the intrusion geometry is irregular. At the contact with the stronger basalt lava at the northern end, it deflects at the interface before progressing through it. When encountering the stiffer, stronger ignimbrite at Húsafell West, the intrusion forms a bedding-parallel sill periodically injecting pyroclastic material through discontinuities. The intrusion broke through the rigid country rock following the path created by pyroclastic material, propagating as a transgressive sill (Fig.2.4). The thick and horizontal tuffisite vein two metres above the intrusion roof is most likely related to the opening stage of the intrusion, when over-pressured gas entered the country rock, creating a magmatic pathway. At Húsafell East, where the intrusion propagates as a sill through conglomerate, elongated vesicles (<0.2 mean shape ratio, 3mm equivalent diameter, Fig.2.5) indicate rapid lateral propagation with high strain rates. At Húsafell West, where the intrusion propagates as an inclined sheet through the ignimbrite, larger vesicles (12 mm in equivalent diameter) could indicate prolonged growth during slower cooling, significant coalescence, and/or higher vesiculation triggered by higher country rock permeability (through fractures and tuffisite veins). Near-spherical vesicle shapes away from the tip and the increase in shape ratio with vesicle size (Fig.2.5) are consistent with magma stalling at the encounter with the strong lithology, creating a static phase of magma relaxation and extensive vesicle growth during prolonged cooling.

2.6.2 Country rock response

Intrusive processes have both mechanical and thermal impacts on surrounding country rocks. The undamaged lithologies at our field sites consist of both weak, permeable and porous units (hyaloclastite and conglomerate) and strong, less permeable units (basalt and welded ignimbrite) (Table 2.1; Fig.2.9). Geological logs of the contact zone and trends of permeability and hardness in the country rock reveal similarities between the response of hyaloclastite and conglomerate, and between the response of basalt and welded ignimbrite (Figs.2.6; 2.9; 2.10).

These rock responses to the intrusions highlight the role of the undamaged rock properties and could in turn influence the process of intrusion emplacement.

2.6.2.1 Interpreting permeability decrease

Hyaloclastite and conglomerate are affected by a colour change (grey-brown to red-orange, Fig.2.6), pore occlusion with one order of magnitude decrease in matrix permeability (Fig.2.9C, 9D), a moderate increase in fracture density (7-12 and 5-13 fractures per metre, respectively; Fig.2.11B), and decrease in fracture length and width (18 to 7 cm^2 and 4 to 2 cm^2 fracture area, respectively; Fig.2.10B).

Thermal alteration is more pervasive in weak country rocks with originally high permeability and porosity. High-temperature fluids readily propagated through the interconnected pore network, with advection and convection potentially expanding the thermally-affected zone. Weak rocks compacted to accommodate the additional volume of the intrusion and ductile shear failure may have occurred (as demonstrated by laboratory deformation experiments on altered weak brecciated lava margin in Mordensky et al., 2019). Compaction could have destroyed evidence of pre-existing discontinuities and opened short tensile fractures, associated with larger shear fractures. Despite the slight increase in fracture density, we interpret a net pore occlusion and porosity decrease (similar to what was observed in weak, porous, altered andesite by Heap et al., 2015), resulting in decreased matrix permeability. Pore occlusion is likely a result of pore compaction coupled with precipitation of hydrothermal and alteration minerals.

Despite the focus of this study on the field scale fractures and rock properties, our observations are consistent with pervasive chemical, mineralogical, thermal and fluidal impacts in weak country rocks, similar to that observed in porous brecciated lava margins by Mordensky et al. (2018a).

2.6.2.2 Interpreting permeability increase and weakening

Basalt and welded ignimbrite are weakened by a factor >2 (Fig.2.10), with an associated increase in fracture density (18 to ~22 and 22-59 fractures per meter, respectively; Fig.2.11B), and are crosscut by tuffisite veins. Fractures are narrower and/or shorter (10 to 4 cm^2 and 7 to 1 cm^2 in fracture area, respectively; Fig.2.11B).

Mechanical damage dominates in the originally strong country rocks, with accordingly low permeability and porosity (similar to the mechanical damage in the strong, low permeability dense coherent lava and andesite intrusions in Mordensky et al., 2018a, b). Compared to the

hyaloclastite and conglomerate, the fracture density of the welded ignimbrite and the basalt are always higher, revealing brittle deformation. Pre-existing fractures may have been exploited by gas and fragmented magma at the onset of magma propagation, creating the tuffisite veins (as also observed by Stasiuk et al., 1996). These veins were then used as a path for coherent magma ascent, which followed the gas and widened the tuffisite veins into intrusions. Many new fractures were also created, as demonstrated by the lower hardness and high fracture density close to the intrusion (Figs.2.10; 2.11), while matrix permeability was not significantly affected (Figs.2.9A, 9B). However, considering the large amount of fractures at the interface, especially in welded ignimbrite, and the significant decrease in hardness in both rocks, the rock mass permeability in these units likely increases (as in Heap and Kennedy, 2016) towards the intrusions (as observed in originally strong, dense coherent andesite lava and intrusive by Mordensky et al. 2018a).

We have no evidence for chemical, mineralogical or thermal alteration of these strong country rocks, but the intense fracturing suggests the generation of rock mass permeability that is favourable for hydrothermal fluid circulation. Any alteration occurring had a secondary impact compared to mechanical damage.

2.6.3 Overview and implications

We combine our results and field observations (rock properties, geological logs, contact features, vesicle characteristics) into one conceptual model per field site in Figure 2.12, highlighting the emplacement geometry, features indicating intrusive propagation style, and impact on country rocks.

Transposing the models at deeper emplacement and higher confining pressure, we would expect less magma degassing and lower permeabilities in the country rock. Magma vesicularity could be lower and material, fluid and gas injection into country rock as tuffisite veins, or magmatic fluids, would be restricted. Country rock fracturing would also be increasingly influenced by lithological pressure and more dominated by local tectonics. Ductile deformation is likely to dominate below ~7-9 km (Greenfield and White, 2015), although this may be locally shallower associated with more porous altered rocks (Mordensky et al 2019) and hydrothermal reservoirs and rhyolitic intrusions are commonly found significantly shallower in Iceland (e.g. Weber and Castro 2017).

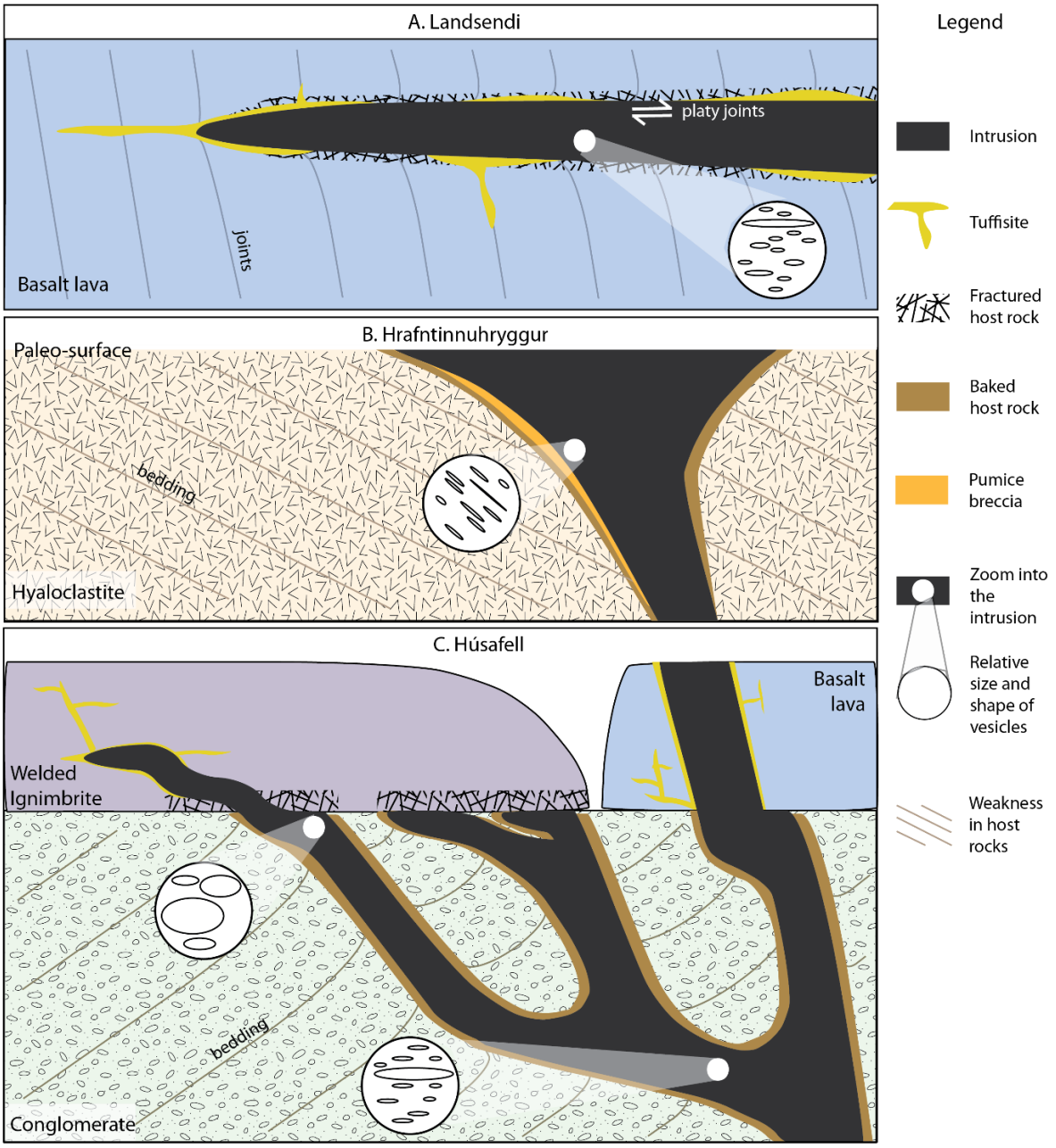

Figure 2.12. Conceptual models of the intrusions emplaced at 100–500 m depth and their contact features, at the three field sites in Icelandic central volcanoes. Schematic cross-sections are based on results and field observations. Vesicle shapes and relative sizes are indicated within the white circles. Not to scale. A) 1-4 m thick sill at Landsendi. Magma emplaced along a fracture network filled with tuffisite veins. Remnant tuffisite breccia is irregular along the contacts with fractured basalt and a few veins cut through the country rock. Rapid lateral propagation induced high strain rates during magma emplacement, which highly deformed the vesicles. High stress and slow cooling create platy jointing within the intrusion, between the quenched margins and micro-crystalline core. B) 3-7 m thick feeder dyke at Hrafntinnuhryggur. Shallow emplacement depth permitted rapid magma decompression, leading to vesiculation, vesicle shear, and formation of pumice at dyke margins. Hyaloclastite at the contact is altered with colour change, pore occlusion and a few tensile fractures. C) 2 m thick intrusion forming a network of dykes and sills at Húsafell. Conglomerate inelastically accommodates magma propagation, resulting

in colour change, pore occlusion and opening of small tensile fractures. Within the magma, vesicles are sheared according to the propagation direction. The intrusion is deflected at the base of stronger basalt lava, but cut through it, emplacing along tuffisite breccia in a similar process to what occurred at Landsendi. Because this section was not characterised in details, variation in fracture population is unknown. The intrusion fractures the base of strong welded ignimbrite, but could have initially failed to intrude it, with repeated injections creating several intrusive fingers. Magma stalling allows vesicle relaxation into rounded shapes, and the melt eventually propagated into the ignimbrite following tuffisitic patterns.

Damaged and altered country rocks are the origin of every overlying hydrothermal system. Their rock properties influence the mode of heat transfer and fluid circulation, and thus hydrothermal system architecture. There is no major variation of matrix permeability between different types of damaged country rocks (~1 order of magnitude difference, Fig.2.9), but high fracture density in rocks responding by weakening suggests a jump in rock mass permeability. Hydrothermal fluids could propagate in a channelized way through the discontinuities, in contrast to a matrix permeability clogging through pore occlusion. Resulting convection and advection of heat and fluids could increase the rate of heat transfer through damage zones, causing a more dynamic hydrothermal system. These more permeable rock masses (as shown in Heap and Kennedy, 2016) could thus make them viable for geothermal fluid extraction, possibly acting as feed zones. We consequently propose that the initial mechanical properties of intrusion-hosting rocks are an important consideration for geothermal exploration and reservoir engineering.

Forecasting of silicic magma mobility at caldera complexes relies on interpretation of deformation and seismic data, and therefore also directly relates to the deformation response of intruded country rock. The strong dependence of intrusion-triggered compaction and fracturing on the initial properties of the country rock highlights the importance of robust characterisation of the mechanical properties of caldera-filling formations, to enable appropriate geophysical data interpretation.

2.7. Conclusions

This study highlights how country rock response to shallow intrusion of silicic magma can vary. Icelandic rhyolitic intrusions were characterised at three field sites and within four country rock lithologies. Results are relevant within the context of Icelandic central volcanoes and shallow magma bodies, above the crustal ductile/brittle transition zone.

At Landsendi, the emplacement of a 1-4 m-thick rhyolitic sill into basaltic lava involved a dynamic lateral propagation, as indicated by tuffisite veins and breccia, platy jointing and elongated vesicles. Basalt at the contact is fractured over ~20 cm and its hardness is decreased by a factor >2.

At Hrafntinnuhryggur, Krafla, a shallow, 3-7 m-thick eruption-feeding dyke contains highly-elongated vesicles. Upward dyke widening and the presence of pumice breccia reflect the shallow degassing of an erupting magma. Basalt hyaloclastite at the contact is discoloured over <30 cm and fractured, with a decrease in matrix permeability by >1 order of magnitude.

At Húsafell, magma ascent within a complex ~2 m-thick rhyolitic sheet was stalled by encounter with strong welded ignimbrite, generating multiple sill tips and large, rounded vesicles in stalled magma that relaxed during prolonged cooling. Welded ignimbrite is highly fractured over 30 cm at the contact and its hardness is decreased by a factor >2. Lateral propagation in the underlying conglomerate resulted in an irregular <50 cm thick discoloured zone in the country rock, crossed by rare short and narrow fractures and corresponding to ~1 order of magnitude decrease in matrix permeability.

We propose a bimodal response behaviour to intrusive processes, based on observed damage and alteration in country rocks which relate to their initial properties, and impact the propagation style:

- Rock response by pore occlusion: in originally weak, porous and highly-permeable conglomerate and hyaloclastite (estimated initial UCS <15), porosity reduces by compaction and/or mineral precipitation, and permeability decreases accordingly by >1 order of magnitude. The inelastic accommodation to magma propagation allows irregular intrusive geometries to form.

- Rock response by weakening: in initially strong, low-permeability basaltic lava and welded ignimbrite (estimated initial UCS >90), intense fracturing and exploitation of fractures by tuffisite veins weaken the rock by a factor >2. These rocks appear to require accumulation of magmatic pressure with systematic formation of tuffisite veins prior to intrusive emplacement.

Our field observations of intrusion-country rock interactions provide critical information about the process of silicic magma ascent in the shallow crust and country rock response. Similar knowledge of geothermal reservoir formations will additionally shed useful light on evolving geothermal resources within intruded geothermal systems. Similarly, such a knowledge of caldera-filling formations will help the forecast of magma mobility.

2.8 Acknowledgements

The authors thank the National Power Company of Iceland (Landsvirkjun) for the accommodation provided at Krafla. We are also thankful to Felix von Aulock (University of Liverpool, UK) and Einar Bessi Gestsson (Uppsala University and Icelandic Meteorological office) for their assistance on the field, and to the farmers at Njarðvík for kindly giving access to the field sites. This work was supported by the Ministry of Business, Employment and Innovation, New Zealand [grant number E6552]; the Mason Trust funding from the University of Canterbury, New Zealand; and a Royal Society University Research Fellowship to HT.

2.9 References

Annen, C., 2017. Factors Affecting the Thickness of Thermal Aureoles. Frontiers in Earth Science, 5.

Albertsson, A., Bjarnason, J. Ö., Gunnarsson, T., Ballzus, C., Ingason, K., 2003. The Iceland Deep Drilling Project: Fluid Handling, Evaluation, and Utilization, 8.

Amaral, P.M., Rosa, L.G., Fernandes, J.C., 1999. Determination of Schmidt rebound hardness consistency in granite. International Journal of Rock Mechanics and Mining Sciences 36, 833 – 837.

ASTM, 2001. Standard test method for determination of rock hardness by rebound hammer method. 04.09 (D 5873-00).

Aydin, A., Basu, A., 2005. The Schmidt hammer in rock material characterization. Engineering Geology 81, 1-14.

Björnsson, A., Johnsen, G., Sigurdsson, S., Thorbergsson, G., Tryggvason, E., 1979. Rifting of the plate boundary in north Iceland 1975–1978. Journal of Geophysical Research: Solid Earth 84(B6), 3029–3038.

Brown, S., Smith, M., 2013. A transient-flow syringe air permeameter. Geophysics 78(5).

Burchardt, S., 2008. New insights into the mechanics of sill emplacement provided by field observations of the Njarðvík Sill, Northeast Iceland. Journal of Volcanology and Geothermal Research 173, 280–288.

Burchardt, S., Tanner, D. C., Krumbholz, M., 2012. The Slaufrudalur Pluton, Southeast Iceland - An example of shallow magma emplacement by coupled cauldron subsidence and magmatic stoping. Geological Society of America Bulletin 124, 213-227.

Burchardt, S., Mattsson, T., Palma, J. O., Galland, O., Almqvist, B., Mair, K., Jerram, D., Hammer, Ø., Sun, Y., 2019. Progressive Growth of the Cerro Bayo Cryptodome, Chachahuén Volcano, Argentina—Implications for Viscous Magma Emplacement. Journal of Geophysical Research: Solid Earth 124(8), 7934-7961.Carrigan, C. R., 1986. A two-phase hydrothermal cooling model for shallow intrusions. Journal of Volcanology and Geothermal Research 28(1), 175–192.

Clemens, J. D., Petford, N., 1999. Granitic melt viscosity and silicic magma dynamics in contrasting tectonic settings. Journal of the Geological Society 156, 1057–1060.

Conway, C., Townsend, D., Leonard, G. Wilson, C., Calvert, A., Gamble, J., 2015. Lava-ice interaction on a large composite volcano: a case study from Ruapehu, New Zealand. Bulletin of Volcanology 77.

Deere, D. U., Miller, R. P., 1966. Engineering classification and index properties for intact rock. Technical report, University of Illinois, Urbana, Illinois, 327p.

Delaney, P. T., Pollard, D. D., Ziony, J. I., McKee, E. H., 1986. Field relations between dikes and joints: Emplacement processes and paleostress analysis. Journal of Geophysical Research: Solid Earth 91(B5), 4920–4938.

Del Potro, R., Hürlimann, M., 2008. Geotechnical classification and characterisation of materials for stability analyses of large volcanic slopes. Engineering Geology 98(1–2), 1–17.

Dingwell, D. B., Lavallée, Y., Hess, K.-U., Flaws, A., Marti, J., Nichols, A. R. L., Gilg, A., Schillinger, B., 2016. Eruptive shearing of tube pumice: pure and simple. Solid Earth 7(5), 1383–1393.

Eggertsson, G. H., Lavallée, Y., Kendrick, J. E., Markússon, S. H., 2018. Improving fluid flow in geothermal reservoirs by thermal and mechanical stimulation: The case of Krafla volcano, Iceland. Journal of Volcanology and Geothermal Research.

Eggertsson, G. H., 2019. Constraining mechanical and permeability properties of the Krafla geothermal reservoir, North-East Iceland. PhD thesis, Liverpool University, UK.

Farquharson, J., Heap, M. J., Varley, N. R., Baud, P., Reuschlé, T., 2015. Permeability and porosity relationships of edifice-forming andesites: A combined field and laboratory study. Journal of Volcanology and Geothermal Research 297, 52–68.

Farquharson, J. I., Wild, B., Kushnir, A. R., Heap, M. J., Baud, P., Kennedy, B., 2019. Acid-Induced Dissolution of Andesite: Evolution of Permeability and Strength. Journal of Geophysical Research: Solid Earth 124(1), 257-273.

Fisher, R. A., 1925. Statistical Methods for Research Workers (Oliver and Boyd). Edinburgh, Scotland, 6.

Galland, O., Cobbold, P. R., Hallot, E., de Bremond d'Ars, J., Delavaud, G., 2006. Use of vegetable oil and silica powder for scale modelling of magmatic intrusion in a deforming brittle crust. Earth and Planetary Science Letters 243(3–4), 786–804.

Galushkin, Y. I., 1997. Thermal effects of igneous intrusions on maturity of organic matter: A possible mechanism of intrusion. Organic Geochemistry 26(11), 645–658.

Greenfield, T., White, R. S., 2015. Building icelandic igneous crust by repeated melt injections. Journal of Geophysical Research: Solid Earth 120(11), 7771–7788.

Gudmundsson, A., 1990. Emplacement of dikes, sills and crustal magma chambers at divergent plate boundaries. Tectonophysics 176(3), 257–275.

Gunnarsson, B., Marsh, B. D., Taylor, H. P., 1998. Generation of Icelandic rhyolites: silicic lavas from the Torfajökull central volcano. Journal of Volcanology and Geothermal Research 83(1–2), 1–45.

Gústafsson, L. E., 1992. Geology and petrography of the Dyrfjöll Central Volcano, eastern Iceland. Selbstverlag Fachbereich Geowissenschaften, FU Berlin 138

Hamada, M., Laporte, D., Cluzel, N., Koga, K. T., Kawamoto, T., 2010. Simulating bubble number density of rhyolitic pumices from Plinian eruptions: constraints from fast decompression experiments. Bulletin of Volcanology 72(6), 735–746.

Healy, D., Rizzo, R., Duffy, M., Farrell, N. J. C., Hole, M. J., Muirhead, D., 2018. Field evidence for the lateral emplacement of igneous dykes: Implications for 3D mechanical models and the plumbing beneath fissure eruptions. Volcanica, 85–105.

Heap, M. J., Kennedy, B. M., Pernin, N., Jacquemard, L., Baud, P., Farquharson, J. I., Scheu, B., Lavallée, Y., Gilg, A., Letham-Brake, M., Mayer, K., Jolly, A. D., Reuschlé, T., Dingwell, D. B., 2015. Mechanical behaviour and failure modes in the Whakaari (White Island volcano) hydrothermal system, New Zealand. Journal of Volcanology and Geothermal Research 295, 26–42.

Heap, M. J., Kennedy, B. M., 2016. Exploring the scale-dependent permeability of fractured andesite. Earth and Planetary Science Letters 447, 139–150.

Heiken, G., Wohletz, K., Eichelberger, J., 1988. Fracture fillings and intrusive pyroclasts, Inyo Domes, California. Journal of Geophysical Research: Solid Earth 93(B5), 4335–4350.

Holness, M. B., 2018. Melt segregation from silicic crystal mushes: a critical appraisal of possible mechanisms and their microstructural record. Contributions to Mineralogy and Petrology 173, 48.

Huppert, H. E., Sparks, R. S. J., 1989. Chilled margins in igneous rocks. Earth and Planetary Science Letters, 397–405.

Hutton, D. H. W., 1988. Granite emplacement mechanisms and tectonic controls: inferences from deformation studies. Earth and Environmental Science Transactions of The Royal Society of Edinburgh 79(2–3), 245–255.

Jónasson, K., 1994. Rhyolite volcanism in the Krafla central volcano, north-east Iceland. Bulletin of Volcanology 56(6–7), 516–528.

Kavanagh, J. L., Menand, T., Sparks, R. S. J., 2006. An experimental investigation of sill formation and propagation in layered elastic media. Earth and Planetary Science Letters, 245(3), 799–813.

Kavanagh, J. L., Sparks, R. S. J., 2011. Insights of dyke emplacement mechanics from detailed 3D dyke thickness datasets. Journal of the Geological Society 168(4), 965–978.

Kavanagh, J. L., 2018. Mechanisms of Magma Transport in the Upper Crust—Dyking. In S. Burchardt (Ed.), Volcanic and Igneous Plumbing Systems, 55-88.

Kennedy, B. M., Wadsworth, F. B., Vasseur, J., Ian Schipper, C., Mark Jellinek, A., von Aulock, F. W., Hess, K., Russel, K., Lavallée, Y., Nichols, A., Dingwell, D. B., 2016. Surface tension driven processes densify and retain permeability in magma and lava. Earth and Planetary Science Letters 433, 116–124.

Krumbholz, M., Hieronymus, C. F., Burchardt, S., Troll, V. R., Tanner, D. C., Friese, N., 2014. Weibull-distributed dyke thickness reflects probabilistic character of host-rock strength. Nature Communications 5, 3272.

Lamur, A., Kendrick, J. E., Eggertsson, G. H., Wall, R., Ashworth, J. D., Lavallée, Y., 2017. The permeability of fractured rocks in pressurised volcanic and geothermal systems. Scientific Reports 7(1).

Le Corvec, N., Menand, T., Lindsay, J., 2013. Interaction of ascending magma with pre-existing crustal fractures in monogenetic basaltic volcanism: an experimental approach. Journal of Geophysical Research 118, 968–984.

Maccaferri, F., Bonafede, M., Rivalta, E., 2011. A quantitative study of the mechanisms governing dike propagation, dike arrest and sill formation. Journal of Volcanology and Geothermal Research 208(1), 39–50.

Magnall, N., James, M. R., Tuffen, H., Vye-Brown, C., Schipper, C. I., Castro, J. M., Davies, A. G., 2019. The origin and evolution of breakouts in a cooling-limited rhyolite lava flow. Geological Society of America Bulletin 131(1–2), 137–154.

Manda, A. K., Mabee, S. B., 2010. Comparison of three fracture sampling methods for layered rocks. International Journal of Rock Mechanics and Mining Sciences. 47(2), 218–226.

Manga, M., Castro, J., Cashman, K. V., Loewenberg, M., 1998. Rheology of bubble-bearing magmas. Journal of Volcanology and Geothermal Research 87(1–4), 15–28.

Mathieu, L., van Wyk de Vries, B., Holohan, E. P., Troll, V. R., 2008. Dykes, cups, saucers and sills: Analogue experiments on magma intrusion into brittle rocks. Earth and Planetary Science Letters 271, 1–13.

Mattsson, T., Burchardt, S., Almqvist, B. S. G., Ronchin, E., 2018. Syn-Emplacement Fracturing in the Sandfell Laccolith, Eastern Iceland—Implications for Rhyolite Intrusion Growth and Volcanic Hazards. Frontiers in Earth Science 6.

McGowan, E. M., 2016. Magma emplacement and deformation in rhyolitic dykes: insight into magmatic outgassing. Ph.D Thesis, Lancaster University, UK.

Miller, J., Rupert, G., 1997. Beyond ANOVA: basics of applied statistics. Chapman and Hall/CRC Texts in Statistical Science.

Mordensky, S. P., Villeneuve, M. C., Kennedy, B. M., Heap, M. J., Gravley, D. M., Farquharson, J. I., Reuschlé, T., 2018a. Physical and mechanical property relationships of a shallow intrusion and volcanic host rock, Pinnacle Ridge, Mt. Ruapehu, New Zealand. Journal of Volcanology and Geothermal Research 359, 1–20.

Mordensky, S. P., Villeneuve, M., Farquharson, J. I., Kennedy, B. M., Heap, M. J., Gravley, D. M., 2018b. Rock mass properties and edifice strength data from Pinnacle Ridge, Mt. Ruapehu, New Zealand. Journal of Volcanology and Geothermal Research 367.

Mordensky, S., Heap, M., Kennedy, B., Gilg, H.A., Villeneuve, M., Farquharson, J., Gravley, D., 2019. Influence of alteration on the mechanical behaviour and failure mode of andesite: Implications for shallow seismicity and volcano monitoring. Bulletin of Volcanology 81(8),, 44

Mordensky, S.P., Kennedy, B.M., Villeneuve, M.C., Lavallée, Y., Reichow M., Wallace, P.A., Siratovich, P.A., Gravley, D.M. Increasing the permeability of hydrothermally altered andesite by transitory heating, Geology, Geochemistry and Geophysics, in press.

Okumura, S., Nakamura, M., Tsuchiyama, A., 2006. Shear-induced bubble coalescence in rhyolitic melts with low vesicularity. Geophysical Research Letters 33(20).

Okumura, S., Nakamura, M., Takeuchi, S., Tsuchiyama, A., Nakano, T., Uesugi, K., 2009. Magma deformation may induce non-explosive volcanism via degassing through bubble networks. Earth and Planetary Science Letters 281(3), 267–274.

Papale, P., Neri, A., Macedonio, G., 1998. The role of magma composition and water content in explosive eruptions: 1. Conduit ascent dynamics. Journal of Volcanology and Geothermal Research 87(1), 75–93.

Parmentier, E. M., Schedl, A., 1981. Thermal Aureoles of Igneous Intrusions: Some Possible Indications of Hydrothermal Convective Cooling. The Journal of Geology 89(1), 1–22.

Paterson, S. R., Fowler, T. K., Miller, R. B., 1996. Pluton emplacement in arcs: a crustal-scale exchange process. Earth and Environmental Science Transactions of The Royal Society of Edinburgh 87(1–2), 115–123.

Pirajno, F., 2008. Hydrothermal Processes and Mineral Systems. Springer Science & Business Media.

Pollard, D. D., 1973. Derivation and evaluation of a mechanical model for sheet intrusions. Tectonophysics 19(3), 233–269.

Reid, F., 1983. Origin of the rhyolitic rocks of the taupo volcanic zone, New Zealand. Journal of Volcanology and Geothermal Research 15(4), 315–338.

Rust, A. C., Manga, M., Cashman, K. V., 2003. Determining flow type, shear rate and shear stress in magmas from bubble shapes and orientations. Journal of Volcanology and Geothermal Research 122(1–2), 111–132.

Saemundsson, K., Noll, H., 1974. K/Ar ages of rocks from Húsafell, Western Iceland, and the development of the Húsafell central volcano. Jökull 24, 40–59.

Saubin, E., Tuffen, H., Gurioli, L., Owen, J., Castro, J. M., Berlo, K., McGowan, E., Schipper, I., Wehbe, K., 2016. Conduit Dynamics in Transitional Rhyolitic Activity Recorded by Tuffisite Vein Textures from the 2008–2009 Chaitén Eruption. Frontiers in Earth Science 4.

Schmiedel, T., Galland, O., Breitkreuz, C., 2017. Dynamics of Sill and Laccolith Emplacement in the Brittle Crust: Role of Host Rock Strength and Deformation Mode. Journal of Geophysical Research: Solid Earth 122(11), 8860–8871.

Scott, S., Driesner, T., Weis, P., 2017. Boiling and condensation of saline geothermal fluids above magmatic intrusions. Geophysical Research Letters 44(4), 1696–1705.

Shea, T., Houghton, B. F., Gurioli, L., Cashman, K. V., Hammer, J. E., Hobden, B. J., 2010. Textural studies of vesicles in volcanic rocks: An integrated methodology. Journal of Volcanology and Geothermal Research 190(3–4), 271–289.

Sigurdsson, H., 1977. Generation of Icelandic rhyolites by melting of plagiogranites in the oceanic layer. Nature 269(5623), 25–28.

Siratovich, P. A., Sass, I., Homuth, S., Bjornsson, A., 2011. Thermal simulation of geothermal reservoirs and laboratory investigation of thermally induced fractures. Transactions - Geothermal Resources Council 35, 1529–1535.

Sparks, R. S. J., 1978. The dynamics of bubble formation and growth in magmas: A review and analysis. Journal of Volcanology and Geothermal Research 3(1–2), 1–37.

Spence, D. A., Turcotte, D. L., 1985. Magma-driven propagation of cracks. Journal of Geophysical Research: Solid Earth 90(B1), 575–580.

Stasiuk, M. V., Barclay, J., Carroll, M. R., Jaupart, C., Ratté, J. C., Sparks, R. S. J., Tait, S. R., 1996. Degassing during magma ascent in the Mule Creek vent (USA). Bulletin of Volcanology 58(2–3), 117–130.

Stephens, T. L., Walker, R. J., Healy, D., Bubeck, A., England, R. W., 2018. Mechanical models to estimate the paleostress state from igneous intrusions. Solid Earth 9(4), 847–858,

Thordarson, T., Larsen, G., 2007. Volcanism in Iceland in historical time: Volcano types, eruption styles and eruptive history. Journal of Geodynamics 43, 118–152.

Toramaru, A., 2014. On the second nucleation of bubbles in magmas under sudden decompression. Earth and Planetary Science Letters 404, 190–199.

Tsang, S, Lindsay, J., Coco, G., Wysocki, R., Lerner, G., Rader, E., Turner, G., Kennedy B. The heating of substrates beneath basaltic lava flows, Bulletin of Volcanology, in press.

Tuffen, H., Castro, J. M., 2009. The emplacement of an obsidian dyke through thin ice: Hrafntinnuhryggur, Krafla Iceland. Journal of Volcanology and Geothermal Research 185(4), 352–366.

Tuffen, H., Dingwell, D. B., 2005. Fault textures in volcanic conduits: evidence for seismic trigger mechanisms during silicic eruptions. Bulletin of Volcanology 67(4), 18.

von Aulock, F. W., Nichols, A. R. L., Kennedy, B. M., Oze, C, 2013. Timescales of texture development in a cooling lava dome. Geochimica et Cosmochimica Acta 114, 72–80.

von Aulock, F. W., Kennedy, B. M., Maksimenko, A., Wadsworth, F. B., Lavallée, Y., 2017. Outgassing from Open and Closed Magma Foams. Frontiers in Earth Science 5.

Wadsworth, F. B., Witcher, T., Vasseur, J., Dingwell, D. B., Scheu, B., 2019. When Does Magma Break? In Gottsmann, J., Neuberg, J., Scheu, B., (Eds.), Volcanic Unrest: From Science to Society, 171–184.

Walker, G. P. L., 1974. Eruptive Mechanisms in Iceland. In Kristjansson, L., (Ed.), Geodynamics of Iceland and the North Atlantic Area, 189–201.

Weber, G., Castro, J. M., 2017. Phase petrology reveals shallow magma storage prior to large explosive silicic eruptions at Hekla volcano, Iceland. Earth and Planetary Science Letters 466, 168–180.

Westrich, H. R., Stockman, H. W., Eichelberger, J. C., 1988. Degassing of rhyolitic magma during ascent and emplacement. Journal of Geophysical Research: Solid Earth 93(B6), 6503–6511.

Wong, T., Baud, P., 2012. The brittle-ductile transition in porous rock: A review. Journal of Structural Geology 44, 25–53.

Zaiontz, C., 2018. Real Statistics Using Excel. www.real-statistics.com accessed May 2019.

Zierenberg, R. A., Schiffman, P., Barfod, G. H., Lesher, C. E., Marks, N. E., Lowenstern, J., Mortensen, A., Pope, E. C., Bird, D. K., Reed, M. H., Friðleifsson, G., Elders, W. A., 2012. Composition and origin of rhyolite melt intersected by drilling in the Krafla geothermal field, Iceland. Contributions to Mineralogy and Petrology 165(2), 327–347.

Chapter 3 - Rapid heat transfer at the margins of thin rhyolite intrusions

E. Saubin[1], B. Kennedy[1], H. Wang[1], H. Tuffen[2], M. Villeneuve[1], S. Burchardt[3], J. Davidson[1], and G. Rule[1]

[1] *Department of Geological Sciences, University of Canterbury, Christchurch, NZ*

[2] *Lancaster Environment Centre, Lancaster University, Lancaster, UK*

[3] *Department of Earth Science, Uppsala University, Uppsala, Sweden*

3.1 Abstract

Heat transfer at intrusion margins is central to hydrothermal systems development and subsequent geothermal resource extraction. Current understanding is largely constrained by numerical models, but rarely ground-truthed against field data. Here, we provide field data at 14 fossil shallow rhyolite intrusion sites from fieldwork and literature, to constrain thermal transfer at the magma/host rock interface. We focus on the intrusive dimensions, the thickness of chilled margins and extent of the damaged/thermal aureole (including fracture density and area). Our observations highlight similar thicknesses of chilled margins and aureoles. We compare our data to a diffusion-based heat transfer model. The variability of our data and sensitivity of our model demonstrates that glass formation in chilled margins is highly sensitive to local variations of cooling rate. Theoretical glassy chilled margins reach a maximum thickness of approximatively 7 m, even for very thick intrusions, imposed by a cooling rate limit on glass formation. Our data regarding the thicknesses of thermal aureoles of small intrusion are underestimated by conduction models and hence require additional heat transfer mechanisms. We strongly suggest that high fracture density measured at the intrusion margins can be an explanation for this, facilitating additional heat advection and convection to produce a wider thermal aureole than proposed by conduction models. The model fits the data better when associated with larger intrusions where advection and convection in thermal aureole could be relatively minor compared to the longer lasting diffusion heat transfer and higher release of latent heat. Our data therefore imply that for a given volume of intruded magma, a network of

thin intrusions could have a bigger crustal footprint and short-term impact on the hydrothermal system compared to the smaller but longer lasting footprint of one large intrusion.

3.2 Introduction

The structure of magma chamber margins controls heat and fluid transfer into the sub-volcanic crust, thereby modulating hydrothermal systems. The intrusive volume and style have a direct impact on the thermal budget and the host rock deformation, which in turn control the extent of hydrothermal alteration and mechanical damage, respectively (Bostick and Pawlewicz, 1984; Faulkner et al., 2011). Despite a plethora of laboratory and numerical studies (e.g. Rubin, 1993; Annen et al., 2006; Kavanagh and Sparks, 2011; Krumbholz et al., 2014; Annen, 2017; Heap et al., 2017; Sydnes et al., 2018), there is very little field data that provide the necessary physical description of this interface of frozen magma (chilled margin) in contact with altered and damaged host rock (e.g. Henneberger and Browne, 1988; Huppert and Sparks, 1989).

Temperature contrasts at the margins of magma bodies can trigger quenching to form glass, and even fragmentation of the emplacing magma (Jaeger, 1959). Friction and viscous heating of material at the interface can potentially be an additional source of heat (Schauroth et al., 2016; Lavallée et al., 2018), modifying the heat transfer. Less dynamic environments allow magma chilling, either as fine-grained crystalline margins commonly associated with mafic intrusions (e.g. Holness et al., 2007, and references therein) or as glass when the glass transition temperature, T_g, is crossed at the appropriate cooling rate for a given melt viscosity (Gottsmann et al., 2002). In this paper focussed on rhyolite intrusions, we define the chilled margins by the presence of volcanic glass with few primary microlites or secondary spherulites. Steps of crystal nucleation and growth occur at given undercooling degrees, also releasing fractional latent heat. Undercooling the melt means bringing it to a lower temperature that its solidus. Low undercooling favours microlite formation, whereas high undercooling favours glass formation, which may be followed by spherulite growth at intermediate undercooling (Brandeis et al., 1984; Castro et al., 2008; Befus et al., 2016). Stable glass formation thus requires a quenching rate higher than the crystallisation rates (spherulite growth rate at Krafla is 10^{-10}-10^{-9} m/s; Castro et al., 2008), and higher than the rate of heat supply to avoid re-melting (Huppert and Sparks, 1989). Chilling is therefore more likely to occur with rapid external heat flux and/or a low internal heat flux, e.g. low magma supply, low heat production from latent heat of

crystallisation, or slow internal magma heat transfer mechanisms, such as diffusion dominating over convection (Huppert and Sparks, 1989). The water content also impacts the cooling rate. The high viscosity of rhyolite magma correlates with low diffusivity and thus low magma heat flux via the mechanisms mentioned above, hence chilled margin development is stronger in rhyolite versus basalt (e.g. Otterloo et al., 2015).

The evolving thermal properties of the magma margins will control heat transfer out of the melt. At the interface, diffusivity rapidly increases during magma cooling when crossing the glass transition, but the heat capacity decreases faster, which result in a lower conductivity of quenched margins compared to the melt (Romine et al., 2012). Therefore, the glassy margins could act as insulating layers between magma and host rocks (Claour-Long and Nesbitt, 1985). Glass has brittle behaviour over a large range of strain rates, including that driven by thermal gradients during rapid quenching, which can cause fracture development (Hasselman and Singh, 1986). Additionally, tensile cracking associated with hydration of chilled margins can form a network of joints and perlitic fractures (von Aulock et al. 2013, Otterloo et al., 2015). Glassy margins may consequently be highly fractured, modifying their thermal properties and potentially restricting their insulation effect.

Initial host rock properties are important to the type and extent of hydrothermal alteration and mechanical damage, through the processes of tensile and shear failure, ductile compaction and pore collapse, chemical dissolution or precipitation (Pirajino, 2008; Mathieu et al., 2008, Mordensky et al., 2018; Mordensky et al., 2019a; Saubin et al., 2019). These micro and macro structures eventually control fluid pathways (Heap et al., 2019). Complex heat and fluid exchanges occur at the fractured and permeable interface, with fluid advection and convection in chilled margins, in tuffisite veins and in host rocks, which can accelerate marginal freezing of the intrusion (Tuffen et al., 2002; Tuffen et al., 2003; Goto et al., 2008; Eldursi et al., 2009; Faulkner et al., 2011) and vaporisation of pore water in host rock (Jaeger, 1959). As a result, this interface can be a complex reservoir of supercritical fluids, which are key targets for current geothermal explorations (e.g. Elders et al., 2019).

Thermal models are not well constrained by field data, however, 1D cooling models comparing magmas of similar temperature indicate that magma thickness is the primary control on the maximum temperature and width of thermal aureole (Bostick and Pawlewicz, 1984), with longer cooling time for wide intrusions (Carslaw and Jaeger, 1959; Heap et al., 2017). In contrast, time-varying 2D models of incremental magma emplacement highlight the importance of geometry and diffusivity contrasts between the melt and host rock (Annen et al., 2006;

Barker, 2007; Annen, 2017). The duration of magma emplacement was recently demonstrated as of minor importance for the alteration extent, compared to the intrusion size (Sydnes et al., 2018). For simplification, most of these models have relied on heat transfer by diffusion, despite large magma bodies being prone to magma convection (Turner and Campbell, 1986). Such convection can increase the thickness of thermal aureole by conserving a maximal temperature at the interface (Annen, 2017).

Field studies can provide in-situ information of host rocks and intrusion margins, variations of which are often recorded at an intra-intrusion scale (e.g. Delaney et al., 1986; Kavanagh and Sparks, 2011). Here, we provide a large-scale inter-intrusion comparison of dimensions and fractures in and around fossil silicic magma intrusions, focussing on 14 rhyolite intrusions worldwide (11 from our field work, 3 from literature) and covering a wide range of intrusion types: conduits, sills and dykes, cone-sheets and magma chambers (Burchardt et al., 2018). We provide the extent of the chilled margin and the damage/alteration aureole in the host rocks (called 'thermal aureole' throughout). We complement the field study with a numerical model of heat transfer by diffusion to explore the implication of our results, considering diffusivity contrast at the interface, and discussing effects of latent heat of crystallisation, advection, magma convection and incremental emplacement, through comparison with field data.

3.3 Methods

3.3.1 Fieldwork

Eleven rhyolite intrusions (paleo-depth <1 km) were selected for field work in Iceland, within a range of country rock types (Saubin et al., 2019). We restrict our sites to shallow rhyolite intrusions to minimise the number of variables when making comparisons between intrusion sizes. However, we expect the silica content in our rhyolite range to vary up to 5 wt % (~75 wt % at Hrafntinnuhryggur, Tuffen and Castro, 2009; ~72 wt % at Húsafell, McGowan, 2016) and the water content by up to 1 wt % (0.3-0.4 wt. % at Hrafntinnuhryggur, Tuffen and Castro, 2009; up to 1.5 wt. % expected for deeper intrusions using volatileCalc by Newman and Lowenstern, 2002). This directly impacts viscosity (<1 order of magnitude according to the silicate melt viscosity calculator, Giordano et al., 2008) and, in turn, diffusivity, crystallisation rate and thus latent heat. We combine this field-study with three suitably documented rhyolite intrusions from literature (Thumall intrusion, Tuffen and Dingwell, 2005; Ramsey Island

intrusion, Kokelaar et al., 1985; Mule creek vent, Stasiuk et al., 1996). Characteristics of the intrusive bodies are summarized in Table 3.1 and the end-members in terms of dimensions are presented in Figure 3.1.

Scanlines were used to assess fracture characteristics following Manda and Mabee (2010). All types of discontinuity were measured (joints, bedding, faults, veins), the aperture and persistence (length) of fractures were recorded along the 1D transects through altered host rock and intrusion cores, and fracture density was measured at regular intervals, counting the number of discontinuities over a 50 cm-long line perpendicularly to the transects. This value was averaged for each transect and lithology, and the area of each fracture was calculated by multiplying its aperture by its persistence (length). When the site was not accessible, fractures and dimensions were recorded using 3D structure from motion photogrammetric techniques from images collected with an unmanned aerial vehicle (UAV; e.g. Gomez and Kennedy, 2018).

We describe the interface between the intrusion and host rock in terms of the thickness of the chilled intrusion margin, $H_{CM,}$ and the damaged and altered host rock aureole, H_A (Fig.3.1A). The intrusion thickness is referred to as H_I. In this field study, the aureole is characterised by macro-scale observations of mechanical damage and thermally-driven chemical alteration, therefore the resultant aureole has a higher fracture density and may be discoloured compared to the intact host rock (Saubin et al., 2019; Fig.3.1A). Dimensions we provide are average representative values of our outcrops, with uncertainties estimated at ± 10%.

TABLE 3.1. RHYOLITE INTRUSIONS

Site	Intrusion name	Lat (°N) Lon (°W)	Type	Paleo depth (m)	Country-rock type	H_I (m)	H_A (m)	H_{CM} (m)	Reference
Njardvik, Iceland	Landsendi[3]	65°33'55. 13°48'58.	Sill	500	Basalt lava	3	1.5	0.1	Saubin et al., 2019
	Snotrunes[3]	65°33'17. 13°49'43.	Z-shaped intrusion	400	Basalt lava	50	2	1.6	Current study
	Skjaldardalur[3]	65°35'13. 13°52'15.	Sill	300	Basalt lava	300		0.7	Current study
	Tdarfjall[3]	65°35'31. 13°52'46.	Sill (cone sheet)	150	Basalt lava	7	1.5	0.5	Current study
	Grjotfjall[2]	65°34'40. 13°56'20.	Dyke	200	Basalt lava	4		0.65	Current study
	Geldingafjall[2]	65°33'19. 13°59'35.	Dyke	150	Basalt lava	30		1	Current study
Krafla, Iceland	Hrafntinnuhryggur[1]	65°41'15. 16°43'40.	Conduit	10	Basalt and Hyaloclastite	7.5	1	3.75	Saubin et al., 2019
Húsafell, Iceland	Deildargil West[3]	64°41'22. 20°57'20.	Sill	500	Welded ignimbrite	2	1	0.55	Saubin et al., 2019
	Deildargil East[1]	64°41'25. 20°57'16.	Sill	500	Conglomerate	2	0.7	0.4	Saubin et al., 2019
	Hraunfossar[2]	64°42'07. 20°58'27.	Sill and dyke	500	Basalt lava	4	0.7	0.5	Current study
East Iceland	Slaufrudalur[3]	64°20'. 15°01'.	Magma chamber	1000	Basalt lava	900	10	7	Current study, Burchardt et al., 2012
South Iceland	Thumall, Rauðufossafjöll[2]	63°58'70. 19°24'50.	Conduit	10-50	Rhyolite lava	10		5	Tuffen and Dingwell, 2005
SW Wales, UK	Ramsey Island[2]		Dyke	submarine	Sandstone and conglomerate	190	4.5		Kokelaar et al., 1985
New Mexico, US	Mule Creek vent[2]	33°11'05. 108°56'17.	Conduit	50-350	Andesite lava	75		2	Stasiuk et al., 1996

Note: The names of these shallow rhyolite intrusions of thickness H_I are informal designations based on official names of their geographic sites.

Thickness of chilled margins H_{CM} and aureole (damage and alteration) in host rock H_A were recorded:

[1]At the intrusion floor

[2] On their vertical side

[3] At their roof

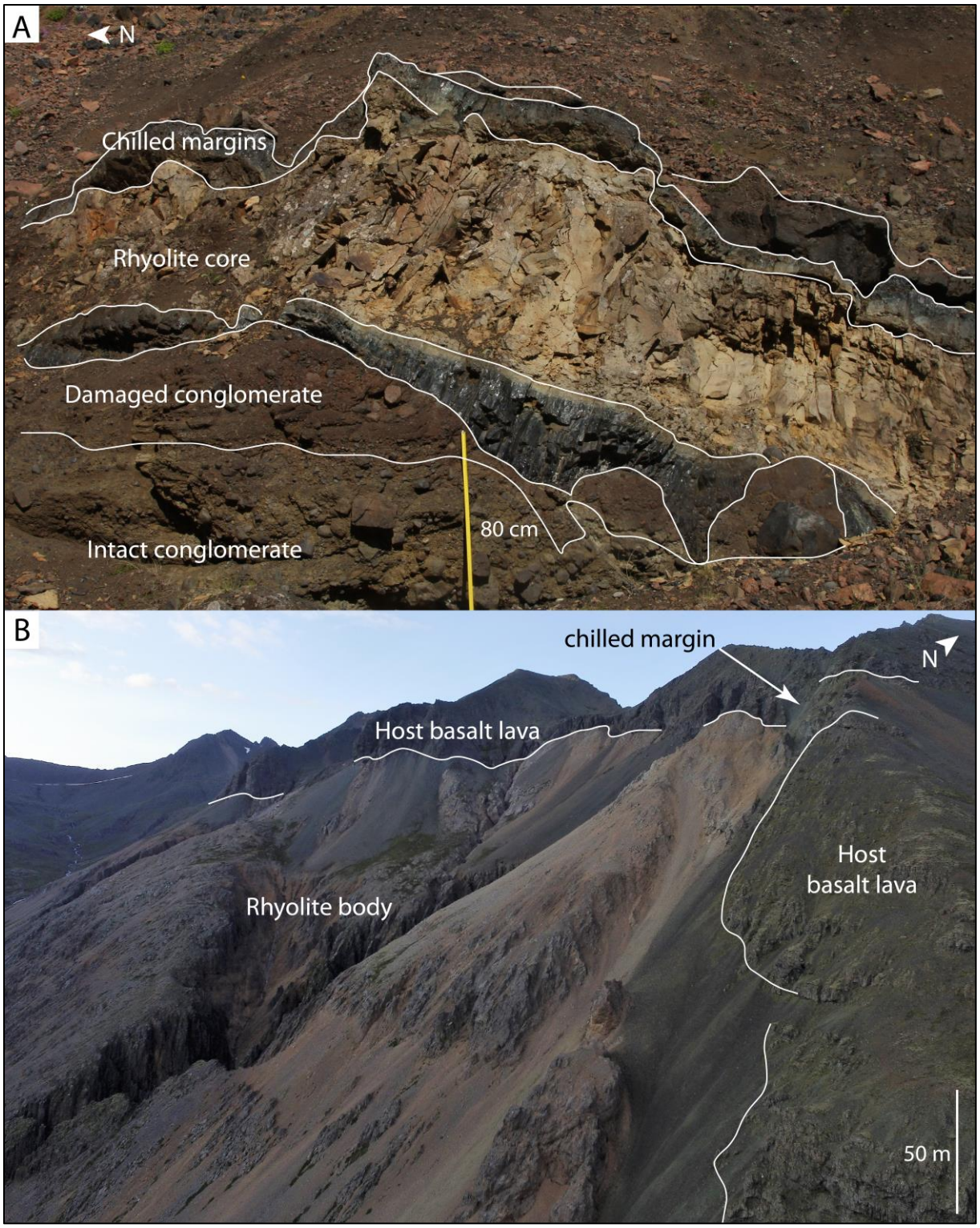

Figure 3.1. End-members of the intrusive dimensions used in this work. A) Narrow 2 m thick rhyolitic sill at Húsafell, Deildargil East. Progressive colour gradient in conglomerate from grey to red towards the intrusion. B) Large 900 m thick fossil rhyolite magma chamber at Slaufrudalur. The irregular glassy margin is ~7 m thick on its northern extremity.

3.3.2 Numerical modelling

We tested our field observations by comparing them to models of 1) the thermal aureole and 2) the chilled margins. Modelling calculations were written in MATLAB. We follow the numerical approach of Annen (2017) to develop a 1D theoretically-constrained empirical model based on heat transfer and energy conservation. The thickness variations of the thermal aureole and chilled margins are calculated as function of the intrusion size. Temperature T in the host rock for instantaneously emplaced intrusions (i.e. one-time temperature injection) of thickness H_I is a function of time t and distance x from the centre of the intrusion. The analytical solution for the temperature at any distance x and time t, $T(x,t)$, affected by diffusion is given by Furlong et al. (1991):

$$T(x,t) = T_0 + \frac{\Delta T}{2}\left(erf\left(\frac{H_I/2 - x}{\sqrt{4Kt}}\right) + erf\left(\frac{H_I/2 + x}{\sqrt{4Kt}}\right)\right) \quad (1)$$

Where T_0 is the initial temperature of country rock, ΔT is the temperature difference between T_0 and magma temperature T_m, and K is thermal diffusivity. Latent heat is neglected for simplification. The Eq. (1) is the controlling equation of the models for thickness calculation of both thermal aureole and chilled margins.

3.3.2.1 Thermal aureole

Whereas the aureole in host rocks in the field corresponds to both mechanical damage and thermal alteration, this numerical model considers only the thermal aureole that exceeded our set maximum temperature (T_{max}). In our thermal aureole model, we define a pre-selected temperature T_{max} corresponding to the threshold beyond which the host rock is considered altered and damaged by the intrusion during both heating up and cooling down. It is reached at any time $t>0$, at any location $x>H_I/2$ (i.e. within the host rock), and is used to identify the thickness of the thermal aureole.

T_{max} = 400°C was selected to represent appropriate undercooling to drive damage of host rocks through cooling contraction (Browning et al., 2016; Eggertsson et al., 2019) and maximal cracking because of phase and volume changes during heat up (Mordensky et al, 2019b). T_{max} is likely to be variable between host rocks and strongly rate dependant (Browning et al., 2016), hence we show model results for the range of T_{max} 350-450°C containing our field data. According to Eq. (1) the distance $x>H_I/2$ to T_{max} is the outer boundary of the thermal aureole, whose thickness, H_A, can be written as the maximum x reaching T_{max} in the host rock:

$$H_A = \max_{T(x>HI/2,t)=T_{max},t>0} x \quad (2)$$

3.3.2.2 Chilled margin

We consider the cooling rate *CR* in the intrusion as the determinant of glassy versus crystalline texture. It is described as the reduction in temperature over a certain time, t:

$$CR(x,t) = \frac{T(x,0) - T(x,t)}{t} \quad (3)$$

At t=0 and $x \leq H_I/2$, Eq. (1) simplifies to $T(x,0) = T_0 + \Delta T$. Therefore, substituting $T(x,0)$ and Eq. (1) into Eq. (3), *CR* at any distance $x \leq H_I/2$, from time 0 to *t* is as follows:

$$CR(x,t) = \frac{\Delta T\left(2 - erf\left(\frac{H_I/2 - x}{\sqrt{4Kt}}\right) - erf\left(\frac{H_I/2 + x}{\sqrt{4Kt}}\right)\right)}{2t} \quad (4)$$

Calorimetry results on Hrafntinnuhryggur obsidian suggest that the glass transition temperature, T_g, is ~690°C for a default viscosity of 10^{12} Pa·s (Castro et al., 2008). The deeper and more water-rich IDDP-1 intrusion (2100 m) at Krafla has a Tg = 500-525 °C (Hess et al., 2015). The values for the < 1 km paleodepth field intrusions in this study could thus correspond to the 600-700 °C range. We chose to run the numerical model for 700°C, as an end-member maximum T_g, for the driest of our intrusions. We complete this boundary condition with the minimum CR_{min} in chilled margins, corresponding to the temperature drop from the magma temperature, T_m, to the glass transition temperature, T_g, divided by the maximum time, t_{max}, needed for this transition. If a point *x* has a lower temperature than T_g at t_{max} then this point cooled at a faster rate than CR_{min}, and can be expected to form a chilled margin. The range of $x \leq H_I/2$ corresponding to the chilled margin is therefore given by:

$$\frac{\Delta T\left(2 - erf\left(\frac{H_I/2 - x}{\sqrt{4Kt_{max}}}\right) + erf\left(\frac{H_I/2 + x}{\sqrt{4Kt_{max}}}\right)\right)}{2t_{max}} \geq CR_{min} = \frac{(Tm - T_g)}{t_{max}} \quad (5)$$

We run the model for a range of CR_{min} determined by the slowest cooling rate in rhyolite from literature and the fastest cooling rate fitting the field data; We increment for a range of intrusion thicknesses H_I to solve Eq. (5) numerically. Using a root finding algorithm ('vpasolve' Matlab function), the solution provides the thicknesses, $x = H_{CM}$, of the chilled margin for the range of H_I. The input parameters used in the models are summarised in Table 3.2.

TABLE 3.2. PARAMETERS USED IN CALCULATION

Name	Symbol	Value	Unit	Reference
Thermal diffusivity	K	$1.5\ 10^{-6}$	$m^2\ s^{-1}$	Annen, 2017
Magma emplacement temperature	T_m	900	°C	Jonasson, 1994 (Krafla)
Initial environment temperature	T_0	15	°C	Eppelbaum et al., 2014
Threshold temperature for host rock alteration	T_{max}	400	°C	Browning et al., 2016
Glass transition temperature	T_g	700	°C	Castro et al., 2008

3.4 Results

The Figure 3.2 presents field data and numerical model results for the thickness of the thermal aureole and chilled margin (Fig.3.2A), both illustrated by evolution of diffusive heat transfer through time (Fig.3.2B). Field dimensions reveal a relationship between the intrusion size and the aureole thickness (H_A), which increases following a linear relation with a positive intercept, according to the numerical resolution with the best correlation coefficient (Fig.3.2A trendline):

$$H_A = a\,H_I + b\ , \quad b > 0 \tag{6}$$

Where *a* and *b* are fitting parameters. However, the numerical results show that the thicker the intrusion, the proportionally thicker the thermal aureole. A straight line in a log-log plot is a relationship of the form $y = a \cdot x^b$, in this case simplifying with b = 1 in:

$$H_A = a_{(T_{max},L)}\,H_I \tag{7}$$

The parameter *a* represents heat transfer by diffusion, depending on the selected *Tmax* according to Eq. (2) and on *L* (neglected in the model). It has similar value in both equations (6) and (7), a ~0.01, although highly variable in the numerical model depending on initial parameters. The positive intercept (parameter *b*) in Eq. (6) is a difference between the trendline of the field data and the numerical prediction. We however propose that this trend is not valid for very small intrusions (<0.5 m thick). The zone of numerical solution in orange in Figure 3.2A is determined by the field data, and corresponds to *Tmax* from ~350 °C to 450 °C when latent heat is ignored. The linear trendline of the field data approaches the slope of the numerical prediction when the intrusion is large (>100 m thick), with the small difference of the parameter

b negligible for wide dimensions. The model of heat diffusion through time on Figure 3.2A also illustrates the increasing thickness of thermal aureole for increasing intrusion size.

The field data for the thickness of the chilled margin is similar to those of the aureole, although data are more scattered (Fig.3.2B). There is no systematic influence on the dimensions of H_A and H_{CM} with either the lithology of host rocks, the intrusion type, or the emplacement depth (Table 3.1). Numerical predictions show intrusions can be entirely chilled (chilled margin thickness is approximately half the intrusion size) when they are very thin, until they reach a threshold depending on the chosen cooling rate. Beyond this threshold, the chilled margin thickness rapidly decreases over a narrow range of intrusion size then remains constant with increasing intrusion size. For a constant and maximum T_g, the zone for model prediction in blue in Figure 3.2B corresponds to a maximum cooling rate of ~5 10^{-2} °C s^{-1} determined by the field data, and the end-member of a minimum cooling rate of ~10^{-5} °C s^{-1}as measured for obsidian in literature (Gottsmann and Dingwell, 2002) and maximum *Tg* as chosen for the driest intrusion. Chilled margins are thinner when *Tg* is lower. The intermediate CR_{min} represented in dashed line in Figure 3.2B corresponds to the best fit with field data among the resolved iterations. The model of heat diffusion through time on Figure 3.2B also illustrates the temperature variations for decreasing intrusion size. Analytical solution of the Eq.(1) highlights that the temperature difference at a same x for various intrusion sizes when time is < a few days is negligible, in regards to that occurring at larger time-scale. In this zone, temperature mostly depends on distance to the interface rather than to the intrusion size (stable zone in Fig.3.2B).

Our field data and numerical models suggest that conductive heat diffusion can explain a portion of the chilled margin and baked margin dimensions. However, we suspect the fractures at the magma/host rock interface are likely to be a critical component that modify the heat transfer. In order to provide further insight into the role of distribution and type of fractures encountered in this environment, we additionally examine fracture characteristics. Figure 3.3 illustrates contrasts in fracture area and density between the intrusion core and margin. Within the rhyolite core, fractures have a narrow range of density (10-13 fractures per metre) and a large magnitude and wide range of areas (10-80 cm² per fracture), and conversely in chilled margins the density is greater with a wider range (15-30 fractures per metre) but the magnitude and range of areas are small (1-4 cm² per fracture). The fracture density increases towards the margins from ~10 to up to 30 discontinuities per metre on average, while the fracture area decreases from 80 cm² to < 10 cm². These values are also compared with data from Saubin et al. (2019), collected on host rocks in Iceland (both intact and damaged/altered by the intrusion)

with the same methodology at the same field sites (Landsendi, Hrafntinnuhryggur and Deildargil). Fracture properties of chilled margins are similar to that of strong host rocks (basalt and welded ignimbrite; Saubin et al., 2019).

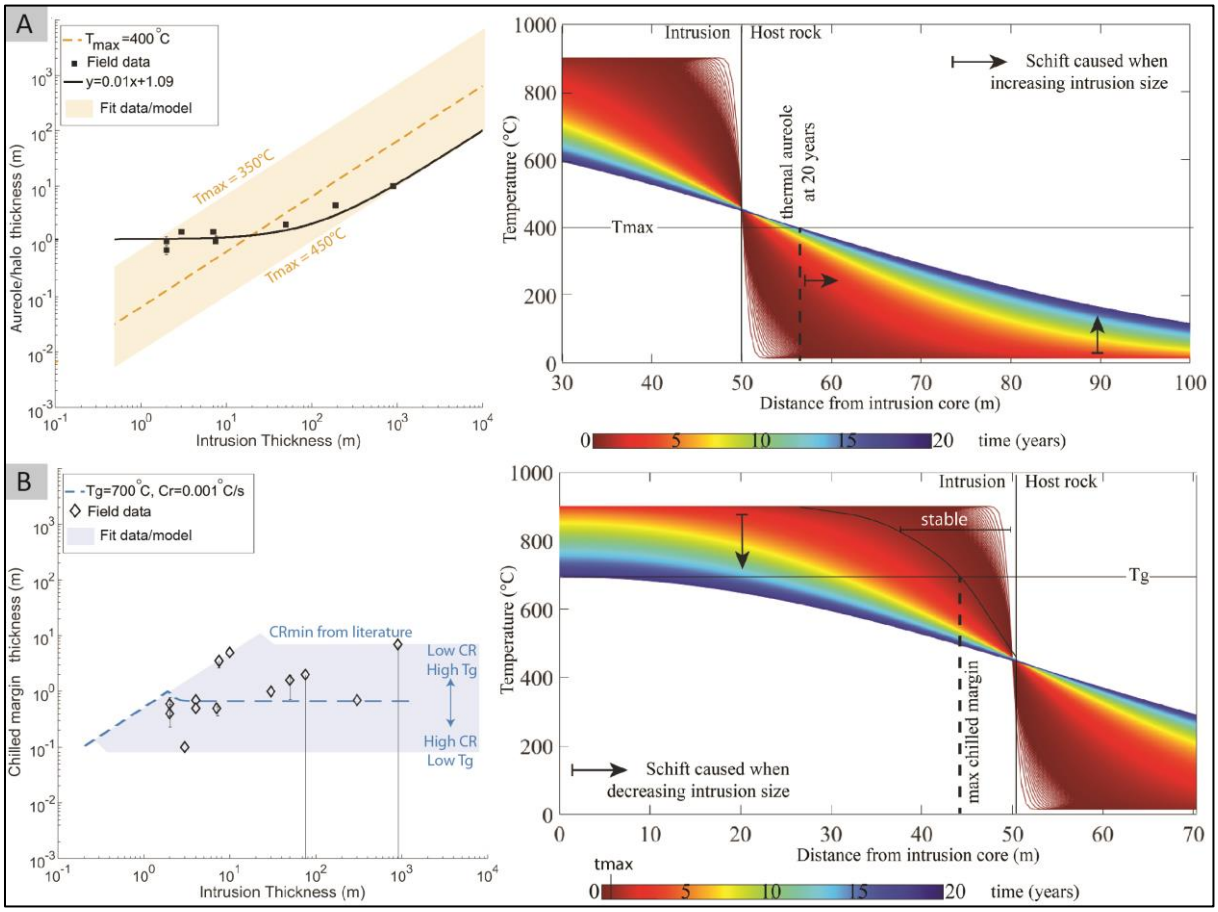

Figure 3.2. Dimension of intrusions, their aureole in host rocks and their chilled margin, from field data and model of heat transfer by diffusion around an instantaneously emplaced intrusion. A) Log-Log plot of aureole and thermal aureole thickness versus intrusion size. Field data (dark squares) with fitted trend line are compared to numerical prediction (orange). Error bars are added when available, although very small. The model is not valid for small intrusions. Involved processes are illustrated on the left, with a model of heat transfer by diffusion in the host rock of a 100 m thick intrusion. B) Log-Log plot of chilled margin thickness H_{CM} versus intrusion size. Scattered field data (diamonds) are compared to numerical prediction (blue), with t_{max}= 2 days solved for the maximum glass transition temperature T_g = 700 °C and the intermediate cooling rate CR_{min} = 0.001 °C s^{-1} using Eq. (3). This iteration of CR_{min} is represented because going through the field data. Note that the two error bars going down out of the blue zone are reaching zero. Involved processes are illustrated on the left, with a model of heat transfer by diffusion in a100 m thick intrusion.

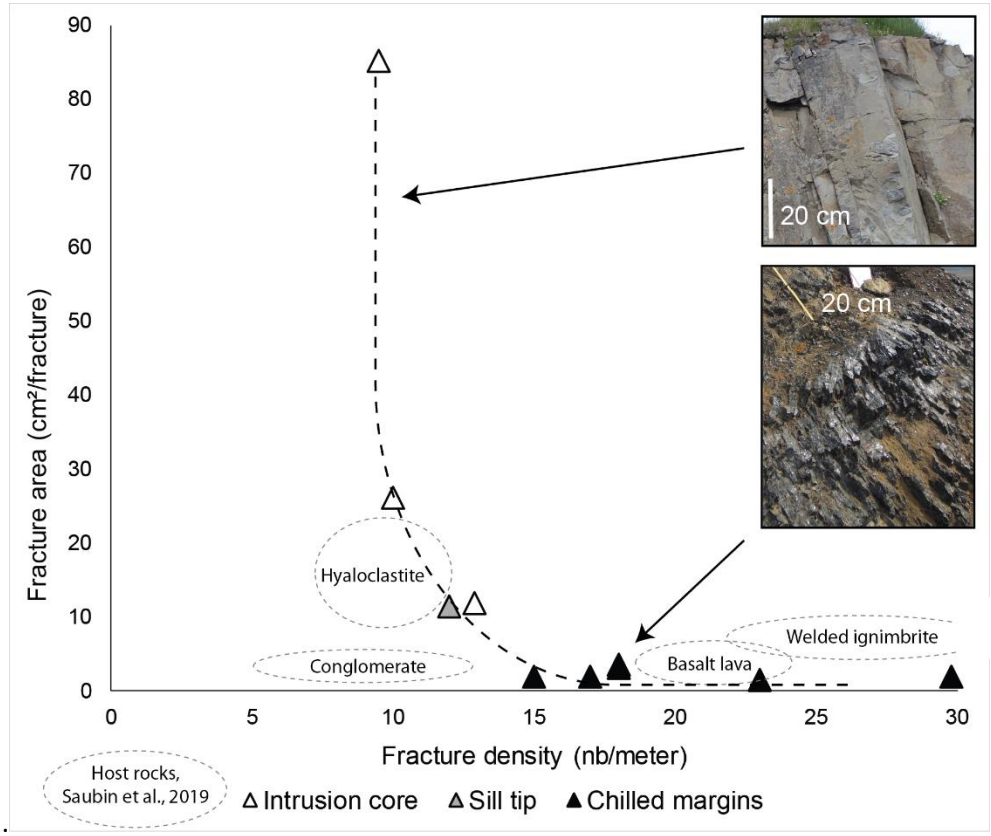

Figure 3.3. Fracture distribution in rhyolite intrusions overlaid with host rocks from Saubin et al. (2019). Data points come from intrusions at Landsendi, Hrafntinnuhryggur, Deildargil East and West (Tables 3.1; S3.1), with values being the average per transect across the intrusion. The fracture area is a function of aperture and persistence: a high area corresponds to wide and/or long fractures, whereas narrow and/or short fractures have a low area. Top picture: rhyolite core at Landsendi. Bottom picture: obsidian dyke at Hrafntinnuhryggur.

3.5 Discussion

In this section we focus on discussing deviation from the conductive heat diffusion trends rather than fully exploring parameter space associated with the initial conditions. In the case of magma emplaced in a single event, increasing the size of the intrusion results in increased thermal mass and higher maximum temperatures reached in the host rocks surrounding the intrusion, and therefore thicker aureoles. Higher thermal masses are also associated with lower cooling rates, limiting the thickness of chilled margins to a maximum value.

3.5.1 Limitations and implications of assumptions

The differences between the numerical solution and the field data (trendlines in Fig.3.2A and the wide range of data versus the trendline in Fig.3.2C) can be explained by many assumptions in our models, and many free variables in our data, which are discussed below.

Composite intrusions are common in Iceland, where propagation of viscous magma is facilitated by lubrication at the walls with a less viscous melt (e.g. Carrigan and Eichelberger, 1990). The presence of such a melt at the margins could delay glass formation (Carrigan et al., 1992), potentially resulting in thinner chilled margins, and the slower cooling rate could impact thermal transfer towards the host rock, with potentially thicker thermal aureoles.

To limit free parameters, our model assumed a single-stage magma emplacement. We note that the assumptions of instantaneous emplacement and dominance of heat transfer by diffusion are significant limitations. Colour layering in the glassy chilled margins gives textural support for possible incremental filling processes at Landsendi, Snotrunes, Grotfjall and Húsafell (Table 3.1, Fig.S3.1A; Huppert and Sparks, 1985; Annen, 2011), which is also supported at Deildargil West by multiple sill tips (Saubin et al., 2019) and at Skjaldardalur by flowing vesicular patterns (Fig.S3.1B). This evidence represents dynamic intrusions (incremental filling, magma flow, erupting magma or magma shearing; Mattsson et al., 2018) rather than instantaneous emplacement with static cooling. It has also been demonstrated that convection of rhyolite melt can sometimes occur in ≤1 km wide magma bodies, despite high magma viscosity (e.g. Huppert and Sparks, 1984). Such magma dynamics can buffer the temperature at the interface at magma temperature, increasing the heat transferred to host rocks and producing a wider thermal aureole. We similarly note that if latent heat was considered in the model, the heat source from the magma would be significantly greater and the thermal aureole significantly wider (Annen, 2017).

The background temperature of host rocks, T_o, is another variable that affects the diffusive gradient and the size of thermal aureoles. The numerical model in this study sets T_0=15 °C, according to the Earth geothermal gradient at shallow depth (Eppelbaum et al., 2014). However, the temperature would be higher in volcanic areas, where drilling often encounters 100-300 °C environments (e.g. Krafla and Reykjanes geothermal fields in Iceland, Taupo Volcanic Zone in New Zealand). Higher background temperature would cause a shift towards a higher middle point temperature (equilibrium temperature) at the interface magma/host rock, and limited cracking because of a lower undercooling degree, hence requiring higher T_{max} for thermal aureole similar to that at low background temperature. Same variations are expected for lower initial magma temperature, *Tm*, and for deeper magma emplacement, where the host rocks have higher T_0.

Within the intrusion, the glass transition temperature, *Tg*, varies depending on the melt viscosity and cooling rate (Gottsmann et al., 2002). It is fixed in this model, with iterated cooling rates,

delimiting the upper boundary condition for a max *Tg* at a minimal cooling rate from literature. Adapting *Tg* to each iterated cooling rates should result in thinner chilled margins, although this was not explored here. The diffusivity in the model is chosen from Annen (2017) and is concordant with our initial conditions, heat capacity and material density assumed in this environment. It is however a constant in the model, rather than varying with rock type, viscosity and temperature as it should (e.g. Kafoussias and Williams, 1995). An increase in host rock temperature would increase diffusivity, and conversely in magma where cooling would progressively lower diffusivity. As a result, thermal aureole could be slightly wider and chilled margins slightly thinner. But the most important change would be the input of a strong diffusivity contrast between magma and host rock, which would affect the temperature profiles, hence affecting the thickness of thermal aureole. In the absence of such contrast, the maximum temperature reached at a given point does not depend on diffusivity (e.g. Annen, 2017).

Our model assumes undercooling is the dominant aureole damage mechanism that would cause development of cooling joints and fractures expansion (Browning et al., 2016; Eggertsson, 2019). This process is rate dependent, which we do not consider (e.g. Gottsmann et al., 2002; Lavallée et al., 2020). Additionally, another major limitation in the model of heat transfer by diffusion is the negligence of hydrothermal fluid flow. The model here is not valid for wet environments, where advective hydrothermal fluid exchanges occur between magma and host rocks, promoting more efficient heat transfer. It is thus most likely that wider thermal aureoles would be encountered in wet environments, although the heat source would be exhausted quicker due to faster magma cooling. Fluid advection would also promote cracking through phase and volume changes during heat up (e.g. Mordensky et al., 2019b). However, we note that the dyke at Ramsey Island (Table 3.1), emplaced in a submarine environment, plots on the linear relationship on Fig.3.2A. In this case, lower background temperature is expected, with a limitless recharge of the hydrothermal system, fed by sea water.

3.5.2 Aureoles

The field results indicate that around shallow rhyolite intrusions, the dimension of the aureole is in the same order of magnitude as chilled margin thickness, and increases linearly with intrusion thickness (Fig.3.2). The trendline of the field data cannot be reproduced with a model of diffusion-driven heat transfer (assuming comparable T_{max} between these shallow rhyolite intrusions), given the positive intercept (parameter *b* in Eq. (6)). This is particularly apparent with smaller intrusions that have a relatively larger aureole than predicted by the model. We

propose that the model is not valid for <0.5 m thick intrusions, where the small-scale impact could be strongly influenced by local heterogeneities in host rocks (e.g. McGowan, 2016).

The *b* parameter is expected to relate to a thermal or mechanical energy, with the mechanical impact being included in the field observations but not in the numerical model. Both should be sourced by the magma volume. The non-dependence of *b* on the intrusion thickness suggests that *b* depends on the contact surface rather than the magma volume. It therefore shows that latent heat of crystallisation is not responsible for the extended aureole around small intrusions. If *b* relates to mechanical damage, the possible processes at the interface is the development of tensile fractures and tuffisite veins, with limited extent. If *b* relates to thermal alteration, the processes occurring at the interface and potentially sources of this additional heat supply include pre-heating of host rocks (by fragmentation or friction), heat transfer from the intrusion through fractured lithologies (outgassing and fluid advection/convection; Fig.3.3), and the heat source effect of tuffisite veins. The heat transfer implications of tuffisite veins is yet unknown and requires further work. The pre-heating process is constrained in time, and we assume that the heat transfer through fractures is equivalent to maintaining the temperature of the interface just below T_g. which prevents remelting or crystallisation.

From our field data we conclude that marginal heat convection and/or advection through fractures could make a major contribution to country rock heating for <10 m thick intrusions, while heating from diffusion – and likely latent heat - could dominate for >100 m thick intrusions, where trendline of field data is similar to that of the model. Examining the implications of this hypothesis, we note that fluid flow efficiency is also strongly controlled by the host rocks permeability. High permeability would favour rapid advection and heat transfer, whilst intermediate permeability would reduce these rates. This in turn impacts the heat distribution, more spread in the case of high permeability rocks, with resulting lower temperature geothermal fluids (e.g. Driesner and Geiger, 2007; Scott et al., 2015). As a result, the thermal aureole could be thinner in highly permeable host rocks (10^{-14} m²; Scott et al., 2015). However, we note that the trendline in Fig. 3.2A is independent on the type of host rock (Table. 3.1). We conclude that the effect of permeability can be negligible in regards to the type of heat transfer around rhyolite intrusions. Independent to the size of the intrusion, fluid convection may dominate over conductive heat transfer when fluids are near supercritical conditions and in fractured rocks within a defined aureole surrounding the magma chamber (Norton and Dutrow, 2001). However, the field intrusions included in this study are too shallow for hydrothermal fluids to be at supercritical pressure, and the observed trends are thus not

impacted neither by the behaviour of such fluids. Deeper intrusions (> ~3 km, Scott et al., 2015), where fluids can be at supercritical conditions, may not fit with our model.

We explain the possible dominance of convective heat and fluid flow around thin intrusions by the density contrast between hot and cold fluids (e.g. Hardee, 1981; Norton and Dutrow, 2001). Around large intrusions, the conductive heat transfer increases host rock temperature over a large distance. This distance is reduced around small intrusions according to the numerical model (Fig.3.2A), and thus a same density contrast of fluids (corresponding to temperatures of T_m and T_0) occurs over a smaller distance. This imples that the relative buoyancy of fluids, will be greater around small intrusions, where fluid density gradients are sharpest.

3.5.3 Chilled margins

The chilled margin field data do not form an obvious systematic relationship with intrusion size and can locally vary within the same intrusion (Fig.3.1A). However, our data are concordant with the highest glass transition temperature for this kind of intrusion, from literature, at 700 °C (Castro et al., 2008), and the slowest cooling rate measured in obsidian from literature, at ~10^{-5} °Cs^{-1} (internal side of a basal obsidian layer in a lava flow, equivalent to the inner part of a chilled margin; Gottsmann and Dingwell, 2002). The fastest rate found by model fitting to the field data is not constrained in the literature, as rates can be much higher, associated with the thinnest chilled margin thicknesses, as illustrated in field data by the error bars (Fig.3.2B). The simple diffusive model approximately fits the field data when a constraint on minimum cooling rate (CR_{min}) is applied. Intrusions >12 m have chilled margin thickness with a maximum of ~7 m.

Incremental emplacement (Annen, 2017) and local dynamic effects are likely to explain the wide range and local variations of chilled margin thicknesses that exist, locally preventing chilling or remelting (Huppert and Sparks, 1989). For medium to large intrusions (>~12 m thick), the temperature at a fixed and short distance from the contact, observed for several iterations of intrusion sizes in the model (Fig.3.2B) varies very little at short time-scale. If chilled margins form at the scale of days, as suggested by the end-member boundary in cooling rate, this could cause its maximum thickness to be stable. Close to the contact, temperature and hence cooling rate mostly depend on distance to the interface rather than to the intrusion size.

The few wide and long fractures in crystalline intrusion cores are associated with slow cooling; this abruptly transitions to numerous short and narrow cracks in rapidly cooled margins (Fig.3.3), due to strong thermal gradients (e.g. Mordensky et al., 2019b; Browning et al., 2016).

A consequence of the strong fracture development in chilled margin is an increased permeability, as observed in host rocks with similar fracture properties (Fig.3.3; Saubin et al., 2019). This could boost the heat flux into the host rock beyond predictions from simple conduction, maintaining a high temperature boundary zone suitable for an inwardly accreting chilled margin (similarly to that calculated in Tuffen et al., 2002), and/or inversely favour the ingress of cold fluids into the intrusion, also increasing the thermal gradient and pushing the chilled margin boundary further into the intrusion. Heat advection and convection via fluid flow through the fractures may thus contribute to the thermal regime at the fractured interface, especially around thin (<10 m wide) intrusions where heat transfer by fluid convection could dominate. Fluids convection through the fractures would increase the cooling rate and thus increase the thickness of the quenched margins. Considering the fit of field data with the upper boundary of numerical solution in Figure 3.2C, this could participate to the diversity of chilled margin thickness measured, but would not affect them beyond the range of thickness permitted by conduction.

3.6 Implications and conclusions

Field data for 14 shallow rhyolite intrusions (<1 km depth, < 1 km thick) demonstrate that:

- Macro-scale chilled margins in the intrusion and aureole in host rocks have thickness in the same order of magnitude, with more variations associated with chilled margin thickness
- Macro-scale aureole thickness in host rocks linearly increases with thickness of intrusion
- The extent of damage and chilling is less sensitive to paleodepth (< 1 km range), host rock type and intrusive geometry compared to the intrusion size.
- Chilled margins are more highly fractured than slowly cooled intrusion interiors

The insight from comparison of our data to a simple heat conduction numerical model implies that:

- Chilled margins reach a maximum thickness for >12 m wide intrusions (considering the minimal cooling rate found in literature), beyond which they are not impacted by intrusion size
- Small intrusions (<10 m) have larger thermal aureoles than predicted by conduction models.
- The additional thermal or mechanical energy required to explain the difference in thermal aureole thickness between the model results and field observations depends on the contact surface of fractured aureoles and chilled margins.

We propose that the swift heat-up of host rock (swifter than predicted by conduction) could be caused by advective and/or convective heat transfer through fractures in chilled margins and host rocks, potentially combined with additional heating and fracturing via tuffisite veining. Additionally, chilled margin thickness is highly variable, indicating a variable internal heat flux. This data taken together with our textural changes leads us to imply that emplacement was likely incremental, with flux that was varying with many of our intrusions.

The width of aureoles measured in the field is representative of the highest heat flux out of the intrusion, which depends on the intrusion size. The linear trend on Figure 3.2A can, therefore, be used to deduce intrusive dimensions for fossil or active magma bodies that fall within the limitations of this study (e,g, IDDP-1 intrusion, Krafla; Elders et al., 2011). This inversion, however, necessitates a careful approach considering all assumptions and limitations, including the dominance of heat transfer through convecting fluids around small intrusions, and the temporal delay corresponding to diffusivity (an intrusion reaching its maximum size will cause maximum alteration of the host rock according to the time required for heat diffusion to reach this maximum distance).

Our results highlight the existence of a threshold in the chilled margin thickness, depending on the cooling rate and glass transition temperature, and caused by the short time scale at which the chilled margin form, where temperature at the margins is dominated by the distance to the contact rather than the intrusion size. It is reached for intrusions > ~12 m thick. The maximal chilled margin thickness, calculated for the highest *Tg* and the lowest *CRmin*, is 7 m thick. Field observations also support that the permeability development occurring at the magma/host rock interface potentially plays a major role in thermal damage and alteration of host rocks around small intrusions, by permitting heat transfer by advection/convection from outgassing and fluid flow. Spatially close injections of thin magma layers can create a hydrothermal system more

dynamic than expected from conduction, and have a potentially stronger impact on host rock than a single large intrusion, although over shorter period.

3.7 Acknowledgments

The authors thank the National Power Company of Iceland (Landsvirkjun) for the accommodation provided at Krafla. We are also thankful to Felix von Aulock (University of Liverpool, UK) and Einar Bessi Gestsson (Uppsala University and Icelandic Meteorological office) for their assistance on the field, and to the farmers at Njardvik for kindly giving access to the field sites. This work was supported by the Ministry of Business, Employment and Innovation, New Zealand [grant number E6552]; Mason Trust funding from the University of Canterbury, New Zealand; and a Royal Society University Research Fellowship to HT.

3.8 References

Annen, C., 2011. Implications of incremental emplacement of magma bodies for magma differentiation, thermal aureole dimensions and plutonism–volcanism relationships. Tectonophysics 500, 3–10, doi:10.1016/j.tecto.2009.04.010

Annen, C., Scaillet, B., Sparks, R.S.J., 2006. Thermal constraints on the emplacement rate of a large intrusive complex: the Manaslu leucogranite, Nepal Himalaya. Journal of Petrology 47, 71–95, doi: 10.1093/petrology/egi068

Annen, C., 2017. Factors affecting the thickness of thermal aureoles. rontiers in Earth Science 5, doi: 10.3389/feart.2017.00082

Barker, D.S., 2007. Endogenous and exogenous plutons: the influence of emplacement style on contamination of granitic magma. The Canadian Mineralogist 45, 63–70, doi: 10.2113/gscanmin.45.1.63

Befus, K. S., 2016. Crystallization kinetics of rhyolitic melts using oxygen isotope ratios. Geophysical Research Letters 43(2), 592–599, doi: 10.1002/2015GL067288

Bostick, N.H., Pawlewicz, M.J., 1984. Paleotemperatures based on vitrinite reflectance of shales and limestone in igneous dike aureoles in the Upper Cretaceous Pierre Shale, Walsenburg, Colorado.

Brandeis, G., Jaupart, C., Allègre, C. J., 1984. Nucleation, crystal growth and the thermal regime of cooling magmas. Journal of Geophysical Research: Solid Earth 89(B12), 10161–10177, doi: 10.1029/JB089iB12p10161

Browning, J., Meredith, P. G., Gudmundsson, A., 2016. Cooling-dominated cracking in thermally stressed volcanic rocks. Geophysical Research Letters 42, doi:10.1002/2016GL070532

Burchardt, S., Tanner, D., Krumbholz, M., 2012. The Slaufrudalur pluton, southeast Iceland—An example of shallow magma emplacement by coupled cauldron subsidence and magmatic stoping. Geological Society of America Bulletin 124, 213–227.

Burchardt, S., Walter, T. R., Tuffen, H., 2018. Chapter 4 - Growth of a Volcanic Edifice Through Plumbing System Processes—Volcanic Rift Zones, Magmatic Sheet-Intrusion Swarms and Long-Lived Conduits. In S. Burchardt (Ed.), Volcanic and Igneous Plumbing Systems, 89–112.

Carrigan, C. R., Eichelberger, J. C., 1990. Zoning of magmas by viscosity in volcanic conduits. Nature 343(6255), 248–251, doi: 10.1038/343248a0

Carrigan, C. R., Schubert, G., Eichelberger, J. C., 1992. Thermal and dynamical regimes of single- and two-phase magmatic flow in dikes. Journal of Geophysical Research: Solid Earth 97(B12), 17377–17392, doi: 10.1029/92JB01244

Carslaw, H. S., Jaeger, J. C., 1959. Conduction of heat in solids. Oxford: Clarendon Press, 2nd ed.

Castro, J. M., Beck, P., Tuffen, H., Nichols, A. R. L., Dingwell, D. B., Martin, M. C., 2008. Timescales of spherulite crystallization in obsidian inferred from water concentration profiles. American Mineralogist 93(11–12), 1816–1822, doi: 10.2138/am.2008.2904

Claour-Long J.C., and Nesbitt R.W., 1985. Contaminated komatiites: a discussion. Nature 313, 247-248.

Delaney, P.T., Pollard, D.D., Ziony, J.I., McKee, E.H., 1986. Field relations between dikes and joints: Emplacement processes and paleostress analysis. Journal of Geophysical Research: Solid Earth 91, 4920–4938, doi: 10.1029/JB091iB05p04920

Driesner, T., Geiger, S., 2007, Numerical simulation of multiphase fluid flow in hydrothermal systems. Reviews in Mineralogy and Geochemistry. 65, 187–212

Eggertsson, G. H., 2019. Constraining mechanical and permeability properties of the Krafla geothermal reservoir, North-East Iceland [Doctoral thesis], Liverpool.

Elders, W. A., Friðleifsson, G. Ó., Zierenberg, R. A., Pope, E. C., Mortensen, A. K., Guðmundsson, Á., Lowenstern, J. B., Marks, N., Owens, L., Bird, D. K., Reed, M., Olsen, N., Schiffman, P., 2011. Origin of a rhyolite that intruded a geothermal well while drilling at the Krafla volcano, Iceland. Geology 39(3), 231–234, doi: 10.1130/G31393.1

Elders, W. A., Osborn, W. L., Raju, A. S. K., Martinez-Morales, A., 2019. The Future Role of Geothermal Resources in Reducing Greenhouse Gas Emissions in California and Beyond. Proceedings 44th Workshop Geothermal Reservoir Engineering, 9.

Eldursi, K., Branquet, Y., Guillou-Frottier, L., Marcoux, E., 2009. Numerical investigation of transient hydrothermal processes around intrusions: Heat-transfer and fluid-circulation controlled mineralization patterns. Earth and Planetary Science Letters288(1), 70–83, doi: 10.1016/j.epsl.2009.09.009

Eppelbaum, L. V., Kutasov, I., Pilchin, A., 2014. Applied geothermics. Berlin: Springer.Faulkner, D. R., Mitchell, T. M., Jensen, E., Cembrano, J., 2011. Scaling of fault damage zones with displacement and the implications for fault growth processes. Journal of Geophysical Research: Solid Earth116(B5), doi: 10.1029/2010JB007788

Furlong, K. P., Hanson, R. B., Bowers, J. R., 1991. Modelling thermal regimes in contact metamorphism. Ed Kerrick, D. M. (Chelsea, MI: Mineralogical Society of America), 437–498.

Giordano, D., Russell, J. K., Dingwell, D. B., 2008. Viscosity of magmatic liquids: A model. Earth and Planetary Science Letters 271 (1), 123–134, doi: 10.1016/j.epsl.2008.03.038

Gomez, C., Kennedy, B., 2018. Capturing volcanic plumes in 3D with UAV-based photogrammetry at Yasur Volcano – Vanuatu. Journal of Volcanology and Geothermal Research 350, 84–88, doi: 10.1016/j.jvolgeores.2017.12.007

Goto, Y., Nakada, S., Kurokawa, M., Shimano, T., Sugimoto, T., Sakuma, S., Hoshizumi, H., Yoshimoto, M., Uto, K., 2008. Character and origin of lithofacies in the conduit of Unzen volcano, Japan. Journal of Volcanology and Geothermal Research 175(1), 45–59, doi: 10.1016/j.jvolgeores.2008.03.041

Gottsmann, J., Dingwell, D. B., 2002. The thermal history of a spatter-fed lava flow: the 8-ka pantellerite flow of Mayor Island, New Zealand. Bulletin of Volcanology 64(6), 410–422, doi: 10.1007/s00445-002-0220-7

Gottsmann, J., Giordano, D., Dingwell, D. B., 2002. Predicting shear viscosity during volcanic processes at the glass transition: a calorimetric calibration. Earth and Planetary Science Letters 198(3), 417–427, doi: 10.1016/S0012-821X(02)00522-8

Hardee, H., C., 1981. Convective heat extraction from molten magma. Journal of Volcanology and Geothermal Research 10, 175-193

Hasselman, D. P. H., Singh, J. P., 1986. Criteria for the thermal stress failure of brittle structural ceramics. Thermal stresses I. 1, 263-298.

Heap, M.J., Violay, M., Wadsworth, F.B., Vasseur, J., 2017. From rock to magma and back again: The evolution of temperature and deformation mechanism in conduit margin zones. Earth and Planetary Science Letters 463, 92–100, doi: 10.1016/j.epsl.2017.01.021

Heap, M. J., Gravley, D. M., Kennedy, B. M., Gilg, H. A., Bertolett, E., Barker, S. L. L., 2019. Quantifying the role of hydrothermal alteration in creating geothermal and epithermal mineral resources: The Ohakuri ignimbrite (Taupō Volcanic Zone, New Zealand). Journal of Volcanology and Geothermal Research 106703, doi: 10.1016/j.jvolgeores.2019.106703

Henneberger, R. C., Browne, P. R. L., 1988. Hydrothermal alteration and evolution of the Ohakuri hydrothermal system, Taupo volcanic zone, New Zealand. Journal of Volcanology and Geothermal Research 34(3), 211–231, doi: 10.1016/0377-0273(88)90034-0

Hess, K.-U., Dingwell, D. B., von Aulock, F., Lavalee', Y., 2015. The solidification of obsidian glass during drilling of the IDDP-1 drill hole. EGU General Assembly, Vienna, 17, 12338H.

Holness, M. B., Nielsen, T. F. D., Tegner, C., 2007. Textural maturity of cumulates: a record of chamber filling, liquidus assemblage, cooling rate and large-scale convection in mafic layered intrusions. Journal of Petrology 48(1), 141–157, doi: 10.1093/petrology/egl057

Huppert, H. E., Sparks, R. S. J., 1984. Double-diffusive convection due to crystallization in magmas. Annual Review of Earth and Planetary Sciences 12(1), 11–37, doi: 10.1146/annurev.ea.12.050184.000303

Huppert, H. E., Sparks, R. S. J., 1989. Chilled margins in igneous rocks. Earth and Planetary Sciences Letters, 397–405.

Jaeger, J. C., 1959. Temperatures outside a cooling intrusive sheet. American Journal of Science257(1), 44–54, doi: 10.2475/ajs.257.1.44

Jónasson, K., 1994. Rhyolite volcanism in the Krafla central volcano, north-east Iceland. Bulletin of Volcanology56(6–7), 516–528, doi: 10.1007/BF00302832

Kafoussias, N. G., Williams, E. W., 1995. Thermal-diffusion and diffusion-thermo effects on mixed free-forced convective and mass transfer boundary layer flow with temperature dependent viscosity. International Journal of Engineering Science 33(9), 1369–1384, doi: 10.1016/0020-7225(94)00132-4

Kavanagh, J.L., Sparks, R.S.J., 2011. Insights of dyke emplacement mechanics from detailed 3D dyke thickness datasets. Journal of the Geological Society 168, 965–978, doi: 10.1144/0016-76492010-137

Kokelaar, B.P., Bevins, R.E., Roach, R.A., 1985. Submarine silicic volcanism and associated sedimentary and tectonic processes, Ramsey Island, SW Wales. Journal of the Geological Society 142, 591–613, doi: 10.1144/gsjgs.142.4.0591

Krumbholz, M., Hieronymus, C.F., Burchardt, S., Troll, V.R., Tanner, D.C., Friese, N., 2014. Weibull-distributed dyke thickness reflects probabilistic character of host-rock strength. Nature Communications 5, 3272, doi: 10.1038/ncomms4272

Lavallée, Y., Lamur, A., Kendrick, J. E., Eggertsson, G. H., Weaver, J., Eichelberger, J. C., Papale, P., Sigmundsson, F., Dingwell, D. B., Markússon, S. H., Mortensen, A. K., 2020. Thermal manipulation of magma boundaries: advancing controls on fluid flow via the Krafla Magma Testbed (KMT). Proceeding World Geothermal Congress, 11.

Manda, A. K., Mabee, S. B., 2010. Comparison of three fracture sampling methods for layered rocks. International Journal of Rock Mechanics and Mining Sciences 47 (2), 218-226, doi: 10.1016/j.ijrmms.2009.12.004

Mathieu, L., van Wyk de Vries, B., Holohan, E. P., Troll, V. R., 2008. Dykes, cups, saucers and sills: Analogue experiments on magma intrusion into brittle rocks. Earth and Planetary Science Letters 271, 1–13, doi: 10.1016/j.epsl.2008.02.020

Mattsson, T., Burchardt, S., Almqvist, B.S.G., Ronchin, E., 2018. Syn-Emplacement Fracturing in the Sandfell Laccolith, Eastern Iceland—Implications for Rhyolite Intrusion Growth and Volcanic Hazards. Frontiers in Earth Sciences 6, doi: 10.3389/feart.2018.00005

McGowan, E. M., 2016. Magma emplacement and deformation in rhyolitic dykes: insight into magmatic outgassing. Thesis. Lancaster University.

Mordensky, S.P., Villeneuve, M.C., Kennedy, B.M., Heap, M.J., Gravley, D.M., Farquharson, J.I., Reuschlé, T., 2018. Physical and mechanical property relationships of a shallow intrusion and volcanic host rock, Pinnacle Ridge, Mt. Ruapehu, New Zealand. Journal of Volcanology and Geothermal Research 359, 1–20, doi: 10.1016/j.jvolgeores.2018.05.020

Mordensky, S., Heap, M., Kennedy, B., Gilg, H.A., Villeneuve, M., Farquharson, J., Gravley, D., 2019a. Influence of alteration on the mechanical behaviour and failure mode of andesite: Implications for shallow seismicity and volcano monitoring. Bulletin of Volcanology, accepted.

Mordensky, S. P., Kennedy, B. M., Villeneuve, M., Lavallée, Y., Reichow, M. K., Wallace, P. A., Siratovich, P. A., Gravley, D. M., 2019b. Increasing the permeability of hydrothermally altered andesite by transitory heating. Geochemistry, Geophysics, Geosystems, doi: 10.1029/2019GC008409

Newman, S., Lowenstern, J.B., 2002. VolatileCalc: a silicate melt-H2O-CO2 solution model written in Visual Basic for Excel: Computers and Geosciences 28 (5), 597-604.

Norton, D., L., Dutrow, B., L., 2001. Complex behaviour of magma-hydrothermal processes: Role of supercritical fluid. Geochimica et Cosmochimica Acta. Vol. 65, No. 21, pp. 4009-4017.

Otterloo, J. V., Cas, R. A. F., Scutter, C. R., 2015. The fracture behaviour of volcanic glass and relevance to quench fragmentation during formation of hyaloclastite and phreatomagmatism. Earth-Science Reviews 151, 79–116, doi: 10.1016/j.earscirev.2015.10.003

Pirajno, F., 2008. Hydrothermal processes and mineral systems. Springer Science & Business Media.

Romine, W. L., Whittington, A. G., Nabelek, P. I., Hofmeister, A. M., 2012. Thermal diffusivity of rhyolitic glasses and melts: effects of temperature, crystals and dissolved water. Bulletin of Volcanology 74(10), 2273–2287, doi: 10.1007/s00445-012-0661-6

Rubin, A.M., 1993. Dikes vs. diapirs in viscoelastic rock. Earth and Planetary Science Letters 117, 653–670, doi: 10.1016/0012-821X(93)90109-M

Saubin, E., Kennedy, B. M., Tuffen, H., Villeneuve, M., Davidson, J., Burchardt, S., 2019. Comparative field study of shallow rhyolite intrusions in Iceland: emplacement mechanisms and impact on country rocks. Journal of Volcanology and Geothermal Research, doi: 10.1016/j.jvolgeores.2019.106691

Schauroth, J., Wadsworth, F. B., Kennedy, B., von Aulock, F. W., Lavallée, Y., Damby, D. E., Vasseur, J., Scheu, B., & Dingwell, D. B., 2016. Conduit margin heating and deformation during the AD 1886 basaltic Plinian eruption at Tarawera volcano, New Zealand. Bulletin of Volcanology 78(2), 12: 10.1007/s00445-016-1006-7

Scott, S., Driesner, T., Weis, P., 2015. Geologic controls on supercritical geothermal resources above magmatic intrusions. Nature communications, 6:7837, doi: 10.1038

Stasiuk, M.V., Barclay, J., Carroll, M.R., Jaupart, C., Ratté, J.C., Sparks, R.S.J., Tait, S.R., 1996. Degassing during magma ascent in the Mule Creek vent (USA). Bulletin of Volcanology 58, 117–130, doi: 10.1007/s004450050130

Sydnes, M., Fjeldskaar, W., Løtveit, I. F., Grunnaleite, I., Cardozo, N., 2018. The importance of sill thickness and timing of sill emplacement on hydrocarbon maturation. Marine and Petroleum Geology 89, 500–514, doi: 10.1016/j.marpetgeo.2017.10.017

Tuffen, H., Pinkerton, H., McGarvie, D. W., Gilbert, J. S., 2002. Melting of the glacier base during a small-volume subglacial rhyolite eruption: evidence from Bláhnúkur, Iceland. Sedimentary Geology 149(1), 183–198, doi: 10.1016/S0037-0738(01)00251-2

Tuffen, H., Dingwell, D. B., Pinkerton, H., 2003. Repeated fracture and healing of silicic magma generate flow banding and earthquakes? Geology 31(12), 1089, doi: 10.1130/G19777.1

Tuffen, H., Dingwell, D. B., 2005. Fault textures in volcanic conduits: evidence for seismic trigger mechanisms during silicic eruptions. Bulletin of Volcanology 67(4), 18.

Tuffen, H., Castro, J.M., 2009. The emplacement of an obsidian dyke through thin ice: Hrafntinnuhryggur, Krafla Iceland. Journal of Volcanology and Geothermal Research185, 352–366, doi: 10.1016/j.jvolgeores.2008.10.021

Turner, J. S., Campbell, I. H., 1986. Convection and mixing in magma chambers. Earth-Science Reviews 23(4), 255–352, doi: 10.1016/0012-8252(86)90015-2

von Aulock, F. W., Nichols, A. R. L., Kennedy, B. M., Oze, C., 2013. Timescales of texture development in a cooling lava dome. Geochimica et Cosmochimica Acta 114, 72–80, doi: 10.1016/j.gca.2013.03.012

Chapter 4 – Textural and geochemical window into the IDDP-1 rhyolitic melt, Krafla, Iceland, and its reaction to drilling

E. Saubin[1], B. Kennedy[1], H. Tuffen[2], A. R. L. Nichols[1], M. Villeneuve[1], I. Bindeman[3], A. Mortensen[4], C. I. Schipper[5], F.B. Wadsworth[7], T. Watson[1], R. Zierenberg[6]

[1] *School of Earth and Environment, University of Canterbury, Christchurch, New Zealand*

[2] *Lancaster Environment Centre, Lancaster University, Lancaster, UK*

[3] *Department of Earth Sciences, University of Oregon, Eugene, OR, USA*

[4] *Landsvirkjun National Power Company of Iceland, Reykjavik*

[5] *School of Geography, Environment and Earth Sciences, Victoria University of Wellington, NZ*

[6] *Earth and Planetary Sciences, University of California, Davis, California, CA, USA*

[7] *Department of Earth Sciences, Lower Mountjoy, Durham University, Durham, UK*

4.1 Abstract

The unexpected interception of rhyolitic magma and retrieval of quenched glass particles by the IDDP-1 geothermal well in 2009 at Krafla, Iceland, provides unprecedented opportunities to characterise the genesis, storage and behaviour of subsurface silicic magma. This study adds to pre-existing literature by analysing the chemistry and detailed bubble textures of the full time-series of glass particles retrieval after magma was intercepted.

Detailed analysis of the particles reveals a bimodal magma texture and composition. Early-retrieved clear glass has higher SiO_2, crystal and vesicle contents, whereas later-retrieved dense brown glass has lower SiO_2 and crystal content, and several vesicle populations distinguished based on size distribution. The individual and texturally distinct glass chips δvaries in δD, from -120 to -80 ‰, and water from 1.3 to 2 wt%, although the majority of glass exhibit a narrower range. Textures indicate that volatile overpressure release predominantly occurred prior to the

late stage magma ascent, combined with vesiculation occurred in response to drilling-induced decompression. We interpret the rhyolitic melts to have formed via bimodal degree of partial melting of a felsite body with the heat source likely being a shallow intrusion, and re-melting promoted by hydration from alteration minerals and/or hydrothermal fluids. The brown melt (higher degree partial melt) coexists with the clear melt (lower degree partial melt) at the margins of the IDDP-1 rhyolite body, distributed in discrete pockets or layers. Low-degree melting appears to be ongoing, and the growing intrusion thus has an increasing potential for geothermal energy extraction.

Our conclusions support the hypothesis that rhyolite melt genesis can occurs by remelting of a fossil felsite intrusion driven by the input of heat and hydrothermal fluid. This mechanism produced considerable spatial chemical heterogeneities, and additional tetxural heterogeneities enhanced by drilling perturbations. Potentially such remelting and remobilisation could occur extensively in the crust above magma chambers. Our findings emphasise the need for higher resolution geophysical monitoring of restless calderas, both for hazard assessment and geothermal prospecting.

4.2 Introduction

Our knowledge of the behaviour of subsurface magma is restricted, mostly built on observations and analysis from fossil intrusions or pyroclasts, or from experimental approaches. Neither can provide the insight that observations of *in situ* magma bodies can. The first Iceland Deep Drilling well (IDDP-1) was completed in 2009 at Krafla, with the aim of reaching supercritical fluids at the margins of a magma chamber 4-5 km deep. However, the drilling instead hit previously undetected rhyolite magma at 2104 metres below the surface (mbs), as demonstrated by the retrieval of fresh obsidian after several drilling difficulties (ISOR, 2009; Pálsson et al., 2014). Through this fortuitous drilling event, these retrieved samples of quenched magma represent unique opportunities to characterise in-situ magma from the roof of an active silicic intrusion.

4.2.1 Context

Krafla is a caldera-bearing central volcano located on the northern rift zone of Iceland (Fig.4.1). Its most recent eruptive episode, between 1975 and 1984, involved basaltic fissure eruptions

with repeated episodes of rifting, intrusion, and ground deformation (Björnsson, 1985). Seismic velocity surveying indicates the presence of a 0.7-1.8 km-thick magma body at around 3 km depth (Brandsdottír et al., 1997), extending <3 km N-S and <10 km E-W (Fig. 1). Past eruptive activity indicates the magmatic system is dominated by basalt (Sæmundsson, 1991; Mortensen et al., 2015; Kennedy et al., 2018 and references therein), however, remelting of basaltic crust has generated rhyolite magma reservoirs at its peripheries, and a mixed rhyolite-basalt eruption is thought to have been responsible for most of the caldera subsidence (Marsh et al., 1991; Jónasson, 1994; Rooyakkers et al., 2017. Fig. 4.1). A low-V_p/V_s zone at 2–3 km depth beneath Víti, inferred from earthquake and active seismic data (Schuler et al., 2017), may correspond to a shallow rhyolitic intrusion, or superheated steam at its margin. Two other eruptive phases have created rhyolitic domes and ridges both within the caldera and at its margins (Jónasson 1994; Tuffen and Castro 2009). The complex magmatic system extends between 2 and 8 km depth, and is the heat source of a ~40 km² geothermal system that has hosted an operating geothermal power station since 1977 (Einarsson, 1978; Armannsson et al, 2014; Mortensen et al., 2014).

Geophysical data including the distribution of seismicity and resistivity were used to choose the site and depth for IDDP-1, as the best target for supercritical fluids with no evidence for shallow magma (Friðleifsson et al., 2014. Fig. 4.1). However, drilling had to be stopped when rhyolitic magma was unexpectedly encountered at a depth of only 2104 mbs (Friðleifsson et al., 2010). The drill bit approached magma three times, with two side-tracks necessary due to repeated sticking. These events of magma interception occurred on 21st April, 8th June and 24th June 2009, corresponding to intervals of 50 and 16 days between interception events (Friðleifsson et al., 2010; Pálsson et al., 2014). On the third approach, magma pushed up on the drill bit that was 9 m above the bottom of the well, and ultimately plugged the lowest ~20 m of the hole. The retrieval of fresh silicic glass in cuttings revealed the cause of drilling difficulties, which were initially unknown (ISOR, 2009; Friðleifsson et al., 2013). Despite these difficulties, IDDP-1 became the hottest (452° C at the well head, Friðleifsson et al., 2013) and one of the most productive geothermal wells worldwide, until it was abandoned in 2012 following a collapse in the well casing in 2010 (Ingason et al., 2014). It is now a renowned example of a super-hot geothermal well that intercepted magma, and the retrieval of quenched glass makes the well an unprecedented target for the characterisation of in-situ magma from the margins of an active intrusion.

Because the location of the IDDP-1 magma body is well known, the Krafla Magma Testbed project (KMT; http://kmt.is) aims to drill back into this site and create a global testbed for monitoring subsurface magma and assessing both hazards and geothermal productivity (Eichelberger, 2019). The success of any new "magma wells" depends on having a sound understanding of magma behaviour at intrusion margins and its reaction to drilling. The process of melt emplacement/formation, the intrusion size, and its relationship with host rocks are also key parameters that impact the overlying fluid reservoir, and its geothermal potential (e.g. Bostick and Pawlewicz, 1984). In this study, we provide new, detailed textural and compositional data defining a time series of silicic glass from IDDP-1 (the timing of the sample retrievals is referred to as retrieval time throughout this manuscript). We discuss the physical reaction of the magma to drilling, and examine the scenarios for magma storage and the cannibalisation of intrusion margins. Key evidence includes the relation between glass texture (vesicularity, crystallinity, colour) and chemistry (major elements, isotopes and volatile content), as well as the componentry of the cuttings.

4.2.2 Previous work on the IDDP-1 rhyolite

The reported lithologies encountered by the well show that felsite is the host rock for the intrusion (Mortensen et al., 2014). Studies on IDDP-1 rhyolite cuttings to date have revealed much about their texture and chemistry. The mineral assemblage in rhyolitic glass consists of plagioclase, pigeonite, augite and titanomagnetite (Zierenberg et al., 2013; Masotta et al., 2018). The glass is silica-rich (75.1 wt% SiO_2), with low TiO_2 (0.3 wt%) and average isotopic compositions of 3.1 ‰ $\delta^{18}O$ and -121 ‰ δD (Elders et al, 2011; Zierenberg et al, 2013; Schiffman et al, 2014). Glass volatile contents average 1.77 wt% H_2O and 85 ppm CO_2, but vary significantly with glass texture (vesicularity, crystallinity and colour; Trewick, 2015) and retrieval time (Watson, 2018). The H_2O speciation, high OH/H_2Om (1.46 – 2.53, Zierenberg et al., 2013), indicates predominantly magmatic rather than meteoric water, suggesting limited interaction with drilling fluids and quenching of magma between 758 and 939 °C (Zierenberg et al., 2013, using the model of Ihinger et al., 1999), or <500 and 625 °C (Watson, 2018, using the model of Nowak and Behrens). Based on the time-series samples, Watson (2018) suggests OH/H_2Om increases over time during retrieval (0.97 to 2.63), which could indicate an increasing quenching temperature. δD and $\delta^{18}O$ were compared with that of local epidote (Pope, 2011) to determine the origin of the magma, as water-epidote fractionation allows indirect determination of O and H isotope ratios in the fluid phase in hydrothermal systems (exchange effect in Fig.4.7C). This indicates that the rhyolite intrusion is derived from partial melting and

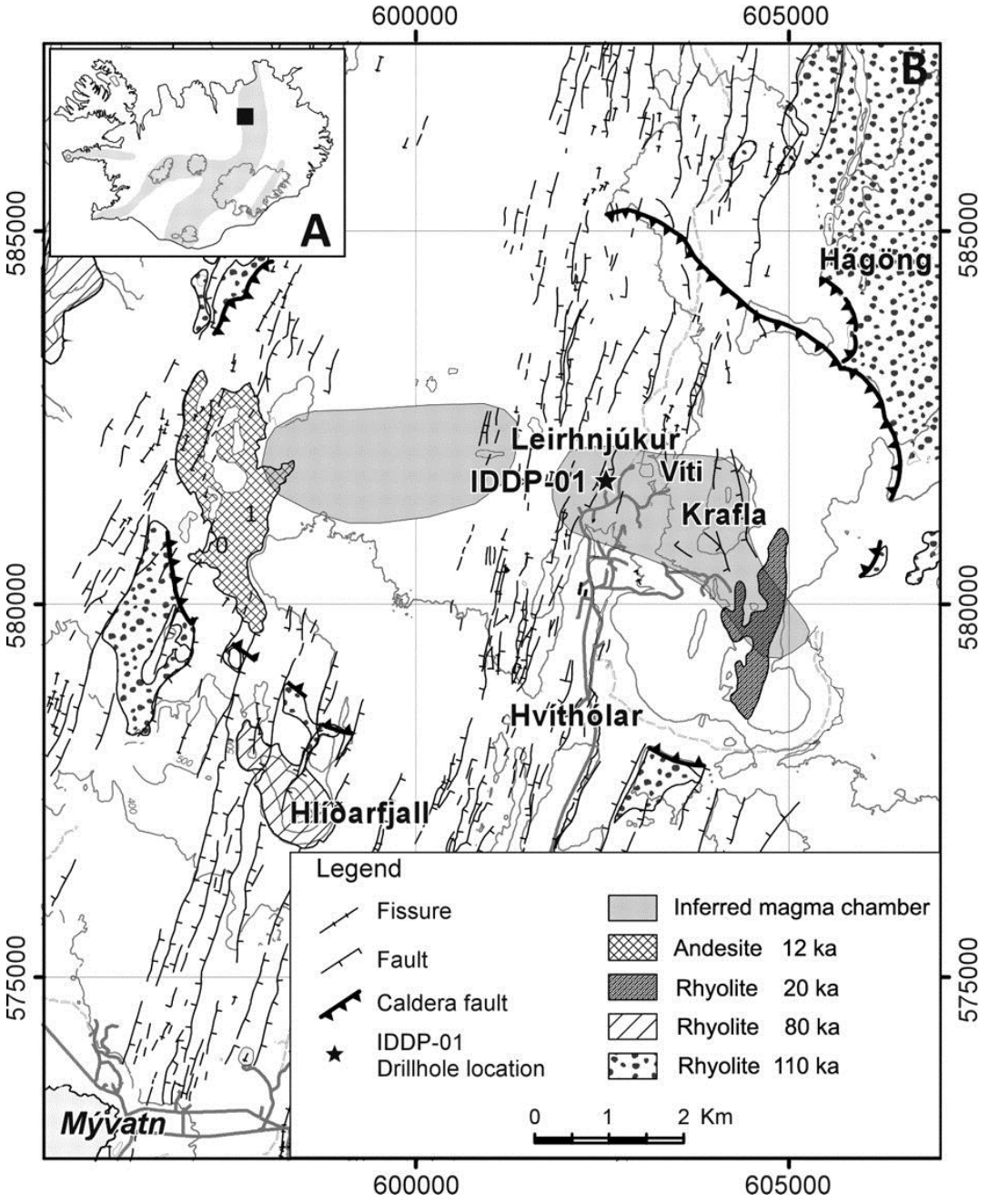

Figure 4.1. Map of the Krafla caldera and geothermal field, from Elders et al. (2011). A) Krafla location on the north Iceland rift zone. B) Location of the IDDP-1 well and surface projection of the ~4 km depth basalt magma chamber, inferred on the basis of S-wave shadows (Einarsson, 1978).

assimilation of hydrothermally altered basalt (Elders et al., 2011). Crystal textures and thermobarometric calculations, however, reveal identical crystallisation conditions in the rhyolitic glass and host felsite, with remelting, mixing, and incorporation of crystals from the felsite into crystal-poor rhyolite (Zierenberg et al., 2013; Masotta et al., 2018). In addition, bulk composition reveals that the rhyolite and host felsite are cogenetic. Felsite partial melting experiments at 950°C allow reproduction of the bimodal glass composition, which thus

represent near-liquidus and sub-solidus states of the same magma (Masotta et al., 2018). The last magmatic activity at Krafla was the 1975-1984 Krafla Fires eruption, and sustained heat input during this eruption, via shallow crustal intrusions, could have enhanced IDDP-1 magma generation (Elders et al., 2011; Masotta et al., 2018).

Most of the previous work published on the IDDP-1 cuttings emphasized a bulk sample of glass retrieved at the same time, 17:00 on 24 June 2009. Here we widen the study to encompass glass recovered over the full time-window of retrieval (over more than 9 hrs). We also examine the vesicular microtextures, using vesicle size distributions to characterise degassing and stresses through nucleation, growth and coalescence (Sparks, 1978; Rust et al., 2003; Okumura et al., 2006; Hamada et al., 2010; Shea et al., 2010), and bubble number density to calculate decompression rates (Toramaru, 2006). We complement published major element chemistry and $\delta^{18}O$ and δD values of IDDP-1 cuttings with additional data, to further explore the magma genesis and degassing dynamics (Taylor et al., 1983; Newman et al., 1988; Zhang et al., 1999; Taylor et al., 2001; Pope et al., 2014; Castro et al., 2014). Our results are set within the context of previous work on IDDP-1 cuttings, and interpretations are informed by the timeline of of drilling events that occurred prior to and during interception of the magmatic intrusion. Our interpreted scenario of rhyolite magma genesis was evaluated using a thermodynamic approach and accordingly adjusted.

4.3 Methodology

The methods employed (protocol in Fig.4.2) include classification of all IDDP-1 cuttings and componentry analysis. Detailed study was restricted to the glass particles, as these represent the quenched magma we aim to understand. Glasses were analysed in terms of texture (vesicle density, size, shape and distribution, crystallinity) and composition (major elements, water content, hydrogen isotope ratio), in relation to the time of sample retrieval. Interpretation of the results is set within the context of drilling using the timeline of evolving drilling parameters, derived from raw data provided by Landsvirkjun (the company responsible for the geothermal power plant and geothermal energy extraction in the Krafla area, Iceland, which paid most of the cost of the IDDP-1 operation). The drilling data are provided in Fig.S4.1 (Supplementary Material), and span the initial magma interception to the end of the cutting retrieval.

Dacite

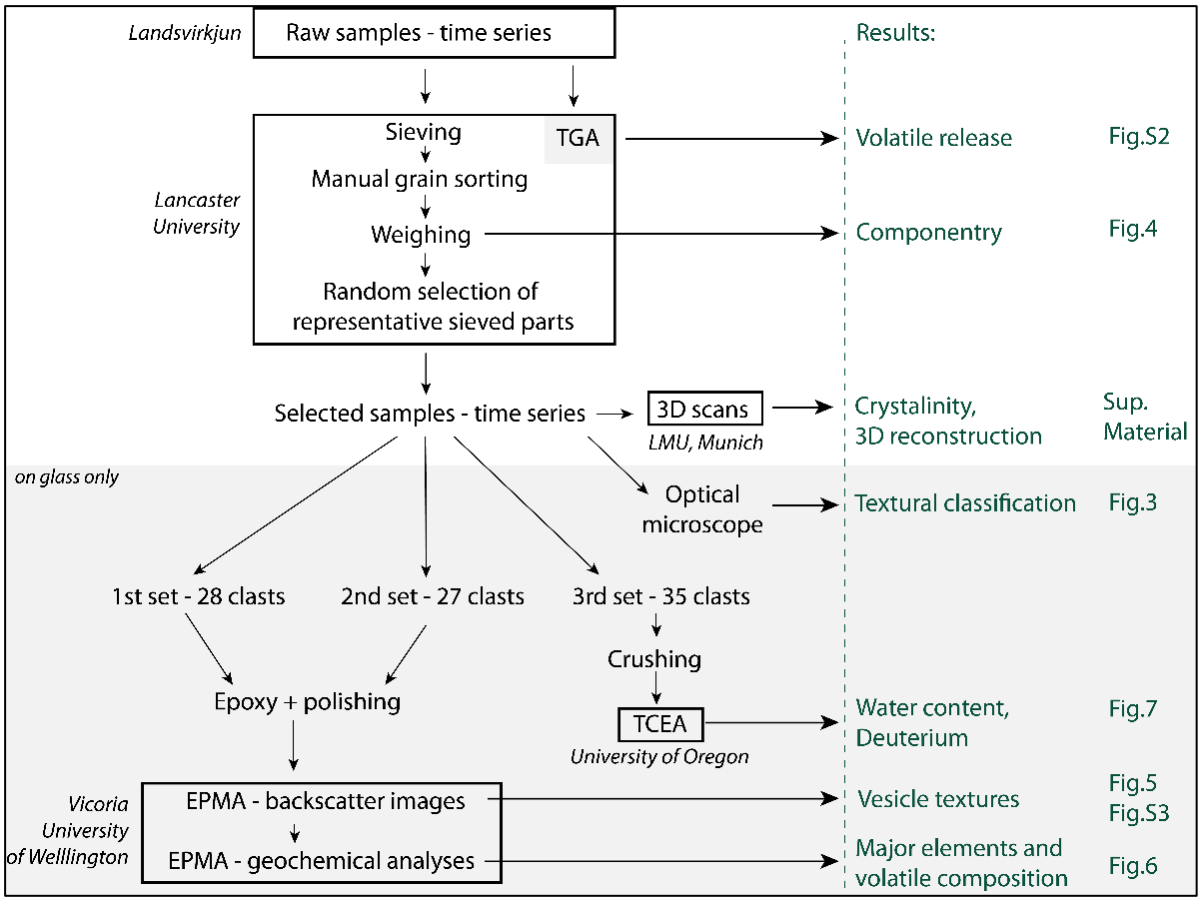

Figure 4.2. Protocol for data collection on IDDP-1 cuttings, conducted at the University of Canterbury, NZ, unless otherwise mentioned. Analyses in the grey area were performed on selected glass cuttings only.

4.3.1 IDDP-1 cutting componentry

Cuttings were recovered from the IDDP-1 well, with 22 sampling episodes done at regular intervals from 15:15 on 24 June 2009 to 00:50 on 25 June 2009, starting two hours after the magma was hit at 13:27, with the drill bit stuck at a constant depth (Fig.S4.1, Supplementary Material). Raw samples were sieved into four grainsize fractions. The largest grains (1-2 mm and 2-4 mm) were sorted using the naked eye into four categories: fresh glass coming from the intercepted magma; crystalline felsite from the intrusion margins and/or host rocks; glassy felsite that is texturally intermediate between glass and crystalline felsite; and drilling contaminants (LCM: lost circulation material, present here as nut shells and mica flakes). Each category was weighed to gain insight into componentry evolution over time. Among the sieved fractions, a portion of the clasts was randomly selected from each category (5-10 clasts). Further analyses were conducted on these representative portions (grey shaded region in Fig.4.2). The sampling times 15:15 and 15:30 are not considered for analyses, as the grain size of particles is too small for sorting with the naked eye.

4.3.2 IDDP-1 glass

We have analysed a total of 251 glassy particles from the 1-2 and 2-4 mm size fractions, 5-35 particles per collection time. These were individually sorted into textural sub-categories using an optical microscope.

Glass vesicularity for each particle was first estimated visually by comparing the apparent vesicle area fraction with a reference chart displaying a range of vesicle area fractions. The vesicularity of 24 particles of various textures was subsequently calculated using the ImageJ software on backscatter electron (BSE) images collected with a JEOL JXA-8230 SuperProbe, at Victoria University of Wellington (VUW). The relative vesicularities estimated in the first instance were thus calibrated using the calculated vesicularities. Among other parameters considered for textural classification (vesicle shape, size, elongation direction and dispersion), we base the final classification on the two criteria showing the most obvious variations and the lowest human bias uncertainty: colour (clear, brown or black glass) and 2D vesicularity (non-vesicular, <1 %, 1-3 % and >3 % vesicularity). The vesicularity values given in this paper refer to the percentage by area. We also refer to the <1 and 1-3 % categories as poorly vesicular, and will call the >3 % category "vesicular", with most clasts having 3-6 % vesicularity and a few up to ~15 %. These relative descriptors are appropriate for this sample set, but we recognize that all IDDP-1 glasses would be considered "poorly vesicular" relative to normal pyroclast classification schemes. Representative cuttings and examples of classified glass particles are shown in Fig.4.3.

In order to reduce bias caused by human colour perception, colour identification was conducted by comparison with reference particles of distinct clear and brown colours. As brown glass can appear clear around vesicles, colour identification was conducted, when possible, on vesicle-free portions of particle borders. Similarly, the impact of particle size (a very thin brown glass can appear clear) was addressed by comparison with similar-sized reference particles.

BSE images were used to characterise vesicle texture and proportion. Vesicle properties were analysed in 25 glass particles that span the time series, the range of vesicularities, and the full range of vesicular textures (distribution, size, shape, orientation). The protocol is similar to that described in Shea et al. (2010): each clast is imaged at four magnifications, with a minimum of 11 images per clast distributed as in Figure 4.3B. The images were processed with Adobe Photoshop™ to select, redraw and attribute a grayscale colour to vesicles prior to analysis with

FOAMS software, which provides the volume fraction size distribution corrected from 2D pictures (Shea et al., 2010).

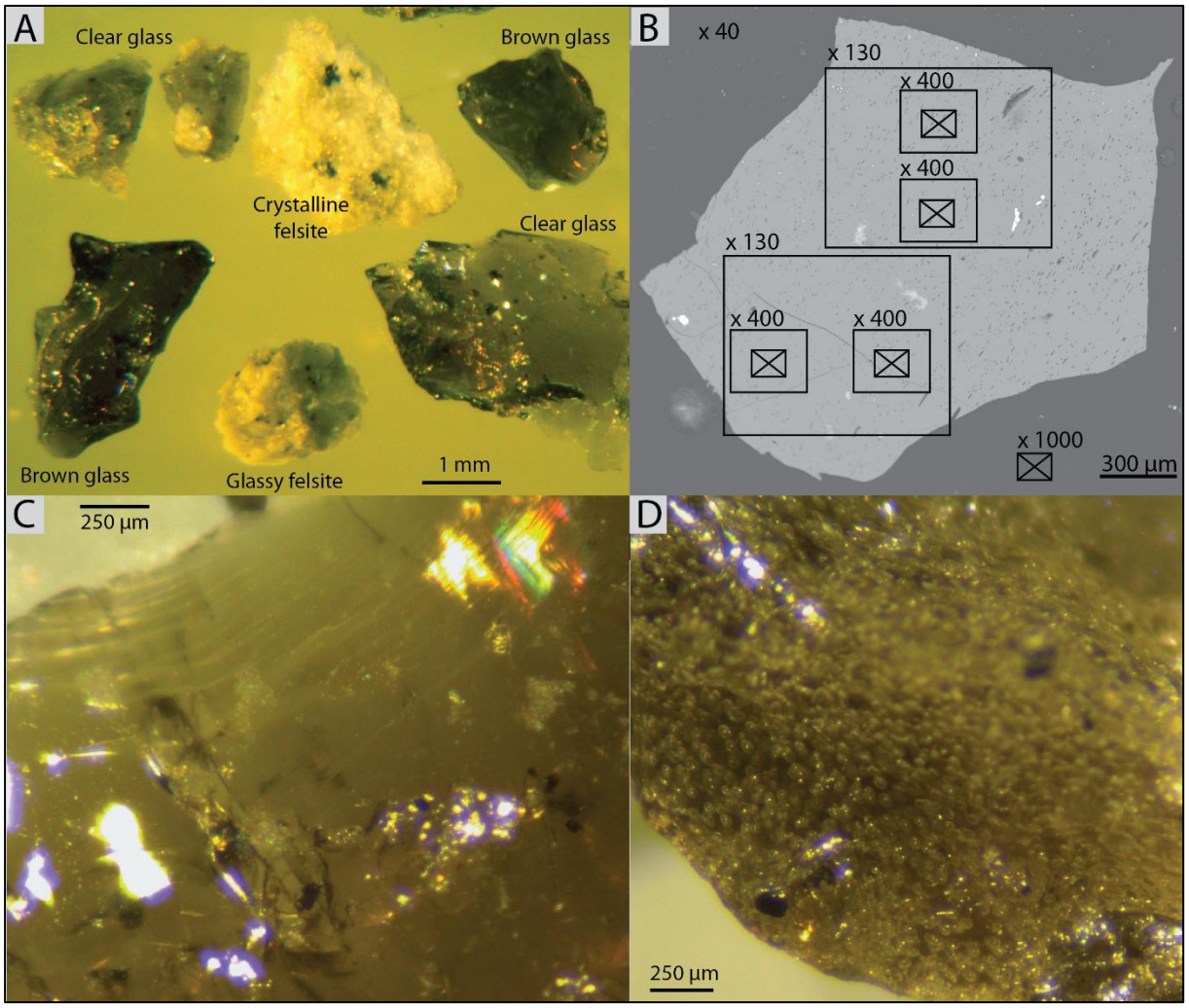

Figure 4.3. IDDP-1 cuttings. A) Particles from the 18.30 sample (1-2 mm size range). Shape parameters were calculated from similar pictures. B) Backscatter image of clear, vesicular glass (>3 % vesicularity) from the 18.00 sample. Methodology of image selection for FOAMS analyses: overview picture at x40 magnification, two areas x130, in which two zones are randomly selected at x400 and x1000. C) Brown, non-vesicular glass, 2-4 mm in diameter, from the 19.30 sample. D) Brown, vesicular glass (>3 % vesicularity), 2-4 mm in diameter, from the 17.00 sample.

Three-dimensional renderings of 9 clasts were reconstructed by x-ray tomography using a GE Phoenix Nanotom E laboratory scanner, operating at 80-90 kV and 120-250 nA, with a 0.1–0.2 mm thick aluminium filter to reduce beam hardening. These conditions resulted in a voxel edge length of 1.7-2.2 µm spatial resolution, determining the cubic voxel dimensions. The filter back projection reconstruction was performed using the GE proprietary software, and visual three-dimensional reconstruction was performed with the Drishti software. Samples imaged include

one clear glass, one brown glass, one crystalline felsite and one glassy felsite clast, for which the digital representations highlight the crystal phases, vesicles and shape of clasts (Supplementary Material). A part of the image stacks was used for crystallinity calculation with ImageJ – 3D object counter plugins according to the software's memory limitation (176 images for clear, brown glass and crystalline felsite, 145 for the glassy felsite). Quartz and feldspar were not readily discriminated from the glass background, so crystallinity calculations concern mafic phases only and will be referred to as mafic crystallinity, and do not represent the full crystal population.

Two sample sets were analysed separately for chemical compositions and isotopic ratios (Fig.4.2). Major elements and volatile species (S, F and Cl) were determined using electron probe micro-analysis (EPMA) with a JEOL JXA-8230 at VUW, at conditions of 15 kV and 8.0 nA. The beam was defocussed to give a beam diameter of 10 µm, with peak and background count times of 30 and 15 s, respectively. Natural and synthetic compounds (Jarosewich et al. 1980; Jochum et al., 2005) were used to calibrate the measurements, and analytical drift and reproducibility were checked by interspersing glass standard analyses among the sample measurements. These analyses were also performed on a third sample set previously used for volatile measurement (Watson, 2018). We conducted five spot analyses on each particle. Water contents and hydrogen isotope ratios were measured with a Thermal Conversion Elemental Analyser (TCEA-MAT253) at the University of Oregon. Analytical errors are ± 2 δD and ± 0.03 wt% H_2O (e.g. Martin et al. 2017; Hudak and Bindeman, 2018). All data is reported on VSMOW scale based on concurrently run standards both liquid waters and solid.

Independent glass particles from the 17:00 bulk sample were used to examine the origin of hydration, with thermogravimetric analysis (TGA-MS) conducted using a Netzsch STA449C Jupiter system at Lancaster University, hyphenated to a Hiden HPR20 mass spectrometer (Applegarth et al., 2013). Uncertainty on temperature is <2 °C. Powdered glass was heated to 1250 °C at 10 °C/min. The sample was then cooled to 25 °C at 10 °C/min and subjected to a second identical heating. The TGA curves presented in Supplementary Material (Fig.S4.2) are buoyancy corrected via subtraction of the second from the first heating segment (e.g. Applegarth et al., 2013), and dTGA curves are calculated from corrected TGA values.

4.4 Results

We separate the results into categories for the clear and brown glass, from big scale to smaller scale analyses (i.e. componentry to texture to chemistry), and relate them to the sample retrieval time where relevant.

4.4.1 Componentry

The proportion of glassy felsite (felsite with visibly high interstitial glass content) over the time series shows similar temporal variations to that of crystalline felsite (with no apparent interstitial glass). As both have felsitic texture, they are paired into a single, broad felsite category. Cutting componentry over the retrieval time (Fig.4.4) shows that glass accounts for almost 100 wt% of the retrieved cuttings over most of the time series (Fig.4.4A). However, the felsite content is higher during the first two hours (up to 70 wt%), with an abrupt decrease around 17:15, and the drilling contaminant portion increases at the end of retrieval up to 60 wt% after 23:00. Temporal variations in glass colour (clear, brown or black) are presented in Figure 4.4B, where brown glass is most abundant. The initially high clear glass proportion abruptly drops from ~45 to ~15 % (in number of particles) at around 17:15. Black glass forms an irregular and minor component throughout the whole series, and we thus dismiss it from further analysis. Up to 60 % of the glass is vesicular until 17:15, when poorly vesicular glass suddenly becomes predominant (Fig.4.4C); vesicular glass then constitutes <20 % of the distribution. The proportion of clear glass correlates with increasing vesicularity (Fig.4.4D), such that non-vesicular glass is mostly brown, whereas vesicular glass is mostly clear. Each observed texture (colour and range of vesicularity) is present within almost every time sample.

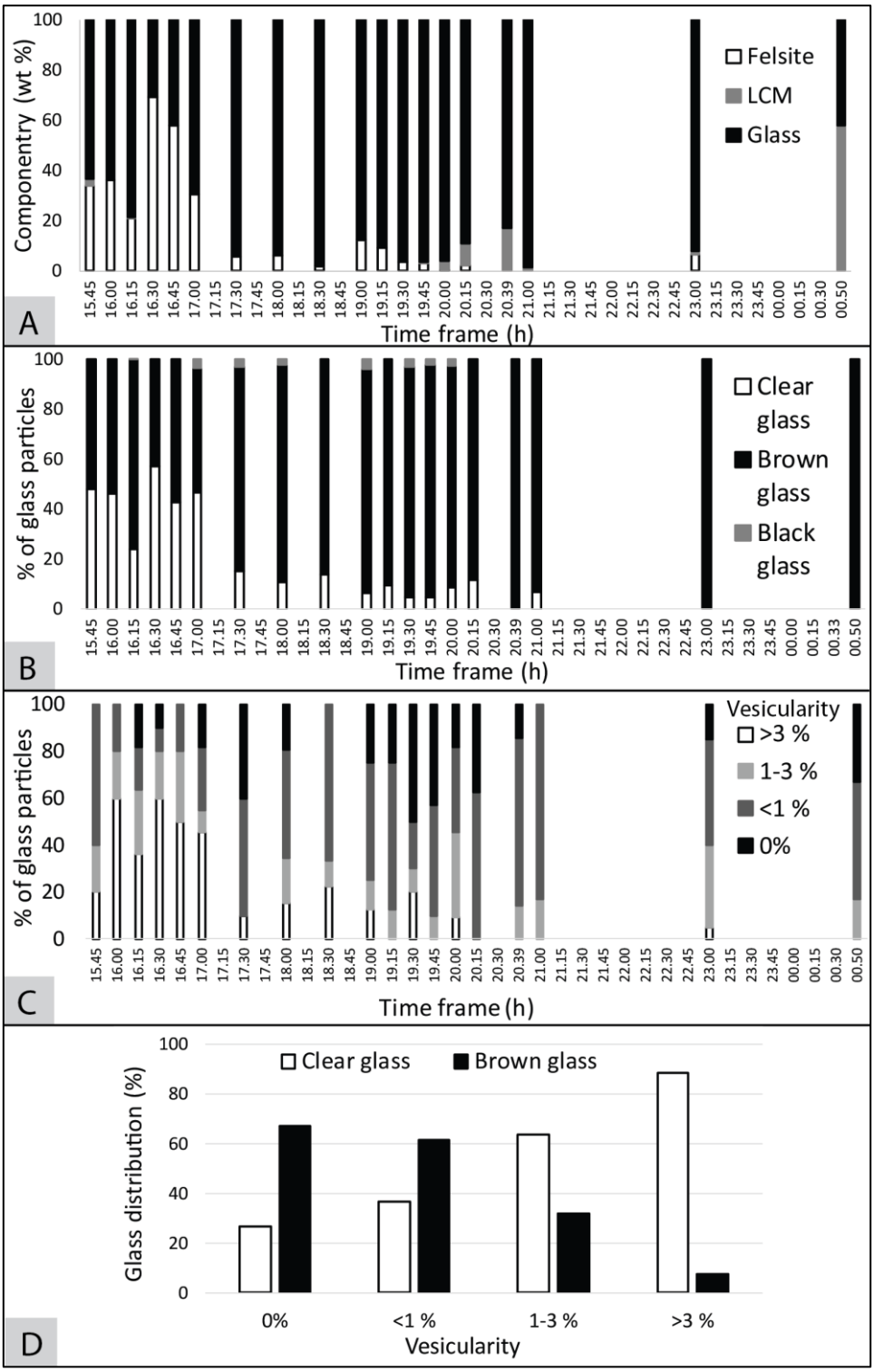

Figure 4.4. Componentry and textural variations in IDDP-1 cuttings. Time frames represent the absolute time of retrieval on 24 June 2009. A) Componentry evolution of glass, felsite and drilling contaminants over time of retrieval. B) Evolution of glass colour over time of retrieval, in % of glass particles. As the contribution from black glass is minor, this type of glass is not considered further. C) Variations of glass vesicularity over time of retrieval. D) Relationship between glass colour and vesicularity, illustrating the similarities in variations of particles over time between panels B and C.

4.4.2 Glass texture

Given the very low content in opaque minerals (<<1 area %), the mafic crystallinity is the highest in crystalline felsite (8.2 area %), and is greater in clear glass than brown glass (3 area % and 0.4 area %, respectively). Three-dimensional reconstruction of glass and felsite samples highlights textures and mafic crystal populations. The crystal phases are distributed as glomerocrystic patches in felsite and as individual crystals with remelted textures in brown glass. Clear glass contains both individual and crystal patches (Supplementary Material). Vesicle collapse textures (irregular convex and/or concave shapes, e.g. Kennedy et al., 2016; Rhodes et al., 2018; Fig.S4.3, Supplementary Material) are present in all sample types (clear, brown glass and glassy felsite), and most common in vesicular glass (>3 % vesicularity).

Size distributions of vesicle volume fraction for glassy felsite, clear and brown glass, before and after the componentry switch at ~17:15, are shown in Fig.4.5. The size distributions within individual particles (Supplementary Material) were sorted by glass colour and time range, and summed to obtain more statistically relevant vesicle size distributions (3 glassy felsite, 6 clear and 3 brown glass before 17:15; 4 clear and 9 brown glass after 17:15). The characterisation of profile shape uses the approach of Shea et al. (2010). The overall distributions of shapes are broadly similar for brown and clear glass, but diverge for different retrieval times. Vesicles in early-retrieved clear glass show a dominantly normal distribution centred at 7.4 μm (17.5 % volume fraction), typical of a single nucleation and growth event (Shea et al., 2010). In brown glass, the distribution is centred at 4.7 μm (14.5 %) and affected by secondary peaks. Both glass types contain slight increaset in larger vesicles that could relate to secondary processes (e.g. coalescence or Ostwald ripening during growth; Fig.4.5A; Shea et al., 2010). Glassy felsite has a similar vesicle population to the clear glass centred at 7.4 μm, but with a significant increase towards the larger sizes reflecting additional growth processes such as coalescence (Fig.S4.3B).

After 17:15, both glass vesicle size distributions flatten similarly (the maximal volume fraction decreases to ~12 %) and clear glass shows greater enrichment in larger vesicles, which is typical of coalescence (Shea et al., 2010) and similar to the shape of the vesicle size distribution for early-retrieved glassy felsite. Conversely, brown glass clasts show an increased proportion of small vesicles. Irregularities in the vesicle size distribution of brown glass are unlikely to be artefacts, given the large number of vesicles analysed (n = 1760), thus we suggest that individual peaks represent punctuated nucleation (i.e. each peak represents a nucleation event).

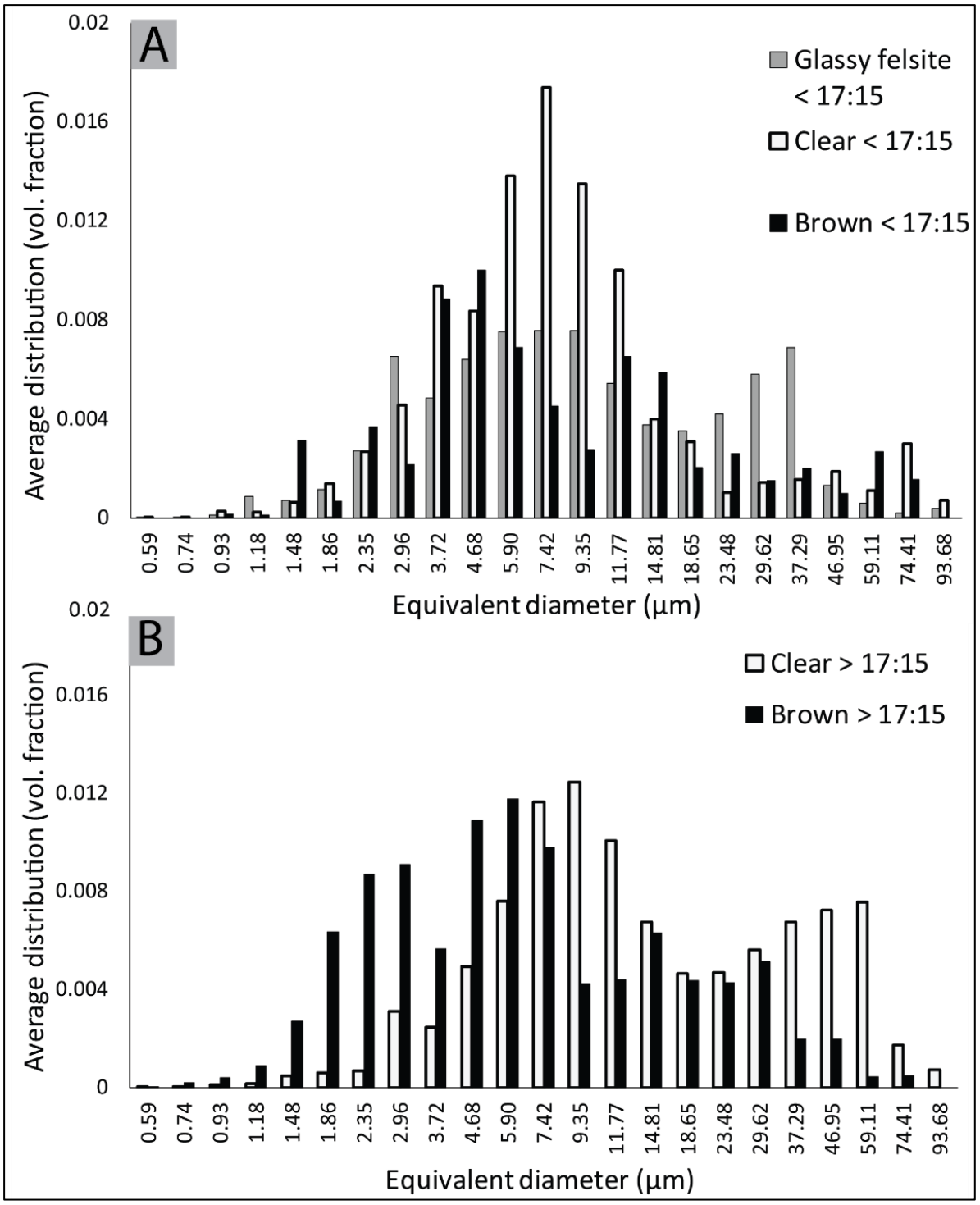

Figure 4.5. Vesicle volume fraction size distribution for glassy felsite, brown and clear glass, (A) before and (B) after the componentry transition around 17:15. The distributions are averaged to avoid any bias from the number of particles analysed.

4.4.3 Major elements

The average major element composition of the clear and brown glass (Fig.4.6; Supplementary Material) indicate that they represent two distinct melts. This is consistent with the findings of Zierenberg et al. (2013) and Masotta et al. (2018). K_2O/TiO_2 is near constant in brown glass and progressively increases in clear glass with increasing SiO_2 (Fig.4.6A). Other oxides exhibit relative compositional differences, with clear glass containing higher SiO_2 and brown glass higher FeO and MgO. Our data overlap with the data from previous studies of IDDP-1 for glass retrieved at 17:00, with each dataset classified slightly differently (Figs.4.6B, 6C). Zierenberg et al. (2013) divided the glass compositions into "Melt 1" (main glass component retrieved at 17:00), "Melt 2" (interstitial glass within felsite) and "Melt 3" (highly crystalline glass). In contrast, Masotta et al. (2018) distinguished between rhyolite glass (retrieved at 17:00, their "RHL") and interstitial glass composed of the two end-members representing >70 % and <8 % partial melting of felsite, which they termed "FLS1" and "FLS2", respectively. Here, we make our classification based on the dominant physical macro property of glass colour. The three respective main glass components consistently overlap (Melt 1, RHL and brown glass). Three of the 12 clear glass particles also fall within this main category and another three deviate from it, instead overlapping with FLS1. Melt 2 and a sub-section of FLS2 overlap, but we did not target the interstitial melt within felsite in this study. It is unclear if the wide range of composition shown by the clear glass represents its true variability or is caused by human subjectivity in colour classification. However, the dominant cluster in clear glass overlaps with Melt 3 and FLS2 (Fig.4.6B, 6C) and we consider it as representative of the clear glass group.

Figure 4.6. Major element chemistry (anhydrous) for brown and clear glass. A) K_2O/TiO_2 versus SiO_2. B) CaO versus SiO_2. Comparison with data from Zierenberg et al. 2013 (Melt 1, 2 and 3) and Masotta et al. 2018 (RHL, FLS1 and FLS2). Melt 1 is described as the main glass component. Melt 2 is interstitial glass within felsite and Melt 3 corresponds to highly crystalline glass, interpreted as mixing of Melt 1 and 2. In Masotta et al., RHL is the main glass component and FLS1 and FLS2 are compositional end-members of interstitial glass in felsite, which fit with experimental results of felsite partial melting at high and poor degrees, respectively. C) FeO versus MgO, with the same comparison to published data. We use convex hulls to enclose the clusters of previously published data points.

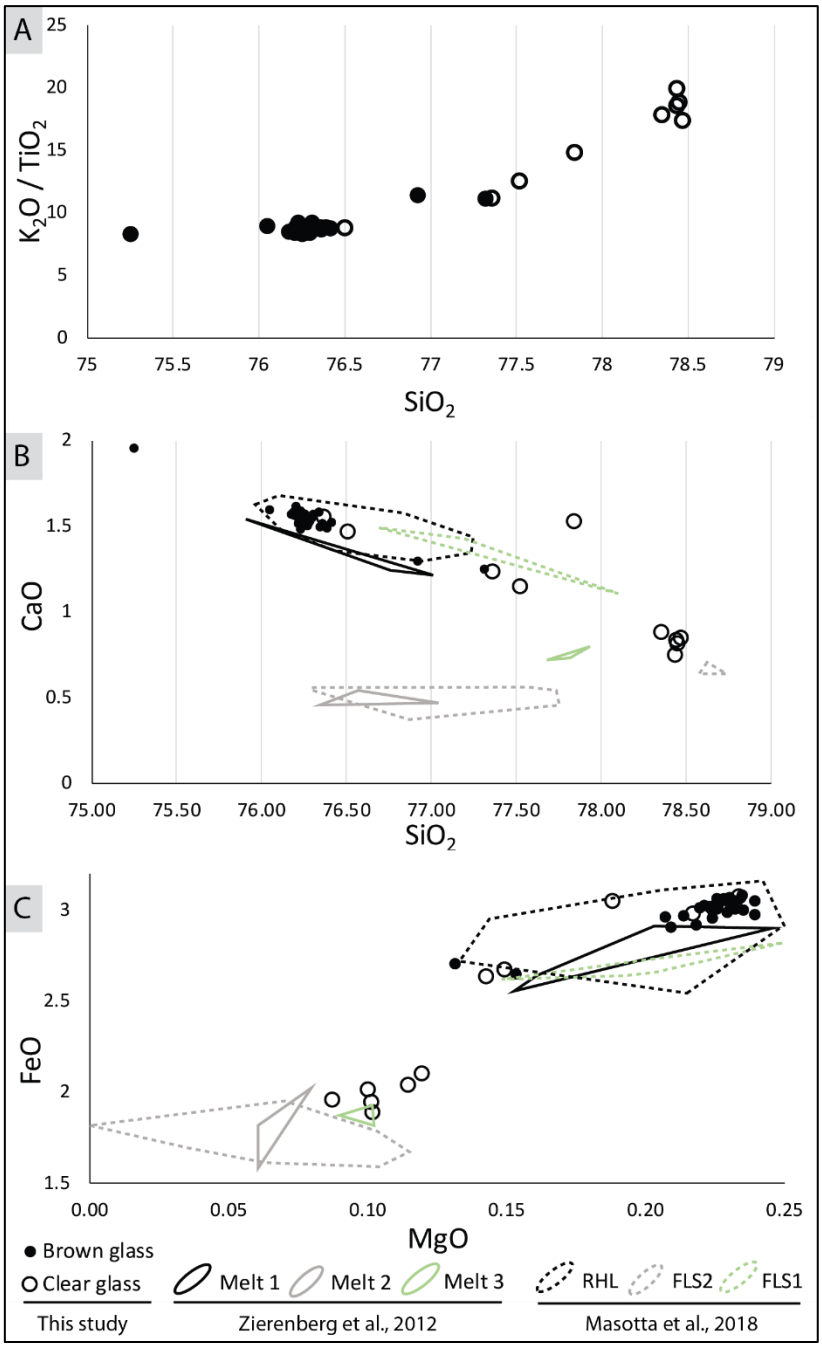

4.4.4 Glass water content and its isotopic values

The TGA heating experiments show predominant mass loss from 600– to 1000 °C (Fig.S4.2). This indicates that insignificant low-temperature hydration occurred (c.f. Denton et al., 2009; Giachetti et al., 2015), and thus the dissolved water is largely magmatic. The dTGA peaks (highest rates of mass loss) occur at 737 °C and 863 °C, matching the H_2O signal as determined by the mass spectrometer (Fig.S4.2), and confirming that dissolved H_2O>>CO_2 concentrations. Total water contents and hydrogen isotope ratios for clear and brown glass show no systematic variation with vesicularity or retrieval time (data provided in Supplementary Material). Water

contents fall within the range 1.3–2 wt %, with the interquartile range 1.64–1.92 wt% H_2O (Fig.4.7A), whereas δD values span a wide range from -120 to -80 ‰, with the interquartile range between -115 and -100 ‰ (Fig.4.7A). Note that we cannot directly compare the range of major element composition of clasts with their water concentrations, as different clasts were used for EPMA and TCEA analyses. Clear and brown glass have a slight but insignificant difference in both: averages of 1.73 and 1.81 wt % for H_2O, and -110 and -107 ‰ for δD, respectively (we used ANOVA statistic to test the null hypothesis that the two glass types are the same, on the basis of their water or deuterium compositions. Resulting p-values of 0.1 and 0.3, respectively, both being >0.05, do not allow the null hypothesis to be rejected). The water and isotope data distribution are scattered, but shows a decrease in δD with water content (Fig.4.7B). The clasts plot in between the trends defined by closed system volcanic degassing (Newman et al., 1988) and secondary hydration (i.e. meteoric water added to the melt after its formation, or to the glass; Seligman, 2016), on which Krafla epidotes also plot (Fig.4.7B). However, we note that the secondary hydration trend relates to hydration of already-quenched pristine glasses, whereas there is no evidence, from water speciation, for post-quenching hydration of clasts. Instead, we attribute low-δD values to pre-melting alteration of the source material or hydration during melting through fluxed hydrothermal fluids from altered mineral phases. Both $\delta^{18}O$ and δD values fall between those of unaltered magma and hydrothermally altered phases. $\delta^{18}O$ values in IDDP-1 glass are higher than in Krafla epidotes (Elders et al., 2011), whilst our data show on average ~10 ‰ higher δD than epidotes and ~40 ‰ lower δD than the unaltered mantle (MORB averages at -60 ‰ δD, Fig.4.7C).

Figure 4.7. Water content and hydrogen and oxygen isotope systematics in individual IDDP-1 glass particles, compared to different styles of degassing, hydration and known reservoir compositions. Analytical errors are ± 2 ‰ δD and ± 0.03 wt% H_2O. A) Box plots of H_2O and δD for clear and brown glass (label in B: black=brown) . Results show no relationship with vesicularity (Supplementary Material). B) δD as a function of H_2O. The degassing trends are the minimum values for rhyolite, with starting conditions at 3 wt% H_2O, 0.1 wt% CO_2, 500 bars (Newman et al., 1988); and the secondary hydration line corresponds to the trend for high latitude samples (Seligman, 2016). The initial unaltered rocks are represented by the MORB composition (values from Clog et al., 2013). C) Relationship between hydrogen and oxygen isotopes, adapted from Zakharov et al. (2019). Krafla data of epidotes, well fluid and estimated fluids composition are from Pope (2011). δD range values in IDDP-1 glass data (the dark section represents the interquartile range) are combined with $\delta^{18}O$ range from Elders et al. (2011).

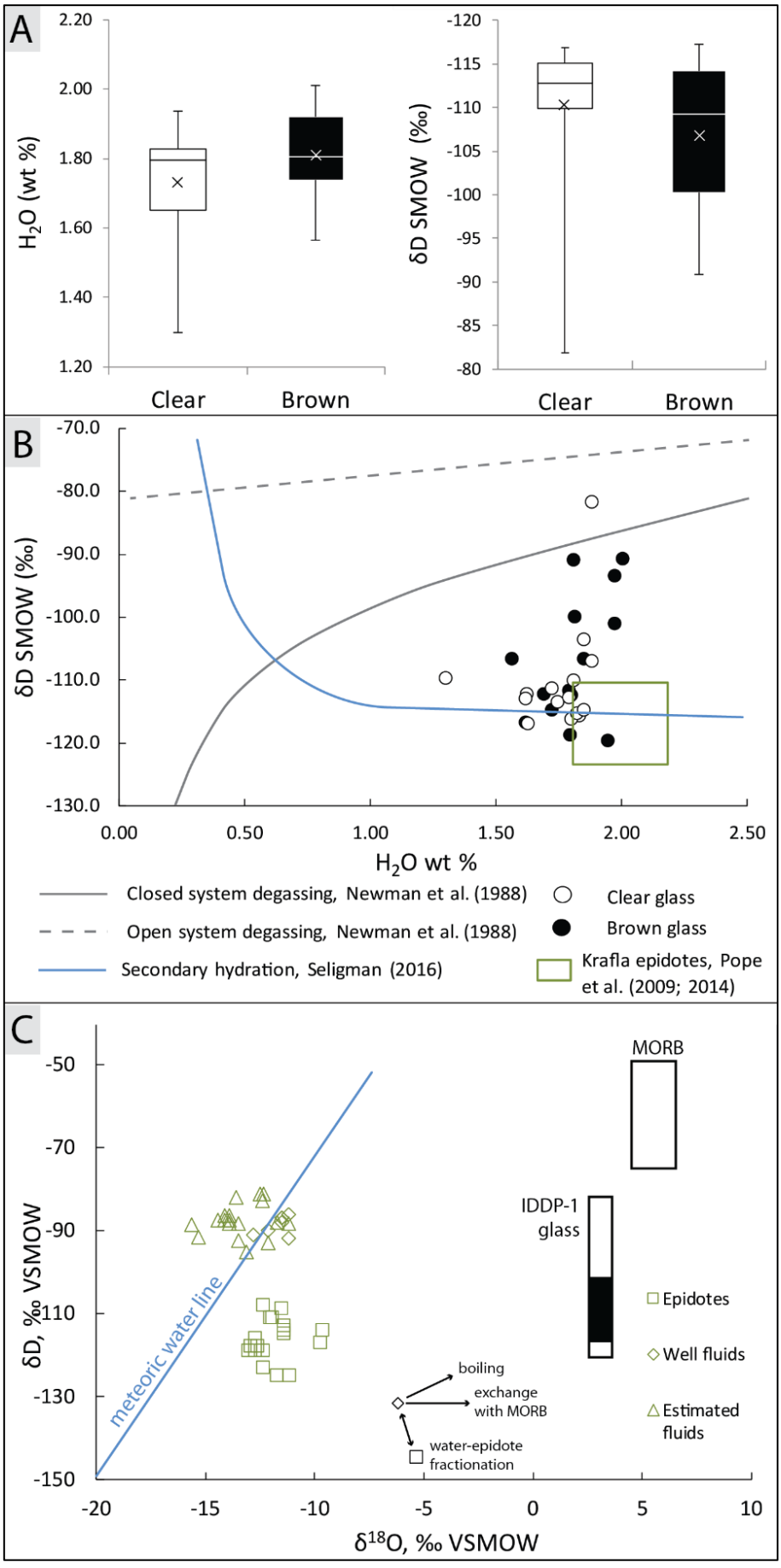
A
2.20
2.00
1.80
1.60
1.40
1.20
H2O (wt %)
Clear
Brown
-120
-115
-110
-105
-100
-95
-90
-85
-80
δD SMOW (‰)
Clear
Brown
B
-70.0
-80.0
-90.0
-100.0
-110.0
-120.0
-130.0
δD SMOW (‰)
0.00
0.50
1.00
1.50
2.00
2.50
H2O wt %
Closed system degassing, Newman et al. (1988)
Open system degassing, Newman et al. (1988)
Secondary hydration, Seligman (2016)
Clear glass
Brown glass
Krafla epidotes, Pope et al. (2009; 2014)
C
-50
-70
-90
-110
-130
-150
δD, ‰ VSMOW
-20
-15
-10
-5
0
5
10
δ18O, ‰ VSMOW
meteoric water line
MORB
IDDP-1 glass
Epidotes
Well fluids
Estimated fluids
boiling
exchange with MORB
water-epidote fractionation

4.5 Discussion

We interpret the time-series as a representation of the stratigraphic sequence at depth. Cuttings progressively accumulated at the bottom of the well while drilling, when circulation in drilling fluids was lost, to produce a sequence with the deeper drilled cuttings remaining beneath the shallower and older drilled cuttings. The rise of magma and the recovery of circulation would have then pushed up the particles, with the shallowest cuttings being the first to be retrieved. This is supported by the existence of a gradual change in componentry over time, starting with felsite country rock, meaning an order of retrieval is conserved. Geophysical data logs and shallower cuttings strongly support that felsite is the host rock (e.g. Mortensen et al., 2014). In addition, drilling difficulties present evidences that magma was hit at the bottom of the well and is the source of quenched rhyolite (ISOR, 2009; Friðleifsson et al., 2010). The cuttings would thus represent the host rock drilled prior to magma encounter, and magma quenched during the events of magma encounter and rising. The presence of various textures and particles type at any time suggest mixing of cuttings has also occurred (particles falling from the borehole walls, and/or dynamic mixing caused by fluids circulation), although a sequence is visible and dominant (Fig.4.4). Alternative scenarios for relating time recovery to the cuttings origin are still constrained to the same conclusion: the time-series of retrieval should be consistent with the conservation of a sequence in componentry, from felsite to deeper quenched rhyolite. Cuttings are therefore representing the lithologies at depth retrieved in the stratigraphic order.

The reason for fluids circulation retrieval after magma was hit the third time, but not occurring in the two first legs, is unclear. It may have been caused by the rise of magma which efficiently sealed the permeable borehole walls, or related to the decision to continue to drill ahead without cutting returns after a drilling delay, which allowed the driller to free the stuck drill string.

The results of this study are consistent with the presence of magma bimodal in both composition and texture. Both clear melt and felsite moved into the well and were subsequently flushed earlier than the brown melt. The clear melt has higher vesicularity, with vesicle size distributions that indicate a single dominant stage of nucleation and vesicle growth (using interpretations of vesicle size distributions from Shea, 2010), has a higher crystal and SiO_2 content. The brown melt comprises the majority of the cuttings, with vesicle populations indicating punctuated stages of vesicle nucleation and growth, and is crystal poor with higher FeO and MgO content.

The bimodal magma composition and texture can reflect genesis from two sources, or from one common source experiencing differentiation through fractional crystallisation, fractional melting or hydrothermal interaction. Previous geochemical data on IDDP-1 rhyolite glass support melt formation by partial melting of a felsite body that itself was derived from partial melting of hydrated basalt (Elders et al., 2011; Masotta et al., 2018). Our bimodal glass composition fits with these interpretations and these form the starting point for refining (1) how the magma was generated and (2) how it reacted to drilling.

In Table 4.1, we collate and critically appraise evidence for the alternative scenarios presented in Figure 4.8. Drilling may have affected the retrieved glass by triggering decompression-induced degassing, imparting stress that caused deformation, accompanied hydration affecting volatile chemistry, or filtering particles into a componentry that is not reflecting the initial melt distribution. In the following sections, we discuss the results according to the partial melting scenario, exploring the structure of the magma body and the timescale of the processes. Key observations and interpretations are summarized in Table 4.1, and the IDDP-1 intrusion is sketched in Figure 4.9 according to our conclusions.

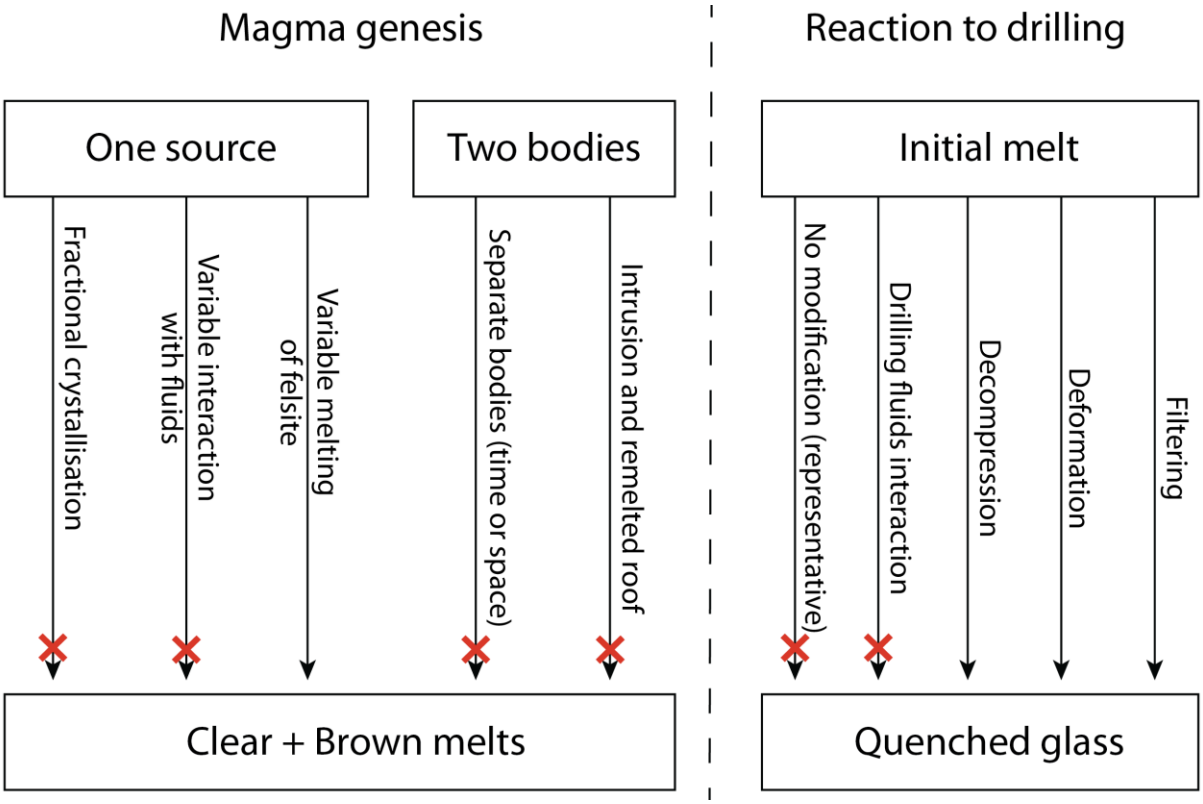

Figure 4.8. Processes involved in the genesis of bimodal melt and possible alteration processes caused by drilling. Our results refute (red cross) the occurrence of crystal fractionation, the presence of spatially separated melts, or an intrusion independent on the remelted roof, and strongly support the scenario of various degrees of felsite partial melting (one source). Results are concordant with melt reacting to drilling by decompression, deformation, and possibly limited filtering, but without alteration by drilling fluids.

TABLE 4.1. KEY OBSERVATIONS AND INTERPRETATIONS

Observation	Interpretation	Constraints on scenarios of Fig.4.8
Componentry:		
Clear glass retrieved simultaneously with felsite	Close spatial relationship between clear melt and felsite	
Brown glass retrieved later	Located at greater depth	
Crystals:		
Higher mafic crystallinity in clear glass, spatial distribution similar to that in felsite	Close spatial relationship between clear melt and felsite, favours assimilation or melting	
Vesicles:		
Higher vesicularity in clear glass	Clear glass experienced more degassing than brown	
Larger vesicles in clear glass as time progresses	Clear glass experienced more coalescence associated with magma ascent	Drilling-induced deformation
Smaller vesicles in brown glass as time progresses	Brown glass experienced more nucleation triggered by decompression, with higher initial water content	Drilling-induced decompression
Initial normal size distribution in clear glass	Homogenous melt, homogenous reaction to drilling, not interstitial melt	Only limited filtering through drilling
Secondary peaks in size distribution in brown glass	Punctuated nucleation or heterogenous melt	
Texture of vesicle collapse in >3 % vesicularity glass	Melts were vesicular and outgassing before interaction with the drilling	
Chemistry:		
Bimodal composition of interstitial melt	Bimodal heat distribution at the same location. Two discrete episodes of heat input.	Melts genesis separated in time
Brown glass chemistry is similar to high degree partial melting, conversely for clear glass	Brown melt represents almost complete partial melting of felsite. Clear melt formed by low degree of partial melting	
No decrease in alkaline elements with SiO_2 increase	No signature of fractional crystallisation	No genesis by fractional crystallisation
Progressive decrease in K_2O/TiO_2 with SiO_2 in clear glass	Early stage of felsite partial melting in clear melt	
Little variation in K_2O/TiO_2 in brown glass, progressive transition to clear glass	Later stage of partial melting in brown melt. Genetic relationship between clear and brown glass	No spatially independent melts
Volatiles:		
No second hydration peak in glass	No sub-Tg hydration by meteoric or drilling fluids.	No meteoric fluid hydration, no alteration by drilling fluids
δD slightly decreases with decreasing H_2O	Slight degassing	
Large range of δD values, plotting between MORB and epidotes	Mixing of magmatic water with water from hydrothermal minerals	

4.5.1 Structure and generation of intrusion

The three main observations from the data comparison with previously-published compositional datasets (Zierenberg et al., 2013; Masotta et al., 2018) (Figs.4.6B, 6C) are: (1) the composition of clear glass is close to that obtained from a small degree of felsite partial melting, and similar to crystal-rich glass bearing textures of felsite assimilation; (2) chemistry of the brown glass corresponds to higher degrees of felsite partial melting; and (3) interstitial glass in felsite contains a bimodal composition, together with an additional composition not found in individual glass chips. We conclude from the third observation that the bimodal mode of melting occurs at the same location, and thus likely required two discrete melting processes or pulses of heat flux: an initial higher- and then lower-temperature event. The resulting clear and brown melts segregated into layers or pockets whereas a last incipient melt was interstitially trapped in the parent felsite. If the interpretation of a layered structure is correct, then convection is unlikely, or minor.

K_2O/TiO_2, both incompatible, progressively changes between clear and brown melt rather than representing two distinct clusters, thus highlighting a genetic relation between the melts (Fig.4.6A). K_2O/TiO_2 decreases with silica in the clear melt, associated with increased TiO_2. Ti can be released by Ti-bearing mineral phases while K is diluted in the early stages of melting, and therefore fits the genetic model of partial melting of the felsite roof. A higher degree of partial melting for the brown melt accordingly results in little change in K_2O/TiO_2, as both being incompatible they behave similarly once they are diluted into the melt phase.

Melting of the largely anhydrous felsite (0.23 wt% LOI, Zierenberg et al., 2013) would not generate a melt with the water content as high as that measured in the rhyolitic glass (1.77 wt %) and thus the water in the rhyolite must have been added from another source. However, the TGA dehydration experiment shows no peaks associated with secondary hydration by meteoric water, as the measured patterns of volatile release indicate high-temperature diffusive loss of magmatic water (Denton et al., 2009; Giachetti et al., 2015; Fig.S4.2). High OH/H_2Om ratios similarly do not support secondary hydration (Zierenberg et al., 2013; Watson, 2018). The absence of secondary hydration also refutes the hypothesis that there was any significant post-quenching addition of drilling fluids (water) into the glass, especially considering the slow rate of water diffusion in rhyolite glass (~$9\text{-}12\times10^{-8}$ cm^2/s at 900 °C; Doremus, 1995). However, both the δD and $\delta^{18}O$ data are consistent with a hydrated source (Seligman and Bindeman, 2019). A basalt magma saturated in gas and underplating the felsite body could hydrate and promote fast felsite melting (Bachmann and Bergantz, 2006). But the broad range of δD,

covering epidotes and well fluids, suggests a hydrothermal origin of fluids. Their slight decrease with decreasing water content (~-30 ‰ for ~-0.4 wt % H_2O, Figs.4.7B, 7C) is best explained by fractionation restricted to an early stage of degassing. High δD water is lost during fractionation and thus close to the initial isotopic signature, which plots on the degassing trend (Fig.4.7B). However, the degassing gradient in the IDDP-1 data is steeper than that of mantle-derived rhyolite from Newman et al. (1988). An isotopic composition obtained from mixing magmatic water (-80 to -40 ‰ δD in 0.23 wt % H_2O in felsite; Elders et al., 2011) with water from hydrothermal minerals (-120 ‰ δD in epidotes, for 1.54 wt % additional H_2O; Fig.4.7B) could cause the steep observed fractionation trend. This agrees with the previous interpretation from Elders et al. (2011) who suggest basalt containing hydrous hydrothermal minerals is partially remelted, and dehydrated.

We propose that repetitive injection of basaltic magma in the shallow crust during the most recent eruptive activity (Krafla Fires, 1974–1985) could have promoted the release of low $\delta^{18}O$ and low δD fluids from alteration minerals that had developed via hydrothermal processes. These could have driven flux melting above the intruding basalts, at depths >2 km, similarly to that described by Bachmann and Bergantz (2006). Hydration of the IDDP-1 felsite would have enhanced a high degree of melting by lowering its liquidus temperature, leading to the generation of the brown melt (high-degree partial melting; Fig.4.9). The transition to a lower degree of melting could have been associated with a switch to felsite melting driven by the brown silicic melt itself, or by a sudden decrease in heat and fluid input from the underlying source. An alternative explanation involves only one phase of heat input, with progressive dehydration of the parental felsite and thus a decrease in the melt proportion. This, however, contradicts the higher δD values in brown glass that are closer to the "dry" closed-system degassing curve (Fig.4.7B), which is what would be expected of the low-proportion clear melt. Several models can be envisaged. For example, the brown melt could have intruded through the felsite and contacted virgin felsite (i.e. not melted yet) to trigger a second phase of lower-degree melting to form the clear melt. This agrees better with the transition in the glass composition, rather than a progressive change (Fig.4.6). Alternatively, felsite melting events could be modulating through the ingress of liberated magmatic and hydrothermal fluids from a deeper intrusion to fit our observations (Table 4.1). If volatile-saturated, the brown melt could have degassed with vesicles nucleating over several events, causing the decrease in δD as observed in our data. We conclude that an end-member scenario for the generation of the active

IDDP-1 rhyolite intrusion is remelting of felsite entirely caused by heat advection and hydration from hydrothermal fluids.

We examine the validity of the end-member scenario using a thermodynamic energy budget model for two end-member volumes of generated rhyolite magma: 1 km^3 and 100 m^3. We calculate the energy needed to generate this amount of magma, plus the quantity of fluids involved and the corresponding volume of deeper basalt magma that is required to crystallise for sufficient energy to be released. For simplification, we consider an adiabatic system and do not include calculation of energy loss during fluid flow from the deep basalt magma chamber and the shallower rhyolite magma.

We first estimate the quantity of fluids dissolved within the rhyolite melt. The host felsite containing 0.23 wt % LOI, assumed to represent the water content (Zierenberg et al., 2013), and the rhyolite melt 1.77 wt %, 1.54 wt % comes entirely from hydrothermal fluids. A rhyolite melt 1 km^3 in volume therefore requires a mass $M_R = 2.3\ 10^{12}$ kg of felsite plus $3.5\ 10^{10}$ kg of water, according to their respective density (Table 2). This corresponds to the absorption of 0.1 km^3 of hydrothermal fluids (for 100 m^3 of rhyolite melt, $M_R = 2.3\ 10^5$ kg, with ~9 m^3 of dissolved hydrothermal fluids).

The energy E_R required to increase the temperature of the mass M_R of felsite from its background temperature T_0 to the rhyolite magma temperature T_R, then to melt it, is calculated following the laws of thermodynamic:

$$E_R = Cp_R \Delta T_R M_R + L_R M_R \quad (1)$$

with Cp_R the specific heat capacity of felsite and L_R its latent heat of fusion. Substituing the values we have define for a 1 km^3 rhyolite intrusion (Table 4.2) in Eq.(1) gives $E_R = 1.8\ 10^{18}$ J ($E_R = 1.8\ 10^{11}$ J for 100 m^3 of rhyolite melt)

The heat and energy source are the fluids migrating upwards from the deep basalt magma chamber to the point of fusion in felsite. The energy E_W they provide mostly corresponds to the maximum energy lost when cooling from the temperature at the margins with basalt magma T_B to the temperature of liquidus of the felsite T_R. This must at least be equal to E_R, in order for the rhyolite body to be generated.

$$E_R = E_W = Cp_W \Delta T_W M_W \quad (2)$$

with Cp_W the specific heat capacity of the fluids. We can re-organise Eq.(2) to extract M_W, the mass of fluids involved in the heat transfer. Using the parameters for the 1 km^3 of rhyolite, M_W

= 1.9 10^{12} kg, corresponding to a volume of 19 km^3 according to the fluids density at T = 1000° C and P = 700 bar (M_W = 2 10^5 kg for 100 m^3 of rhyolite, thus 2000 m^3 of transferred fluids).

We assume that the hydrothermal fluids mostly have a meteoric origin and as such are not exsolved from the basalt magma. In the first instance, to heat this fluid mass from T_0 to T_B at the roof of the basalt magma chamber, the magma must crystallise to provide the required energy E_B as follows:

$$E_B = Cp_W \Delta T_B M_W = L_B M_B \quad (3)$$

with L_B the latent heat of crystallisation of a mass M_B of basalt melt. Eq.(3) thus provides the mass of basalt magma to crystallise, M_B = 9.1 10^{12} kg, which is equivalent to a volume of 3.5 km^3 to generate 1 km^3 of rhyolite (M_B = 9.6 10^5 kg, equivalent to 300 m^3, for generating 100 m^3 of rhyolite melt).

In summary, this energy budget assumes that to produce 1 km^3 of rhyolite melt, 19 km^3 of hydrothermal fluids at high pressure and temperature is required, a minor amount of which is incorporated into the melt. As the only source of heat, 3.5 km^3 of basalt magma has to crystallise. If we consider only 100 m^3 of rhyolite magma, 2000 m^3 of hydrothermal fluids need to circulate, with 300 m^3 of crystallising basalt magma.

Bodvarsson et al. (1984) provide an estimate of the average fluid flow through hydrothermal reservoirs at Krafla, 20 kg/s, with an average heat recharge from the main chamber of 2W/m². The fluid mass required in our model above could thus be transferred to the IDDP-1 reservoir in ~3000 years or ~3 hours, for 1 km^3 and 100 m^3 of rhyolite melt genesis respectively. Similarly, the required energy would be provided over >70,000 years or 350 years, respectively, at the roof of the basalt magma chamber through the same surface as the generated rhyolite body, simply assuming a cubic geometry. These values are underestimates, mostly because of the simplification related to assuming an adiabatic system (loss of energy during fluid transfer, and loss of heat from the roof of the rhyolite intrusion, are neglected), but also due to the fluid flow process between the two magma bodies, which is not captured in this model. Given the unstable conditions in geothermal systems, which are highly sensitive to changes in magmatic storage such as eruptive or intrusive episodes, the calculated timescales are too long to make the model realistic. The volume of basalt magma required to crystallise is another limitation: the volume of the main Krafla reservoir is unknown, but its thickness is estimated to be <2 km (e.g. Brandsdottír et al., 1997). This strongly refutes the model as providing a realistic

mechanism to generate large rhyolite magma bodies, since they require 3.5 km^3 of basaltic magma to crystallise.

We conclude that partial melting of felsite at Krafla, if uniquely triggered by transfer of heat and fluids through the hydrothermal system, is unlikely to generate a large enough volume of rhyolite melt, being mostly limited by the timescale of processes. As a result, alternative scenarios consider (1) the existence of an old rhyolite reservoir located at the margins of the main basalt magma chamber, formed by partial melting of the basalt host rock (Marsh et al., 1991; Winslow et al., 2019). this would source an intrusive system of shallow rhyolitic intrusions, which crystalise into felsite. (2) A shallow intrusion of basalt into the host felsite could trigger felsite remelting and generation of rhyolite at its margins. (3) Rhyolite melt could episodically intrude its own fossil felsitic component, with similar remelting consequence. Intense remelting at the margins (brown melt), could abruptly decrease in intensity (generating the clear melt) with magma flow, or with cooling from an emplacement temperature > 900° C to the residence temperature ~900° C (Fig.9). The hydrothermal system could still contribute to felsite remelting, through hydration of the intruding basalt or rhyolite melt, in turn hydrating the host felsite. These scenarios of IDDP-1 rhyolite melt genesis are illustrted in Figure 4.9.

TABLE 4.2. PARAMETERS USED IN CALCULATION

Density of rhyolite magma	ρ_R	2300	kg / m^3	Axelsson et al., 2014; Lesher and Spera, 2015
Density of basalt magma	ρ_B	2600	kg / m^3	Lesher and Spera, 2015
Density of fluids at supercritical conditions	ρ_W	100	kg / m^3	Ingebritsen et al., 2016
Water content in rhyolite magma	w	1.77	wt %	This study; Elders et al., 2011
Temperature of rhyolite magma	T_R	900	°C	Elders et al., 2011
Temperature of host rock	T_0	400	°C	Axelsson et al., 2014
Temperature of basalt magma	T_B	1200	°C	Approximate
Latent heat of melting for rhyolite	L_R	$3\ 10^5$	J / kg	Lesher and Spera, 2015
Latent heat of crystallisation for basalt	L_B	$5\ 10^5$	J / kg	Lesher and Spera, 2015
Specific heat capacity of solid rhyolite	Cp_R	1000	J / kg / °C	Hartlieb et al., 2015, Annen et al., 2017
Specific heat capacity of fluids near supercritical conditions	Cp_W	3000	J / kg / °C	Axelsson et al., 2014

4.5.2 Timescale of degassing

It is debatable whether the drill directly intersected a pocket of melt or instead intersected a melt distributed within mushy interstices (Eichelberger et al., 2017; c.f. Holness, 2018). The evolution of drilling parameters indicates an encounter with a ductile, weak lithology (Fig.S4.1; Pálsson et al., 2014), which could be a magmatic melt pocket, a partially-molten felsite, or a highly fractured/altered rock (Mordensky et al., 2019). During the ~45-60 minute interval between interception of the ductile layer and the rise of magma into the well (Fig.S4.1), the pressure differential between the drilling fluids (water) and the ambient downhole environment (between lithostatic and hydrostatic pressure) could have drawn magma from further away, before causing the magma to rise. However, we observe that a component in the interstitial glass composition previously recorded is absent from individual glass clasts (Melt 2, Zierenberg et al., 2013; a sub-set of FLS2, Masotta et al., 2018; Fig.4.6). This observation does not support an efficient draw-out of interstitial melt, as it is not sampled in its totality in the same way that the clear and brown glasses were. Additionally, it is worth emphasizing that the predominance of the brown glass and the relative scarcity of felsite, and the high melt viscosity, implies that it would be difficult for flow to occur through restricted interstices. We therefore assume that the drill either reached a melt pocket or was extremely close to one. The intrusion is sketched in Figure 4.8 according to our favoured hypotheses.

The felsite and clear melt have similar crystal clusters and textures, and the clear melt has generally higher crystal content compared to the brown melt (Videos in Supplementary Material), which supports a close spatial and genetic relationship between clear melt and felsite. The componentry is additional evidence for this clear melt/felsite relationship. The transition around 17:15 (Fig.4.4) suggests a shift from (1) retrieval of similar quantities of magma and host felsite, to (2) retrieval of poorly-vesicular brown melt, with minor and similar contributions of felsite and clear glass. We interpret that the clear melt is stored at shallower levels than the brown melt, and could have formed the roof layer of the melt pocket. Thus, the shift in componentry could relate to the disruption of the partially-melted roof of the brown melt pocket (Fig.4.9).

The vesicle size distributions in the glass represent the vesicle populations in the melt at the time of quenching. We assume that quenching induced by drilling fluids was rapid enough to prevent significant water resorption and bubble shrinkage (McIntosh et al., 2014). The normal profile distribution in early-retrieved clear glass supports a single degassing event (Shea et al., 2010) of what we interpret as a homogenous melt stored within a discrete magma pocket, rather

than spread within interstitial space. In brown glass, the distribution features secondary peaks that indicate punctuated nucleation (Shea et al., 2010). The appearance of a new small vesicle population in brown glass after 17:15 suggests that its nucleation was triggered by a step of drilling-induced decompression, which should have occurred after the nucleation and volatile resorption/outgassing of the main vesicle populations within this melt (Fig.4.5). In clear glass, the distribution features an increase in large vesicles after 17:15, indicating secondary growth processes that we propose being mostly coalescence, based on the distribution and the textural evidence in thin section (Fig.S4.3B; Shea et al., 2010). Magma deformation associated with shear stress during drilling-induced magma movement can favour local coalescence even in poorly vesicular and viscous melts (Okumura et al., 2006; Okumura et al., 2009; Carrichi et al., 2011). The rise of the magma into the well is likely to also cause an enrichment in larger vesicles by Ostwald ripening (Lautze et al., 2011). In addition, the vesicle size distribution in early-retrieved glassy felsite is similar to that of the clear glass retrieved after 17:15, with a dominant single stage of nucleation and growth, plus enrichment in larger sizes. It suggests a similar but earlier reaction in the felsite as that in the clear melt, and therefore that this zone was likely decompressed and quenched first, and probably located at a shallower depth - at the transition between felsite and clear melt.

We interpret that the changes in vesicle size distributions after 17:15 are dominantly drilling-related and affect both clear and brown glass, whereas distributions before 17:15 could be related to drilling-induced or natural decompression events. This could be one or both of the two previous magma interceptions (50 and 16 days before), or represent an initial vesicular magma state. The spatial variability in the multiplicity of decompression/nucleation events in shallow, heterogeneous systems is concordant with other studies conducted at similar textural detail (e.g. Saubin et al., 2016). The nature of the single nucleation peak indicates that it is unlikely the melt felt the decompression related to both the nearby previous magma interceptions.

Given constraints on the spatial relationship between the melts and their surroundings, we explore the timescale of degassing, which depends on the melt viscosity. The bubble number density corresponding to the smallest nucleated population in the brown melt is in the range $10^{14} – 10^{15}$ m-3 (vesicles <3 μm in diameter for 8 brown glass retrieved after 17:15). Using the bubble rate meter developed by Toramaru (2006) for explosive eruptions and homogeneous nucleation, we therefore estimate the maximum decompression rate of brown melt in the range $10^{7} – 10^{8}$ Pa s-1.

Here, using the glass compositions and water contents (Supplementary Material) in the silicate melt viscosity calculator of Giordano et al. (2008), we obtain viscosities of $10^{6.14}$ and $10^{5.95}$ Pa.s at 900 °C for clear and brown melts, respectively. 900°C represents the highest likely temperatures indicated by mineral geobarometry (Zierenberg et al., 2013) rather than quench temperatures (e.g. Watson et al., 2018). Crystals and vesicles are not included in the calculation and would modify the magma rheology, but their low proportion makes this effect negligible (e.g. Mader et al. 2013). Considering both decompression and cooling exerted by the drilling on magma, the timescale for vesicle growth, nucleation, coalescence or outgassing are reduced compared to that calculated from decompression only (Martel and Iacono-Marziano, 2015; Yoshimura et al., 2019). The maximum time frame of magma to react to drilling-induced decompression (Fig.S4.1) highlights a 45-60 minutes interval between the magma being intercepted and its ascent into the well, and a further maximum period of 3 h between magma ascent and the observation of the coalescence signature in the glass. We suggest that either of these intervals are sufficient to develop the full variety of vesicle textures observed in the clear and brown glass.

It is also useful to consider whether the recorded magma rise indicated in drilling parameters (9 m rise of magma in the well over ~4 min; Fig.S4.1) could be the driver of vesiculation. However, this rise corresponds to a minimum of 0.1 – 0.2 MPa of decompression for hydrostatic and lithostatic pressure, respectively (assuming a rock density of ~2500 kg/m3, Elders et al, 2011; Zierenberg et al, 2013). The calculated decompression rate during magma ascent in the well is therefore only $4\text{-}8*10^{2}$ Pa s^{-1} for magmastatic pressure, which is far lower than the maximum rate required to produce the nucleation observed in the brown glass. An intrusive pressure higher than the magmastatic could cause a few orders of magnitude increase in the calculated decompression rate, which would still be in the range triggering nucleation. Another calculation has been proposed by Eichelberger (2020) considering decompression from stored magma at lithostatic pressure to magma intercepted by the well at hydrostatic pressure (with a 400 m thick water column). This results in a higher pressure difference of 36 MPa. Considering the time interval of 9 mins between the last magma approach and the first evidence of magma response in drilling parameters, it corresponds to a minimal decompression rate of $6.7\ 10^{4}$ Pa s^{-1}, still allowing brown melt reaction to decompression by nucleation. However, if magma reaction is delayed by the presence of a plug at the interface, such as quenched magma, the decompression when magma breaks through could be near-instantaneous. This would limit vesiculation of magma, also with quick quenching at the immediate contact with cold drilling

fluids. The variation in bubble population over time of recovery (Fig.4.5) could in this case relate to stratigraphic heterogeneities in the melt prior to drilling-induced decompression. Such heterogeneities within rhyolite melts have been observed before (e.g. Saubin et al., 2016), but the net transition observed over time in bubbles population, and the interpretation of a homogeneous clear melt with a single stage of degassing, make the scenario of temporal evolution more likely. Quenching fragmentation of magma in the well could have slowed down magma ascent by abrupt release of overpressure, and following magma could thus have vesiculated before quenching, constituting the second set of particles (Fig.4.5).

We consequently propose that most of the vesicularity in intercepted melts was initiated prior to magma ascent into the well. The quick rise of magma could have had limited effect on degassing, with restricted bubble nucleation in the brown melt and bubble growth in the clear melt. The clear glass quenched earlier during this process only recorded the early phase of this decompression, whereas the brown glass took longer to quench and experienced a larger range of pressure conditions.

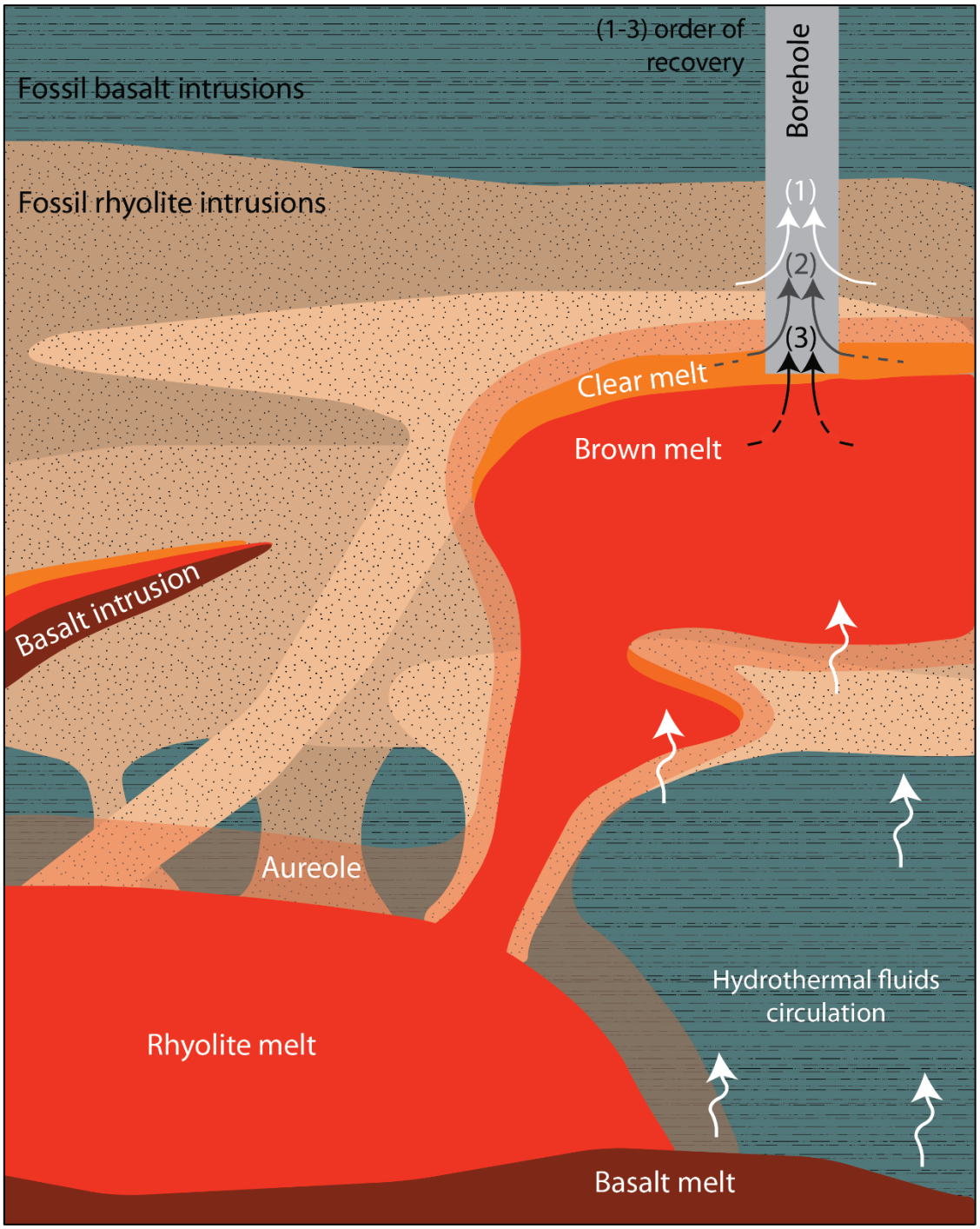

Figure 4.9. Schematic of IDDP-1 intrusion and well. Not to scale. The intrusion shape is not constrained. Heat and hydration from the main basalt magma chamber at 4 km depth triggers rhyolite genesis at the margins by partial melting of fossil basalt bodies. This rhyolite melt is the source of a network of silicic intrusions up to ~2300 m depth. These intrusions crystallise and form the cogenetic host felsite. Repeated pulses of fresh magma can emplace within, and trigger remelting of felsite at the margins, aided by hydration from the circulation of hydrothermal fluids. Intruding rhyolite magma incorporates the main cogenetic crystal-poor brown melt generated by high degree of felsite melting. This melt is saturated in volatiles and outgassing. Episodic variations in heat input, and local movement or propagation of the intrusion, causes a lower degree of melting at the margins, forming the vesicular clear melt that is SiO_2- and crystal-rich. Re-melting of host rocks prevents the formation of a chilled

margin. Also, the segregation of the melts indicates magma convection is unlikely, or minor, in opposition with the hypothesis favoured so far in literature (Eichelberger et al., 2017). Intrusion of basalt magma within felsite can trigger similar remelting and observations. When intercepted by the well, the host felsite was recovered, then the clear melt and eventually the brown melt (order of retrieval 1-3 on the figure). Decompression and melt deformation prior to quenching by drilling fluids triggered additional coalescence and nucleation. Low-degree melting at the margins is ongoing. Note that despite the scenario of IDDP-1 felsite remelting initiated by the intrusion of a rhyolite melt favoured in this sketch, the possibility of felsite remelting triggered by a basalt intrusion is likely as well.

4.5.3 Implications

A detailed characterisation of the textures, compositions and volatile species within IDDP-1 rhyolite yields new constraints on the scenario of partial melting and provides insights into magma genesis, storage and reaction to drilling. Drilling-induced decompression drove local vesicle nucleation and coalescence in the melts. Consistent with previous studies, the retrieved glasses are representative of quenching of a layer of clear melt at the magma chamber roof, at the transition to partially molten host felsite, which overlies a pocket of brown rhyolite melt. The clear melt formed from lower degrees of partial melting (temperature and proportion) than the brown melt. The approach of lower-pressure well conditions to the magma during drilling could have permitted limited degassing. In addition, the later stage of magma ascent within the well allowed vesicles in the clear melt to grow, deform and coalesce, whilst inducing nucleation in the deeper brown melt (Fig.4.9).

The numerous intrusions emplaced during the 1975-1984 Krafla Fires may have generated a number of secondary magma volumes such as that intercepted by IDDP-1. Other shallow silicic magma bodies at Krafla, for example the rhyolite erupted at Hrafntinnuhryggur (Tuffen and Castro, 2009) could have formed via similar processes, i.e. partial melting enhanced by hydrothermal hydration and triggered by the heat and magma released during a period of intense volcanic activity. Subsurface generation of rhyolite melt in active magmatic-hydrothermal systems could depend on similar system dynamics. This is a key process to consider for deep geothermal prospecting and volcanic hazard assessment; remelted rhyolite may infest the intrusive systems. In deeper and more water-rich systems, rhyolite can be generated directly at the margins of magma chambers (Marsh et al., 1991; Winslow et al., 2019). Importantly, the IDDP-1 rhyolite intrusion at Krafla does not appear to be crystallising at its roof; crystals with remelted margins suggest on-going partial melting, and it is surrounded by felsite containing a

high proportion of interstitial melt (glassy felsite). We conclude that the intrusion is at the very least maintaining its volume, and likely continuing to enlarge, with a low degree of partial melting of host felsite occurring at the margins. Its geothermal potential is therefore likely to continue to increase, and with its fast rate of heat recharge, the IDDP-1 intrusion could be exploited as a source of geothermal energy. Thorough understanding of the extent of the re-melting process and adequate geophysical detection of such shallow silicic intrusions are critical in the monitoring of restless calderas, and exploration of geothermal energy resources at magmatic intrusion margins.

4.6 Conclusion

The IDDP-1 geothermal well at Krafla is the most studied example of where drilling has intercepted subsurface magma. The development of plans to redrill the currently-capped well and re-intercept the magma (KMT project; Eichelberger, 2019) requires detailed knowledge of the magma genesis, storage and reaction to drilling. Here we have characterised the texture and chemistry of the cuttings retrieved at regular time intervals after magma interception. Our results support the model of rhyolite melt genesis via remelting of felsite, and provide a gamut of additional information. A wide range of evidence (componentry, vesicularity, crystallinity, magma chemistry) support a bimodal magma composition, segregated into clear and brown melt, and highlight the close relationship between the clear melt and the host felsite. Although textural types overlap, clear glass is generally more vesicular than brown glass (up to ~15 % in clear, <1 % in brown). A shift in componentry occurs two hours after the beginning of the retrieval, from ~50 % felsite, 25 % clear vesicular glass and 25 % poorly vesicular brown glass, to 10 % felsite, 10 % clear glass and 80 % brown glass. Accompanying this change in components, vesicle populations shift towards larger sizes in clear glass due to growth and coalescence. Smaller vesicle sizes in brown glass may relate to additional, punctuated nucleation, and reflect the decompression impact of drilling on the silicate melt pockets. K_2O/TiO_2 shows a genetic relationship between the melts, and clast compositions of IDDP-1 cuttings overlap with clusters from the literature. The large range of δD (-120 to -80 ‰ SMOW) indicates restricted degassing and fits with mixing of magmatic water from the felsite and water liberated from Krafla hydrothermal minerals.

We conclude that the encountered IDDP-1 magma was generated by two-step partial melting of felsite, occurring at the same location. The main heat source triggering the melting is likely to be an intrusion of rhyolite or basalt within the host felsite. Hydration from hydrothermal fluid circulation or hydrothermal minerals contributed to the remelting processes, although not by its own, and probably restricted to the genesis of the source magma. The melts were segregated into layers or pockets, indicating an absence of strong convective cells. The clear melt was formed from low degree partial melting at the margins and the main brown melt resulted from initial high degree partial melting. Melts experienced restricted degassing prior to the well interception and quenching. The drilling however triggered some decompression, and thus limited degassing and vesicle deformation.

The intrusion appears to be currently experiencing low degree melting of felsite at its margins, with no evidence of rapid crystallisation. It is therefore likely to be growing, and so offers increasing potential as a geothermal energy source. The IDDP-1 rhyolite magma is an example of re-melting triggered by intrusion into an active hydrothermal system, possibly common in caldera settings. Real-time monitoring of well-bottom conditions could inform its future impact on system dynamics and magmatic activity, and assist assessment of hazards associated with this type of intrusive process in calderas.

4.7. Acknowledgments

The authors thank the IDDP and Landsvirkjun for providing the raw samples. This work was supported by the Ministry of Business, Employment and Innovation, New Zealand [grant number E6552]; and a Royal Society University Research Fellowship to HT. IB thanks NSF grant EAR1822977 for support.

4.8. References

Annen, C., 2017. Factors affecting the thickness of thermal aureoles. rontiers in Earth Science 5, doi: 10.3389/feart.2017.00082

Applegarth, L. J., Tuffen, H., James, M. R., Pinkerton, H., 2013, Degassing-driven crystallisation in basalts. Earth-Science Reviews, 116, 1–16, doi: 10.1016/j.earscirev.2012.10.007

Ármannsson, H., Fridriksson, T., Gudfinnsson, G. H., Ólafsson, M., Óskarsson, F., Thorbjörnsson, D., 2014, IDDP—The chemistry of the IDDP-01 well fluids in relation to the geochemistry of the Krafla geothermal system. Geothermics, 49, 66–75, doi: 10.1016/j.geothermics.2013.08.005

Axelsson, G., Egilson, T., Gylfadóttir, S. S., 2014, Modelling of temperature conditions near the bottom of well IDDP-1 in Krafla, Northeast Iceland. Geothermics, 49, 49–57, doi: 10.1016/j.geothermics.2013.05.003

Bachmann, O., Bergantz, G. W., 2006, Gas percolation in upper-crustal silicic crystal mushes as a mechanism for upward heat advection and rejuvenation of near-solidus magma bodies. Journal of Volcanology and Geothermal Research, 149(1), 85–102, doi: 10.1016/j.jvolgeores.2005.06.002

Björnsson, A., 1985, Dynamics of crustal rifting in NE Iceland. Journal of Geophysical Research: Solid Earth, 90(B12), 10151–10162, doi: 10.1029/JB090iB12p10151

Bodvarsson, G. S., Pruess, K., Stefansson, V., Eliasson, E. T., 1984. The Krafla geothermal field, Iceland: 2. The natural state of the system. Water Resources Research, 20(11), 1531-1544

Bostick, N. H., Pawlewicz, M. J., 1984, Paleotemperatures based on vitrinite reflectance of shales and limestone in igneous dike aureoles in the Upper Cretaceous Pierre Shale, Walsenburg, Colorado.

Buckland, H. M., Eychenne, J., Rust, A. C., Cashman, K. V., 2018, Relating the physical properties of volcanic rocks to the characteristics of ash generated by experimental abrasion. Journal of Volcanology and Geothermal Research, 349, 335–350.

Büttner, R., Dellino, P., Volpe, L. L., Lorenz, V., Zimanowski, B., 2002, Thermohydraulic explosions in phreatomagmatic eruptions as evidenced by the comparison between pyroclasts and products from Molten Fuel Coolant Interaction experiments. Journal of Geophysical Research: Solid Earth, 107(B11), ECV 5-1-ECV 5-14, doi: 10.1029/2001JB000511

Caricchi, L., Pommier, A., Pistone, M., Castro, J., Burgisser, A., Perugini, D., 2011, Strain-induced magma degassing: insights from simple-shear experiments on bubble bearing melts. Bulletin of Volcanology, 73(9), 1245–1257, doi: 10.1007/s00445-011-0471-2

Castro, J. M., Bindeman, I. N., Tuffen, H., Ian Schipper, C., 2014, Explosive origin of silicic lava: Textural and δD-H2O evidence for pyroclastic degassing during rhyolite effusion. Earth and Planetary Science Letters, 405, 52–61, doi: 10.1016/j.epsl.2014.08.012Denton, J. S., Tuffen, H., Gilbert, J. S., Odling, N., 2009, The hydration and alteration of perlite and rhyolite. Journal of the Geological Society, 166(5), 895–904, doi: 10.1144/0016-76492008-007

Doremus, R. H., 1995, Diffusion of water in silica glass. Journal of Materials Research, 10(9), 2379–2389, doi: 10.1557/JMR.1995.2379

Eichelberger J., Carrigan, C., Sun, Y., Lavallée, Y., 2017, Why is there an abrupt transition from solid rock to low crystallinity magma in drilled magma bodies. AGU Fall Meeting Abstracts, NH11A-0097

Eichelberger, J., 2019. Magma: a journey to inner space. Eos, 100, 26-31.

Eichelberger, J., 2020. Distribution and transport of thermal energy within magma-hydrothermal systems. For peer review in Geosciences

Einarsson, P., 1978, S-wave shadows in the Krafla Caldera in NE-Iceland, evidence for a magma chamber in the crust. Bulletin Volcanologique, 41(3), 187–195, doi: 10.1007/BF02597222

Elders, W. A., Friðleifsson, G. Ó., Zierenberg, R. A., Pope, E. C., Mortensen, A. K., Guðmundsson, Á., Lowenstern, J. B., Marks, N., Owens, L., Bird, D. K;, Reed, M., Olsen, N;, Schiffman, P., 2011, Origin of a rhyolite that intruded a geothermal well while drilling at the Krafla volcano, Iceland. Geology, 39(3), 231–234, doi: 10.1130/G31393.1

Friðleifsson, G. Ó., Ármannsson, H., Guðmundsson, Á., Árnason, K., Mortensen, A. K., Pálsson, B., Einarsson, G. M., 2014. Site selection for the well IDDP-1 at Krafla. Geothermics, 49, 9-15

Friðleifsson, G. Ó., Elders, W., Bignall, G., 2013, A plan for a 5 km-deep borehole at Reykjanes, Iceland, into the root zone of a black smoker on land. Scientific Drilling, 16, 73–79, doi: 10.5194/sd-16-73-2013

Friðleifsson, G. Ó., Pálsson, B., Stefánsson, B., Albertsson, A., Gunnlaugsson, E., Ketilsson, J., Lamarche, R., Andersen, P., 2010, Iceland Deep Drilling Project. The first IDDP drill hole drilled and completed in 2009. Proceedings World Geothermal Congress.

Giachetti, T., Gonnermann, H. M., Gardner, J. E., Shea, T., Gouldstone, A., 2015, Discriminating secondary from magmatic water in rhyolitic matrix-glass of volcanic pyroclasts using thermogravimetric analysis. Geochimica et Cosmochimica Acta, 148, 457–476, doi: 10.1016/j.gca.2014.10.017

Hamada, M., Laporte, D., Cluzel, N., Koga, K. T., Kawamoto, T., 2010, Simulating bubble number density of rhyolitic pumices from Plinian eruptions: constraints from fast decompression experiments. Bulletin of Volcanology, 72(6), 735–746, doi: 10.1007/s00445-010-0353-z

Hartlieb, P., Toifl, M., Kuchar, F., Meisels, R., Antretter, T., 2015. Thermo-physical properties of selected hard rocks and their relation to microwave-assisted comminution. Minerals Engineering. Conference Physical Separation 15

Holness, M. B., 2018, Melt segregation from silicic crystal mushes: a critical appraisal of possible mechanisms and their microstructural record. Contributions to Mineralogy and Petrology, 173(6), 48, doi: 10.1007/s00410-018-1465-2

Ihinger, P. D., Zhang, Y., Stolper, E. M., 1999, The speciation of dissolved water in rhyolitic melt. Geochimica et Cosmochimica Acta, 63(21), 3567–3578, doi: 10.1016/S0016-7037(99)00277-X

Ingason, K., Kristjánsson, V., Einarsson, K., 2014, Design and development of the discharge system of IDDP-1. Geothermics, 49, 58–65, doi: 10.1016/j.geothermics.2013.05.002

Ingebritsen, S., Bergfeld, D., Clor, L., 2016, The Lassen hydrothermal system. American Mineralogist, 101, p 343-354, 2016, doi: 10.2138/am-2016-5456

ISOR Iceland geosurvey, 2009, IDDP-1 - Krafla, Vitismor - Production casing, drilling report no. 119Jochum, K. P., Nohl, U., Herwig, K., Lammel, E., Stoll, B., Hofmann, A. W., 2005, GeoReM: A New Geochemical Database for Reference Materials and Isotopic Standards. Geostandards and Geoanalytical Research, 29(3), 333–338, doi: 10.1111/j.1751-908X.2005.tb00904.x

Jónasson, K., 1994, Rhyolite volcanism in the Krafla central volcano, north-east Iceland. Bulletin of Volcanology, 56(6–7), 516–528, doi: 10.1007/BF00302832

Kennedy, B. M., Wadsworth, F. B., Vasseur, J., Ian Schipper, C., Mark Jellinek, A., von Aulock, F. W., Hess, K., Russel, K., Lavallée, Y., Nichols, A., Dingwell, D. B., 2016, Surface tension driven processes densify and retain permeability in magma and lava. Earth and Planetary Science Letters, 433, 116–124, doi: 10.1016/j.epsl.2015.10.031

Kennedy, B. M., Holohan, E. P., Stix, J., Gravley, D. M., Davidson, J. R. J., Cole, J. W., 2018, Magma plumbing beneath collapse caldera volcanic systems. Earth-Science Reviews, 177, 404–424, doi: 10.1016/j.earscirev.2017.12.002

Lautze, N. C., Sisson, T. W., Mangan, M. T., Grove, T. L., 2011, Segregating gas from melt: an experimental study of the Ostwald ripening of vapor bubbles in magmas. Contributions to Mineralogy and Petrology, 161(2), 331–347, doi: 10.1007/s00410-010-0535-x

Lesher C. E., Spera F. J., 2015. Thermodynamic and transport properties of silicate melts and magma. The encyclopedia of volcanoes

Mader, H. M., Llewellin, E. W., Mueller, S. P., 2013, The rheology of two-phase magmas: A review and analysis. Journal of Volcanology and Geothermal Research, 257, 135–158, doi: 10.1016/j.jvolgeores.2013.02.014

Marsh, B. D., Gunnarsson, B., Congdon, R., Carmody, R., 1991, Hawaiian basalt and Icelandic rhyolite: Indicators of differentiation and partial melting. Geologische Rundschau, 80(2), 481–510, doi: 10.1007/BF01829378

Martel, C., Iacono-Marziano, G., 2015, Timescales of bubble coalescence, outgassing, and foam collapse in decompressed rhyolitic melts. Earth and Planetary Science Letters, 412, 173–185, doi: 10.1016/j.epsl.2014.12.010

Martin E, Bindeman I.N., Balan E., Palandri J., Seligman A., Villemant B., 2017, Hydrogen isotope determination by TC/EA technique in application to volcanic glass as a window into secondary hydration. Journal of Volcanology and Geothermal Research, doi: 10.1016/j.jvolgeores.2017.10.013

Masotta, M., Mollo, S., Nazzari, M., Tecchiato, V., Scarlato, P., Papale, P., Bachmann, O., 2018, Crystallization and partial melting of rhyolite and felsite rocks at Krafla volcano: A

comparative approach based on mineral and glass chemistry of natural and experimental products. Chemical Geology, 483, 603–618, doi: 10.1016/j.chemgeo.2018.03.031

McIntosh, I. M., Llewellin, E. W., Humphreys, M. C. S., Nichols, A. R. L., Burgisser, A., Schipper, C. I., Larsen, J. F., 2014, Distribution of dissolved water in magmatic glass records growth and resorption of bubbles. Earth and Planetary Science Letters, 401, 1–11, doi: 10.1016/j.epsl.2014.05.037

Mordensky, S. P., Heap, M. J., Kennedy, B. M., Gilg, H. A., Villeneuve, M. C., Farquharson, J. I., Gravley, D. M., 2019, Influence of alteration on the mechanical behaviour and failure mode of andesite: implications for shallow seismicity and volcano monitoring. Bulletin of Volcanology, 81(8), 44, doi: 10.1007/s00445-019-1306-9

Morizumi, M., Nakashima, S., Okumura, S., Yamanoi, Y., 2009, Color-change processes of a plinian pumice and experimental constraints of color-change kinetics in air of an obsidian. Bulletin Volcanologique, 71, 1–13, doi: 10.1007/s00445-008-0202-5

Mortensen, A. K., Egilson, Gautason, B., Arnadottir, S., Gudmundsson, A., 2014, Stratigraphy, alteration mineralogy, permeability and temperature conditions of well IDDP-1, Krafla, NE-Iceland. Geothermics, 49, 31–41, doi: 10.1016/j.geothermics.2013.09.013

Mortensen, Anette K., Guðmundsson, Á., Steingrímsson, B., Sigmundsson, F., Axelsson, G., Ármannsson, H., Björnsson, H., Ágústsson, K., Sæmundsson, K., Ólafsson, M., Karlsdóttir, R., Halldórsdóttir, S., Hauksson, T., 2015, The Krafla conceptual Model Revision - Translation of Report LV-2009/111. In: Landsvirkjun report no. LV-2015-098

Newman, S., Epstein, S., Stolper, E., 1988, Water, carbon dioxide, and hydrogen isotopes in glasses from the ca. 1340 A.D. eruption of the Mono Craters, California: Constraints on degassing phenomena and initial volatile content. Journal of Volcanology and Geothermal Research, 35(1), 75–96, doi: 10.1016/0377-0273(88)90007-8

Okumura, S., Nakamura, M., Tsuchiyama, A., 2006, Shear-induced bubble coalescence in rhyolitic melts with low vesicularity. Geophysical Research Letters, 33(20), doi: 10.1029/2006GL027347

Okumura, S., Nakamura, M., Takeuchi, S., Tsuchiyama, A., Nakano, T., Uesugi, K., 2009, Magma deformation may induce non-explosive volcanism via degassing through bubble

networks. Earth and Planetary Science Letters, 281(3), 267–274, doi: 10.1016/j.epsl.2009.02.036

Pálsson, B., Hólmgeirsson, S., Guðmundsson, Á., Bóasson, H. Á., Ingason, K., Sverrisson, H., Thórhallsson, S., 2014, Drilling of the well IDDP-1. Geothermics, 49, 23–30, doi: 10.1016/j.geothermics.2013.08.010

Pope, E. C., 2011, Hydrogen and oxygen isotope fractionation in hydrous minerals as indicators of fluid source in modern and fossil metasomatic environments. Doctoral dissertation, Stanford University

Pope, E. C., Bird, D. K., Arnórsson, S., Fridriksson, T., Elders, W. A., Friðleifsson, G. O., 2009, Isotopic constraints on ice age fluids in active geothermal systems: Reykjanes, Iceland. Geochimica et Cosmochimica Acta, 73, 4468–4488, doi: 10.1016/j.gca.2009.03.033

Pope, E. C., Bird, D. K., Arnórsson, S., 2014, Stable isotopes of hydrothermal minerals as tracers for geothermal fluids in Iceland. Geothermics, 49, 99–110, doi: 10.1016/j.geothermics.2013.05.005

Rausch, J., Grobéty, B., Vonlanthen, P., 2015, Eifel maars: Quantitative shape characterization of juvenile ash particles (Eifel Volcanic Field, Germany). Journal of Volcanology and Geothermal Research, 291, 86–100, doi: 10.1016/j.jvolgeores.2014.11.008

Reiser, F., Schmelzbach, C., Sollberger, D., Maurer, H., Greenhalgh, S., Planke, S., Kästner, F., Flóvenz, Ó., Giese, R., Halldórsdóttir S., Hersir, G. P., 2018, Imaging the high-temperature geothermal field at Krafla using vertical seismic profiling. Journal of Volcanology and Geothermal Research, doi: 10.1016/j.jvolgeores.2018.10.019

Rhodes, E., Kennedy, B. M., Lavallée, Y., Hornby, A., Edwards, M., Chigna, G., 2018, Textural insights into the evolving lava dome cycles at santiaguito lava dome, Guatemala. Frontiers in Earth Science, 6, doi: 10.3389/feart.2018.00030

Rooyakkers, S. M., Stix, J., Berlo, K., Tuffen, H., 2017. Mafic spatter-rich and lava-like welded ignimbrites linked with collapse of a basaltic caldera: the Halarauður eruption, Krafla, Iceland. In AGU Fall Meeting Abstracts.

Rose, H. E., 1961, Particle shape and surface area. Powders in Industry, 130–149.

Rust, A. C., Manga, M., Cashman, K. V., 2003, Determining flow type, shear rate and shear stress in magmas from bubble shapes and orientations. Journal of Volcanology and Geothermal Research, 122(1–2), 111–132, doi: 10.1016/S0377-0273(02)00487

Sæmundsson, K., 1991, "Geology of the Krafla system (in Icelandic)." Náttúra Mývatns (The Natural History of Lake Mývatn). The Icelandic Natural History Society Reykjavík, 24-95.

Saubin, E., Tuffen, H., Gurioli, L., Owen, J., Castro, J. M., Berlo, K., McGowan, E., Schipper, C. I., Wehbe, K., 2016, Conduit dynamics in transitional rhyolitic activity recorded by tuffisite vein textures from the 2008–2009 Chaitén eruption. Frontiers in Earth Science, 4, doi: 10.3389/feart.2016.00059

Schiffman, P., Zierenberg, R. A., Mortensen, A. K., Frioleifsson, G. O., Elders, W. A., 2014, High temperature metamorphism in the conductive boundary layer adjacent to a rhyolite intrusion in the Krafla geothermal system, Iceland. Geothermics, 49, doi: 10.1016/j.geothermics.2012.11.002

Seligman, A. N., Bindeman, I. N., Watkins, J. M., Ross, A. M., 2016, Water in volcanic glass: From volcanic degassing to secondary hydration. Geochimica et Cosmochimica Acta, 191, 216–238, doi: 10.1016/j.gca.2016.07.010

Seligman A.N., Bindeman I.N., 2019, The δ18O of primary and secondary waters in hydrous volcanic glass. Journal of Volcanology and Geothermal Research. V. 371, 72-85.

Shea, T., Houghton, B. F., Gurioli, L., Cashman, K. V., Hammer, J. E., Hobden, B. J., 2010, Textural studies of vesicles in volcanic rocks: An integrated methodology. Journal of Volcanology and Geothermal Research, 190(3–4), 271–289, doi: 10.1016/j.jvolgeores.2009.12.003

Sparks, R. S. J., 1978, The dynamics of bubble formation and growth in magmas: A review and analysis. Journal of Volcanology and Geothermal Research, 3(1–2), 1–37, doi: 10.1016/0377-0273(78)90002-1

Taylor, B. E., Eichelberger, J. C., Westrich, H. R., 1983, Hydrogen isotopic evidence of rhyolitic magma degassing during shallow intrusion and eruption. Nature, 306, 541–545, doi: 10.1038/306541a0

Taylor, B. E., 2001, Hydrogen isotope composition of magmatic water: review of variations due to source, igneous environment, and degassing processes. AGU Spring Meeting Abstracts, V41C-01.

Tuffen, H., Castro, J. M., 2009, The emplacement of an obsidian dyke through thin ice: Hrafntinnuhryggur, Krafla Iceland. Journal of Volcanology and Geothermal Research, 185(4), 352–366, doi: 10.1016/j.jvolgeores.2008.10.021

Trewick, L., 2015, Vesiculation of rhyolite magma in the IDDP-1 borehole at Krafla, Iceland. MSc thesis, Lancaster University.

Watson, T., 2018, Evolution of magmatic volatiles during drilling into a magma body, Krafla, Iceland. MSc thesis, University of Canterbury, New Zealand

Winslow, H., Philipp, R., Helge, G., Patrick, P., Matthew, P., Francisco, D., Carolina, M., Alvaro, A., 2019, Exploring the role of mafic magmas and their volatile content during the 2011-12 Puyehue-Cordon Caulle eruption. AGU Fall Meeting Abstracts, V23D-0243.

Zakharov, D. O., Bindeman, I. N., Tanaka, R., Friðleifsson, G. O., Reed, M., Hampton, R. L., 2019, Triple oxygen isotope systematics as a tracer of fluids in the crust: A study from modern geothermal systems of Iceland. Chemical Geology. In press

Zhang, Y., 1999, H2O in rhyolitic glasses and melts: Measurement, speciation, solubility, and diffusion. Reviews of Geophysics, 37(4), 493–516, doi: 10.1029/1999RG900012

Zierenberg, R. A., Schiffman, P., Barfod, G. H., Lesher, C. E., Marks, N. E., Lowenstern, J. B., Mortensen, A., Pope, E. C., Bird, D. K., Reed, M. H., Friðleifsson, G., Elders, W. A., 2013, Composition and origin of rhyolite melt intersected by drilling in the Krafla geothermal field, Iceland. Contributions to Mineralogy and Petrology, 165(2), 327–347, doi: 10.1007/s00410-012-0811-z

Chapter 5 – A method to inform rock properties from drilling logs. Application to the IDDP-1 well

E. Saubin[1], M. Villeneuve[1], A. Mortensen[2], Ben Kennedy[1]

[1] *Department of Geological Sciences, University of Canterbury, Christchurch, New Zealand*

[2] *Landsvirkjun National Power Company of Iceland, Reykjavik*

5.1 Abstract

Supercritical fluids located at the roots of geothermal systems are new targets for geothermal exploitation, as they can provide greater power with greater extraction efficiency. These fluids are often circulating at the fractured margins of magma bodies, and drilling into these zones often causes a total loss of circulation in drilling fluids, which thus prevents cutting retrieval and insight into the geology of these critical formations. The only consistent indications about rocks encountered in these "blind zones" comes from monitoring the drilling parameters.

This chapter reviews the response of these parameters to rock properties encountered, their inter-dependence and the ways drillers influence the recorded data. We propose a method for interpreting rock properties from drilling logs only, and develop a chart of correspondence between lithology changes and variations in drilling parameters.

The method is applied to the IDDP-1 well, at Krafla, for which drilling difficulties and subsequent side-tracking occurred when approaching magma around 2100 m depth. It resulted in three vertical legs going through the same blind zone from ~2070 to 2100 m depth, thus offering three insights into this zone. When approaching magma, parameters fluctuate similarly for all three drilling attempts, highlighting a common signature recognisable for future drilling into this zone, and revealing that magma was approached 9 times over the three drilling attempts. Comparison between the three legs also highlights major and common variations through the blind zone. It reveals a ~14.5 m thick weak interval with high fracture density, likely enhanced by thermal contraction in response to the interaction with cold drilling fluids. These fluids are lost at the contact with this lithology, which is underlain by a ~8 m thick stronger rock mass, before strength progressively decreases towards the magma. The stronger zone is interpreted as the aureole in host rocks, impacted by the intrusion, less damaged by

drilling-induced undercooling. Using the relationship aureole/intrusion size observed in Chapter 3, we propose the IDDP-1 magma body to be between 700-1100 m thick.

The major variations in rock mass properties and lithologies through the blind zone overlying the IDDP-1 magma body are crucial for future drilling planned into the same interval, to adapt drilling technology and response to conditions at depth. The constraints on the intrusion dimensions highlights the importance of monitoring this large magma reservoir for safety, supports the existence of a long-lasting geothermal resource, and suggests it could have been generated earlier than the last eruptive activity at Krafla.

5.2 Introduction

Geothermal energy is reaching a turning point in the current search for renewable energy sources, with worldwide drilling exploration into the deep roots of geothermal systems. Challenging targets and concerns to be addressed are crossing the barriers of our knowledge, regarding drilling technology and geothermal reservoir behaviour.

The new targets for deep or hot drilling are the supercritical fluids found at high pressure and temperature (374 °C at 22.1 MPa for pure water; Bischoff and Rosenbauer, 1988), often located at the margins of magma chambers. Energy production from such fluids can yield one magnitude greater power than shallower, lower temperature wells (Friðleifsson and Elders, 2005). Fluids are extracted from feed zones, i.e. permeable rock masses with flowing hydrothermal fluids. However, drilling fluid circulation can be lost in these highly permeable zones, triggering drilling difficulties, preventing cuttings recovery and later affecting production efficiency. When the circulation loss is total, these intervals are called blind zones. For geothermal well operations, identifying feed zones and other high permeability zones is crucial for targeting the production intervals. Dealing with the common occurrence of blind zones therefore appears to be a critical challenge faced by geothermal drilling, as it is often encountered in conjunction with major feed zones. Drilling of geothermal wells commonly stops because of the encounter with such a problematic interval of highly permeable, fractured rock mass (Table 5.1; Reinsch et al. 2017), where the borehole responds poorly to sealing by cement, and circulation recovery attempts using lost circulation materials (LCM - a mixture of materials that are pumped into the well to fill in the fractures, such as walnut shells, fibrous material, cellophane flakes and diesel/bentonite; Azar and Samuel, 2007) rarely succeed. As a

result, tens to hundreds of meters of crucial geological formation are drilled without cuttings retrieval and therefore without direct insight into lithology at these depths. Because of their proximity to targeted reservoirs (e.g. Table 5.1), the rock masses within these blind zones are key for geological understanding of natural resource behaviour: rock mass properties at reservoir margins could inform their suitability for energy extraction, record the drilling impacts on the system and facilitate suitable technology improvement for future drilling, casing and energy extraction.

At the vicinity with magma in geothermal areas, host rocks are often of volcanic origin. Their storage and flow capacity for hydrothermal fluids depends on their porosity and thus permeability, which can vary widely. The primary control on the porosity are the macro-fractures, along with the important micro-fracturing (Lamur et al., 2017; Eggertsson et al., 2018). Local conditions impact the mechanical properties of the rocks, with increasing uniaxial compressive strength (UCS), tensile strength and Young's modulus associated with strain rate and rock temperature (Schaefer et al., 2015; Coats et al., 2018; Heap et al., 2018; Lavallée et al., 2018). But the strength of volcanic rocks also depends on their mineralogy, crystallinity and fabrics (e.g. Lavallée et al., 2020). This complexity can be simplified with the overview observation from experimental studies that rock strength commonly decreases with porosity increase (i.e. permeability; Schaefer et al., 2015; Coats et al., 2018; Harnett et al., 2019). Porosity also strongly influences the deformation regime of volcanic rocks, in particular the brittle/compact transition, with high porosity rocks favouring compacting behaviour (e.g. Siratovich et al., 2016; Saubin et al., 2019; Lavallée et al., 2020).

This chapter proposes a new method to inform and interpret rock mass properties in blind zones from drilling logs only, which can be the single available source of information in such situations. The correspondence of drilling parameters with in situ rock strength and porosity has been investigated in a few previous studies. Although it still lacks accuracy, the validity of this approach is supported by laboratory experimental data (Karasawa et al., 2002), comparison of logs interpretations with known lithologies or structures (e.g. sediments and faults; Ujiie et al., 2016; Hamada et al., 2018), and comparison with complementary downhole wireline data (e.g. Wolcott and Bordelon, 1993). However, most of the discussions are based on offshore drills, for environments encountered in the context of the oil and gas industry, and use methods requiring advanced understanding of drilling engineering (e.g. Teale, 1965; Hamada et al., 2018). Because the new challenges associated with deep drilling are creating closer collaborations between scientific communities, such as volcanology and geothermal energy

(e.g. Papale et al., 2020), this chapter aims to be understandable to non-driller scientists. Therefore, the aims of this chapter are to (1) review drilling parameters and their relationship to rock properties at depth, and use this to develop a method for interpreting blind zones. (2) Apply the method for interpreting the blind zone encountered by the IDDP-1 well above magma, and interpret the rock mass near the intrusion margins aided by observations and conclusions from Chapters 2, 3 and 4. Because knowing the size of magma reservoirs is critical to assess their potential in terms of geothermal exploitation, through information on the heat source, on the system's recovery time and geothermal fluids reservoir, the final aim (3) is to constrain the size of the IDDP-1 magma body. A list of acronyms is available at the end of the Chapter.

TABLE 5.1. WORLDWIDE ENCOUNTERS OF BLIND ZONES ABOVE TARGETED DEPTH

Borehole	Depth (m)	Blind zone interval (m)	Attempts to resolve the issue	Reference
IDDP-1 Krafla	2104.4	2075-2104	LCM	Hólmgeirsson et al., 2010
IDDP-2 Reykjanes	4500	3180-4500	12 cementing attempts and LCM	Friðleifsson et al., 2018
KG-25 Krafla	2105	2094-2105	None	Gudmundsson et al, 2008
KJ-39 Krafla	2865	2654-2865	Polymer pills to clean	Mortensen et al., 2010a
IID-14 USA	2073	2033-2073	n/a	Reinsch et al., 2017

Here, we focus on the case study of the IDDP-1 well drilled in 2009 at Krafla, in Iceland. This well aimed to reach supercritical conditions at the margins of the main basaltic magma chamber predicted to lie at ~4 km depth. The drill, however, hit an undetected rhyolite intrusion at ~2 km depth, after crossing a ~30 m thick blind zone (Friðleifsson et al., 2010). Geological units crossed by the IDDP-1 well are composed of basalt and dolerites above 2030 m depth and increasingly more felsite below. Patches of granophyric textures are found within the felsite and the terms granophyre and felsite are both used in literature and drilling reports to refer to this host rock. In this chapter, we will use the term felsite throughout for consistency. The absence of cuttings in the blind interval at 2070-2104 m depth means that the lithologies are unknown below 2070 m. It is, however, expected that felsic facies are the main constituent, as suggested by gamma ray logs over this interval (Mortensen et al., 2014). Drilling difficulties around 2100 m depth caused the drill to be stopped and side-tracked twice. On the 21st of April, the IDDP-1A drill bit reached 2102 m and became stuck. Retrieving it was unsuccessful. The bit was abandoned and a side-track was used for further drilling. On the 8th of June, the depth of 2103.4 m was reached by the IDDP-1B drill. The drill bit became stuck again and drillers proceeded to a second side-track. On the 24th of June, the IDDP-1C drill bit reached 2104.4 m

and was pushed up by magma before circulation returned, carrying cuttings of fresh glass and felsite (Pálsson et al., 2014). It is now known that these three events are related to the presence of magma at about 2100 m depth (Hólmgeirsson et al, 2010; Friðleifsson et al., 2010). Texture and chemical analyses conducted on the retrieved particles revealed a bimodal magma likely generated in-situ through two-step partial melting of felsite, initially itself generated from remelting of basalt (Elders et al., 2011; Masotta et al., 2018; Saubin et al., in review; Chapter 4). The intrusion margins are thus expected to be high-temperature felsite with a low-degree of interstitial partial melt, underlain by a layer of low crystallinity low-degree partial melt at the roof of the intrusion, and of a wider main body of low crystallinity magma beneath, generated by a high-degree of partial melting (Saubin et al., in review; Fig.4.9).

The IDDP-1 well was cased, completed and capable of producing at a high rate, before being plugged in 2012 because of a failure on the wellhead and subsequent damage on the casing (Ingason et al., 2014). Because the location of this intrusion is known, the Krafla Magma Testbed project is planning to re-drill into the intrusion for exploring, researching, and monitoring the geothermal potential (Eichelberger, 2019). In this context, in order to optimise drilling efficiency and suitably improve drilling technology, it is crucial to constrain the country rock properties above the targeted depth.

5.3 Usage of drilling parameters

In this section, we review the mechanics of geothermal drilling and describe the monitored drilling parameters. We highlight their response to geological variations and propose a method for interpreting drilling logs in terms of rock property and lithology. Geothermal drilling mechanics and processes are illustrated in Figure 5.1, with the name of the main drill parts constituting a drill rig and used in this chapter, and with the measurement location of drilling parameters.

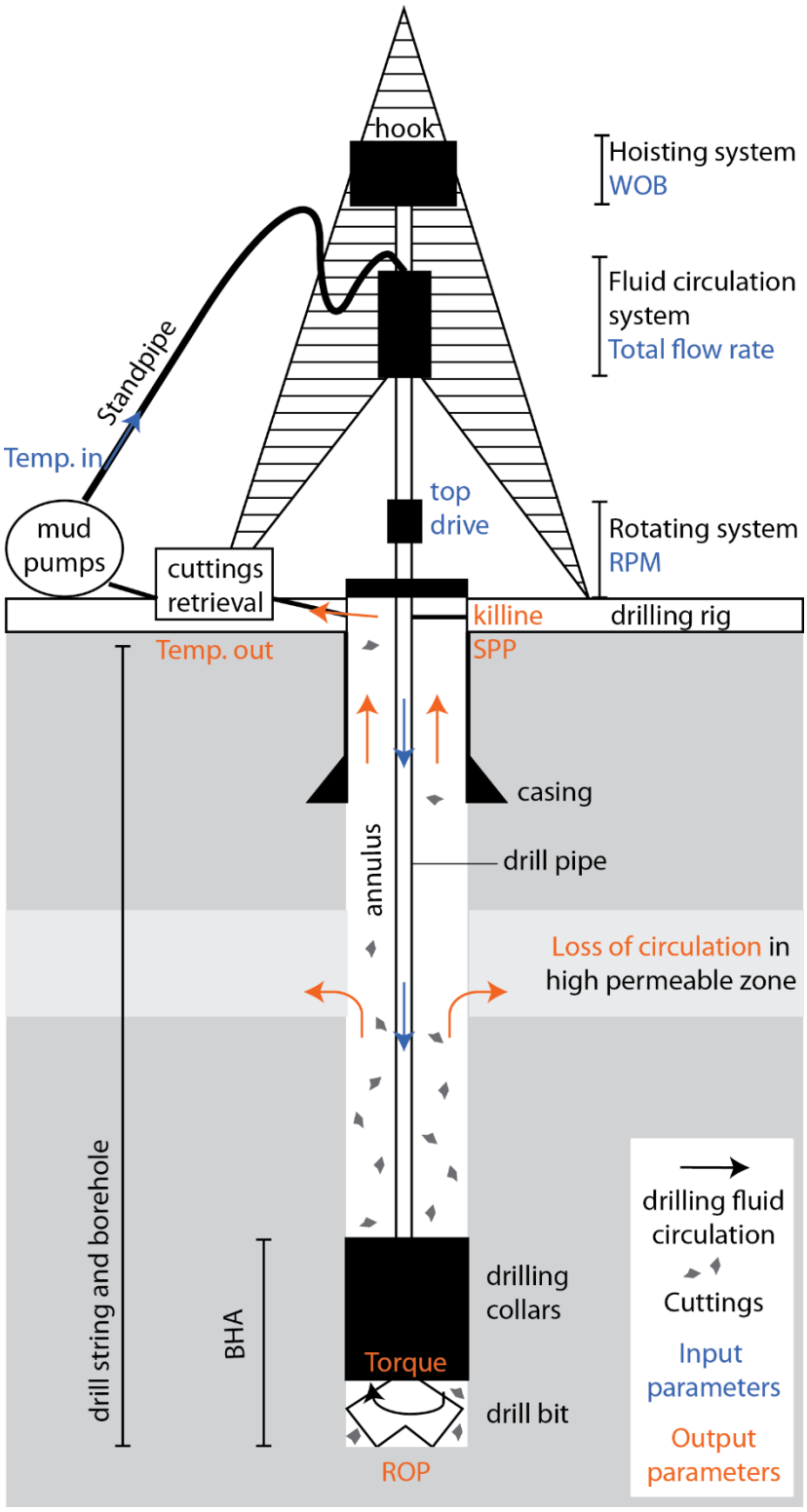

Figure 5.1. Geothermal drill rig. Drilling mud or fluids are sent into the drill pipe through the standpipe and come back to the surface through the annulus. The circulation and cuttings they carry can be lost in high permeable zones on their way up. The monitored parameters on which drillers can act directly are in blue, and the output parameters are in orange. WOB: weight on bit. RPM: revolution per minute. SPP: standpipe pressure. ROP: rate of penetration. BHA: bottom hole assembly.

5.3.1 Description of drilling parameters

A wide range of parameters are recorded during geothermal drilling, at a regular frequency such as 5 or 10 seconds (Archer et al., 2005; Millett et al., 2016; Wyering et al., 2017). This section reviews the drilling parameters related to drilling fluids (temperature, pressure, circulation loss, flow rate) and drill bit advance (rate of penetration, revolution per minute, torque, weight on bit) to develop interpretations of the subsurface. We describe their significance and measurement location, their inter-relationship and their sensitivity to rock properties. The depth of the bottom of the hole (MD) is measured from the drill rig deck, in meters (m).

The rate of penetration (ROP) of the drill bit into the rock at the bottom of the hole, in meters per hour (m/h), is a key parameter for identifying changes in rock mass properties. The main property affecting it is rock mass strength (e.g. Kahraman et al., 2003). It is generally accepted that the stronger the rock mass, the lower the ROP (Azar and Samuel, 2007). The rock mass strength partly depends on the effective confining pressure, i.e. the formation pressure relative to that of the drilling fluid pressure. An increasing formation pore pressure and/or decreasing drilling fluid pressure can cause ROP to gradually increase, with better drilling efficiency (Maurer, 1962), as the pressure difference could cause the rock to fragment into the borehole (Azar and Samuel, 2007). Regardless of formation pore pressure, initially fractured rocks are partially fragmented and thus also easier to drill (Nield, 1985). In addition, wide fractures or formations with high fracture density can make the drill bit drop in a similar way as into cavities, because the lack of resistance results in sudden increases in ROP. ROP can conversely decrease because of the presence of a denser or higher strength rock mass, increased effective confining pressure, or as a result of operational issues such as build-up of cuttings at the bottom of the hole, drill bit vibration, mud that is too heavy or wear on the drill bit. (Maurer, 1962; Azar and Samuel, 2007).

The rotary speed of the drill string, in revolution per minute (RPM), is one of the few parameters that can be controlled from the surface, together with the weight exerted on the bit (WOB), in tonnes (t). The WOB is the portion of the total weight of the drill string that is applied by the drill bit to the rock at the bottom of the hole and provides the force required to fragment it (Azar and Samuel, 2007). The remaining drill string weight is suspended by the drill rig and buoyancy in the drilling fluid. Highly variable WOB makes interpretation difficult, as it affects other parameters. Interpreting rock mass therefore requires either a constant WOB or applying corrections to affected parameters. For efficient drilling (higher ROP) in the same rock unit,

either higher WOB or higher RPM are needed. Typically, the stronger the rock, the higher the WOB required to maximise ROP (Azar and Samuel, 2007).

The torque applied by the drill rig to rotate the drill string, in decinewtonmetre (dNm), is influenced by the drill configuration and operation, such as hole size, depth, bottom hole assembly (BHA), drill pipe, RPM, type of the drill-bit and mud properties, as well as rock mass properties (Azar and Samuel, 2007). Typically, with constant WOB, a change in rock mass properties will cause ROP or torque or both to vary. The main factor affecting torque is the WOB (Warren, 1984). As torque is a function of forces opposing rotation (friction, shearing, abrasion at the drill bit/rock interface; Boghdady, 2010), an increase in WOB increases the friction resistance and often results in an increase in torque to maintain constant RPM. More porous (or weaker) rocks have lower resistance to rotation. But they may also result in deeper penetration of the drill bit, causing drag on the bit and increasing the friction, thus the torque. Poor clearing of cuttings from the annulus and bottom of the hole, or hole closure due to squeezing or instability can also lead to increasing torque (Azar and Samuel, 2007). We note that the torque can directly relate to rock properties when it is adequately corrected from friction between drill string and bit, drilling fluids and borehole walls. This requires careful calculation and knowledge of the drilling tools, and the resulting torque in studies using this approach does not represent the raw torque used in this chapter (e.g. Ujiie et al., 2016; Hamada et al., 2018).

In geothermal drilling, loss of circulation of drilling fluids into the rock mass, in litres per second (L/s), is considered total when a threshold is reached (50 L/s for conventional fluids as used in Iceland); the operations are then referred to as blind drilling (Azar and Samuel, 2007). Loss of circulation is a critical parameter in feed zone detection, as these highly permeable zones are favourable for fluid flow. Formations with a permeability of 10-100 Darcy (10^{-10} to 10^{-11} m^2) can result in total loss of circulation, when pressure of drilling fluids is higher than pore pressure (Datwani, 2012). This loss also depends on fluids pressure relative to pore pressure, and can occur at any depth along the borehole. It is therefore especially difficult to confidently interpret loss of circulation as permeable zones.

The standpipe pressure (SPP) is the available pump surface pressure (Azar and Samuel, 2007) and is measured where fluids enter the drill string, in bars (Chowdhury et al., 2009). The mud pump exerts pressure by pumping drilling fluids, and must overcome the friction between the fluid and the surface connections, drill pipe, drill collar, and annulus, as well as pressure loss across the drill bit (Azar and Samuel, 2007). SPP consequently reflects the pressure drop between the mud pump and the fluid at the bottom of the hole. Drilling fluid pressure has to be

high enough to effectively remove cuttings from the bottom of the hole, higher than pore pressure to prevent influx of formation fluid into the borehole, and lower than the rock mass tensile strength to prevent hydraulic fracturing and circulation losses (Azar and Samuel, 2007). If the drilling fluid pressure is too low, the fluid pressure can reach equilibrium with the pore pressure on the way up the annulus and cuttings may become blocked and unable to return to surface, again leading to loss of circulation. A sudden SPP increase can be related to an increase in mud weight, density or viscosity, which could be caused by an increase in ROP and thus in cuttings amount generated into the drilling mud. Similarly, a flux of water or gas from country rocks into the borehole can affect the drilling mud properties and in turn the SPP (e.g. Nield, 1985; Azar and Samuel, 2007; Chowdhury et al., 2009), and a loss of circulation through a fractured zone can be associated with a sudden SPP decrease (Chowdhury et al. 2009).

The temperature change of drilling fluids, in Celsius, is the difference between the fluid into and out of the well, and is related to temperature at depth. The temperature of fluids going into the well is typically < 30 °C. Temperature of fluids can increase in an over-pressured zone, where pore-pressure is higher than the drilling fluid pressure and hot hydrothermal fluids can flux into the well (e.g. Nield, 1985; Majidi et al, 2017). In geothermal reservoirs, this can be associated with feed zones.

The total flow rate of fluid sent into the hole, in litres per second (L/s), is calculated from the summation of flow rates through three pumps. It directly impacts SPP, and thus is worth monitoring. An increase in flow rate can indicate an influx of hydrothermal fluids (Azar and Samuel, 2007), whereas a decrease can indicate a loss of circulation.

The top drive is the motor used to rotate the drill string. Its height, measured from the drill rig, in meters (m), decreases during drilling, then increases when a new drill pipe is added to the drill string. This parameter gives an indication about drilling operations such as pulling out of hole (POOH) or tripping in, where the height of the top drive increases and decreases repeatedly. It also provides information about encountered problems such as sticking, where the height stays constant, or dropping into a void, where the height of the drive abruptly decreases. Importantly, the occurrence of a sudden change slightly before or slightly after a variation in the other drilling parameters can indicate whether the origin of that change is artificial or geological, respectively. In some cases, downhole motors driven by mud pumping are used rather than a top drive.

In addition to these drilling parameters, wireline data can also be recorded and consist of a large set of physical measurements (multi-armed caliper, temperature), imaging (downhole camera and acoustic log) and geophysical measurements (Gamma, Resistivity, Neutron, Seismic) not all of which are always used together. As the wireline data are not always available for geothermal wells nor for their full length, we base this study on drilling parameters only.

5.3.2 Rock-induced variations

There is no straight-forward correlation between drilling parameters and rock mass properties for geothermal reservoirs, although there are a number of methods for oil and gas reservoirs (as described in Azar and Samuel, 2007 and Wyering et al., 2017) and more recently in other crustal rocks (e.g. Ujiie, 2016; Hamada et al., 2018). This is because of the shorter history of drilling into, and the wide range of rock masses encountered in, geothermal reservoirs, compared to the 'simple' geology of conventional oil and gas reservoirs (typically sandstones, siltstones/shales and limestones). In addition, as highlighted in previous sections, the factors impacting these parameters are interdependent and complex, and are sometimes not related to the geology, but to drill string-wellbore interactions (friction), drilling fluid hydraulics, BHA including bit type, drill pipe assembly, length of drill collars, and position and types of stabilizers (non-exhaustive list). Yet, the drilling aspects targeted in this study are rock-bit interactions at the bottom of the well, rock mass strength and formation pore pressure. For the interpretation of raw drilling data, it is therefore critical to be aware of typical drilling performance to separate driller-induced from rock-induced variations. A change of BHA or drilling mud will, for instance, affect most parameters. Drilling operations reported in drilling reports consequently have to be carefully combined with raw data.

Many studies that use cuttings and drilling data to interpret the subsurface focus on ROP (e.g. Archer et al. 2005; Millett et al. 2016). Because the parameters are interrelated, and their response could be due to a number of geological or operational changes, simply using one parameter to interpret the rock mass may not provide the best interpretation. In order to facilitate these interpretations, we developed a visual chart in Figure 5.2 to identify lithologies from associated variations of main drilling parameters: ROP and Torque, with insight on WOB, RPM, SPP, circulation loss and fluid temperature. We consider four ranges of rock strength, two kinds of fractures, molten rock as well as permeability and the pressure of the formation relative to the borehole pressure.

Figure 5.2 illustrates that the most efficient geological scenario for drilling, with high rate of penetration and the lowest energy input, is a strong rock (Fig.5.2A, row 2). Very strong rocks would decrease ROP and increase torque (Fig.5.2A, row 1) and weaker rocks would increase both ROP and torque (Fig.5.2A, rows 3 and 4; Fig.5.4A). Weak rocks exert higher horizontal resistance to rotation because of the wider surface of the drill bit driven inside the formation. In the extreme case of a near-ductile interval, ROP will increase rapidly as the bit sinks into the rock, before nearly becoming stuck as the ductile rock traps it ("boot-into-the-mud" effect). When rocks are highly fractured, ROP and torque will tend to increase as a consequence of easier excavation and uneven bottom hole surface (Fig.5.2B). Fractures can make borehole walls less stable and increase the quantity of cuttings at the bottom, which would also increase the torque. ROP and torque may fluctuate as the bit encounters alternating intact rock and fractures (Ghosh et al., 2018; Fig.5.4B; 4C). In the case of a wide fracture or a cavity (Fig.5.2B), ROP will suddenly and temporarily increase, associated with a drop in torque and WOB. Because fractured zones or cavities are often unexpected and have a sudden transition, the change in WOB does not result from driller's adjustment but is the direct effect of the rock mass.

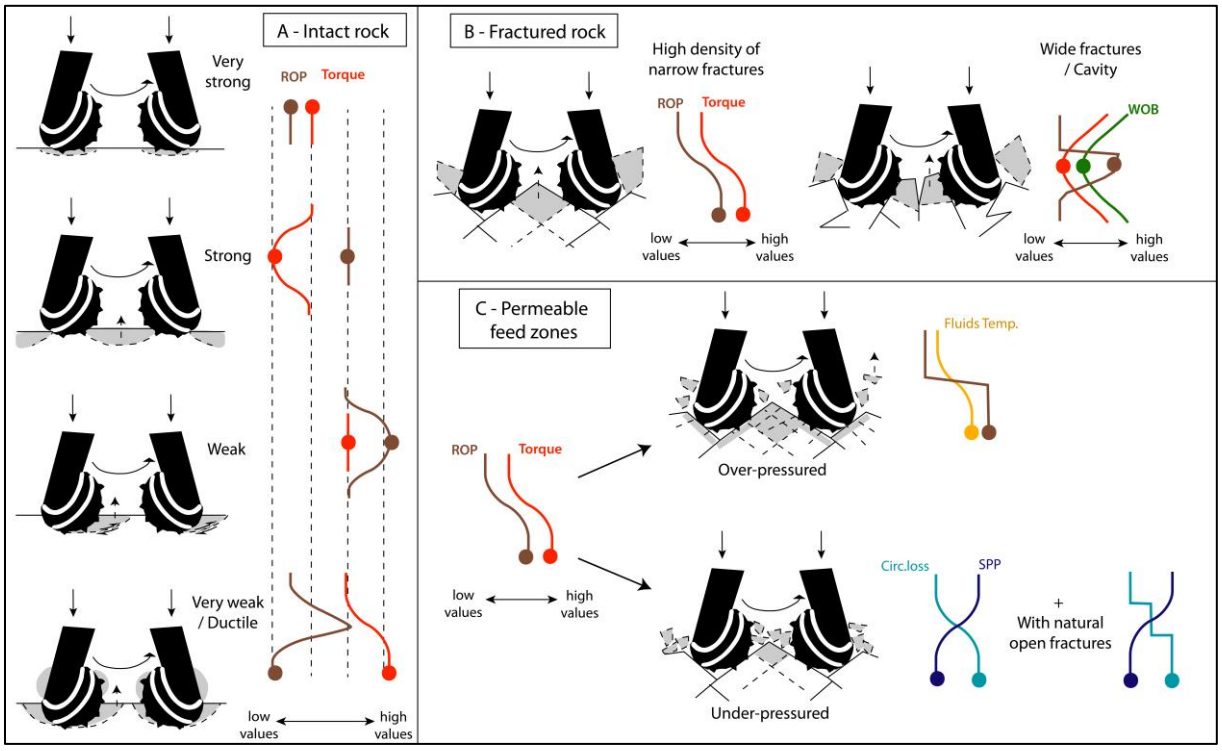

Figure 5.2. Chart of key drilling parameters evolution for various geological scenarios, based on literature review, drilling knowledge and engineering experience of the authors. Variations in parameters should be read from top (initial values) to bottom (for B and C) and from left (low values) to right (high values). The values corresponding to the lithology are highlighted on variations with a circle. A): four categories of intact rocks with relative values

in Torque and ROP at their encounter during drilling. Encounter with a very weak or ductile formation should for instance cause an increase in Torque and a sudden increase in penetration rate before it reverses to a very low value. B) Natural fractures encountered in brittle formations. C) Feed zones (porous permeable rocks) with relative pressures, affecting scenarios of A and B.

For permeable rock masses, a decrease in SPP is often related to loss of drilling fluids within un under-pressured formation (Fig.5.2C). When permeability is caused by natural fractures, circulation loss can occur through successive and additional steps while the fluids are flowing into the connected network. The lower water level in the well lowers the borehole pressure exerted at the bottom and thus can additionally increase ROP. In the reverse case, where there is an over-pressured rock formation compared to drilling fluids, decompression can fragment the country rock and facilitate break-up of the walls and base of borehole, also increasing ROP, and the influx of hot hydrothermal fluids can increase the recorded temperature of fluids within the well. The end-member scenarios concerning permeable feed zones (under and over pressured) consequently result in an increase in ROP, as well as an increase in torque caused by accumulation of cuttings at the bottom of the hole (Fig.5.2C).

These signatures in drilling parameters can overprint and mask each other when a change in lithology (Fig.5.2A) is associated with a change in fracture properties (Fig.5.2B) or overall permeability and/or pressure (Fig.5.2C). Feed zones are particularly difficult to detect with this approach, as their signature can be dominated by the variations often associated with rock strength.

5.4 Method for interpreting rock properties from drilling logs

In order to use the chart in Figure.5.2 to interpret lithologies in blind zones, it is first necessary to identify which of the variations in drilling parameters are caused by geology or by drilling operations. To achieve this drilling logs can be created from raw data in parallel with the examination of drilling reports, which provide context and details about the numerous drilling operations (Fig.5.6). The sections where the drilling is stopped, where the drill bit is pulled out or pushed back into the well, can be easily identified using the reports and the height of the top-drive. But the sections where drillers act on the parameters from the surface (WOB, RPM and flow rate; Fig.5.1) to keep the other parameters steady can be identified and discarded only using the drilling logs. Within the sections of drilling data where drillers are not adjusting WOB, RPM and flow rate, changes in ROP and torque can be used to pick changes in geology, which

are the targeted portions of the drilling log. Those may appear only during a short time before being controlled back by the operator (as in Fig.5.4A). Therefore, sudden variations in WOB and RPM that work towards stability should be picked out as being artificial, but variations occurring in a zone where signals are stable should be related to geology.

In addition, any change in drilling material such as BHA and fluids density should be noted on the log, as they impact the values of output parameters, and thus increased caution is required when comparing zones that have been drilled with different materials. Following this methodology should allow differentiation of artificial changes from geological changes, although it does not prevent the opposite and some geological transitions may be missed.

Here, we differentiate depth-logs and time-logs. To interpret the subsurface, drilling logs according to drilled depth are of common use to complement wireline data and cuttings recovery (Archer et al. 2005; Millett et al. 2016), although they are usually not used on their own for systematic interpretations. The time-logs can additionally allow rock/drill interactions to be observed when the drill bit is stuck at a particular depth, which would otherwise be overprinted on the depth-logs (for example during the magma encounter in IDDP-1). Major variations are better highlighted on the large-scale depth-logs, whereas more subtle variations are better detailed on time-logs.

We propose here a simple 5-step methodology to interpret rock properties from drilling logs. Steps are illustrated by the Figures 5.6, 7, 8, 10 and 11, based on the example of the IDDP-1 geothermal well drilled at Krafla, Iceland.

1- Creation of depth-logs across the investigated blind interval, in combination with recorded drilling operations and BHA arrangement. The former should come from raw quantitative data from the data acquisition system on the drill rig and the latter from drilling reports. Simplified drilling logs can be made with key parameters RPM, WOB, ROP and Torque, as in Figure 5.6.

2- Picking of intervals that are not suitable for geological interpretations. These are intervals where the drillers could have directly acted on WOB, RPM or flow rate. From the depth-logs, a first selection of non-suitable zones can be based on 2 criteria: (1) When RPM or WOB abruptly exhibit the full range of value at a single depth, it means the drilling has stopped. (2) When the change makes a fluctuating parameter return back to a constant value, it is probably related to driller's action aiming to stabilise the drilling process. This initial interval pick can then be improved by looking at the other parameters as described earlier in this section.

Where the driller-induced changes are better constrained, or once the data has stabilised, the data can be examined for lithological information. An ideal case for interpretation is when values of input surface parameters (WOB, RPM and flow rate) are constant (e.g. Fig.5.6).

3- Identify key variations in ROP and Torque in intervals suitable for geological interpretations, as resulting from step 2. Time-logs can be additionally used to focus on changes where a better resolution is relevant, with improved insight into the full range of drilling parameters (Figs.5.7, 8).

4- Creation of an informative log of rock properties across the blind interval, as in Figure 5.10, using the chart in Figure 5.2 to interpret the key changes picked in step 3.

5- Conversion to an interpreted geological log (Fig.5.11), which associates a rock type or lithology to each rock property from the informative log in step 4. The comparison with shallower transitions in lithology can help their identification, if the blind zone is expected to be constituted of similar rock types and the same BHA is used.

This straightforward approach is adapted to the example we base this study on. To apply this to another well, it would need to be adjusted depending on available data and information.

5.5 Results: Application to the IDDP-1 well

5.5.1 IDDP-1 upper sections

As for most geothermal drilling, the time allocated for the IDDP-1 well installation at Krafla, Iceland, in 2009, was divided between many operations. Actual drilling represented on average 25 % of the temporal distribution (e.g. Mortensen et al., 2010b; Fig.5.3), indicating the high occurrence of drilling operations affecting the monitored parameters.

The geological log above the blind zone in the IDDP-1C well, built from retrieved cuttings, provides an insight into the lithology encountered (Mortensen et al., 2014). Changes in drilling parameters across known transitions in lithology were compared with the expected changes from the chart in Figure 5.2. The rock type, fracture properties, permeability, alteration degree and grain size, all affected the drilling parameters (Fig.5.4). Some examples of geological transitions are illustrated in Figure 5.4, with the observed variations in drilling parameters, revealing strong correspondence with expectations in Figure 5.2.

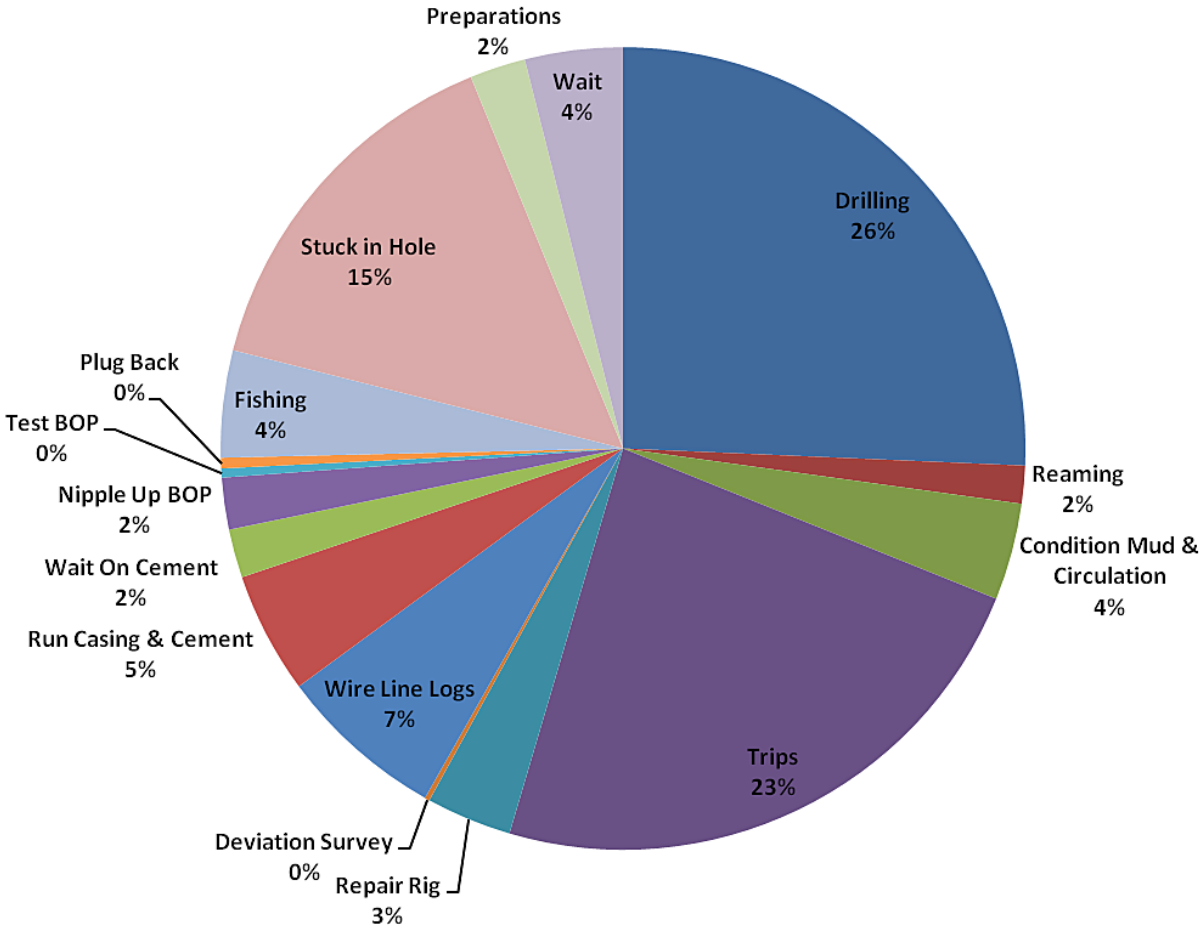

Figure 5.3. Typical time distribution chart during the IDDP-1 drilling operations. This chart covers the period from the 24th of March to the 25th of May 2009. After Mortensen et al., 2010b.

The host rock transitions from mostly basalt to mostly felsite around 2020 m depth (Mortensen et al., 2014). Considering that the IDDP-1 rhyolite magma is interpreted to have been generated by felsite partial remelting at the margins of a shallow (basaltic or rhyolitic) intrusion (Masotta et al., 2018; Saubin et al., in review; Chapter 4), and that felsite host rock was retrieved together with quenched magma from 2104 m depth with evidence of no other rock type (ISOR, 2009), we assume that the full section of the blind zone is felsic, in accordance with what is suggested from the gamma ray logs (Mortensen et al., 2014). Because felsite was rarely encountered shallower in the wells, and only as thin layers through basalt, it was not possible to calibrate our interpretations with shallower observations. However, the drilling signature of shallower felsite encounters is consistent with a weaker rock than the basalt lithologies: ROP abruptly increases and Torque drops, as illustrated in Figure 5.5. The blind zone targeted for interpretation is therefore constituted mostly of one felsite lithology, with drilling parameters that can identify changes in grain size and relative strength, alteration, fractures, permeability and relative pressure.

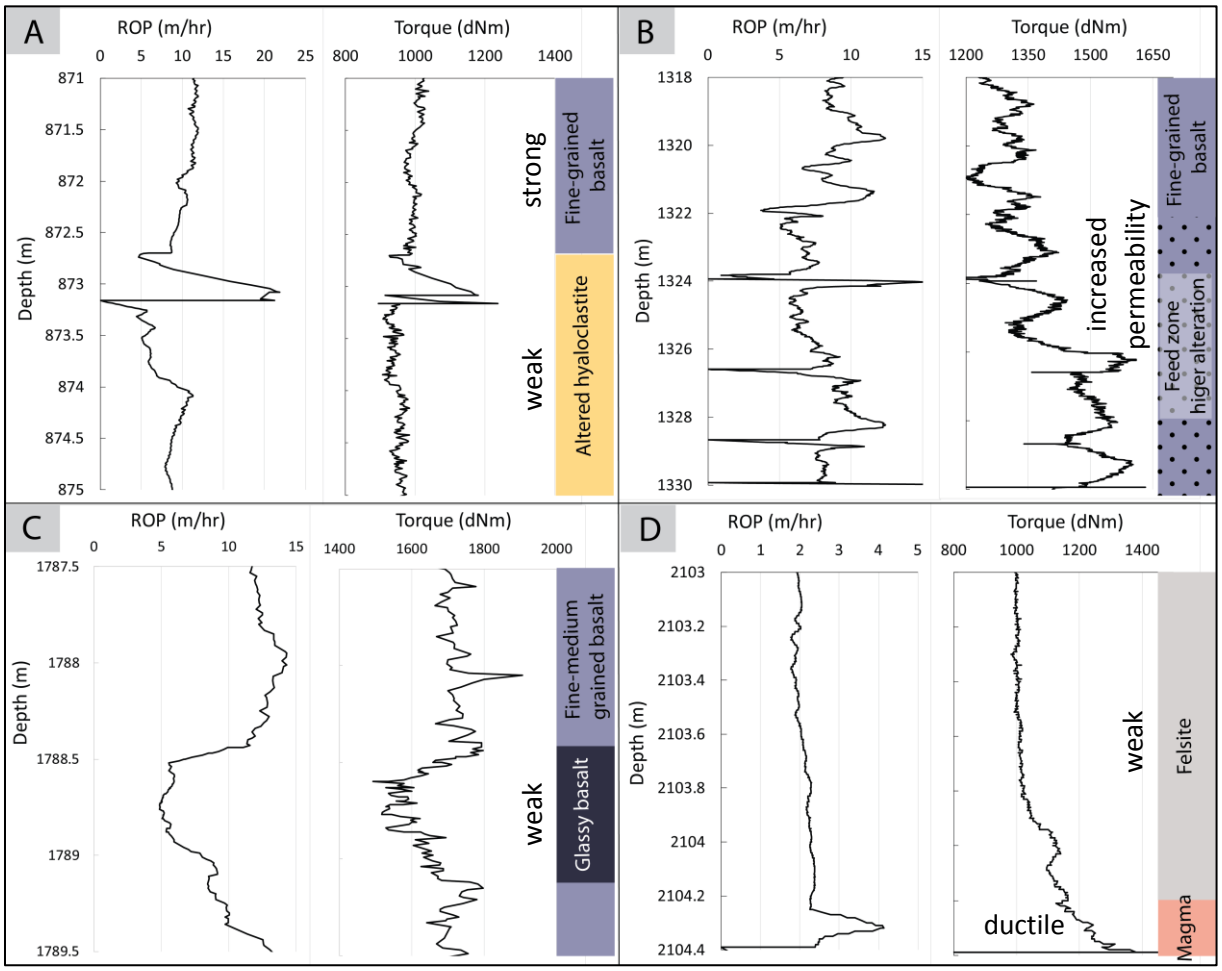

Figure 5.4. IDDP-1C logs of ROP and Torque parameters, constructed from raw data, over intervals of lithology changes according to raw lithology data and Mortensen et al. (2014). A) 871-875 m depth interval highlighting the transition from strong basalt to weak hyaloclastite Both ROP and Torque increase at the contact, before being likely controlled down artificially (the drop is therefore not a natural variation). B) 1318-1330 m depth interval in a constant basalt lithology, where a feed zone is encountered from 1322 m depth, causing a progressive increase in ROP and Torque, with higher variability caused by increased permeability, uneven rock mass condition and higher alteration degree (mineral assemblage of both clay and quartz). C) 1787.5-1789.5 m depth interval, where a weaker layer of glassy basalt is encountered within a lithology of fine-medium grained basalt. This causes a sudden decrease in Torque, fluctuating rapidly as a result of difficult, uneven chipping, and a decrease in ROP despite the lower strength. The reason for the chipping may be that the particles were smaller than the ideal size for extraction, which results in accumulation at the bottom of the well. D) Encounter of IDDP-1C with magma at 2104.4 m depth. ROP jumps suddenly before dropping, at which point Torque increases.

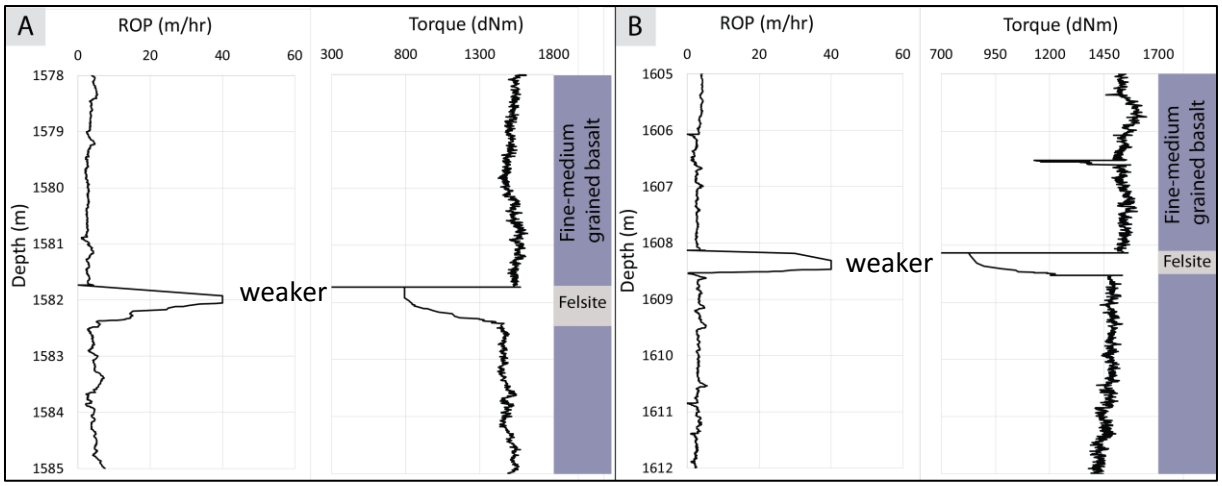

Figure 5.5. Encounter with thin felsite layer in the IDDP-1C leg, above the blind zone. This change in lithology from basalt to weaker felsite relates to better drillability, with increased ROP and decreased Torque. A) Layer around 1582 m depth. B) Layer around 1608 m depth.

5.5.2 IDDP-1 blind zone

This section investigates what drilling logs can reveal about the 2070-2104 m depth blind zone encountered by the IDDP-1 well. We use the method presented earlier to build an interpretive log above the intrusion, and use Chapters 2, 3 and 4 to constrain the interpretations, in terms of damage and alteration around similar shallow rhyolite intrusions, and about structure of the IDDP-1 magma body. As three attempts to drill beyond 2100 m depth were made, three drill logs going through the same 2070-2104 m depth blind zone are available, with drilling parameters monitored at 5 s frequency. Over this time interval, we estimate the precision of raw drilling data on depth at ± 0.01 m. IDDP-1A is the initial vertical well, and IDDP-1B and 1C are laterally spaced less than a few meters apart, with a 50- and 16-day interval between their respective drilling (Mortensen et al., 2014; Pálsson et al., 2014).

5.5.2.1 Depth-logs

The depth-logs of ROP, Torque, WOB and RPM at the three legs are presented in Figure 5.6, together with the zones picked as dominated by artificial changes (red zones in Fig.5.6) and the variations that can be used for interpretation. The fluid flow is not used here, as this parameter is constant in most of the blind zone and does not add to the precision of the segregation. Drilling operations of the IDDP-1 well are recorded in a series of internal reports from ISOR (Iceland Geosurvey), providing real-time observations and major operations, and are also covered in the literature, which provides a critical overview of the drilling history. However, minor drilling operations such as manual control on input parameters (WOB and RPM) are not

reported, and some of the intervals we exclude are based on reported variations of these parameters in the raw drilling logs.

The drilling difficulties and associated adjustments from ~2070 m and ~2100 m cause overprinting on most of the depth-logs, and thus require the use of the time-logs. Because drillers were increasingly cautious from one leg to the next, the IDDP-1C leg provides the steadiest parameters and the fewest excluded zones.

The highlighted key variations (Fig.5.6) are a first selection of the depths at which a change in lithology can be interpreted. The observation of associated variations in complementary parameters (SPP, circulation loss, temperature) using time-logs or going through raw data, help their interpretation.

5.5.2.2 Time-logs

As major difficulties were encountered both around 2070 m (total loss of circulation) and 2100 m (potential encounter with magma), these two zones are rigorously analysed using time-logs. Figure 5.7 presents variations monitored at the three entries within the 2070 m depth blind zone, and Figure 5.8 presents the three interactions with the >2100 m depth magma. As the resolution of events is clearer on the time-logs, some intervals that are discarded from interpretation on the depth-logs (red overlaps in Fig.5.6) can still be cautiously analysed on the time-logs (red overlaps in Figs.5.7 and 8 are reduced compared to Fig.5.6).

Compared to the overall values of the drilling parameters at shallower depths, the 2070-2100 m interval is generally characterised by a lower SPP (~150 bar in average at shallower depth, <130 bar in the blind zone) associated with a total loss of circulation (>50 L/s). This total loss occurred progressively from 2073.5 to 2074 m and quickly at 2071 m depth for IDDP-1A and 1C, respectively. In both of the legs, this is associated with a decrease in ROP, SPP and Torque. These variations are not visible in the IDDP-1B leg, where WOB increased steadily and possibly artificially while total loss occurred at ~2073.5 m depth. Partial loss of circulation regularly occurred at shallower depth, although with less fluid loss and over shorter intervals (Mortensen et al., 2014).

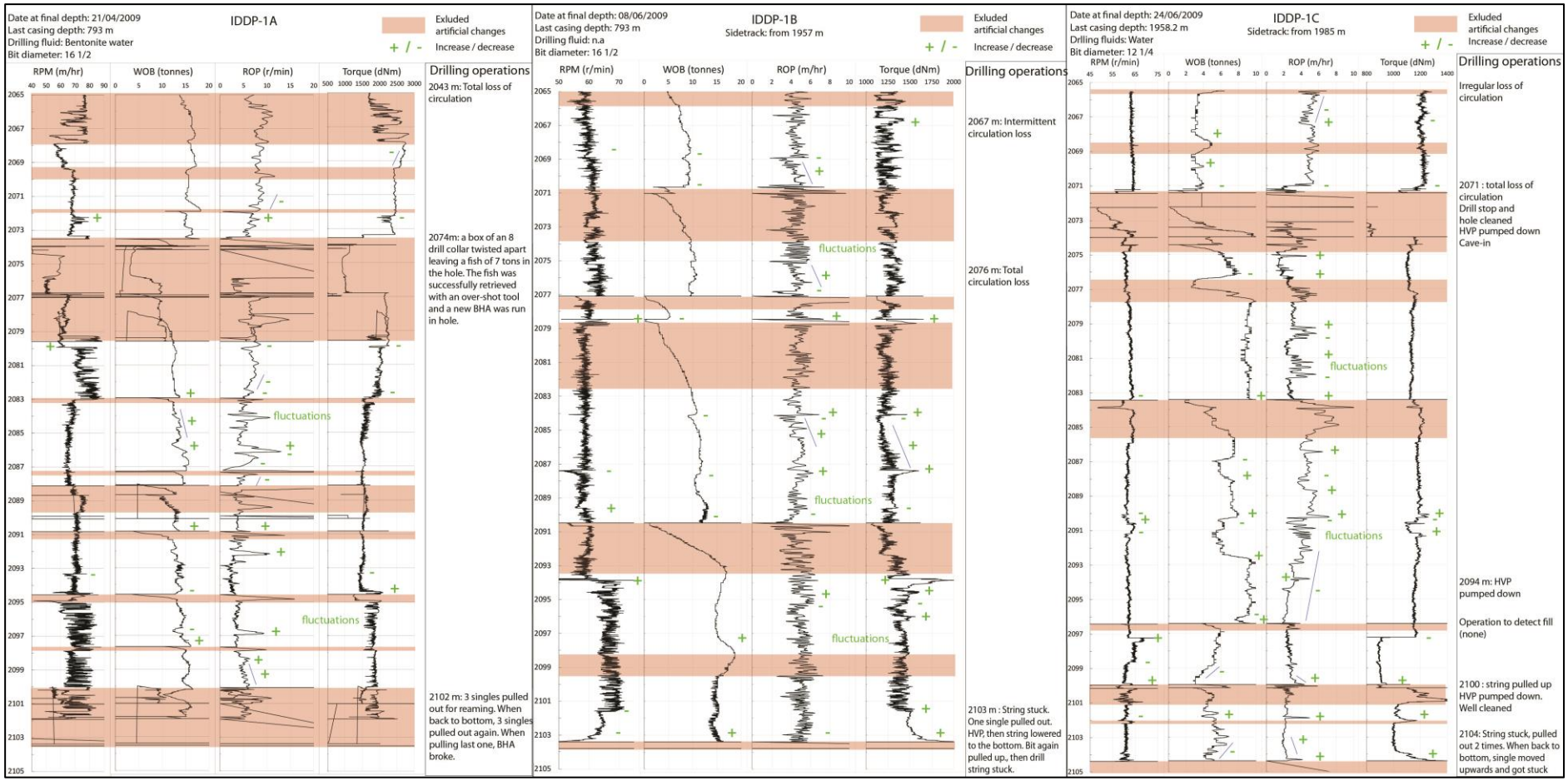

Figure 5.6. Depth-logs of the three legs of the IDDP-1 well drilled in 2009 at Krafla, Iceland. Main parameters helping the interpretation of rock properties are plotted versus the drilled depth, in the blind zone interval above the rhyolite intrusion: the input surface parameters RPM and WOB, and the output downhole parameters ROP and Torque. The major drilling operations conducted in this interval are reported on the right side of each log. The zones excluded for interpretation, because they are potentially dominated by artificial drilling manoeuvres, are highlighted in orange. The main variations in drilling parameters that could be caused by encountered lithologies are highlighted with the green + and - symbols.

On the 21st of April when the IDDP-1A drill bit approached 2101.8 m depth, SPP decreased, then a slight increase in the height of the top drive indicates that the drilling was stopped (Fig.5.8A). When drilling continued to 2102 m depth, WOB and Torque progressively increased and RPM progressively decreased, then Torque increased sharply, RPM dropped and ROP increased. Following this, the drill bit was pulled out and pushed back to the bottom four times. Each of these occurrences triggered the same response in drilling parameters. On the 8th of June when the IDDP-1B drill bit reached 2101.6 m depth, Torque and RPM signals stabilised and ROP slightly increased by ~1 m/hr on average (Fig.5.8B). At 2103.4 m, Torque temporarily increased while RPM temporarily decreased, and these variations abruptly intensified. The string was stuck, but successfully pulled out. When back to bottom, the parameters fluctuated the same way as during previous occurrences at 2102 m with IDDP-1A. On the 24th of June when the IDDP-1C drill bit approached 2104.4 m, ROP temporarily increased (Fig.5.8C). Torque increased progressively with a final sharp increase and RPM progressively decreased with a final drop. The string was stuck and pulled up. When drilling continued at the bottom, Torque reacted the same way again, but RPM increased. The bit was pulled up again, and when it was returned toward the base of the borehole, an upward movement on the bit was recorded by a high increase in WOB, Torque, RPM and SPP, before the string became stuck.

The comparison of variations highlights very similar reaction at the bottom of each IDDP-1 leg: Torque progressively increases, and RPM progressively decreases, with these changes getting suddenly stronger. WOB generally slightly increases, progressively. When the IDDP-1A reached 2102 m, and 1C reached 2104.4 m, in addition of this reaction, ROP jumped. As the retrieval of fresh obsidian cuttings strongly suggests that the signals recorded for the IDDP-1C were triggered by the encounter with partially molten rock (ISOR, 2009), we suggest that the IDDP-1A also encountered magma at 2102 m depth, and we name this signature in drilling parameters ‘magma encounter’, and ‘magma approach’ the similar signature that excludes the ROP jump (Fig.5.9). This demonstrates that magma was approached and/or encountered 9 times over the three drilling attempts. A legitimate consideration is whether this consistent signature is caused by the proximity to magma or by the manual pulling up of the strings, since they occur nearly concurrently. A close inspection of the time-logs (Fig.5.8) demonstrates that the height of the top-drive increases after the consistent signature, which is therefore caused by the downhole encounter immediately prior to pulling up. Additionally, drilling reports and literature relate the variations in Torque to geological difficulties, and to drilling operations (e.g. ISOR, 2009; Pálsson et al., 2014).

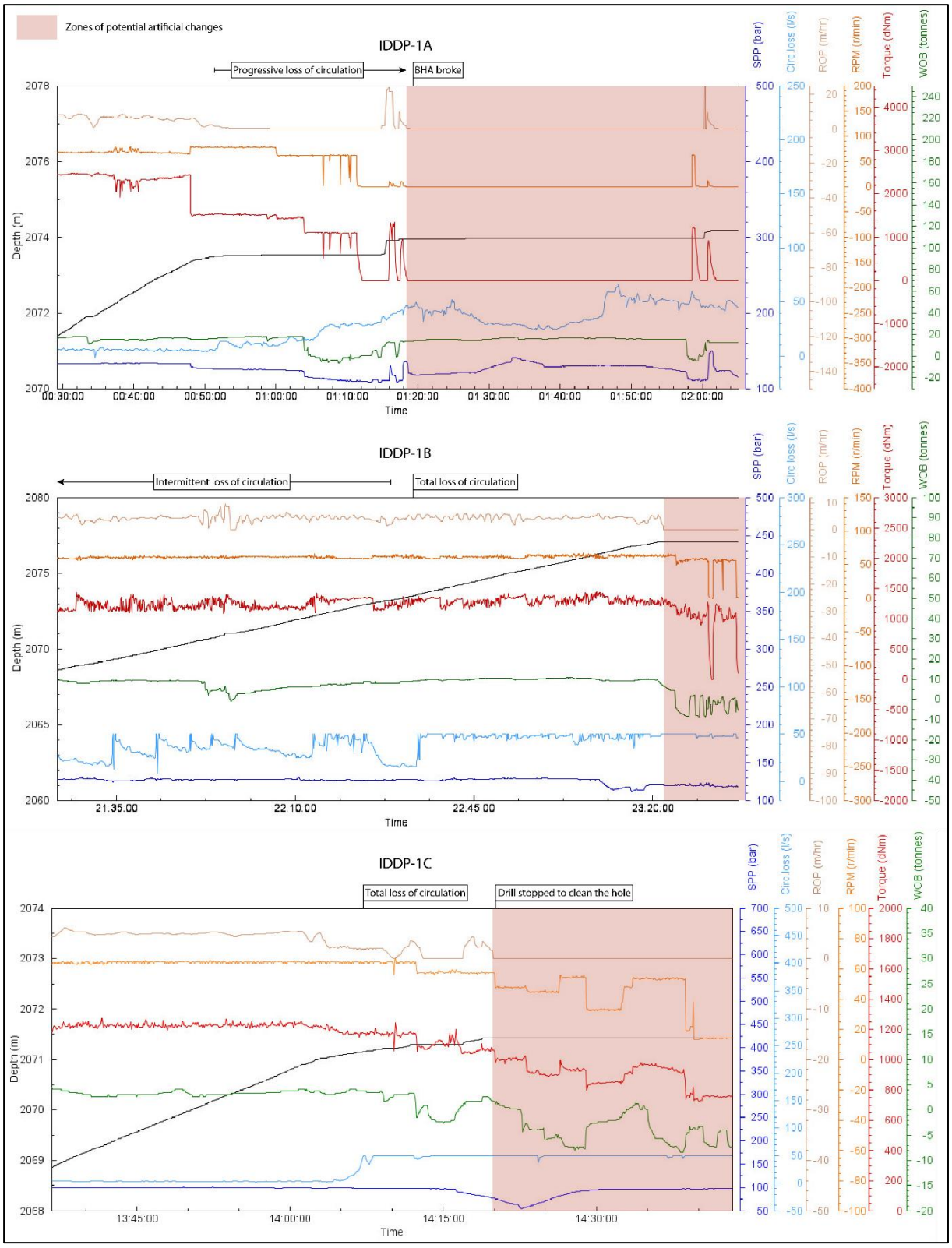

Figure 5.7. Time-logs of the three IDDP-1 legs when entering into the blind zone around 2070 m depth. IDDP-1A is the initial vertical well, IDDP-1B and 1C are the side-tracks, a few metres apart. Black line denotes depth of hole.

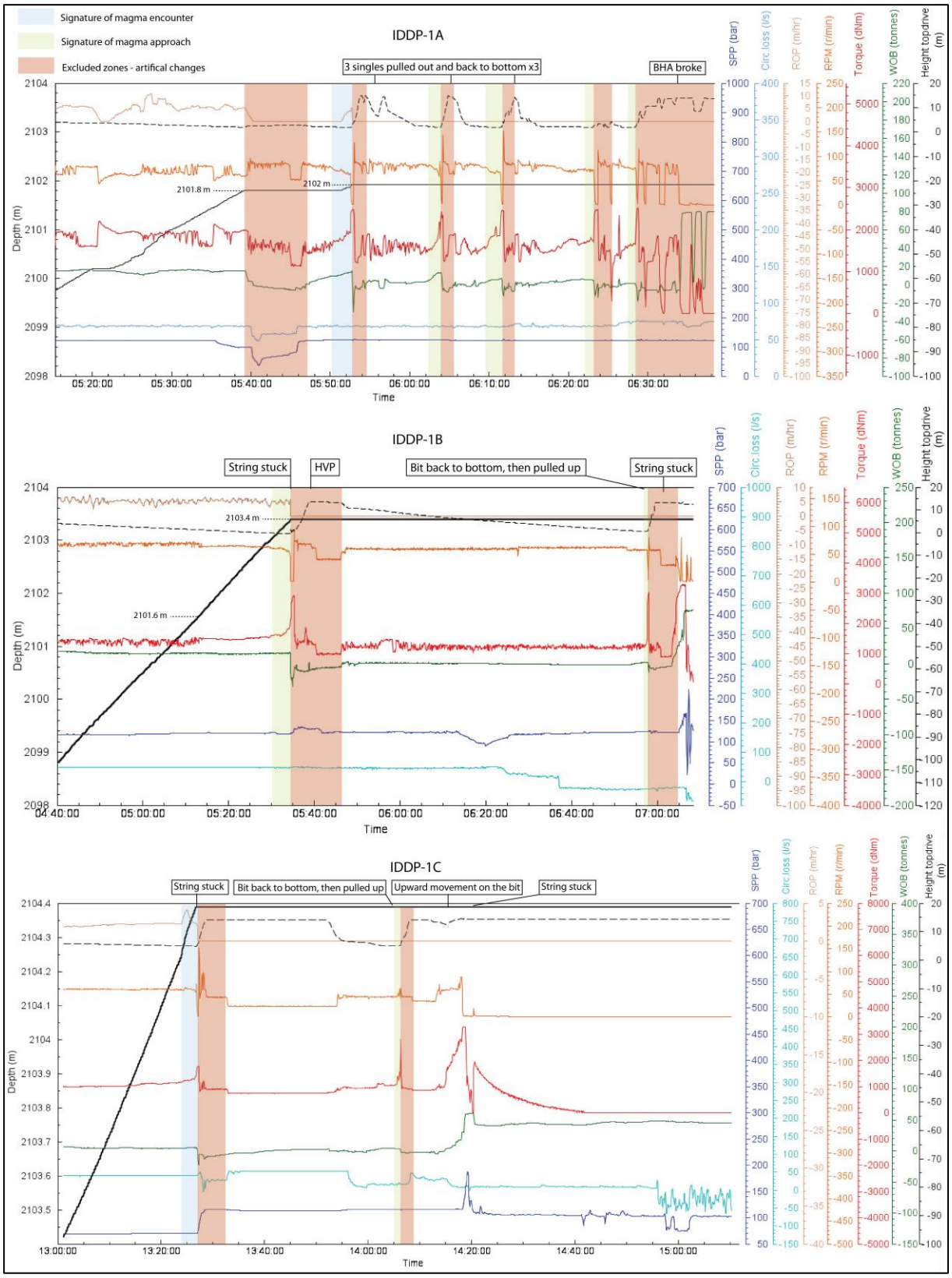

Figure 5.8. Time-logs of the three IDDP-1 legs when approaching the major difficulties beyond 2100 m depth. IDDP-1A is the initial vertical well, IDDP-1B and 1C are the side-tracks, each a few metres apart. Solid black line denotes depth of hole.

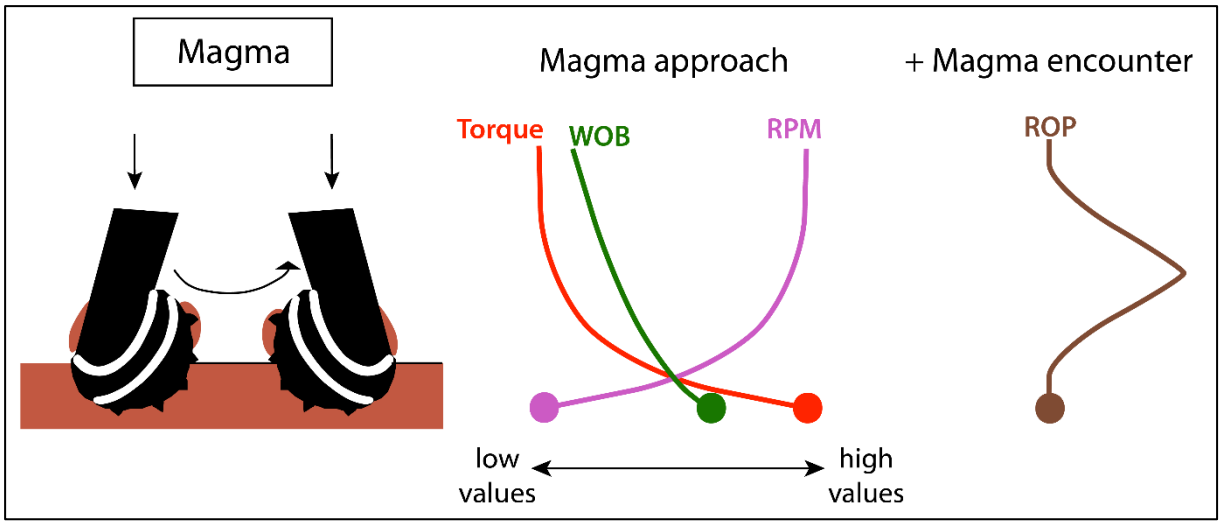

Figure 5.9. Key drilling parameter evolution at the vicinity of magma, based on observations of raw drilling data from the IDDP-1 well. Variations in parameters should be read from top (initial values) to bottom and from left (low values) to right (high values). This reaction to magma is a new addition to the range of scenarios presented in Fig.5.2.

5.6 Interpretations

5.6.1 Interpreting rock properties

The observations from depth-logs and time-logs are combined to build three logs of rock properties, in Figure 5.10, following the methodology and the interpretations suggested in the chart in Figures 5.2 and 5.9. Detailed interpretation processes are illustrated in Supplementary Material, Figures S5.1, S5.2 and S5.3. The resulting logs mostly provide relative rock strength and fracture information, with some highlighted feed zones and the depths of occurrence of the total loss in drilling fluids circulation.

The evolution of drilling parameters with rock properties, proposed in the chart in Figure 5.2, relates to ideal case scenarios. Many of the variations identified here differ in part from the proposed signature, because of a range of complications associated with drilling in challenging heterogeneous hydrothermally altered materials.

We base the rock strength interpretations on the relative variations of ROP and Torque, with stronger confidence in the ROP fluctuations than Torque. We interpret wide fractures or voids when ROP sharply increases and WOB sharply decreases, and additionally support the presence of fracture networks for intervals with faster fluctuations of the parameters. We note, however,

that despite following the method, a part of the interpretive process is subjective with multiple interpretations possible.

The precision of the interpreted rock masses is estimated at ± 0.2 m using depth-logs, and ± 0.1 m using time-logs. Each leg corresponds to a different BHA, and the magnitude of fluctuations in drilling parameters can thus not be directly compared to one another. The comparison of individual interpretations of rock masses, however, reveal differences from one leg to another despite their proximity (a few meters apart). Minor differences were already observed when comparing cuttings from these legs at shallower depths (e.g. intrusions of dolerite in IDDP-1A that are not found in IDDP-1B and 1C, Mortensen et al., 2014). Despite this variability, the comparison also reveals similar trends, whose existence support the consistency of the method and highlight consistent depth-dependent changes in the blind zones:

(1) The rock strength increases prior to the occurrence of the total loss of circulation (from 2068.5 to 2073.5 m depth in IDDP-1A, 2074 to 2077 in IDDP-1B, 2066 to 2072 in IDDP-1C). This is additionally supported in the third leg by the geophysical logging: resistivity and the dual neutron response at 2067 m depth indicate stronger, denser rock (Mortensen et al., 2014). Within this interval of increasing rock strength is a thinner weak zone, interpreted as a wide fracture, a weaker fractured interval or weaker lithology (at 2072.5, 2070.5-2075 and 2067.5-2071 m depth in IDDP-1A, 1B and 1C, respectively).

(2) The total loss of circulation is likely associated with fractures, as wide fractures are located within 4 m of this occurrence (immediately following the total loss in IDDP-1A and 1B, 4 m below in 1C). After circulation is lost, the rock strength is generally lower over a long interval (18.5 m in IDDP-1A, 17 m in IDDP-1B, 21 m in IDDP-1C) with a succession of fractured and/or very weak zones.

(3) The rock strength progressively increases again after this weaker interval, until it reaches a similar strength to what was encountered at the point of total loss of circulation (from 2087.5 to 2092, 2089.5 to 2093.5 and 2090.5 to 2093.5 m depth in IDDP-1A, 1B and 1C, respectively). The strength remains relatively strong over an irregular interval (up to 8 m thick in IDDP-1B).

(4) Finally, rock strength mostly decreases until reaching magma (at 2102, 2103.4 and 2104.4 m depth for IDDP-1A, 1B and 1C, respectively), where fluctuations indicate a sudden encounter with a ductile layer in IDDP-1A and 1C, and at least a very close approach in IDDP-1B. The drill bit penetrated over ~20 cm into this zone before being stuck (20 cm for IDDP-1A, 20 cm for IDDP-1B and 15 cm for IDDP-1C).

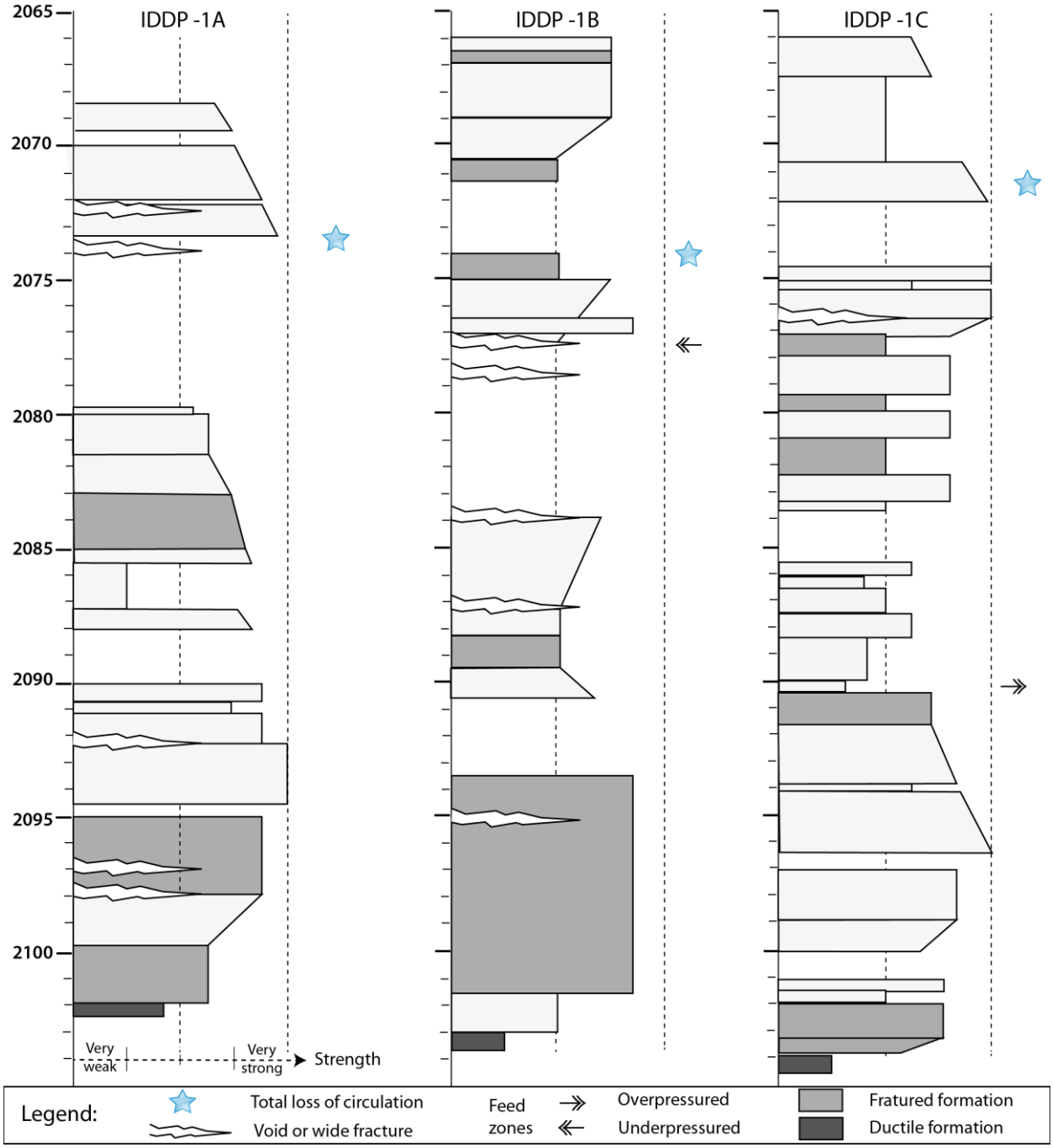

Figure 5.10. Interpreted logs of rock properties, across the blind zone, for the three IDDP-1 legs. The empty intervals correspond to variations in drilling parameters that are dominated by drilling operations rather than lithology, thus preventing any interpretation.

5.6.2 Interpreting lithologies

In Figure 11, we propose a geological model based on the general trends in rock properties highlighted by the comparison of the blind interval between the three legs. The depth and

thickness of the units are averaged from the three legs, with reported standard variation in thicknesses and the major variations in drilling parameters characterising the units.

The cuttings recovered from 2060-2070 m depth are medium-coarse grained dolerite in IDDP-1A, intruded within felsite, and fine-medium grained felsite in IDDP-1B and 1C (Mortensen et al., 2014). We associate the progressive increase in rock strength towards 2074 m depth to a decrease in grain size of felsite (Fig.5.11).

The main feed zone for all three legs is identified between 2035 and 2080 m depth (Mortensen et al., 2014), hence the blind zone was interpreted as the conductive boundary layer separating the magma from the overlying convective hydrothermal system (Lowell and Germanovitch, 1994; Axelsson et al., 2014; Halldorsdottir et al., 2019). However, the interval we interpret as a weak, highly permeable rock mass, from 2074 to 2090 m depth, is likely to also be part of this main feed zone. This section is recognisable in the drilling logs by repeated occurrence of strong fluctuations in ROP (Fig.5.6), which we associate to unstable intervals caused by higher fracture density, or weaker or coarse-grained felsite. The temperature and pressure differential around the borehole as it drilled through the hot rocks (~350 °C; Axelsson et al., 2014) caused intense fracturing of the rock (Lavallée et al., 2020). The weakness of this interval could therefore have been accelerated and exacerbated by drilling, although it does suggest that the stronger layer from ~2089.5 m depth (labelled Damaged aureole in Fig.5.11) was less affected. There, these irregularities stop, suggesting lower fracture density, with an overall increase in rock strength that could be related to a finer grained interval, and thus lower permeability. We associate this interval with the conductive boundary layer (CBL). Another possible interpretation is the presence of a cooling front of the intrusion from ~2075 m depth to ~2097 m depth. It could be a quenched margin, with high fracture density on the outside where quenching was fast (fractured zone in Fig.5.11), and progressively more widely spaced joints with slower cooling towards the inner side (Damaged aureole in Fig.5.11). This cooling and associated thermal contraction could have been natural or drilling-induced. However, this structure of a cooling magma body with quenched margin is not supported by the IDDP-1 glass particle texture and chemistry (Saubin et al., submitted; Chapter 4), and we conclude that this interval represents undercooled host rock rather than undercooled magma.

Below, the rock strength progressively decreases towards the magma and there are high fluctuations in the RPM, which could be caused by interstitial melt impeding the rotation, through zones of viscous trapping and brittle failure (Partially molten felsite in Fig.5.11).

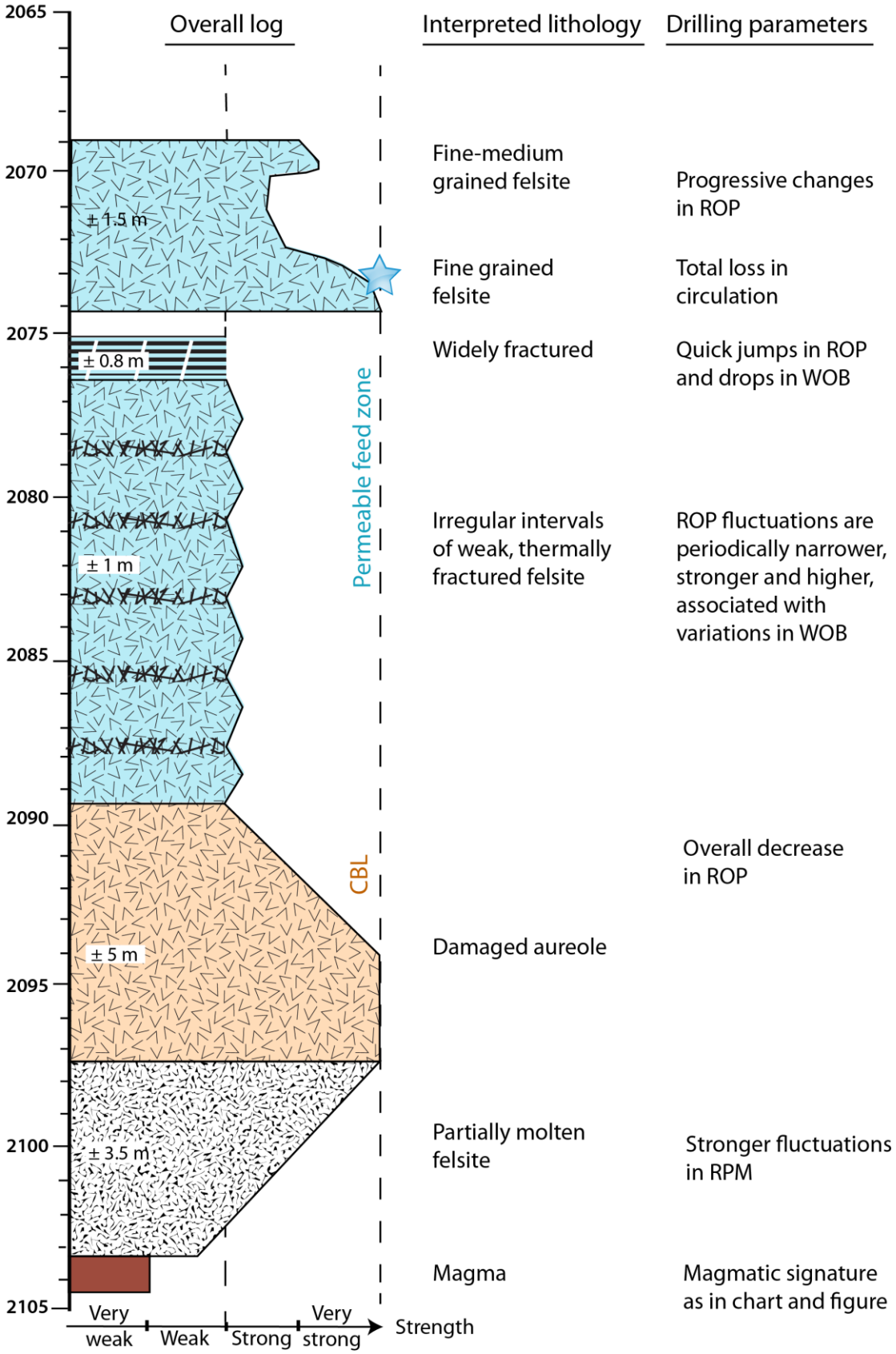

Figure 5.11. Geological model across the IDDP-1 blind zone, converted from the interpreted logs of rock properties. Only the main similarities between the three legs are considered. Thickness and depth of units are calculated from the average, and the uncertainties on the model correspond to the unit thickness.

5.6.3 Implications for IDDP-1 intrusion

In this section, we use the results and conclusions from previous chapters to examine how the geological log we propose contributes to future drilling into the same IDDP-1 magma body, how it further informs the interpretations about the intrusion and what the implications are for general worldwide hot/magma drilling.

Shallow rhyolite intrusions studied in Chapters 2 and 3 were initially chosen to be analogue to the IDDP-1 intrusion. However, results from Chapter 4 regarding the IDDP-1 melts support genesis through partial melting of the host felsite and there is no evidence of this in any of our analogues. The alteration and damaging impact on host rocks can therefore differ, considering that the IDDP-1 magma emplacement process additionally melts the host rock. However, the volume increase caused by the transition to the melt phase could trigger a similar type of mechanical damage as that caused by an intrusive volume. Chapter 2 highlights that strong host rocks around an intrusion (basalt and welded ignimbrite) can be damaged by fracturing, with decreased strength and increased permeability, whereas weak host rocks (conglomerate and hyaloclastite) can be affected by decreased permeability associated with pore occlusion (Saubin et al., 2019). Measurement of Krafla rock properties reveal that felsite is less porous than other lithologies such as basalt and hyaloclastite, and has medium permeability (10^{-15}-10^{-13} m², compared to 10^{-16}-10^{-13} m² in basalt and $6{\cdot}10^{-14}$-10^{-13} in hyaloclastite; Eggertsson 2019). Laboratory experiments demonstrate that Krafla basalt is stronger than Krafla felsite, which has a mechanical behaviour close to that of Krafla hyaloclastite with very similar Young's modulus, uniaxial compressive strength and tensile strength (respectively < 5 GPa, <20 MPa and <2 MPa difference between felsite and hyaloclastite, and ~50 GPa, 60 MPa and 10 MPa difference between felsite and dense basalt; Eggertsson, 2019). This lower strength is confirmed by the two shallower encounters of thin felsitic layers in the IDDP-1C leg, each causing an increase in ROP and drop in Torque (Fig.5.5). We consequently assume that the host felsite has a behaviour close to that of weak host rocks studied in Saubin et al. (2019; Chapter 2). This implies reaction to intrusive volume via permeability reduction. However, the low porosity of felsite would strongly restrict the amount of pore occlusion by mineral precipitation or compaction under stress, and the increase in strength would be limited.

The transition from crystallised felsite or glass to a melt is associated with a volume increase (e.g. Lavallée et al., 2020). This pressure exerted by the IDDP-1 magma on the host rock, and local magma flux at the roof, could cause felsite compaction in the limit allowed by its micro- and macro-fracturing degree. The 2089.5.5-2097.5 m depth interval above the magma,

interpreted as increasing strength, fine-grained felsite (Damaged aureole in Fig.5.11), could correspond to such an impacted host rock. The closure of micro-fractures and the high internal stress could have prevented drilling-induced thermal fracturing on its inner side. This zone could thus be seen as the damaged and altered aureole caused by the intrusion, and could potentially extend over the full length of the blind zone depending on thermal fracturing intensity versus increase of compacting strength. The presence of this dense layer in between the magma and the permeable zone could have potentially confined drilling-induced magma decompression to the local contact point.

In Chapter 3, the aureoles measured in the field around 14 shallow fossil rhyolite intrusions reveal a linear relationship between aureole thickness and intrusion size. This trend can be used to infer the size of an intrusion knowing the thickness of its aureole. The IDDP-1 intrusion differs in its mode of emplacement, as it could be stored where it is generated. The heat source should be sustained longer during in-situ melting than for a swift magma emplacement as in our analogues. The impacted host rock, accordingly, should be wider, as the interface would be maintained at magma temperature in a similar way as that caused by convection (Annen et al., 2017; Chapter 3). The use of the trend would thus result in an overestimate of the size of the magma body. What we interpret as the damaged and altered host rock above the IDDP-1 intrusion is ~8 m thick as a minimum (Damaged aureole in Fig.5.11), and 22 m as a maximum if we consider thermal fracturing on its outer side (Damaged aureole + fractured zone in Fig.5.11). These values fall in the range of aureoles impacted by conductive heat transfer over (but not excluding) hydrothermal fluids convection (Fig.3.2A). Using the relationship from Chapter 3 for a size estimate of the rhyolite magma body, these values correspond to a 700-1100 m wide magma body (Fig.3.2A). We note that this is a restricted estimate from the larger range considering uncertainties. Although it is less likely, the minimum estimate is 200 m thick.

The 700-1100 m wide estimate is much larger than the previous estimate of a >50-100 m thick magma sheet (Axelsson et al., 2014), modelled based on heat flux observed during and after drilling and assuming that the intrusion was emplaced during the last volcanic episode (Krafla Fires, 1975-1984). The larger size suggests that the IDDP-1 intrusion could be older than the Krafla Fires, or that the heat discharged during this active period was considerably higher than assumed. Other wells at the vicinity with the IDDP-1 have intercepted magma: the KG-25 located 80 m away, which reached 2105 m depth, and the KJ-39 drilled ~2 km away until 2865 m depth. Studies on these drilling suggest that the same rhyolite magma body could have been encountered by both IDDP-1 and KG-25, thus having a minimal lateral extent of 80 m.

However, preliminary studies on cuttings from the KJ-39 well suggest a different magma (e.g. Gudmundsson et al., 2008; Mortensen et al., 2010a). The large volume IDDP-1 rhyolite reservoir could still be growing by partial melting at its margins (Chapter 4), withvery high heat capacity for geothermal extraction. It also raises the concern of its eruptive potential. Such a wide and shallow magma body requires careful monitoring, and disaster mitigation.

The return of circulation that occurred after IDDP-1C encountered magma could have been caused by an efficient plugging and healing of the fractured zone in the host rocks by hot sintered magmatic particles (Wadsworth et al., 2016). This is supported by the rise of magma into the well prior to cuttings retrieval, with an initial 9 m push above the well bottom, and a final plug of ~20 m (Friðleifsson et al., 2010).

The geological model across the IDDP-1 blind zone (Fig.5.11) can be used for assessment of host rock properties during future drilling into this interval, as planned by the KMT, and the major variations in drilling parameters characterising the units could help identification of proximity to the magma in real time. The method proposed here could help with examining the lithologies in other blind zones, facilitating the advance of hot drilling technologies. It is a first attempt of considering the drilling logs to interpret rock properties and as such has many limitations, including the uncertainties related to driller operations, the subjectivity of the interpretation, and in the case of the IDDP-1 well side-tracks, the uncertainties related to the averaged depth of the main lithological transitions.

This work constitutes a base towards the development of a robust technique of rock properties interpretation from logs recorded while drilling in on-land installations. The method development is on-going (Villeneuve et al., in prep) and will transpose the advanced tools of tunnel engineering into the field of vertical drilling. In a similar way than the method developed by Hamada (2018), it will use equivalent parameters calculated from basic drilling parameters, to remove artificial variations and allow relative comparison in between stratigraphic sections. As in this chapter, the fully developed methodology will be applied to the IDDP-1 case study where lithologies are known (e.g. Figs.5.4, 5). Once the methodology is validated via comparison with sampled cores, it will be reapplied to provide more constrained information on the blind zone. The conclusions from this chapter are therefore preliminary, and the progress towards publication is cautionary until the full methodology is published in Villeneuve et al. (in prep).

5.7 Conclusion

Based on literature, on drilling knowledge of the authors and with the insight from geothermal scientists and drillers, we propose scenarios of geological encounters with their associated impact on monitored drilling parameters.

Using our simplified scenarios, we propose a method for interpretation of rock properties in blind zones, which requires (1) constructing depth-logs of drilling parameters, and time-logs in intervals where higher resolution is needed, (2) selecting the zone where drilling operations could affect the drilling parameters, therefore not properly suitable for interpretations, (3) picking the variations in the main drilling parameters (ROP, Torque, WOB and RPM) which can be used for interpretations, (4) using the chart to relate to changes in rock properties and building a log of these interpreted properties, (5) interpreting these rock properties in terms of lithology and rock mass characteristics, using calibration with shallower units when relevant.

Comparing the signature in drilling parameters recorded at the bottom of each of the three IDDP-1 holes, we observe a common response of parameters to the magma approach and encounter. This identification reveals that magma was approached nine times during the IDDP-1 drilling and could allow adapted operations during future drilling attempts.

The application of the interpretation method to the IDDP-1 2070-2100 m depth blind zone reveals a ~14.5 m- thick, weak and fractured interval that could be part of the main feed zone and chamber aureole, likely widened by drilling-induced thermal contraction. Below this, the rock strength increases within an irregular ~8 m thick stronger lithology, interpreted as the conductive boundary layer insulating the magma from the fractured zone above. This increase in strength could relate to limited compaction of the weak, low-porosity host felsite in response to the magmatic volume increase.

Assuming that this rhyolite magma body could have been generated in-situ as concluded in Chapter 4, we discuss the analogy with swiftly emplaced intrusions studied in Chapters 2 and 3. We propose the use of the relationship intrusion size/aureole extent (Chapter 3) to estimate the maximum dimension of the Krafla rhyolite magma body, in the range of 700-1100 m thick, with a less likely minimum of 200 m. This proposed size constraint for the IDDP-1 intrusion is crucial for determining the geothermal potential at its margins. Such a large and shallow magma body will require advanced monitoring for eruptibility and drilling impact during the next step of the KMT. The interpretations of the drilling logs proposed in this work could be verified by

core sampling during the next drilling foray into this blind zone. If the results are proven valid, the method could be used worldwide for other geothermal wells.

5.8 Acronyms

BHA – bottom hole assembly

CBL – conductive boundary layer

HVP – high viscous pills (similar to LCM)

IDDP – Iceland Deep Drilling Project

KMT – Krafla Magma Testbed

LCM – lost circulation material

POOH – pulling out of the hole

ROP – rate of penetration

RPM – rotation per minute

SPP – standpipe pressure

UCS – uniaxial compressive strength

WOB – weight on the bit

5.9 References

Annen, C., 2017. Factors affecting the thickness of thermal aureoles. Frontiers in Earth Science, 5, doi: 10.3389/feart.2017.00082

Archer, S., Bergman, S., Iliffe, J., Murphy, C., Thornton, M., 2005. Palaeogene igneous rocks reveal new insights into the geodynamic evolution and petroleum potential of the Rockall Trough, NE Atlantic Margin. Basin Research 17, 171–201.

Axelsson, G., Egilson, T., Gylfadóttir, S. S., 2014. Modelling of temperature conditions near the bottom of well IDDP-1 in Krafla, Northeast Iceland. Geothermics, 49, 49–57, doi: 10.1016/j.geothermics.2013.05.003

Azar, J. J., Samuel, G. R., 2007. Drilling Engineering. PennWell Books.

Boghdady, G. Y., 2010. Mechanical and geological Influences on drilling limestone rock at low rotary speed. Journal of Engineering Sciences, 38(1), 259–270.

Chowdhury, D., Skalle, P., Rahman, M. M. (2009). Prediction of stand pipe pressure using conventional approach. Chemical Engineering Research Bulletin, 13(1), 7-11

Coats, R., Kendrick, J. E., Wallace, P. A., Miwa, T., Hornby, A. J., Ashworth, J. D., Matsushima, T., Lavallée, Y., 2018. Failure criteria for porous dome rocks and lavas: a study of Mt. Unzen, Japan. Solid Earth, 9(6), 1299–1328, doi: 10.5194/se-9-1299-2018

Datwani, A., 2012. Review of lost circulation mechanisms with the focus on loss to natural and drilling induced fractures. Dalhousie University, Halifax, Nova Scotia.

Eggertsson, G. H., Lavallée, Y., Kendrick, J. E., Markússon, S. H., 2018. Improving fluid flow in geothermal reservoirs by thermal and mechanical stimulation: The case of Krafla volcano, Iceland. Journal of Volcanology and Geothermal Research, doi: 10.1016/j.jvolgeores.2018.04.008

Eggertsson, G. H., 2019. Constraining mechanical and permeability properties of the Krafla geothermal reservoir, North-East Iceland. PhD Thesis, University of Liverpool.

Eichelberger, J., 2019. Planning an International Magma Observatory. Eos, 100.

Elders, W. A., Friðleifsson, G. Ó., Zierenberg, R. A., Pope, E. C., Mortensen, A. K., Guðmundsson, Á., Lowenstern, J. B., Marks, N. E., Owens, L., Bird, D. K., Reed, M., Olsen, N. J., Schiffman, P., 2011. Origin of a rhyolite that intruded a geothermal well while drilling at the Krafla volcano, Iceland. Geology, 39(3), 231–234, doi: 10.1130/G31393.1

Friðleifsson, G. O., Elders, W. A., 2005. The Iceland Deep Drilling Project: a search for deep unconventional geothermal resources. Geothermics, 34(3), 269–285, doi: 10.1016/j.geothermics.2004.11.004

Friðleifsson, G. Ó., Pálsson, B., Stefánsson, B., Albertsson, A., Gunnlaugsson, E., Ketilsson, J., Lamarche, R., Andersen, P., 2010. Iceland Deep Drilling Project. The first IDDP drill hole drilled and completed in 2009.

Ghosh, R., Gustafson, A., Schunnesson, H., 2018. Development of a geological model for chargeability assessment of borehole using drill monitoring technique. International Journal of Rock Mechanics and Mining Sciences 109, 9–18.

Gudmundsson, A., Steingrimsson, B., Sigursteinsson, D., Gislason, G., Sigvaldason, H., Holmjarn, josef, Helgadottir, H., 2008. Krafla – Well KG-25 Drilling, geology and geochemistry. ISOR Iceland geosurvey, p.30

Halldorsdottir, S., Axelsson, G., Berre, I., Keilegavlen, E., 2019. Enhanced fluid convection and heat transfer near the bottom of the IDDP-1 well in Krafla, NE Iceland. European Geothermal Congress

Hamada, Y., Kitamura, M., Yamada, Y., Sanada, Y., Sugihara, T., Saito, S., Moe, K., Hirose, T., 2018. Continuous depth profile of the rock strength in the Nankai accretionary prism based on drilling performance parameters. Scientific Reports, 8, 1–9, doi: 10.1038/s41598-018-20870-8

Harnett, C. E., Kendrick, J. E., Lamur, A., Thomas, M. E., Stinton, A., Wallace, P. A., Utley, J. E. P., Murphy, W., Neuberg, J., Lavallée, Y., 2019. Evolution of mechanical properties of lava dome rocks across the 1995–2010 eruption of Soufrière Hills volcano, Montserrat. Frontiers in Earth Science, 7, doi: 10.3389/feart.2019.00007

Heap, M. J., Coats, R., Chen, C., Varley, N., Lavallée, Y., Kendrick, J., Xu, T., Reuschlé, T., 2018. Thermal resilience of microcracked andesitic dome rocks. Journal of Volcanology and Geothermal Research, 367, 20–30, doi: 10.1016/j.jvolgeores.2018.10.021

Hólmgeirsson, S., Gudmundsson, A., Pálsson, B., Bóasson, H. Á., Ingason, K., Þórhallsson, S., 2010. Drilling operations of the First Iceland Deep Drilling Well (IDDP). Proceeding World Geothermal Congress.

Ingason, K., Kristjánsson, V., Einarsson, K., 2014. Design and development of the discharge system of IDDP-1. Geothermics, 49, 58–65, doi: 10.1016/j.geothermics.2013.05.002

ISOR Iceland geosurvey, 2009. IDDP-1 - Krafla, Vitismor - Production casing (No. 119).

Kahraman, S., Bilgin, N., Feridunoglu, C., 2003. Dominant rock properties affecting the penetration rate of percussive drills. International Journal of Rock Mechanics and Mining Sciences, 40, 711–723.

Karasawa, H., Ohno, T., Kosugi, M., Rowley, J. C., 2002. Methods to estimate the rock strength and tooth wear while drilling with roller-bits—part 1: milled-tooth bits. Journal of Energy Resources Technology, 124(3), 125-132

Lamur, A., Kendrick, J. E., Eggertsson, G. H., Wall, R. J., Ashworth, J. D., Lavallée, Y., 2017. The permeability of fractured rocks in pressurised volcanic and geothermal systems. Scientific Reports, 7

Lavallée, Y., Heap, M. J., Kendrick, J. E., Kueppers, U., Dingwell, D. B., 2019. The Fragility of Volcán de Colima—A Material Constraint. In N. Varley, C. B. Connor, J.-C. Komorowski (Eds.), Volcán de Colima: Portrait of a Persistently Hazardous Volcano, 241–266, Springer, doi: 10.1007/978-3-642-25911-1_7

Lavallée, Y., Lamur, A., Kendrick, J. E., Eggertsson, G. H., Weaver, J., Eichelberger, J. C., Papale, P., Sigmundsson, F., Dingwell, D. B., Markússon, S. H., Mortensen, A. K., 2020. Thermal manipulation of magma boundaries: advancing controls on fluid flow via the Krafla Magma Testbed (KMT). Proceeding World Geothermal Congress, 11.

Lowell, R. P., Germanovich, L. N., 1994. On the temporal evolution of high-temperature hydrothermal systems at ocean ridge crests. Journal of Geophysical Research: Solid Earth, 99(B1), 565–575, doi: 10.1029/93JB02568

Majidi, R., Albertin, M., Last, N., 2017. Pore-pressure estimation by use of mechanical specific energy and drilling efficiency. SPE Drilling & Completion, 32(02), 97–104, doi: 10.2118/178842-PA

Masotta, M., Mollo, S., Nazzari, M., Tecchiato, V., Scarlato, P., Papale, P., Bachmann, O., 2018. Crystallization and partial melting of rhyolite and felsite rocks at Krafla volcano: A comparative approach based on mineral and glass chemistry of natural and experimental products. Chemical Geology, 483, 603–618, doi: 10.1016/j.chemgeo.2018.03.031

Maurer, W. C., 1962. The ‘perfect - cleaning’ theory of rotary drilling. Journal of Petroleum Technology, 14(11), 1 270-1 274, doi: 10.2118/408-PA

Millett, J. M., Wilkins, A. D., Campbell, E., Hole, M. J., Taylor, R. A., Healy, D., Jerram, D. A., Jolley, D. W., Planke, S., Archer, S. G., Blischke, A., 2016. The geology of offshore drilling through basalt sequences: Understanding operational complications to improve efficiency. Marine and Petroleum Geology, 77, 1177–1192, doi: 10.1016/j.marpetgeo.2016.08.010

Mortensen, Anette K., Grönvold, K., Gudmundsson, Á., Steingrímsson, B., Egilson, Þ., 2010a. Quenched silicic glass from well KJ-39 in Krafla, North-Eastern Iceland. Proceeding World Geothermal Congress, 6.

Mortensen, A., Egilson, Þ., Arnadottir, S., Gautason, B., Sigurgeirsson, M., Ingimarsdottir, A., Tryggvason, H., Gunnarsson, H. S., Jónsson, R. B., Sveinbjörnsoon, S., Þorsteinsson, E., 2010b. Krafla – IDDP-1. Drilling completion and geology report for drilling stage 3. Landsvirkjun LV-2010/130, p. 118

Mortensen, A. K., Egilson, Gautason, B., Arnadottir, S., Gudmundsson, A., 2014. Stratigraphy, alteration mineralogy, permeability and temperature conditions of well IDDP-1, Krafla, NE-Iceland. 49, 31–41, doi: 10.1016/j.geothermics.2013.09.013

Nield, T., 1985. Onshore oil is all set to grow. New Scientist, 39.

Pálsson, B., Hólmgeirsson, S., Guðmundsson, Á., Bóasson, H. Á., Ingason, K., Sverrisson, H., Thórhallsson, S., 2014. Drilling of the well IDDP-1. Geothermics, 49, 23–30, doi: 10.1016/j.geothermics.2013.08.010

Papale, P., Eichelberger, J., Ingolfsson, H. P., Lavallée, Y., Ludden, J., Markusson, S., 2020. the KMT – Krafla Magma Testbed breaking-through perspective. Proceeding World Geothermal Congress, 5.

Reinsch, T., Dobson, P., Asanuma, H., Huenges, E., Poletto, F., Sanjuan, B., 2017. Utilizing supercritical geothermal systems: a review of past ventures and ongoing research activities. Geothermal Energy, 5(1), doi: 10.1186/s40517-017-0075-y

Saubin, E., Kennedy, B. M., Tuffen, H., Villeneuve, M., Davidson, J., Burchardt, S., 2019. Comparative field study of shallow rhyolite intrusions in Iceland: emplacement mechanisms and impact on country rocks. Journal of Volcanology and Geothermal Research, doi: 10.1016/j.jvolgeores.2019.106691

Saubin, E., Kennedy B. M., Tuffen, H., Nichols A., Villeneuve, Bindeman I., Mortensen A., Schipper C. I., Wadsworth F. B., Watson T., Zierenberg R., 2020. Textural and geochemical

window into the IDDP-1 rhyolitic melt, Krafla, Iceland, and its reaction to drilling. In review for Geological Society of America Bulletin.

Saubin, E., Kennedy B. M., Wang H., Tuffen, H., Villeneuve, M., Burchardt S., Davidson J., Rule G., 2020. Rapid heat transfer at the margins of thin rhyolite intrusions. In prep

Schaefer, L. N., Kendrick, J. E., Oommen, T., Lavallée, Y., Chigna, G., 2015. Geomechanical rock properties of a basaltic volcano. Frontiers in Earth Science, 3, doi: 10.3389/feart.2015.00029

Siratovich, P.A., Heap, M.J., Villeneuve, M.C., Cole, J.W., Kennedy, B.M., Davidson, Reuschlé., 2016. Mechanical behaviour of the Rotokawa Andesites (New Zealand): Insight into permeability evolution and stress-induced behaviour in an actively utilised geothermal reservoir. Geothermics 64, 163–179. doi: 10.1016/j.geothermics.2016.05.005

Teale, R., 1965. The concept of specific energy in rock drilling. In International Journal of Rock Mechanics and Mining Sciences & Geomechanics Abstracts, Vol. 2, No. 1, pp. 57-73

Ujiie, K., Inoue, T. & Ishiwata, J., 2016. High-velocity frictional strength across the Tohoku-Oki megathrust determined from surface drilling torque. Geophysical Research Letters 43, doi: 10.1002/2016GL067671.

Villeneuve, M., Saubin, E., Mortensen, A., Kennedy, B., in prep. A method to inform rock properties from drilling logs.

Wadsworth, F. B., Vasseur, J., Llewellin, E. W., Schauroth, J., Dobson, K. J., Scheu, B., Dingwell, D. B., 2016. Sintering of viscous droplets under surface tension. Proceedings of the Royal Society A: Mathematical, Physical and Engineering Sciences, 472(2188), 20150780, doi: 10.1098/rspa.2015.0780

Warren, T. M., 1984. Factors affecting torque for a roller cone bit. Journal of Petroleum Technology, 36(09), 1 500-1 508, doi: 10.2118/11994-PA

Wolcott, D. S., Bordelon, D. R., 1993. Lithology determination using downhole bit mechanics data. In SPE annual technical conference and exhibition. Society of Petroleum Engineers.

Wyering, L. D., Villeneuve, M. C., Kennedy, B. M., Gravley, D. M., Siratovich, P. A., 2017. Using drilling and geological parameters to estimate rock strength in hydrothermally altered rock – A comparison of mechanical specific energy, R/N-W/D chart and Alteration Strength Index. Geothermics, 69, 119–131, doi: 10.1016/j.geothermics.2017.05.008

Chapter 6 – Conclusions

6.1 Key findings

This thesis aimed to constrain various aspects of the active Krafla rhyolite intrusion encountered by the IDDP-1 well, and the results are summarised in the overview sketch of Figure 6.1. These successfully answered the following general research questions:

1. What are the rock properties at the margins of shallow rhyolite intrusions, specifically around the active Krafla rhyolite magma body?

2. What are the size and structure of the active Krafla rhyolite intrusion?

3. How does magma react to drilling, and drilling react to magma?

These questions are targeted with three complementary geological approaches: the analogy of rock properties of fossil rhyolite intrusions in Iceland are used in Chapters 2 and 3 to answer question (1) and help resolve question (2); textural and geochemical analyses on the obsidian particles retrieved from the IDDP-1 well are used in Chapter 4 to answer questions (2) and (3); the engineering analysis of the drilling parameters recorded in the vicinity of the intrusion is used in Chapter 5 to answer questions (1) and (3).

The field case-studies of three shallow rhyolite intrusions in Iceland (Landsendi at Njardvik, Hrafntinnuhryggur at Krafla and Deildargil at Húsafell), within four country-rock types (basalt lava, basalt hyaloclastite, welded ignimbrite and conglomerate, respectively), reveal that host rocks are impacted differently by the intrusion depending on their initial rock properties, which in turn impacts the magma propagation style. Initially weak, porous and highly-permeable conglomerate and hyaloclastite (estimated initial UCS <15) respond by pore occlusion, with porosity reduced by compaction and/or mineral precipitation, with discoloration and permeability decreased accordingly by >1 order of magnitude. The inelastic accommodation to magma propagation allows irregular intrusive geometries to form. In contrast, initially strong, low-permeability basaltic lava and welded ignimbrite (estimated initial UCS >90) respond by weakening, with intense fracturing and exploitation of fractures by tuffisite veins weakening the rock by a factor >2. These rocks require accumulation of magmatic pressure with systematic formation of tuffisite veins prior to intrusive emplacement.

Widening the field study to 14 shallow rhyolite intrusions in Iceland and worldwide, <1 km depth and < 1 km thick, from field-work in this thesis and existing literature, the comparison of dimensions reveals large-scale trends. The thickness of the macro-scale aureole in host rocks increases with the intrusion size, and is larger than predicted by conduction models (depending on initial assumptions) when the intrusion is small (<10 m). At the interface chilled margins thickness can vary strongly, but results are in accordance with heat transfer by conduction: glass formation cannot extend beyond a maximum of 7 m thick for >12 m wide intrusions.

The micro-scale study of obsidian and felsite cuttings retrieved from IDDP-1 well, after it had intercepted molten rock, provides information on the magma genesis, its storage structure and its reaction to drilling. The encountered magma was generated by two-steps of partial melting of felsite, likely at the margins of an intrusive basalt or silicic magma, and promoted by hydration via hydrothermal fluid circulation. The melts were segregated into layers or pockets, with clear melt, formed from low degree partial melting, overlaying the main brown melt that formed from higher degrees of partial melting. Melts experienced restricted degassing probably prior to the well interception and quenching. The drilling triggered additional rapid but stunted decompression, with limited degassing and vesicle deformation.

When approaching the magma at 2104.4 m depth, the drilling fluids were lost into permeable rocks and no cuttings were retrieved over the ~2070-2104 m interval. The response of drilling parameters within this blind zone and when encountering magma help to constrain rock properties around the intrusion. It reveals a ~14.5 m thick weak and fractured interval that is interpreted as part of the circulating hydrothermal system, enhanced by drilling-induced thermal fracturing, and possibly affected by the intrusion. A part of an 8 m thick stronger lithology is interpreted to be the conductive layer separating the hydrothermal system from the magma beneath. The high strength of this aureole in the host rock could have been caused by compaction. An 8-22 m thick damaged layer corresponds to a 700-1100 m thick magma chamber using the relationship from Chapter 3, and discussing analogy. I additionally identify how drilling parameters react as the drill approaches and encounters the magma, which reveals that the rhyolite melt was approached nine times during the IDDP-1 drilling.

TABLE 6.1. THESIS OUTCOMES

	Questions addressed	Outcomes
Chapter 2	*What are the properties of country rocks at the margins of shallow rhyolite intrusions?* *How might country rock influence the emplacement of the intrusion?*	Host rock reaction to shallow intrusion by rhyolite depends on initial rock properties. Strong rocks (basalt and welded ignimbrite) are fractured, with decreased strength and increased permeability. Weaker rocks (conglomerate and hyaloclastite) have decreased permeability, pore occlusion and increased fracturing. These responses in turn affect the intrusive emplacement, allowing various intrusive shapes in weak rocks, but following initial fracture planes in strong rock with development of tuffisite veining.
Chapter 3	*Does the thickness of intrusion impact the extent of damage and alteration in country rocks and the extent of the chilled margins?* *What are the dominant mechanisms of heat transfer between the magma and the country rock?*	The thickness of host rocks damaged and altered by the intrusion increases with intrusion size. Thermal aureoles around <10 m thick intrusions cannot be caused by conduction alone. Convection/advection of hot fluids through the fractured interface is also suggested. The maximum extent of chilled margins (7 m) is reached for ~12 m thick intrusions, beyond which there is no direct relationship to intrusion size.
Chapter 4	*What is the magma structure in the intrusion margin?* *How did magma react to drilling?* *What is the origin of the IDDP-1 intrusion?*	Componentry, texture and chemistry support that IDDP-1 melt is generated by in-situ bimodal partial melting of the host felsite, with high degree melting in the core and low degree at the margins. Vesicle textures highlight that melts are not interstitial, and responded to drilling by decompression, which triggered bubble nucleation and coalescence. Chemistry and thermodynamic analyses suggest that currently ongoing felsite melting is triggered by heat released from a shallow intrusion, and promoted by hydration via hydrothermal fluids.
Chapter 5	*What are the rock properties in the blind zone as the IDDP-1 intrusion is approached?* *What is the size of the intrusion?*	Drilling parameters response to geological scenarios are reviewed. A method is proposed for interpretation of rock properties from drilling parameters only. Above the IDDP-1 intrusion, a strong 8 m thick layer is potentially damaged by the intrusion. It insulates magma from the overlying weak ~14.5 m thick zone, the permeability of which is enhanced by interactions with drilling and potentially by the intrusion. Synthesising conclusions from Chapters 2-5, the IDDP-1 intrusion is estimated to likely be 700-1100 m thick.

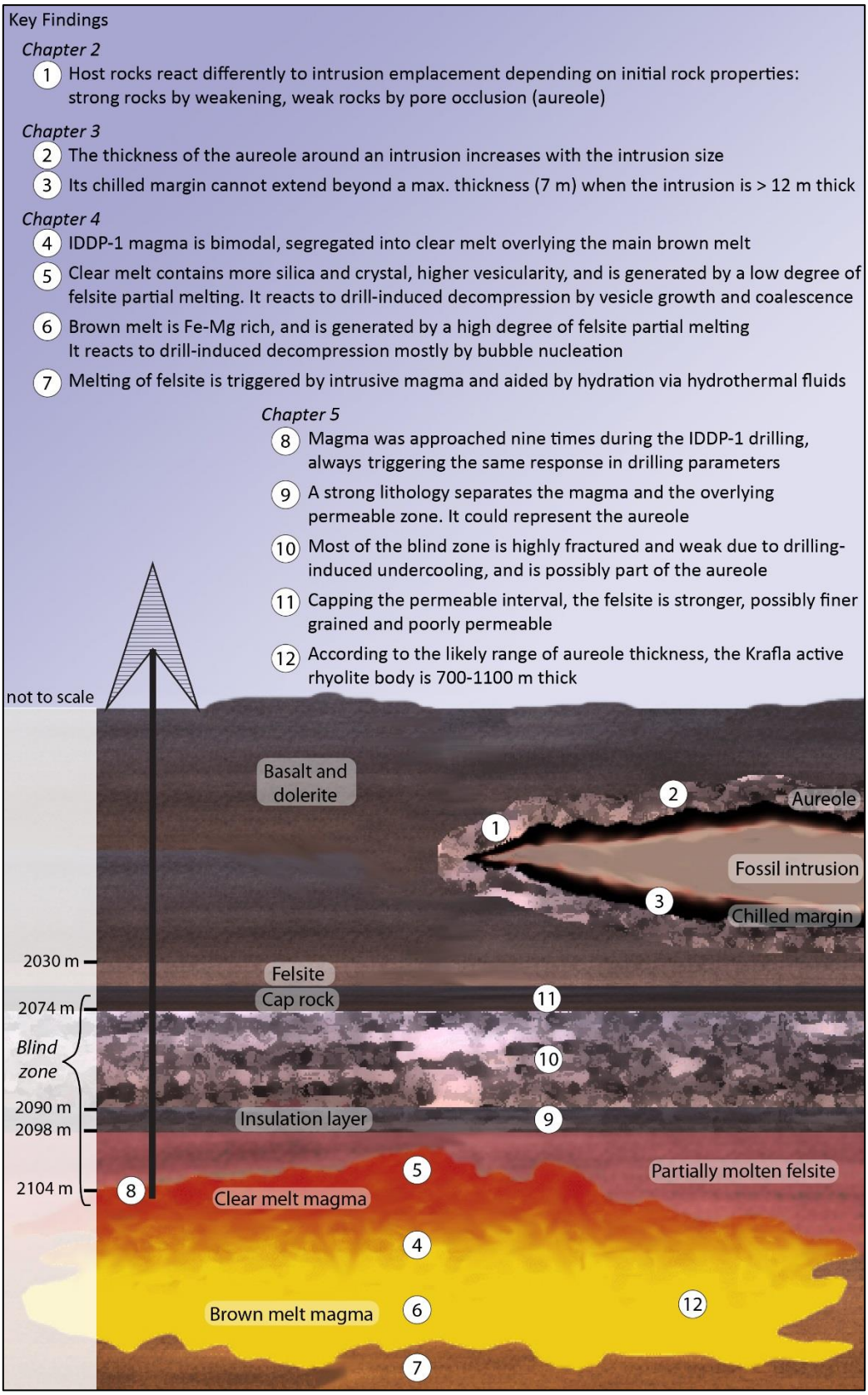

Figure 6.1. Key findings from the core chapters of this dissertation: properties of the IDDP-1 magma body and the rocks hosting it (main intrusion in the sketch) and contributions to our understanding of shallow rhyolite intrusions (smaller intrusion in the sketch). For more details about specific findings, see the related chapter. Adapted from Carricchi and Blundy, 2015.

6.2 Future work

This Ph.D has successfully answered most of the questions that initially drove this research. There are, however, a few initial questions that remain unanswered, which I highlight below. Several preliminary results obtained were not fully explored because of insufficient time or space. These will form the basis for future and on-going work in our wider research group.

The key question of *Why did not the magma interception trigger an eruption?* was initially critical to address. However, after discussion with key geothermal scientists and volcanologists (AGU 2017 pod meeting), I realised it was commonly accepted that quenching of magma by drilling fluids before catastrophic decompression prevented any surface eruption in the case of IDDP-1, as well as for the other encounters that there have been between drilling and magma (K-39 in Iceland, MW-04 and MW-06 in Kenya, KS-13 in Hawaii; Reinsch et al., 2017). However, this question still remained in my mind, in case I could find any evidence to support the assumption. It also influenced a secondary question, *Which processes caused magma fragmentation within the well?* The initial hypotheses were fragmentation by quenching, by decompression and degassing, or by drill abrasion. I aimed to investigate these hypotheses based on the shape of the obsidian cuttings. The results are intriguing but not included in the thesis, as the methods chosen and the results require additional analysis. However, results were promising and the 3-D reconstruction of these particles using X-ray scans later provided unprecedented insights into their texture and shape, which strongly suggest that texture and shape depend on the type of fragmentation involved. I therefore plan to pursue this investigation with more 3D scans, in collaboration with Ben Kennedy and Ian Schipper.

The answers to the main questions driving this thesis can still be further developed, and these themes can be broadened.

1. What are the rock properties at the margins of shallow rhyolite intrusions, specifically around the active Krafla rhyolite magma body?

2. What are the size and structure of the active Krafla rhyolite intrusion?

3. How does magma react to drilling, and drilling react to magma?

Rock properties around the IDDP-1 magma body are informed by how the drilling parameters evolved during the drilling and by analogies with field intrusions. The interpretive method developed in Chapter 5 to constrain rock mass properties in blind zones is the first attempt to

extract this type of information from drilling parameters alone. This requires a more robust approach and rigorous testing with well-known drilled geological intervals before publication. Development of this methodology is on-going, led by Marlene Villeneuve, transposing well-informed tunnel engineering tools into vertical geothermal drilling. Once the methodology is tested and published, it will be again applied to the IDDP-1 blind zone in order to provide a rigorous basis to interpret the lithology. This is a critical step in improving reservoir knowledge and developing drilling engineering to tackle blind zones.

The future direction for using fossil intrusions as analogues to the IDDP-1 magma body, would be to target rhyolite intruding though granite or felsite, although currently I do not know of any suitable locations. This would allow the implications of *in situ* remelting at the margins of the active Krafla rhyolite body to be better interpreted.

The paleodepths of the fossil intrusions studied in this thesis are <1 km. Our results on rock alteration and damage around rhyolite intrusions thus need to be extrapolated to greater depths to examine the broader implications. High temperature and pressure laboratory analogy experiments (e.g, Mordensky et al., 2018) could help in identifying the expected mineralogies and textures when intrusions are emplaced at greater depth.

The hypothesis raised in Chapter 3, concerning a quick heat transfer via fluids advection and convection through fractures around shallow intrusions of rhyolite, could be examined using mineral precipitation within fractures. As it is already observed by Liotta et al. (2018), circulation of hydrothermal fluids may seal the fractures and affect permeability around the intrusion, impacting the whole hydrothermal system above. This requires further consideration of the fault network and fractured state of surrounding formations.

Further information on *the size and structure of the IDDP-1 magma body* (Chapters 4 and 5) could be gained from comparing the cuttings and cores from IDDP-1 with those from other wells that encountered magma (Reinsch et al., 2017). Analysis of obsidian cuttings from KJ-39 at Krafla, provided by Anette Mortensen from Landsvirkjun (National power company of Iceland), is currently underway by UC Masters student Georgie Rule, aiming to constrain the horizontal extent of the active Krafla magma.

The size of the IDDP-1 intrusion is estimated using the relationship between aureole thickness and intrusion size, revealed in Chapter 3 for shallow rhyolite intrusions. The analogy that these have with the IDDP-1 magma is discussed in the same chapter. The relationship is based on 14 field case-studies, but a higher number is still required to confidently confirm the trend. Fossil

rhyolite intrusions in the TVZ in New Zealand could be investigated to complete the data set, as they fit within the scope of this work.

The drilling parameters that have been identified to respond as the magma is approached need to be examined in other wells worldwide, in order to establish whether they respond in every case that magma is encountered. Is what is valid for the IDDP-1 magma body and the type of technology used there also valid in identifying the proximity of magma in other wells?

A further area of study arising from our field observations in Chapters 2 and 3 is the quantification and modelling of the macro scale permeability and heat transfer related to the high fracture density in the strong rocks hosting the intrusions and in the chilled margins. This permeability development is assumed to play a major role in the heat transfer at the interface, possibly by convection and advection by outgassing and fluid circulation. However, the quantification of such permeability development is still to be addressed, as is the role of chilled margin fracturing in the extent of the thermal aureole around intrusions.

The initial objective of using 3-D X-ray tomography for vesicle analysis in order to examine *How the IDDP-1 magma responded to drilling* had to be shifted to the use of 2-D backscatter images, in Chapter 4. This method allowed larger datasets to be collected faster, and use FOAMS software to adjust to 3-D results. However, better-quality and more detailed insights into the degassing and vesiculation history of the IDDP-1 magma could still be gained from 3-D X-ray tomography of the cuttings. As the X-ray tomography also provides data for clast shape analysis, a new study is planned to combine this with vesicle shape and distribution analyses, including additional mapping of water content focussed around collapse textures. Along with the timeline of drilling events, it will better constrain timescales of degassing, magma decompression and fragmentation interpreted in Chapter 4.

The conclusions of this thesis will hopefully be tested during future drilling by the KMT project (Eichelberger et al., 2019). Core sampling through the blind zone will conclusively answer what the nature of these rocks and magma is, and help constrain the present state of the intrusion and the processes occurring at the interface with the host rocks. The planned sampling of magma over time periods would also allow the impact of drilling on magma to be monitored in detail.

6.3 Applications and limitations for the future

Our results highlight that the active rhyolite magma body, targeted at Krafla for future development in geothermal energy, is likely to be large, have ongoing melting at its margins, and thus constitute a powerful and sustained heat source. The highly fractured and permeable overlying interval is suitable for hydrothermal fluid circulation, confirming the viability of the KMT. However, as this thesis contributes to the field of geothermal research, it is crucial to examine the conditions in which our conclusions will favour sustainable energy development. This section develops the role of geothermal energy in the current transition towards sustainable energy production, with an insight on Iceland, New Zealand and KMT, and the ecological implications.

Many studies and media support geothermal energy as a part of the solution in the current global crisis we face (e.g. Friðleifsson et al., 2018; Schnell et al., 2019; Elders et al., 2019). This positive image assures a comfortable reputation, but overlooks the longer-term consequences arising from geothermal exploitation. Oil and gas industries, nuclear power plants and plastic were created in times when we needed them. These examples illustrate that satisfying our immediate needs with immediate solutions can endanger the future generations and the world they live in (e.g. Commoner, 1971). Therefore, approaching geothermal development from an ecological point of view is required to anticipate and possibly prevent a future global emergency. A critical and overall examination of the proposed solutions for global warming is required to fully understand their long-lasting consequences and thus their sustainability.

Geothermal energy is recognised as one of the lowest carbon emission energies with a low ecological footprint. It is a stable, renewable energy source generating reliable power and heat, and thus balancing supplies from other renewable sources that are intermittent owing to their dependence on weather, climate, and/or daylight conditions (Eichelberger, 2019; Schnell et al., 2019). Whereas ‘renewable’ concerns the nature of the geothermal resource, ‘sustainable’ concerns the way we use it. Geothermal energy exploits a resource, and is thus only sustainable as long as it does not exhaust the source. Preventing this is a major concern in any geothermal field, which requires a production rate that is lower than the system recovery rate, an incremental, monitored increase in production, or intermittent energy production to allow the system to recover. In the competitive energy market, geothermal energy is only attractive to end-users if it produces stable and constant power, so fallow periods may be infeasible.

The balance between sustainable exploitation and economic needs therefore often results in exploitation of the resources at a continuous rate below a sustainable threshold appropriate for each system. Modelling can provide a maximum energy production rate under which the production can be maintained for 100-300 years (Axelsson and Stefansson, 2002; Axelsson, 2010; Burnell et al., 2016). Although this timescale is long from an individual point of view, and potentially twice as long as petroleum exploitation, it also suggests that systems are inevitably exhausted in the future, and energy production will cease in the long-term - unless the geothermal industry can be developed to be sustainable at an improved scale. This risk of overexploitation is one among the many issues reviewed by Shortall et al. (2015), considering that sustainability includes the management of all the impacts the exploitation of geothermal energy has on the environment and population.

The monitoring of the Krafla geothermal field in Iceland reveals a stable heat capacity for the overall system, and stable production, with local variations. Some sub-areas are in decline, with natural end-of-life for old geothermal resources promoted by cooling from cold reinjection fluids (Weisenberger et al., 2015). In the Taupo Volcanic Zone in New Zealand, the exploitation of geothermal fields is shared between several geothermal industries, with no central repository of data. The regional councils classified the fields according to permitted level of production that would not have adverse effects, and expect this resource management to sustain 100 years of production (Burnell et al., 2016).

For a responsible transition, one needs to take into account both short-term as well as long-term concerns, especially for the visionary and ambitious project of the KMT. Identifying the risks and possible negative consequences will not help us to resolve the ecological crisis. In this context, constructive solutions are preferable to obstructing worries. Assuming the necessity to counter global warming and to better adapt to our environment eventually leads to a drastic change within industrial management, all renewable resources that we can develop need to be combined to undertake the transition that is required, with none of them put aside (e.g. Schnell et al., 2019). Regarding geothermal resources, evidence for their energetic potential are stacking up and we keep discovering new ways to use them and improve the extraction efficiency (e.g. Schnell et al., 2019; Elders et al., 2019). In this context, the most significant achievement of the KMT will be a step towards greater sustainability in exploiting geothermal energy - by economic improvements, increased production efficiency, greater monitoring of the system, better information on recharge rate, and controlled environmental footprint (deep wells are drilled from existing shallower wells; Friðleifsson et al., 2018; Eichelberger, 2019).

A complete review of the risks, difficulties and ecological consequences related to the KMT, together with proposed solutions, is a necessary step. I note that this is partly highlighted in recent studies (e.g. Lavallée et al., 2020) and that work on risk assessment is ongoing (Ilic et al., 2020). It is likely that these questions will be addressed by an increased number of studies in the months and years to come.

6.4 Scientific implications

The research I present has a swath of large-scale implications. On the local scale, it concerns the IDDP-1 magma body; therefore, the Krafla caldera, the Landsvirkjun geothermal power station located there, and the on-going KMT project. On the national scale, the location of our fieldwork contributes to understanding the geology of Iceland. On the international scene, it addresses the worldwide development of geothermal energy and critical questions regarding how magma intrudes, is stored and eventually cools. What I have learnt from the case studies in Iceland can be transposed to other countries that have the potential to, or already exploit geothermal energy, such as New Zealand, where the funding for this work comes from.

My results, specifically on the IDDP-1 magma body at Krafla, suggest that low degree melting is still occurring at the margins (Chapter 4) and that the intrusion is 700-1100 m thick (Chapter 5). The last eruptive activity of the Krafla Fires (1975-1984) could have generated a heat flux fron intrusive basalts high enough to melt the required volume of felsite to produce the IDDP-1 magma body, however the idea of a longer-lived magma body should also be considered. Such a growing large reservoir at this shallow depth (2 km) could have dangerous consequences if it catastrophically erupts, highlighting the need and the importance of continued and improved monitoring. The development of plans to re-drill and re-intercept the magma (KMT project; Eichelberger, 2019) therefore needs a robust risk management plan, and the monitoring objective of the project should remain central.

Additionally, such a large intrusion maintained by heat flux from a deeper basaltic magma could sustain long-term and powerful geothermal energy production, with fast rate of heat recharge constituting an adequate renewable energy source. The 8 ± 5 m thick strong conductive boundary layer, identified between the molten felsite and the overlying permeable feed zone (Chapter 5), implies that most of the high geothermal gradient could be concentrated into this layer rather than in the full 30 m interval of the blind zone (Schiffman et al., 2014). The major

lithological variations within this interval, including the magma that was encountered during the drilling, are each characterised by a response in drilling parameters, common to all three drill legs that went through the blind zone (Chapter 5). These typical signatures could help real time identification of rock properties during future drilling towards the IDDP-1 magma body. The precise location of these geological units would help in the real time decision-making process, for drill operations and in adapting the tools for engineering. In addition, the method proposed to assess rock properties in blind zones could be applied worldwide where drilling encounters similar difficulties (deep drilling projects, reviewed in Reinsch et al., 2017).

Hydrothermal systems are often associated with shallow intrusions at restless calderas such as Krafla (Lipman, 1992; Stix et al., 2003; Stelling et al., 2016). The understanding of the extent of re-melting process in restless calderas, as identified for the IDDP-1 intrusion (Chapter 4), and adequate geophysical detection of such shallow silicic intrusions, are critical for monitoring at this type of volcanoes. Subsurface generation of rhyolite melt could depend on magma genesis by re-melting, which could be a key process to consider when both prospecting for geothermal energy exploitation and conducting volcanic hazard assessment. Additionally, forecasting of silicic magma mobility relies on the interpretation of deformation and seismic data, and therefore also directly relates to the deformation response of intruded country rock (Newman et al., 2006; Masterlark et al., 2010). The strong dependence of this response on the initial properties of the country rock (Chapter 2) highlights the importance of robustly characterising the mechanical properties of caldera-filling formations, to enable appropriate geophysical data interpretation. Our field data reveal that the larger the intrusion, the larger the extent of the impacted country rocks (Chapter 3). Thus, inversely, knowing the thickness of the aureole can inform the size of the magma chamber, for both active and fossil bodies that fall within the limitations of this study.

This thesis has provided a greater understanding of fossil shallow rhyolite intrusions, especially the studied Icelandic locations of Njardvik (East fjords), Hrafntinnuhryggur (Krafla) and Húsafell (West Iceland). This includes mapping of key areas and 3D photogrammetry, with information on lithologies, rock properties, fracturing and emplacement processes of the intrusions.

The examination of heat transfer for geothermal resources was initiated within the context of Icelandic central volcanoes and shallow rhyolite magma bodies, but the findings can be applied more widely, to other locations and settings. The properties of damaged and altered country

rocks influence the mode of heat transfer and fluid circulation and the origin and extent of overlying hydrothermal systems, and thus the architectures of hydrothermal systems (Chapter 2). Comparison of field data with numerical modelling of heat diffusion demonstrates that other processes of heat transfer are likely (Chapter 3). The extensive fracturing at the interface magma/host rocks strongly suggests higher rates of heat convection and advection through outgassing and fluid flow (Chapters 2 and 3). The aureole in host rocks around small intrusions is therefore larger than predicted by conduction, and the accumulation of small magma bodies could in some cases result in more dynamic hydrothermal systems than around single large intrusions. Small magmatic bodies may thus provide a previously under-exploited source of geothermal energy.

The multidisciplinary approach used in this thesis has contributed to building a bridge between the fields of drilling engineering, rock mechanics and volcanology, which is essential for future developments in geothermal energy production. The results and implications of this thesis are a new step towards the development of geothermal energy, and a new piece in the jigsaw to understand shallow rhyolite intrusions as roots for hydrothermal systems.

6.5 References

Axelsson, G., Stefansson, V., Xu, Y., 2002. Sustainable management of geothermal resources, Proceedings. In 2002 Beijing International Geothermal Symposium, China Geological Publishing House.

Axelsson, G., 2010. Sustainable geothermal utilization – Case histories; definitions; research issues and modelling. Geothermics, 39(4), 283–291, doi: 10.1016/j.geothermics.2010.08.001

Burnell, J., Campen, B. van, Kortright, N., Lawless, J., McLeod, J., Luketina, K., Robson, B., 2016. Sustainability of TVZ geothermal systems: The regulatory perspective. Geothermics, 59, 225–235, doi: 10.1016/j.geothermics.2015.08.001

Caricchi, L., Blundy, J., 2015. The temporal evolution of chemical and physical properties of magmatic systems. Geological Society, London, Special Publications, 422(1), 1–15, doi: 10.1144/SP422.11

Commoner B., 1971. The Closing Circle: Nature, Man, and Technology. New York: Knopf, chapter 1.

Eichelberger, J., 2019. Planning an International Magma Observatory. Eos, 100.

Elders, W. A., Osborn, W. L., Raju, A. S. K., Martinez-Morales, A., 2019. The future role of geothermal resources in reducing greenhouse gas emissions in california and beyond. Proceedings 44th Workshop Geothermal Reservoir Engineering, 9.

Friðleifsson, G. Ó., Elders, W. A., Zierenberg, R. A., Fowler, A. P. G., Weisenberger, T. B., Mesfin, K. G., Sigurðsson, Ó., Níelsson, S., Einarsson, G., Óskarsson, F., Guðnason, E. Á., Tulinius, H., Hokstad, K., Benoit, G., Nono, F., Loggia, D., Parat, F., Cichy, S. B., Escobedo, D., Mainprice, D., 2018. The Iceland Deep Drilling Project at Reykjanes: Drilling into the root zone of a black smoker analog. Journal of Volcanology and Geothermal Research, doi: 10.1016/j.jvolgeores.2018.08.013

Ilic, O., Sigmundsson, F., Lavallée, Y., 2020. Geological risk associated with drilling into magma at Krafla caldera, Iceland: Preliminary Evaluation. 10.

Lavallée, Y., Lamur, A., Kendrick, J. E., Eggertsson, G. H., Weaver, J., Eichelberger, J. C., Papale, P., Sigmundsson, F., Dingwell, D. B., Markússon, S. H., Mortensen, A. K., 2020. Thermal manipulation of magma boundaries: Advancing controls on fluid flow via the Krafla Magma Testbed (KMT). Proceeding World Geothermal Congress, 11.

Liotta, D., Brogi, A., Ruggieri, G., Rimondi, V., Zucchi, M., Helgadóttir, H. M., Montegrossi, G., Friðleifsson, G. Ó., 2018. Fracture analysis, hydrothermal mineralization and fluid pathways in the Neogene Geitafell central volcano: insights for the Krafla active geothermal system, Iceland. Journal of Volcanology and Geothermal Research 391

Lipman, P.W., 1992. Ash-flow calderas as structural controls of ore deposits - Recent work and future problems: US Geological Survey Bulletin 2012, p. L1–L12.

Masterlark, T., Haney, M., Dickinson, H., Fournier, T., Searcy, C., 2010. Rheologic and structural controls on the deformation of Okmok volcano, Alaska: FEMs, InSAR, and ambient noise tomography. Journal of Geophysical Research, 115(B2), B02409, doi: 10.1029/2009JB006324

Mordensky, S. P., Villeneuve, M. C., Kennedy, B. M., Heap, M. J., Gravley, D. M., Farquharson, J. I., Reuschlé, T., 2018. Physical and mechanical property relationships of a shallow intrusion and volcanic host rock, Pinnacle Ridge, Mt. Ruapehu, New Zealand. Journal of Volcanology and Geothermal Research, 359, 1–20, doi: 10.1016/j.jvolgeores.2018.05.020

Newman, A. V., Dixon, T. H., Gourmelen, N., 2006. A four-dimensional viscoelastic deformation model for Long Valley Caldera, California, between 1995 and 2000. Journal of Volcanology and Geothermal Research, 150(1), 244–269, doi: 10.1016/j.jvolgeores.2005.07.017

Reinsch, T., Dobson, P., Asanuma, H., Huenges, E., Poletto, F., Sanjuan, B., 2017. Utilizing supercritical geothermal systems: a review of past ventures and ongoing research activities. Geothermal Energy, 5(1), doi: 10.1186/s40517-017-0075-y

Schiffman, P., Zierenberg, R. A., Mortensen, A. K., Frioleifsson, G. O., Elders, W. A., 2014. High temperature metamorphism in the conductive boundary layer adjacent to a rhyolite intrusion in the Krafla geothermal system, Iceland. Geothermics, 49, doi: 10.1016/j.geothermics.2012.11.002

Shnell, J., Elders, W. A., Orcutt, J., Osborn, W. L., 2019. Exploration and development of supercritical geothermal resources on the ocean floor. Proceedings 44th Workshop Geothermal Reservoir Engineering, p 10.

Shortall, R., Davidsdottir, B., Axelsson, G., 2015. Geothermal energy for sustainable development: A review of sustainability impacts and assessment frameworks. Renewable and Sustainable Energy Reviews, 44, 391–406, doi: 10.1016/j.rser.2014.12.020

Stelling, P., Shevenell, L., Hinz, N., Coolbaugh, M., Melosh, G., and Cumming, W., 2016. Geothermal systems in volcanic arcs: Volcanic characteristics and surface manifestations as indicators of geothermal potential and favorability worldwide: Journal of Volcanology and Geothermal Research, v. 324, p. 57–72, doi: 10.1016/j.jvolgeores.2016.05.018.

Stix, J., Kennedy, B., Hannington, M., Gibson, H., Fiske, R., Mueller, W., and Franklin, J., 2003. Caldera-forming processes and the origin of submarine volcanogenic massive sulfide deposits: Geology, v. 31, p. 375–378.

Weisenberger, T. B., Axelsson, G., Arnaldsson, A., Blischke, A., Óskarsson, F., Ármannsson, H., Blanck, H., Helgadottir, M., Berthet, J.-C., Árnason, K., Ágústsson, K., Gylfadóttir, S. S., Gudmundsdóttir, V., 2015. Revision of the conceptual model of the Krafla geothermal system (LV-2015–040; p. 111). Landsvirkjun (http://gogn.lv.is/files/2015/2015-040.pdf)

Supplementary Material

This section gathers the Supplementary Materials of all chapters. The large sets of data can be numerically consulted on the depositary of the University of Canterbury. This concerns the textural and chemical raw data of the IDDP-1 cuttings, and the 3D motion reconstruction of these particles, for Chapter 4.

Chapter 2

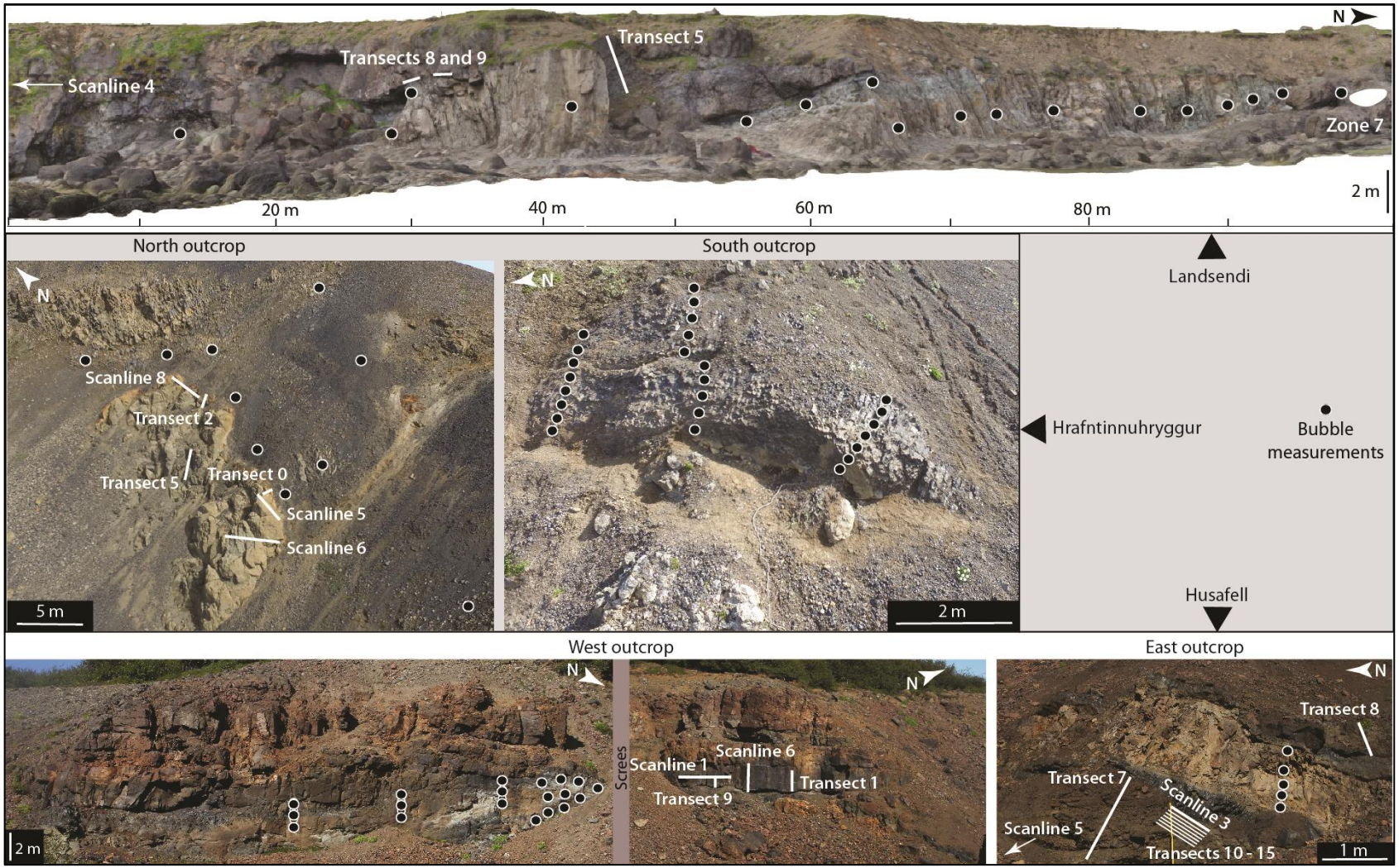

Figure S2.3. Location of measurements. Top: Landsendi. Middle: Hrafntinnuhryggur. Bottom: Húsafell. Transects refer to measure of rock properties. Scanlines are transects where we additionally conducted detailed fracture mapping. Measurements along transects 8 and 9 at Landsendi and 10 to 15 at Húsafell East were numerically performed, based on high-quality pictures from handled camera and three-dimensional photogrammetric reconstruction.

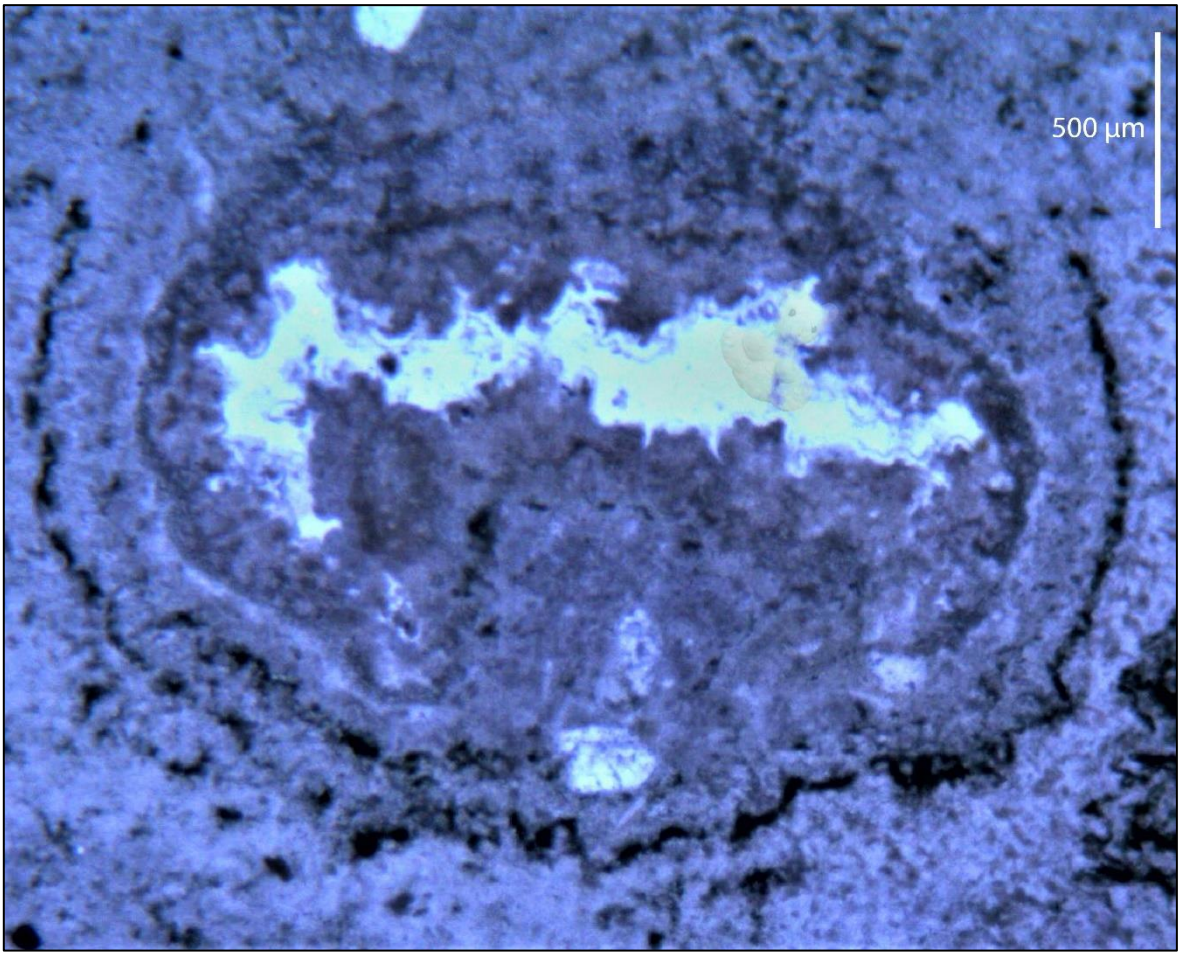

Figure S2.4. Subsolidus glass recrystallisation (spherulite or lithophysa) in thin section, PPL light. Devitrified margin of rhyolite Landsendi intrusion, at ~2 cm from the upper contact.

TABLE S2.1. ROCK PROPERTIES

	Distance (cm)	TinyPerm			Schimdt hammer		
		#	Average	std	#	Average	std
Landsendi Transect 5 Basalt	20	1	3.0E-14		4	10.0	0.8
	30				9	12.7	3.8
	30	1	1.6E-13		9	10.9	1.5
	40	1	5.6E-14		11	16.3	2.8
	50	1	1.2E-14		16	14.1	4.0
	70	1	6.7E-14		13	23.9	5.3
	90	1	1.7E-14		1	10.0	
	110	1	4.1E-14		13	34.6	7.2
	130	1	2.4E-14		14	45.1	6.5
	150	1	2.2E-14		10	38.8	6.6
	170	1	1.8E-14		10	33.3	4.0
	210	1	1.7E-14		11	35.6	9.8
	320	1	8.1E-15		10	32.0	4.1
Landsendi Zone 7 Basalt	3	1	1.3E-13				
	8	1	2.6E-14				
	15	1	5.8E-14				
	15	1	8.6E-14				
	15	1	1.3E-14				
	60	1	1.5E-14				
	60	1	1.6E-14				
Hranftinnuh-ryggur Transect 0	2	2	4.4E-14	1.9E-14			
	4	1	3.0E-13				
	7	1	2.8E-13				
	10	1	5.0E-13				
	12	1	6.1E-13				
	15	1	6.6E-13				
Hrafntinnuhryggur Transect 2 Hyaloclastite	10	4	3.0E-12	1.2E-12			
	15	4	4.7E-12	1.0E-12			
	20	4	3.2E-12	1.3E-12			
	25	4	6.2E-12	3.3E-12			
	30	4	4.2E-12	1.6E-12			
	35	4	3.4E-12	4.9E-13			
	40	4	4.1E-12	1.3E-12			
	50	4	4.6E-12	6.5E-13			
	65	4	3.4E-12	4.7E-13			
	75	4	6.4E-12	1.2E-12			
	85	4	4.5E-12	9.9E-13			
	95	4	7.6E-12	2.0E-12			
	105	4	5.2E-12	2.0E-12			
Hrantinnuh-ryggur Transect 5	150	4	5.7E-12	1.9E-12			
	155	4	7.9E-12	2.9E-12			
	160	4	1.1E-11	4.8E-12			
	165	4	8.9E-12	4.9E-12			
	170	4	8.1E-12	5.9E-12			

	Distance (cm)	TinyPerm			Schmidt hammer		
		#	Average	std	#	Average	std
Húsafell West Scanline 6 – Welded ignimbrite	0	1	4.8E-14		9	16.6	3.4
	10	1	2.3E-14		9	17.8	2.0
	20	1	1.9E-14		10	22.4	7.0
	30	1	8.2E-15		10	29.9	4.6
	40	1	9.9E-15		9	20.8	2.5
	50	1	1.7E-14		9	19.4	1.6
	60	1	1.7E-14		10	26.6	3.9
	70	1	1.5E-14		9	40.9	4.8
	80	1	1.4E-14		10	41.9	3.5
	90	1	1.9E-14		11	44.5	7.4
	100	1	1.8E-14		10	42.7	5.3
	110	1	8.8E-14		8	31.0	6.3
	120	1	9.5E-15		10	41.6	4.1
	130	1	1.5E-14		8	37.8	6.1
	140	1	2.2E-14		9	35.9	3.5
Húsafell East Transect 7 - Conglo	3	2	8.8E-15	9.1E-16			
	5	2	1.1E-14	2.2E-15			
	15	2	9.2E-14	9.0E-15			
	25	3	1.3E-13	4.0E-14			
	30	2	6.2E-13	1.9E-13			
	35	2	4.7E-14	3.2E-14			
	45	4	5.7E-13	3.0E-13			
	130	2	1.2E-13	1.8E-14			
Húsafell East Transect 8 - Conglo	1	2	7.8E-15	3.4E-15			
	5	2	4.1E-15	4.2E-16			
	23	2	3.7E-14	3.7E-14			
	50	3	7.4E-13	1.3E-13			

TABLE S2.2. FRACTURES

Site	lithology	Average area (cm^2 per fracture)	Average fracture density (m^{-1})	Measurement type
Landsendi	Fresh basalt	7.0	18.0	Scanline 4
	Damaged basalt	1.5	20.0	picture - Transect 8
	Damaged basalt	1.3	24.0	picture - Transect 9
Hrafntinnuhryggur	Fresh hyaloclastite	17.5	7.0	Scanline 5
	Fresh hyaloclastite	26.4	7.0	Scanline 6
	Damaged hyaloclastite	6.6	12.0	Scanline 8
Húsafell	Fresh welded ignimbrite	9.5	22.3	Scanline 1 + 6
	Damaged Welded ignimbrite	3.6	59.0	Scanline 1 + 6
	Fresh conglomerate	3.9	5.2	Scanline 5
	Damaged conglomerate	2.2	13.0	Scanline 3
	Lithology	**Distance from contact (cm)**	**Fracture density (m^{-1})**	**Measurement type**
Húsafell	Welded ignimbrite	1	51.3	direct - Transect 1
		3	45.0	
		5	35.0	
		10	30.0	
		15	18.8	
		20	16.3	
		30	15.0	
	Welded Ignimbrite	2	35.0	direct - Transect 9
		4	41.3	
		6	32.5	
		8	22.5	
		10	25.0	
		12	30.0	
		14	28.8	
		16	26.3	
		18	28.8	
		20	23.8	
		22	17.5	
		24	15.0	
		26	11.3	
		30	12.5	
	Welded Ignimbrite	30	19.0	direct - Scanline 6
		40	13.0	
		50	21.0	
		60	14.0	
		70	8.0	
		80	7.0	
		90	7.0	
	Conglomerate	2	8.0	Scanline 3
		5	11.0	picture - Transect 10
		10	10.0	picture - Transect 11
		15	7.0	picture - Transect 12
		20	6.0	picture - Transect 13
		25	4.0	picture - Transect 14
		30	3.0	picture - Transect 15
		50	2.0	Scanline 5

TABLE S2.3. VESICLES

	Max. 2D dimensions (mm)	Shape ratio	Equivalent diameter (mm)	Max. 2D dimensions (mm)	Shape ratio	Equivalent diameter (mm)
		Landsendi			Hrafntinnuhryggur	
	80 x 4	0.05	17.9	2 x 1	0.50	1.4
	50 x 30	0.60	38.7	4 x 1	0.25	2.0
	10 x 2	0.20	4.5	5 x 0,5	0.10	1.6
	5 x 1	0.20	2.2	5 x 1	0.20	2.2
	3 x 1	0.30	1.7	10 x 2	0.20	4.5
	2 x 1	0.50	1.4	13 x 1	0.08	3.6
	8 x 3	0.34	4.9	15 x 1	0.07	3.9
	6 x 1	0.17	2.4	12 x 2	0.17	4.9
	7 x 2	0.29	3.7	12 x 2	0.17	4.9
	5 x 2	0.40	3.2	5 x 1	0.20	2.2
	5 x 2	0.40	3.2	10 x 2	0.20	4.5
	12 x 2	0.17	4.9	10 x 1	0.10	3.2
	18 x 4	0.22	8.5	20 x 0,5	0.03	3.2
	15 x 2	0.13	5.5	5 x 0,5	0.10	1.6
	5 x 1	0.20	2.2	10 x 0,5	0.05	2.2
	8 x 1	0.13	2.8	18 x 0,5	0.03	3.0
	11 x 2	0.18	4.7	7 x 0,5	0.07	1.9
		Husafell West		7 x 2,5	0.36	4.2
8.5 m from sill tip	5 x 5	1.00	5.0	10 x 1	0.10	3.2
	8 x 10	0.80	8.9	12 x 0,5	0.04	2.4
	45 x 50	0.90	47.4	20 x 0,5	0.03	3.2
	30 x 40	0.75	34.6	15 x 1	0.07	3.9
	30 x 25	0.83	27.4	12 x 0,1	0.01	1.1
	30 x 10	0.33	17.3	9 x 0,5	0.06	2.1
5.5 m	5 x 1.5	0.30	2.7	6 x 1	0.17	2.4
	15 x 20	0.75	17.3	12 x 1	0.08	3.5
	10 x 25	0.40	15.8	9 x 1,5	0.17	3.7
	20 x 30	0.67	24.5	10 x 1	0.10	3.2
1.5 m	5 x 20	0.25	10.0	12 x 1	0.08	3.5
	10 x 30	0.33	17.3	16 x 1	0.06	4.0
	25 x 40	0.63	31.6	12 x 0,5	0.04	2.4
	2 x 10	0.20	4.5	14 x 1	0.07	3.7
Sill tip	6 x 20	0.30	11.0	17 x 1,5	0.09	5.0
	6 x 20	0.30	11.0	18 x 0,5	0.03	3.0
	7 x 26	0.27	13.5	6 x 0,5	0.08	1.7
	15 x 38	0.39	23.9	20 x 0,5	0.03	3.2
	4 x 15	0.27	7.7	10 x 2	0.20	4.5
	2 x 8	0.25	4.0	15 x 0,5	0.03	2.7
	1 x 15	0.07	3.9	11 x 0,5	0.05	2.3
	2 x 9	0.22	4.2	10 x 1,5	0.15	3.9
	0.3 x 4	0.08	1.1	12 x 1,5	0.13	4.2
	1 x 5	0.20	2.2	17 x 1,5	0.09	5.0
	2 x 11	0.18	4.7	15 x 1	0.07	3.9
	3 x 16	0.19	6.9	7 x 1	0.14	2.6
	11 x 23	0.48	15.9	10 x 1	0.10	3.2
		Husafell East				
	1 x 10	0.10	3.2			
	1 x 10	0.10	3.2			
	0.5 x 10	0.05	2.2			
	1 x 5	0.20	2.2			
	2 x 10	0.20	4.5			

Chapter 3

TABLE S3.1. FIELD DATA - FRACTURES

Lithology	Fracture density (fractures per metre)	Fracture area (cm²/fracture)	Measurements location
Intrusion core	10	26.1	Landsendi
	9.5	85.1	Hrafntinnuhryggur
	12.9	11.9	Deildargil West
Sill tip	12	11.5	Landsendi
Chilled margins	23	2	Landsendi
	15	3.1	Hrafntinnuhryggur
	18	3.5	Hrafntinnuhryggur
	18	2	Hrafntinnuhryggur
	17	1.5	Hrafntinnuhryggur
	29.8	2	Deildargil East

Note: values are average calculated per >1 m-long transects across units

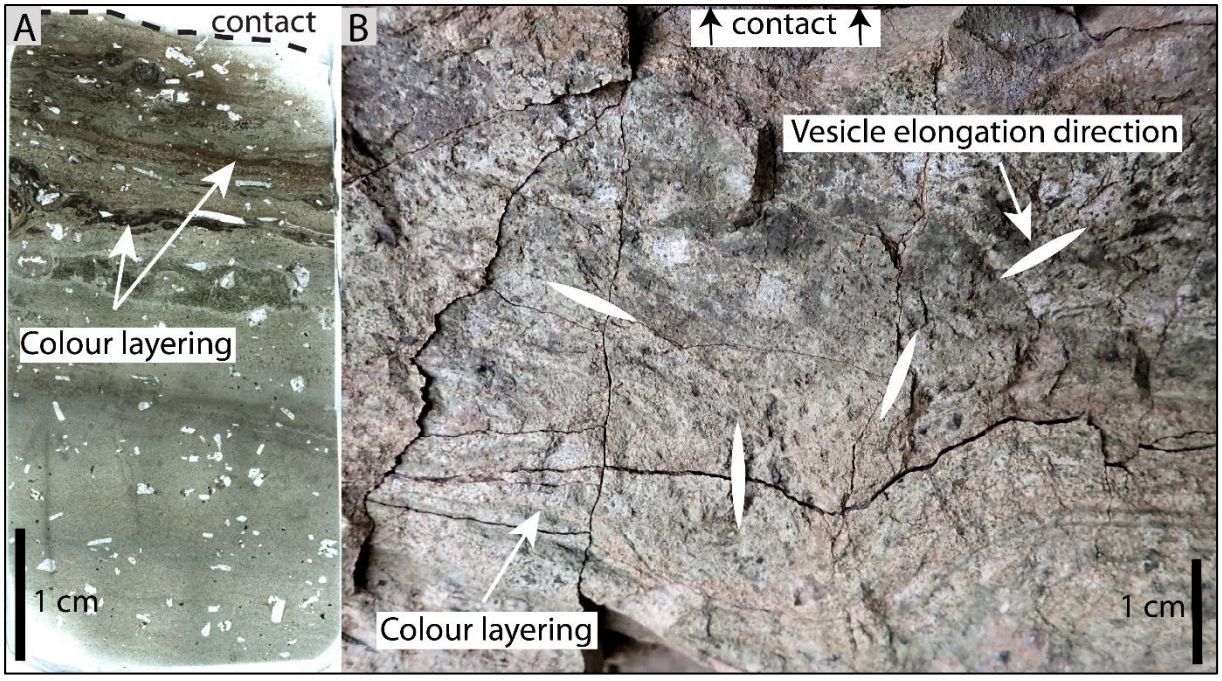

Figure S3.1. Evidence of magma flow in intrusion during chilling. A) Thin section of the devitrified chilled margins at the upper contact of the Landsendi sill, which conserved flowing colour bands (e.g. Saubin et al., 2019). B) Altered upper margin of Skaldardalur intrusion. Elongated vesicles indicate flowing deformation. Some light colour bands are visible on the bottom part of the picture.

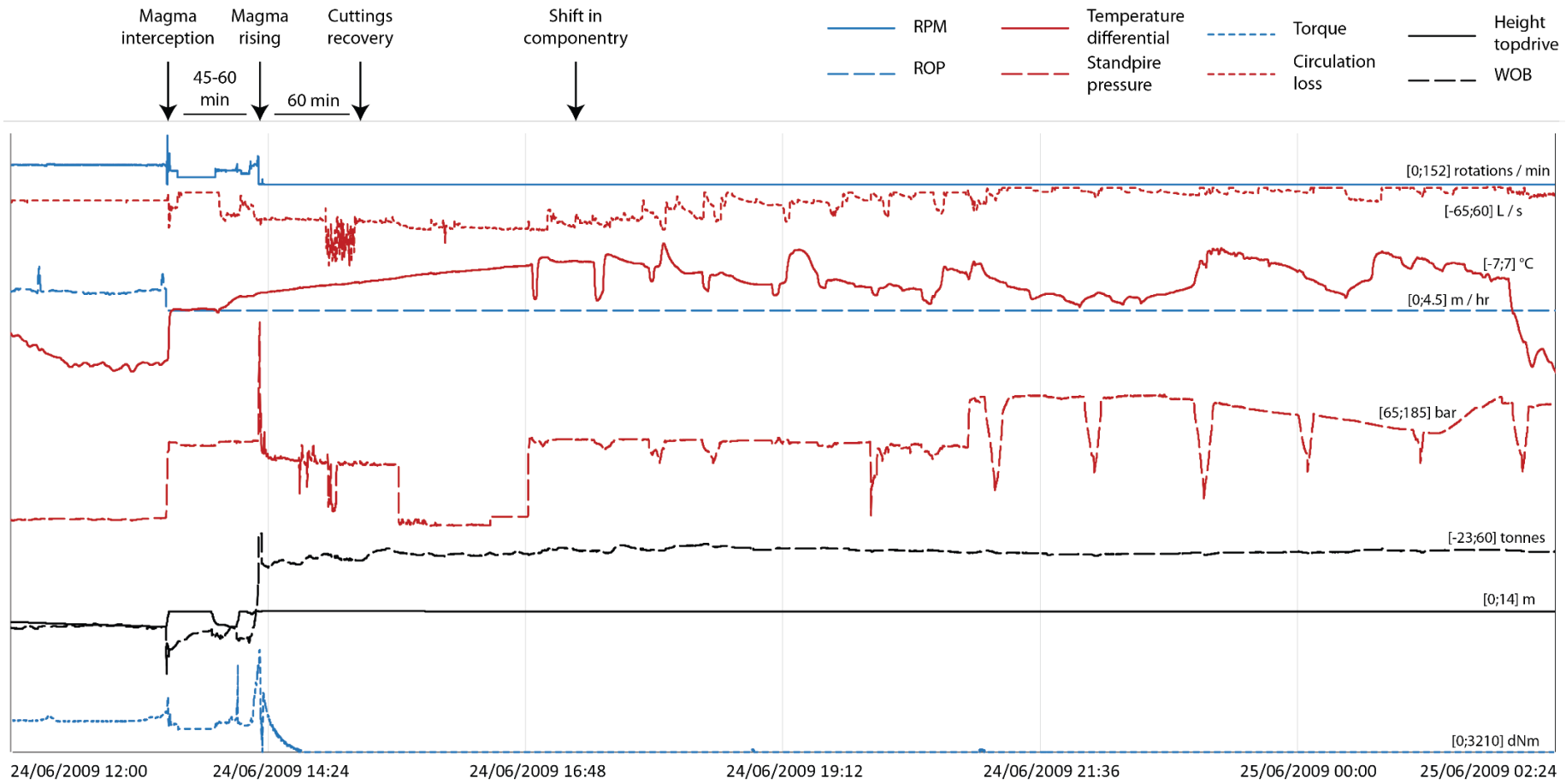

Figure S4.5. Time evolution of drilling parameters during the magma interception by the IDDP-1C well over the total duration of cuttings retrieval (15:15-00:50). In blue are the parameters referring to the drill bit (RPM, the rotation per minute; ROP, the rate of penetration; Torque, the resistance to rotation). In red are the parameters that can inform the conditions and properties at depth (Temperature differential of drilling fluids in and out of the well, Standpipe pressure, Loss of drilling fluids circulation). The height of the topdrive informs the up and down movements of the drill bit, associated with WOB, the weight put on the bit at the surface.

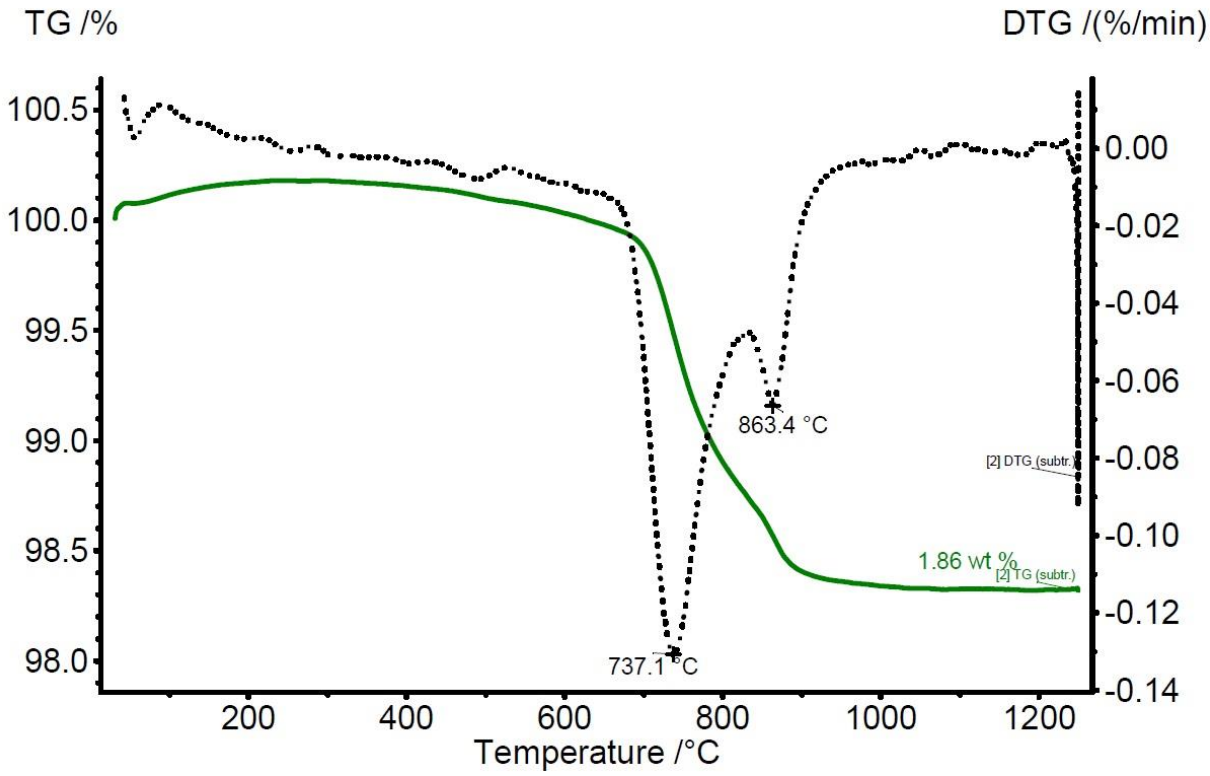

Figure S4.2. TGA (green) and dTGA (black) curves from dehydration experiments on IDDP-1 glass. The TGA curve shows a total mass loss of ~1.86 wt %. The dTGA curve indicates that the vast majority of mass loss occurred over the temperature interval 600-1000 °C. This corresponds to the high-temperature diffusive loss of magmatic water, as opposed to lower temperature loss of water added via secondary hydration (Denton et al., 2009; Giachetti et al., 2015). The dTGA peaks, which occur at 737 °C and 863 °C, exactly match the H_2O signal as determined by the mass spectrometer, indicating that the vast majority of the exsolved volatile phase is H_2O. The origin of the two pulses of H_2O loss is unclear but may reflect diffusive loss from the matrix (broader, lower temperature peak), followed by more abrupt H_2O release from melt inclusions during phenocryst resorption. The measured patterns of volatile release indicate that low-temperature hydration was insignificant, and thus that the volatile concentrations indicate magmatic volatile species at magmatic temperatures.

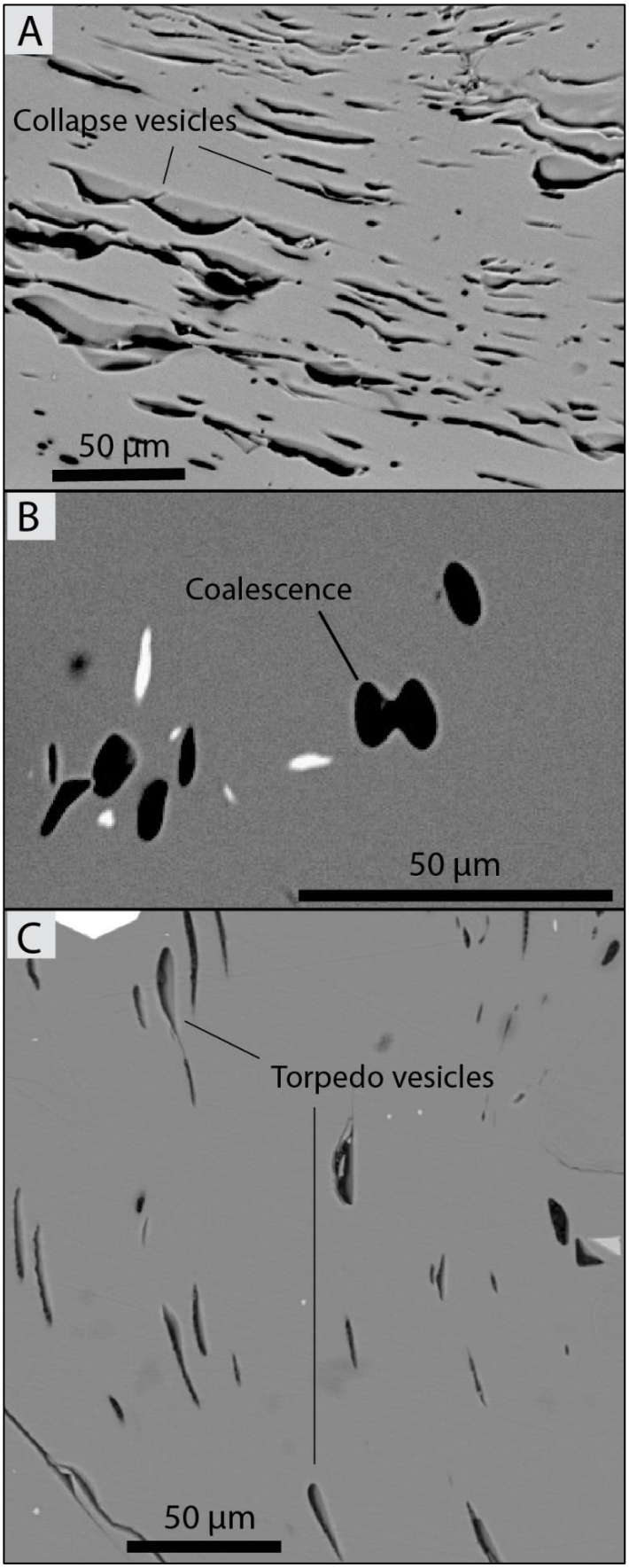

Figure S4.3. Vesicles textures shown in BSE images. A) Glassy felsite particle sampled at 16:30, >3 % vesicularity. Deformed vesicles shape is caused by vesicle collapse. B) Coalescence texture in clear glass with <1 % vesicles sampled at 16:00. C) Elongated vesicles with torpedo shapes in a clear glass with <3 % vesicularity, sampled at 23:00.

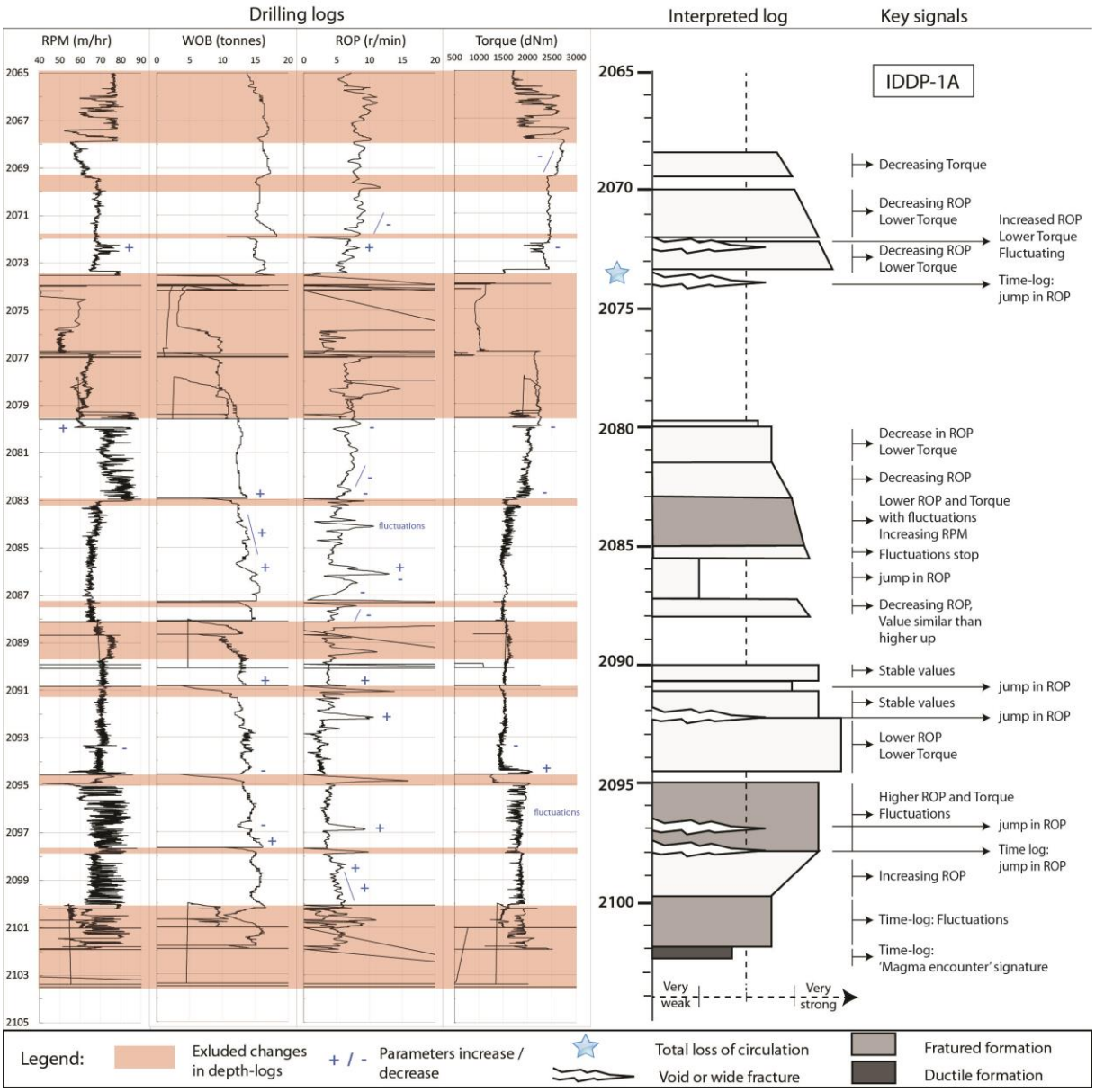

Figure S5.1. Transition from drilling logs to interpreted log of rock properties for the IDDP-1A leg. The key changes in drilling parameters used to effectively interpret the types of lithology encountered are listed on the right column. Some changes have been observed exclusively on the time-logs.

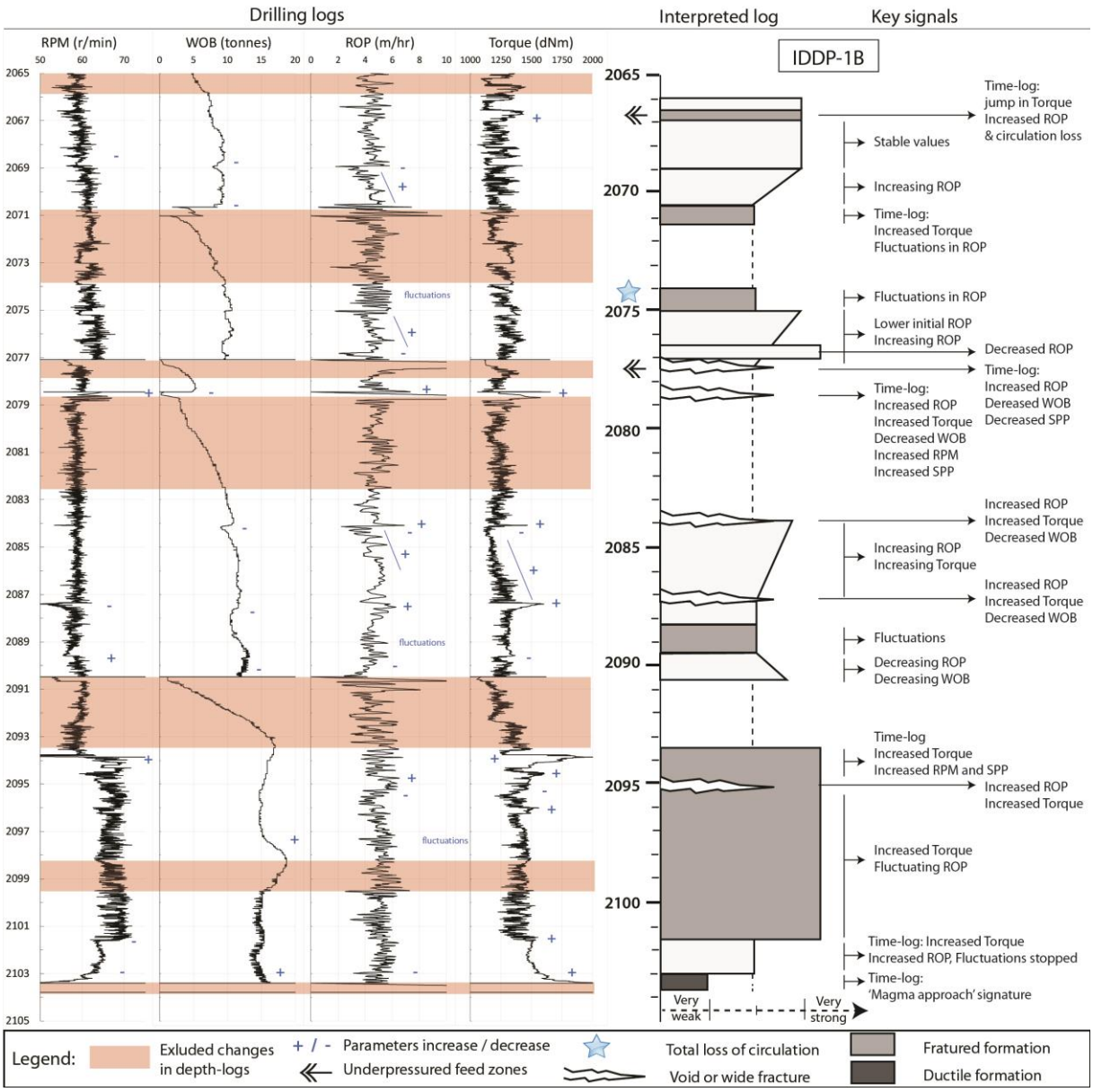

Figure S5.2. Transition from drilling logs to interpreted log of rock properties for the IDDP-1B leg. The key changes in drilling parameters used to effectively interpret the types of lithology encountered are listed on the right column. Some changes have been observed exclusively on the time-logs.

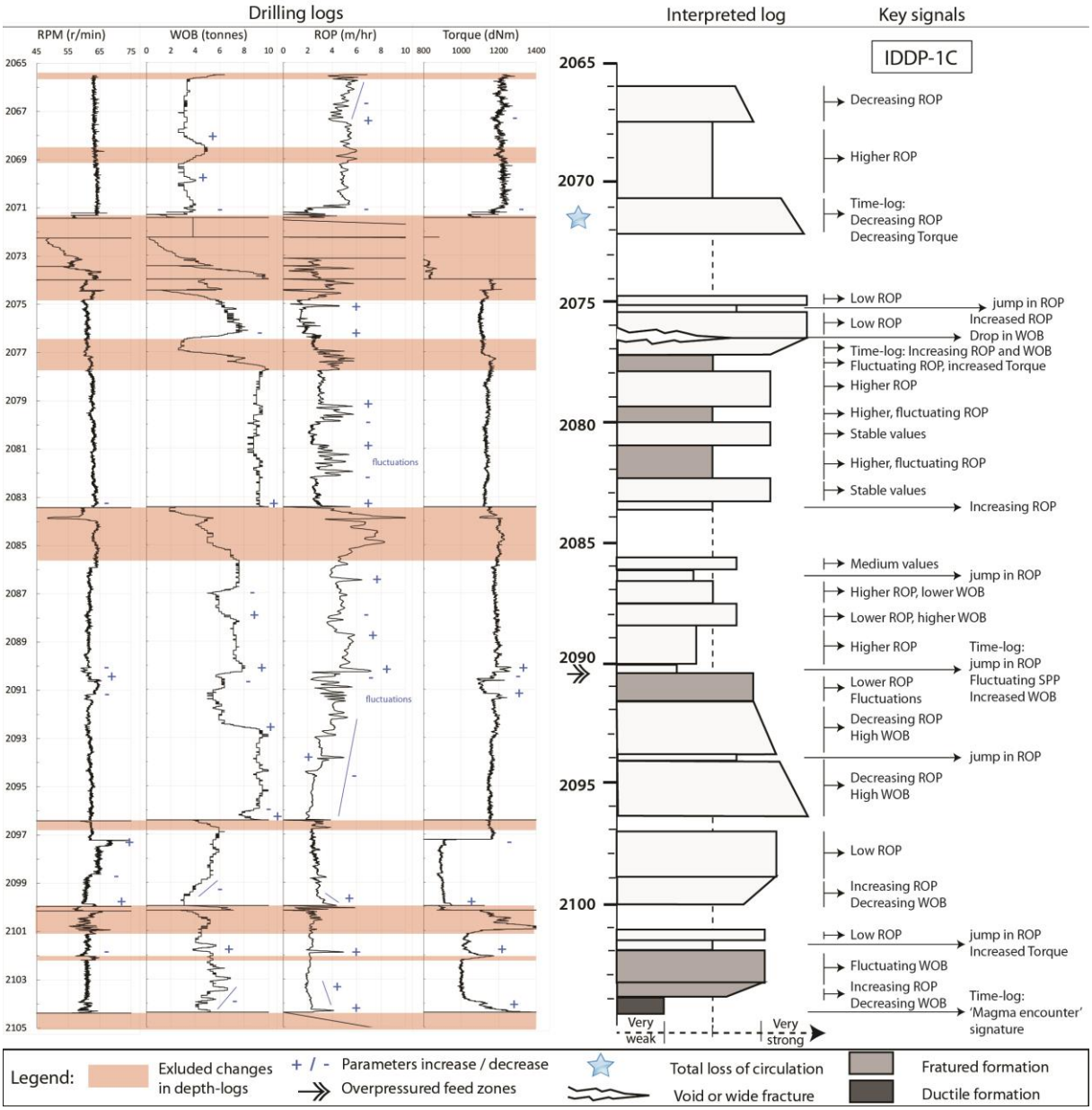

Figure S5.3. Transition from drilling logs to interpreted log of rock properties for the IDDP-1C leg. The key changes in drilling parameters used to effectively interpret the types of lithology encountered are listed on the right column. Some changes have been observed exclusively on the time-logs.

Kia Ora